MITTEILUNGEN

Institut für Geotechnik (IGtH)

Leibniz Universität Hannover

Heft 74

Numerical Modeling of Spatial Passive Earth Pressure

von

Ghassoun Somar

Hannover 2012

Numerical Modeling of Spatial Passive Earth Pressure

Von der

Fakultät für Bauingenieurwesen und Geodäsie
der
Gottfried Wilhelm Leibniz Universität Hannover

zur Erlangung des akademischen Grades

DOKTOR-INGENIEUR
Dr.-Ing.

genehmigte Dissertation
von

M.Sc. Somar Ghassoun

geboren am 28.08.1977, in Damaskus / Syrien

2012

Die vorliegende Arbeit wurde als Dissertation im Rahmen des Promotionsverfahrens an der Fakultät für Bauingenieurwesen und Geodäsie der Leibniz Universität Hannover eingereicht und angenommen.

Referent: Prof. Dr.-Ing. M. Achmus
Korreferent: Prof. Dr.-Ing. N. Meyer
Korreferent: Prof. Dr.-Ing. N. A. Fouad
Vorsitz: Prof. Dr.-Ing. U. Nackenhorst

Tag der Promotion: 23.07.2012

Vorwort des Herausgebers

Die Berechnung von Erddrücken und Erdwiderständen ist ein zentrales Problem der Bodenmechanik, da sie bei der Lösung fast jeder grundbaulichen Fragestellung erforderlich ist. In den meisten Anwendungsfällen kann man in guter Näherung annähernd zweidimensionale Verformungszustände, d.h. einen ebenen Verzerrungszustand, unterstellen. Zumindest aus Sicht der Praxis ist das Problem des zweidimensionalen Erddrucks weitestgehend gelöst. Es existieren allgemein anwendbare Lösungen sowohl für die Größe des Erddrucks bzw. Erdwiderstands im Bruchzustand als auch für die Entwicklung des Erddrucks mit zunehmender Verschiebung des betrachteten Bauteils. Für Bauteile mit begrenztem Verhältnis von Breite zu Einbindetiefe kann es jedoch sinnvoll oder auch notwendig sein, das räumliche Erddruckproblem zu betrachten. Beim Erdwiderstand wird die resultierende Kraft durch die räumlichen Effekte größer. Gleichzeitig ist davon auszugehen, dass sich auch die Charakteristik des Kraft-Verschiebungs-Zusammenhangs durch die räumlichen Effekte verändert. Diese Problematik ist bislang bei weitem nicht so intensiv untersucht worden wie das entsprechende zweidimensionale Problem.

Nachdem sich Herr Dr. tom Wörden mit räumlichem aktiven Erddruck befasst hatte (Heft 68 dieser Reihe), hatte sich Herr Dr. Ghassoun die Untersuchung des dreidimensionalen Erdwiderstandsproblems in Sandböden zur Aufgabe gemacht. Als Untersuchungsmethode hat er numerische Simulationen gewählt, in denen der verschiebungsabhängige Erdwiderstand auf starre Wände bei unterschiedlichen Bewegungsmoden bestimmt wurde. Als Stoffgesetz hat er dabei Hypoplastizität gewählt, sodass er auch die durch die Druckabhängigkeit des Reibungswinkels (Barotropie) bedingte Abhängigkeit des Erdwiderstandsbeiwerts von der Wandhöhe untersuchen konnte. In diesem Sinne schließt die Arbeit auch an die Dissertation unseres Oberingenieurs am Institut für Geotechnik, Herrn Dr. Abdel-Rahman, an, welche dieser 1999 an der TU Dortmund angefertigt hatte.

Herr Dr. Ghassoun erhält sehr interessante Ergebnisse und entwickelt daraus auch neue Berechnungsansätze für räumlichen Erdwiderstand. Diese Ansätze bedürfen natürlich noch der – insbesondere experimentellen – Validierung, stellen aber eine sehr gute Grundlage für weitergehende Untersuchungen dar.

M. Achmus

Abstract

The best visualization for the passive earth pressure problem can be done by observing the movement of a rigid wall with a spatial ratio n (n = B/H, width B, embedded depth H) against a soil body. The experimental results show that the value of the passive earth pressure reaches a higher value at smaller values of spatial ratio n, which is defined as the spatial passive earth pressure E_{p3D}.This value decreases by increasing the spatial ratio n till it reaches a plane strain value at $n = \infty$.

The following thesis shed a spot light on the spatial earth pressure problem which is considered in the calculation of many soil construction problems such as retaining walls, anchors plates, piles, foundations, bridge abutment and many other different cases. The spatial passive earth pressure in many studied cases can be calculated using guidelines and recommendations obtained from previous research as well as the German standard DIN 4085.

The goal of this thesis arises from the need for more understanding about the spatial passive earth pressure problem under the influence of different factors which were neglected by the previously mentioned methods. These factors are briefly the effect of the stress level and the mobilization of the spatial passive earth pressure as a function of the corresponding wall displacement. On the other side the general factors such as soil-wall friction angle, spatial ratio and the initial soil density on the correction factor μ which is defined as $\mu=K_{p3D} / K_{p2D}$. For this purpose, a numerically investigation of the spatial passive earth pressure behind rigid vertical walls was done using the FEM. The soil therefore was modeled by using the hypoplasticity constitutive law. This study lighted many other sides of the spatial passive earth pressure problem such as the form of the spatial failure body volume, the value of the peak displacement and the spatial stress distribution along the wall. The results emphasize the importance of this thesis for the development of the calculation methods, and add new aspects for the calculations.

Keywords: spatial passiv earthpressure, FEM, German Standard DIN 4085, scale effect, rigid walls

Kurzfassung

Die beste Visualisierung für das Problem des passiven Erddrucks kann man aus der Beobachtung der Bewegung einer starren Wand (mit einem Verhältnis $n = B / H$, Breite B, Einbindetiefe H) gegen einen Bodenkörper gewinnen. Experimentelle Ergebnisse zeigen, dass die Größe des Erdwiderstandes bei kleinen Verhältnissen von n einen höheren Wert annimmt. Dieser höhere Wert wird als räumlicher Erdwiderstand E_{p3D} bezeichnet. Mit größer werdendem Verhältnis n nimmt der Erdwiderstand ab und erreicht einen minimalen Wert für $n = \infty$, was dem ebenen passiven Fall E_{p2D} entspricht.

Die folgende Dissertation beschäftigt sich mit dem Problem des räumlichen Erddrucks. Der bei einer Vielzahl von Fragestellungen, wie z.B. der Berechnung von Stützmauern, Ankerplatten, Pfählen, Fundamenten und Brückenwiderlagern berücksichtigt werden muss. Der räumliche Erdwiderstand kann in vielen Fällen anhand von Leitlinien und Empfehlungen aus früheren Untersuchungen aber auch aus der deutschen Norm DIN 4085 ermittelt werden.

Das Ziel dieser Arbeit ergibt sich aus der Notwendigkeit ein größeres Verständnis für das Problem des räumlichen Erdwiderstand unter dem Einfluss verschiedener Faktoren zu schaffen, welches durch die zuvor genannten Methoden nicht gegeben ist. Diese Faktoren sind der Effekt des Spannungsniveaus und die Mobilisierung des passiven räumlichen Erddrucks als eine Funktion der Verschiebung der Wand. Darüber hinaus müssen andere Faktoren, wie die Reibung zwischen Boden und Wand, das räumlichen Verhältnis (n) und der Einfluss der Anfangsdichte des Boden auf den Korrekturfaktor μ, der als $\mu = K_{p3D} / K_{p2D}$ definiert ist, berücksichtigt werden. Zu diesem Zweck wurde eine numerische Studie des räumlichen Erdwiderstands hinter starren vertikalen Wänden mit der finiten Elemente Methode (FEM) durchgeführt. Dabei erfolgte die Modellierung des Bodens mit Hilfe des hypoplastisches Stoffgesetzes. Im Rahmen dieser Arbeit werden darüber hinaus auch noch viele andere Seiten des räumlichen Erdwiderstands beleuchtet, wie die Form des räumlichen Bruchkörpers, die Maximalverschiebung und die Spannungsverteilung entlang der Wand. Die Ergebnisse unterstreichen die Bedeutung dieser Arbeit für die Weiterentwicklung von Berechnungsmethoden und geben neu Aspekte für die Berechnungen.

Schlagworte. räumlicher passiver Erddruck, FEM, DIN 4085, Maßstabseffekt, starre Wände

Table of Contents

Figures

Tables

Notations and Abbreviations

Latin Lower Case Letters

Symbol	Dimension / Unit	Meaning
c	kN/m²	The soil cohesion
e_0	-	The initial void ratio
e_c	-	The void ratio at the critical state
e_{co}	-	The void ratio at critic state at isotropic pressure (ps=0)
e_d	-	The void ratio at a maximum compaction using small shear cycles
e_{do}	-	The void ratio at a maximum compaction at isotropic pressure (ps=0)
e_i	-	The void ratio at isotropic compression
e_{ij}	-	The deviator matrix which describes the strain by a constant volume (shear strain)
e_{io}	-	The void ratio at isotropic compression at isotropic pressure (ps=0)
f	kN	The force which is the resultants of normal and friction forces
f_B	-	The relative displacement due to the soil limit state
f_D	-	Factor for the density
f_M	-	Factor for the scale effect
f_S	-	Factor for the degree of saturation
f_λ	-	Factor for the friction of the wall
g	m/sec^2	The gravity acceleration
h_s	MN/m^2	The stiffness of the granular soil particles
m_α	-	A function of the Rankine passive earth pressure coefficient in 2D case.
n	-	The spatial ratio
n	-	The constant parameter related to the soil particles stiffness
n_g	-	An acceleration scale factor due to the gravity acceleration
v	cm or mm	The displacement at 50% of the ultimate state

Latin Upper Case Letters

Symbol	Dimension / Unit	Meaning
B	m	The width of the wall
D	-	The soil relative density
E	kN or kg	Earth pressure load
E_a	kN or kg	Active earth pressure load
E_i	kN/m^2	The initial tangent modulus
E_p	kN or kg	Passive earth pressure load

H	m	The height of the wall
H	m	Embedded height of the wall
I_D	-	The soil density index
K_0	-	The earth pressure coefficient at rest
K_{2D}	-	Earth pressure coefficient in 2D case
K_{3D}	-	Spatial Earth pressure coefficient (3D case)
K_{ah}	-	Horizontal aktive earth pressure coefficient
K_c	-	Earth pressure coefficient due to coesision
K_{max}	kN /m^2	The initial stiffness of the soil deflection load curve
K_{max}	kN /cm/m	Secant stiffness modulus at serviceability limit
K_{ph}	-	Horizontal passive earth pressure coefficient
$K_{p\gamma}$	-	Passive earth pressure coefficient due to soil weight
K_q	-	Earth pressure coefficient due to surcharge loading q
M	-	The Ovesen-Brinch Hansen 3D correction factor
N	kN	The normal force acting on the failure plane
P	kN /m^2	Passive earth pressure
P_{ult}	kN /m^2	Passive earth pressure at the peak
Q	kN	The reaction force on the retaining wall acting normal to the vertical back of the wall.
Q_a	kN	The active reaction force on the retaining wall acting normal to the vertical back of the wall.
Q_p	kN	The passive reaction force on the retaining wall acting normal to the vertical back of the wall.
R_f	-	The failure ratio between asymptotical and curved value for the deviatoric stress
T	kN	The cohesive and frictional forces
U	cm or mm	The displacement of the wall
U(Z)	cm or mm	The moblized displacement of the wall as a function of the depth Z
U/H	-	The relative displacement of the wall
U_B	cm or mm	The wall displacement at the peak
U_{Bd}	mm	The displacement at limit state (at peak)
U_G	cm or mm	The wall displacement at the half amount of the peak
U_{Gb}	mm	The displacement at at half the failure load (serviceability)
U_{max}	mm or cm	Displacement at peak
U_p	cm or mm	The displacement of the wall at the peak
U_p/H	-	The relative displacement of the wall at the peak
W	kN	The weight of the soil
W_e	-	Mobilization function of displacement
Z	m	The depth starting from the soil ground surface

Greek Lower Case Letters

Symbol	Dimension / Unit	Meaning
χ_{Rn}	-	A dimensionless factor, defined according to mobilization earth pressure coefficients
δ_{ij}	-	The unit tensor
ε_m	-	The volumetric strain
λ_R	-	A dimensionless factor, defined according to mobilization relative displacements
α	°	Back face inclination of the structure
β	°	Inclination of the ground surface
γ	kN /m^3	The unit weight of the soil
ε	-	The strain of the soil
η_{pv}	-	Factor for the consideration of a conformity between the theoretical Equation and the experimental results
θ	°	The angle between the failure plane and the horizontal
ξ	-	The relative displacement at peak
ξ_G	-	The relative displacement at the serviceability limit
σ_v	kN /m^2	Soil vertical stress
ν	-	The soil poasson factor
φ	°	The soil friction angle
δ	°	The soil wall friction angle
$\varepsilon_{i,j}$	-	The element axial strain vector
$\gamma_{i,j}$	-	The element shear strain
μ	-	The correction factor for the earth pressure
σ_h	kN /m^2	Soil horizontal stress

Greek Upper Case Letters

Symbol	Dimension / Unit	Meaning
Δl_{Br}	mm	Displacement at peak
$\sum_e \Pi_a^e$	J	Sum of the potential outer energy over all elements e
$\sum_e \Pi_i^e$	J	Sum of the potential internal energy over all elements e
Π	J	The total potential energy of the system
Π_a	J	The potential outer energy of the system
Π_i	J	The potential internal energy of the system
Δl	mm	Mobilized displacement

1 Introduction

Retaining walls are usually constructed in order to support soil surfaces that are either vertical or inclined. The resultant earth pressure developed between a retaining wall and a retained soil system is dependent upon several factors such as mode of wall movement, the shear strength developed on the wall - soil interface, the soil shear strength parameters, the wall geometry and rigidity in addition to the generated soil failure body.

There are three main modes of retaining wall movement namely: parallel translation, rotation around the toe and rotation around the top. During parallel translation, the wall is simply displaced horizontally towards or away from the retained soil mass. For rotation around the toe, the top of the wall is displaced towards or away from the retained soil mass while the bottom remains fixed and acts as a pivot point. On the other hand for rotation around the top, the bottom of the wall moves towards or away from the soil while the top acts as a pivot point. The three main wall movement modes are illustrated in Figure 1-1 below.

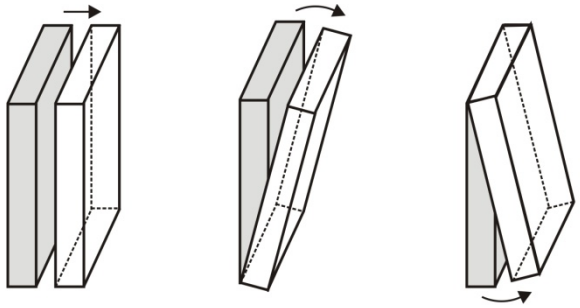

Figure 1-1: Rigid wall displacement modes relative to backfill

The earth pressure developed behind rigid earth retaining walls, in which no deformation and wall relative displacement to the soil occurs, is termed as earth pressure at rest. If the wall is allowed to move away from the soil, the earth pressure decreases after a relatively small displacement and attains a minimum value termed as the active earth pressure. The active earth pressure remains constant for further wall displacement from the soil. On the other hand, if the wall is moved from its original position towards the soil, the earth pressure increases until a maximum constant value is reached, this requires a much greater displacement than in the active earth pressure case. This maximum value is called passive earth pressure.

According to the German Standard (DIN 4085) [31] the retaining wall displacement at failure in dense sand by parallel movement lies within the range of 0.03·h to 0.05·h for the passive earth pressure case and between 0.0005·h to 0.001·h for the active earth pressure case, where h is the embedded wall depth. Figure 1-2 illustrates the passive and active earth pressure for a sandy soil.

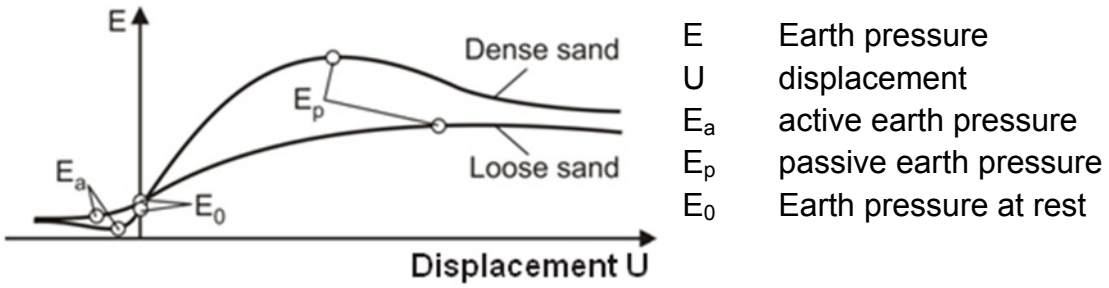

Figure 1-2: Earth pressure E as a function of wall displacement U by parallel movement [31]

The compressible nature of soil results in the development of a much larger failure wedge in the passive earth pressure state. Furthermore, the fact that the minor principal stress in the passive earth pressure state is vertical, as opposed to the active earth pressure state in which the minor principle stress is horizontal coupled with the fact that the deviatoric stress in the passive case is higher than its value in the active case, necessitates larger displacements in the passive earth pressure state in order to attain failure.

Earth pressure calculations generally use coefficients derived from analytical methods based on the classical theories for defined boundary conditions such as the mode of movement of a rigid wall of defined dimensions.

In reality most retaining walls are not rigid and often do not move according to parallel translation, or rotation around the toe or the top. In some instances, other modes of wall movement occur. Examples of such movements may include a combination of parallel with rotation movements, or pivoting of the wall about any other point excluding the top or bottom of the wall. Experience has shown that retaining walls designed using the theory based on these three main modes of wall movement with the inclusion of the requisite factors of safety have stood the test of time without collapsing. This implies that the theory based on the three wall movement modes is a fairly good approximation of the reality. The earth pressure problem is further subdivided into the classical two dimensional (2D) and the three dimensional (3D) passive or active earth pressure. Classical earth pressure theory, used by many geotechnical engineers, considers earth pressure as a 2D case. In the course of the development of the geotechnical engineering field, the measurements on the structures designed using the classical earth pressure theories however, frequently displayed variances from computations in special cases such as piles. The development of new construction and design methods in the geotechnical engineering field such as slurry walls and I-profile walls has led to the definition of a phenomenon later termed as spatial earth pressure. The spatial earth pressure may for simplicity be interpreted as an extrusion of the 2D earth pressure into a space volume. This phenomenon has greatly enhanced the understanding and description of the earth pressure problem including the stresses, the strains and soil behavior within a space volume perspective.

Extensive investigations have been carried out on the two dimensional earth pressures. Civil engineers encounter the spatial earth pressure problem frequently either as passive or active earth pressure. Spatial active earth pressure has been extensively investigated by many researchers. The most recent spatial active earth pressure research was done by tom Wörden [86]. He studied the effect of the soil density, mode of movement and wall dimensions on the spatial active earth pressure. The three dimensional passive pressure on the other hand, has not been as extensively researched. Examples of situations, in which the spatial passive earth pressure is encountered, include special cases such as anchor blocks, anchor plates, the reaction obtained while moving an embedded rigid body of limited dimensions within a soil such as retaining walls with limited breadths to depth ratio or retaining walls with varying penetration depths, pile walls such as the I-Profile walls (soldier pile and lagging soil retaining systems) and finally in stability analysis of structure foundations such as columns, bridges and arching structures.

The 3D passive pressure problem has an influence on the design of some structures such as laterally loaded embedded beams, pile caps and supporting walls used in tunnel (or pipes) heading construction methods. The spatial earth pressure is influenced by many parameters, which are majorly considered in the global earth pressure concept as previously mentioned, in addition to other parameters such as the wall dimensions and scale effect not majorly included in the global earth pressure concept. The research work carried out on these parameters is not yet exhaustive. There is a requirement for further research to be carried out on various aspects of the spatial passive earth pressure. Most of these factors will be discussed in the thesis in hand.

1.1 Objective and methodology

The objective of this thesis is to study the 3D passive earth pressure phenomenon in a granular sandy soil. For this purpose, a 3D-FEM model that consisted of different rigid walls with a horizontal soil surface was developed to simulate 3D passive earth pressure phenomenon. The hypoplastic constitutive material law was used in the numerical model.

The numerical model was validated by studying the effect of varying the following parameters on 3D earth pressure:

- The height of the wall H
- The width of the wall B
- The initial void ratio e_0
- The mode of the wall movement

The ratio of the wall width to wall height was defined as the spatial ratio $\left(\frac{B}{H}\right)$. The effect of the spatial ratio was investigated by moving walls with varied height to width ratio towards the soil. This was done for parallel translation, rotation around the top and rotation around the bottom wall movements and varied soil densities. It is to be noticed that the almost all the studied cases in this thesis are for spatil ratio n>1.

1.2 Structure of the thesis

The introduction, problem statement and methodology are presented in chapter one. The classical spatial earth pressure theories, literature review of previously carried out experimental and numerical researches on this phenomenon are presented in chapter two. Chapter three presents the finite element modeling method. A brief description of the ABAQUS program that was used for carrying out the numerical modeling of spatial earth pressure in this thesis is also included in this chapter. Chapter four highlights the hypoplasticity constitutive material law, the description of the spatial passive earth pressure modeling, the modeling procedure and the model verification. The results obtained from the numerical spatial earth pressure simulations for the three main modes of movement are documented in chapter five. Chapter six deals with the evaluation of the results presented in chapter five. Finally the summary, conclusions and recommendations drawn from the evaluation of the results are presented in chapter seven.

2 Literature review

The design of earth retaining structures requires good expertise in the behavior of the earth pressure against these structures. The earth pressure problem dates back to the beginning of the 18th century. Since then many theoretical and experimental researches have been carried out, especially during the last decades, in order to improve the design of such structures in terms of safety and economy. Some of the experimental investigations carried out, the analytical methods and numerical methods developed for the solution of the earth pressure problem are hereby highlighted.

2.1 Plane Strain (2D) passive earth pressure

2.1.1 Classical theories of plane strain earth pressure

The classical methods that have been widely used to estimate passive earth pressures are based on the Coulomb [26], Rankine [68] and Terzaghi [81] theories. The following is a review of these three theories:

Coulomb theory (1776):

The Coulomb theory [26], which was published in 1776 as ``Essai sur une application des règles de maximis & minimis ä quelques problem de statique``, is one of the most widely used methods for calculating earth pressure in the world. Coulomb's theory, which is based on total stress, considers a rigid wedge shaped mass of soil that has a vertical back face and a horizontal topographic profile. The wedge shaped soil mass is considered to be sliding upon an inclined shear surface behind a rigid retaining wall assuming a frictionless soil-wall interface as shown in Figure 2-1. The forces that act on the sliding wedge are: the weight of the soil (W), the cohesive and frictional forces (T) acting on the shear surface, the normal force acting on the failure plane (N) and the reaction force (Q_a) on the retaining wall acting normal to the vertical back of the wall.

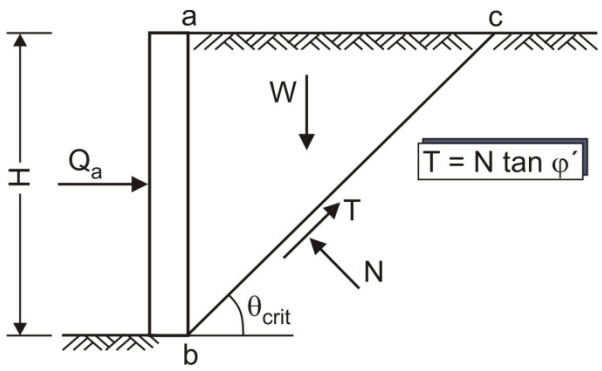

Figure 2-1 Acting forces by earth pressure using Coulomb's wedge supported by a smooth wall (δ = 0)

While analyzing the mathematical equilibrium of the forces, Coulomb observed that the inclination of the shear surface was unknown but that there is a critical shear surface for which a critical value (maximum for active and minimum for passive case) of the wall force Q is obtained. The following Equations [2.1] and [2.2] are obtained by resolving the forces in Coulomb's model along two axes (parallel and normal to the shear plane) for granular sandy soils.

$$N = W\cos\theta + Q\sin\theta \quad [2.1]$$

$$T = W\sin\theta - Q\cos\theta \quad [2.2]$$

Where:

θ The angle between the failure plane and the horizontal
N The normal force acting on the failure plane
T The shear force on the failure plane

And at failure the weight of the failure body is:

$$W = \frac{1}{2}\gamma H^2\cot\theta \quad [2.3]$$

Then by resolving the forces on the failure slip of a soil with a friction angle φ

$$\frac{T}{N} = \tan\varphi \quad [2.4]$$

$$\mathrm{Q} = \frac{1}{2}\gamma\mathrm{H}^2\cot\theta\tan(\theta-\varphi) \quad [2.5]$$

In order to obtain the maximum value of Q, δQ/δθ is set to δQ/δθ =0 which results in the active case of then following value of angle θ as shown below:

$$\theta = 45 + \left(\frac{\varphi}{2}\right) \quad [2.6]$$

And substituting into Equation [2.5] gives

$$Q_{ah} = \frac{1}{2}\gamma H^2 K_{ah} = \frac{1}{2}\gamma H^2\left(\frac{(1-\sin\varphi)}{(1+\sin\varphi)}\right) \quad [2.7]$$

Where: K_{ah} is the active earth pressure coefficient.

Having considered the addition of the force due to cohesion and expressed the retaining force Q as a function to the depth y, Coulomb gave the following Equation [2.8], in the active case, by moving the wall away from the soil.

$$Q_{ah} = \frac{1}{2}\gamma H^2 K_{ah} - 2cHK_{ah} = \frac{1}{2}\gamma H^2\left(\frac{1-\sin\varphi}{1+\sin\varphi}\right) - 2cH\sqrt{\frac{1-\sin\varphi}{1+\sin\varphi}} \quad [2.8]$$

Coulomb observed that the planar shear surface assumed for his theory was sufficiently a good approximation for a smooth wall δ = 0. He further observed that the soil wall friction angle affected the distribution of the failure slope.

Coulomb's theory can be also used to predict the passive earth pressure and forces, when the wall moves towards the soil. The angle of the shear surface to the horizontal (θ) due to the minimum passive earth pressure load Q_{ph} is:

$$\theta = 45 - \left(\frac{\varphi}{2}\right) \quad [2.9]$$

And the passive force for a cohesive soil can be expressed as in Equation [2.10]:

$$Q_{ph} = \frac{1}{2}\gamma H^2 K_{ph} + 2cHK_{ph} = \frac{1}{2}\gamma H^2 \left(\frac{1+\sin\varphi}{1-\sin\varphi}\right) + 2cH\sqrt{\frac{1+\sin\varphi}{1-\sin\varphi}} \quad [2.10]$$

Where: K_{ph} is the passive earth pressure coefficient.

As shown in Figure 2-1 Coulomb obtained a solution in terms of total stresses based on special conditions, a planar shear surface, a soil mass with a horizontal ground surface bounded by a single failure surface and a wall with a vertical back surface. The equation by Coulomb's theory was developed in a general solution for frictional, non-cohesive planar boundaries with a sloping back wall surface. A presence of frictional force between the soil and the wall was considered by Mayniel [24].

Mayniel obtained the critical angle of the planar shear surface θ using Equation [2.11]:

$$\theta_{crit} = \tan^{-1}\left(\tan\varphi + \sec\varphi\sqrt{\frac{\tan\varphi}{\tan(\varphi+\delta)}}\right) \quad [2.11]$$

Substitution of the critical angle θ in Equation [2.11] into Equation [2.5] yields:

$$Q_{ah} = \frac{1}{2}\gamma H^2 \left(\frac{1-sin\,\varphi}{cos\,\delta + (sin(\varphi+\delta))}\right) \quad [2.12]$$

One more time the solution in Equation [2.12] was extended by removing the restrictive hypotheses proposed by Coulomb and taking into consideration the effect of an inclined backfill surface and the existence of friction in the wall-soil interface to give a general solution as shown in Figure 2-2. Equation [2.13] was obtained with modified passive earth pressure coefficient applicable for non-cohesive soils.

$$Q_{ph} = \frac{1}{2}\gamma H^2 K_{ph} \quad [2.13]$$

Where:

K_{ph} The horizontal passive earth pressure coefficient for the case of an inclined backfill surface. K_{ph} is given by the expression in Equation [2.14] for non-cohesive soil:

$$K_{ph} = \frac{\sin^2(\alpha-\varphi)}{\sin^2(\alpha)\sin(\delta+\alpha)\left[1-\sqrt{\frac{\sin(\varphi+\delta)\sin(\varphi+\beta)}{\sin(\alpha+\beta)\sin(\alpha+\delta)}}\right]^2} \quad [2.14]$$

φ Angle of internal friction of soil
δ Angle of friction between the soil and the wall
β Inclination of the ground surface
α Back face inclination of the structure

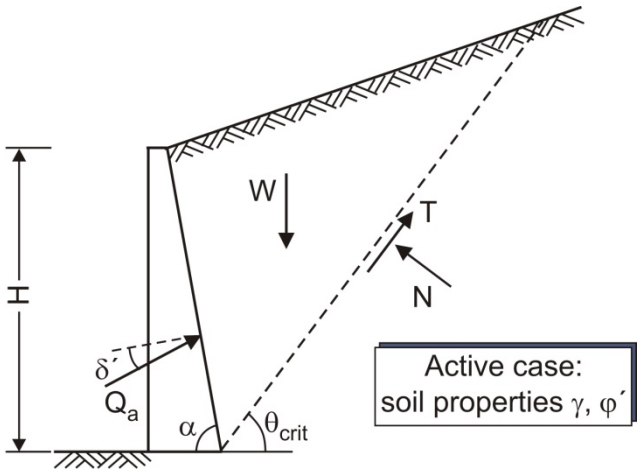

Figure 2-2: Coulomb solution for an inclined backfill surface and granular material

All the previous solutions according to Coulomb's theory were developed in the terms of total stresses for a rigid (incompressible) failure wedge without any consideration of pore water pressure for failure on a critical planar shear surface. In reality however, the surface of the sliding in the backfill behind a retaining wall is slightly curved. Coulomb assumed a plane surface in order to simplify the computations. The error due to this assumption is quite small as long as the friction angle between the soil and the wall is small or equal to zero. This implies that the wall sliding surface is almost smooth. However, according to Terzaghi [81] the error by passive pressure is excessive when wall friction angle (δ) exceeds the value $\frac{\varphi}{3}$. The planar shear surface should not be used in this case. Furthermore, the curvature of the sliding surface must also be taken into account.

The Mohr-Coulomb method offers the advantage of simple applicability by using K_{ph} values from tables or curves. It is also applicable for the use of all soil-wall interface friction angle values. The limitation of the Mohr-Coulomb method is that it can only be used with simple conditions. Increasing complexity of the conditions such as a high wall friction angle leads to a decrease of the accuracy. Therefore another solution is to be illustrated by Rankine in the following.

Rankine (1875):

Rankine [68] assumed that the soil behind a retaining wall is in a condition of incipient failure. The whole soil behind the wall is in state of plastic equilibrium (see Figure 2-3), but the translation between elastic and plastic conditions does not occur until the wall moves into the soil more than a certain limit of the displacements.

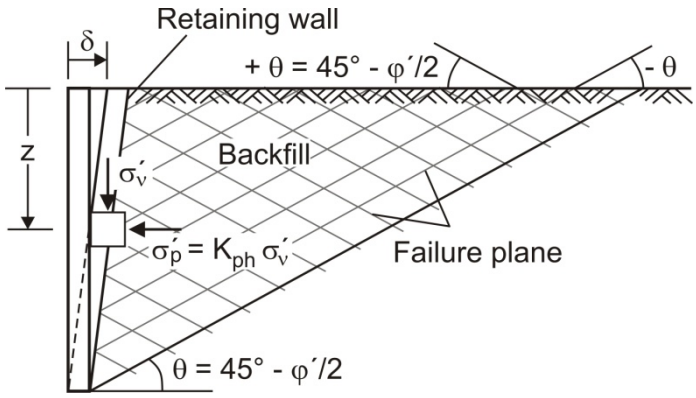

Figure 2-3: Rankine passive earth pressure theory [68]

He extended the earth pressure theory by deriving a solution for a complete soil mass in a state of failure. Rankine assumed that the resultant force on the wall acts parallel to the ground surface. Therefore the value of the soil wall friction angle is equal to the inclination of the ground surface and cannot be varied. The Rankine condition for a horizontal ground surface is only applicable to walls with smooth back surfaces $\delta = 0$.

Whereas the Coulomb's solution considered a soil mass bounded by a single failure surface, Rankine assumed that every element within the sliding wedge is on the verge of failure in his solution. Rankine considered an element of the sand symmetrical with reference to a vertical plane having a depth Z and a cross-sectional area equal to unity, for the development of his theory as shown in Figure 2-3. In the case of passive earth pressure, when the structure moves towards the soil, the element of soil is compressed. As a result of the compression σ_h and the earth pressure coefficient $K = \frac{\sigma_h}{\sigma_v}$ increase while σ_v is constant and smaller than σ_h. The coefficient K increases from K_0 (the earth pressure coefficient at rest) till it becomes equal to K_{ph} (the passive earth pressure coefficient). The minor principle stress in this passive case by Rankine is vertical and the angle of the sliding surface is $\theta = 45^\circ - \frac{\varphi}{2}$.

In 1882 Mohr [24] presented the relation between stresses and strains on and within an element in a solid in plastic equilibrium as a circle as shown in Figure 2-4.

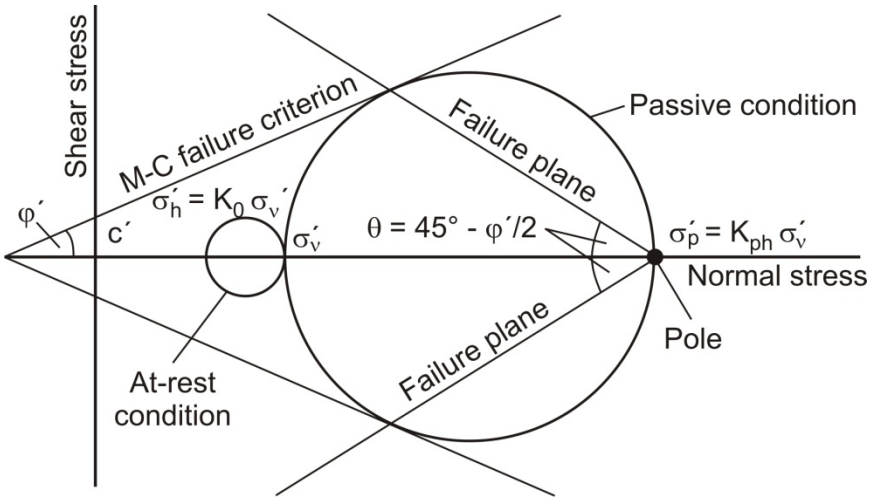

Figure 2-4 : Rankine's theory in Mohr's circles

Rankine used later the Mohr circle to obtain the solution of the passive and active earth pressure. Mohr's circle represents the stress conditions in a soil element located at a depth (Z) below the ground surface as shown in Figure 2-3. When the structure starts moving toward the backfill in the passive earth pressure case, the lateral stress σ_h increases while the vertical stress σ_v essentially remains constant. The lateral stress reaches its maximum possible value, when the Mohr-coulomb failure criteria becomes tangent to Mohr's circle. In Rankine's simple solution there is no shear stress on either the vertical or the horizontal planes of the element. Rankine obtained a solution for passive earth pressure coefficient in a case of a soil with horizontal surface and a vertical back face of a rigid wall as shown in Equation [2.15].

$$K_{ph} = \left(\frac{1+\sin\varphi}{1-\sin\varphi}\right) \qquad [2.15]$$

For the case of a soil mass with its ground surface inclined to the horizontal at an angle β, under the consideration that at failure the Mohr circle must touch the failure envelope or the Mohr–coulomb failure criterion and the horizontal stress σ_h is acting parallel to the ground surface, Rankine obtained the following solution in Equation [2.16] for the passive earth pressure coefficient.

$$K_{ph} = \cos\beta \frac{\cos\beta + (\cos^2\beta - \cos^2\varphi)^{\frac{1}{2}}}{\cos\beta - (\cos^2\beta - \cos^2\varphi)^{\frac{1}{2}}} \qquad [2.16]$$

Where:

β Inclination of the ground surface
φ Angle of internal friction of soil

Rankine's theory is a simple method, but it assumes that the wall friction angle is equal to the ground surface inclination. Rankine is better suited for simple conditions such as horizontal ground surface or homogeneous soil.

Log Spiral Method (1938):

The Log spiral method is an extension of Coulomb's theory [26]. This method is based on the determination of the actual shape of the failure surface in the soil. It is less widely used than the theories of Coulomb and Rankine. The failure slip surface in this method consists of a spiral part and linear part as shown in Figure 2-5. The soil within the area between the wall and the upper straight part of the failure slip surface is assumed in the passive Rankine state, but the resultant passive earth pressure and its distribution over the contact area between the wall and the soil depends on the behavior of the interface contact area.

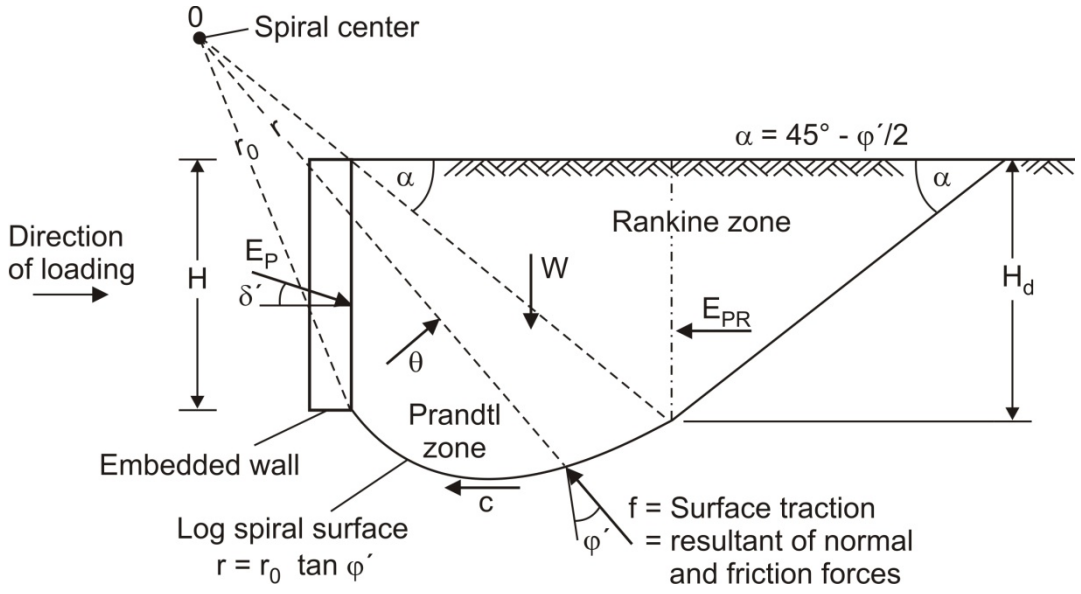

Figure 2-5: Log spiral failure mechanism (Duncan and Mokwa [28])

The curved part of the slip surface is assumed to be a logarithmic spiral. This spiral is tangent to the straight part of the slip surface. The forces acting on the soil wedge are: the weight of the soil (W), the force (f) which is the resultant of normal and friction forces, the cohesion force on the curved part of the slip surface (c) and the force E_{PR} as shown in Figure 2-5. The value of the passive force on the wall is obtained by taking the moment of the forces around the center of the spiral part (O). Similar computations are performed for other arbitrarily selected slip surfaces. The geometry of the critical sliding surface is established through a minimization of the passive earth pressure force required to maintain equilibrium with the soil at failure along the shear surface, by varying the position of the spiral centre, until the smallest passive pressure is approached. Tables and diagrams for K_{ph} were established by Caquot and Kerisel [45] based on the Log-spiral theory as shown in Figure 2-6.

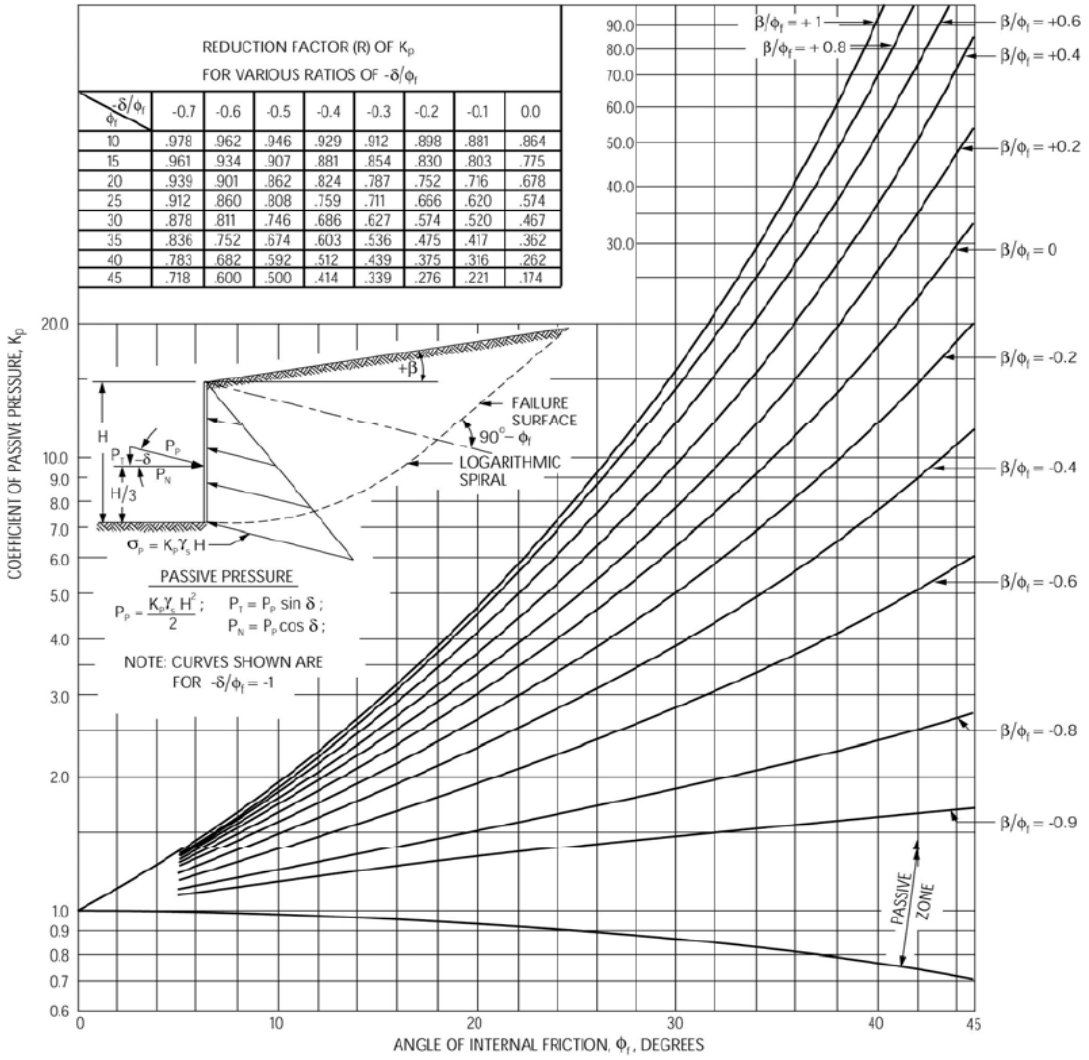

Figure 2-6: Coefficients for active and passive earth pressure using log spiral method [45]

In this method the form of the non linear failure slope is intermediate between an arc of a circle and of a spiral. The error due to replacing this non linear failure slope with either a circular or logarithmic spiral is very small.

The log spiral theory is a good approximation and offers a high accuracy for any values of soil-wall friction angle δ. It is also applicable for spatial earth pressure using Ovesen - Hansen correction factors, which will be illustrated later. The solution of earth pressure problems using the log spiral method requires numerical programs. These numerical programs are mostly applicable only for simple conditions such as level ground surface, vertical wall and homogeneous soil. The Log spiral method yields higher accuracy in comparison to the Mohr Coulomb theory for wall friction angles $\delta > 0.4\varphi$.

2.1.2 Experimental Investigations on plane strain passive earth pressure

Laumans (1977):

Laumans [47] carried out experiments using an embedded wall model that rotated around a point near the wall bottom. Furthermore the occurrence of bending deformation is permitted. The model wall was embedded to a depth of 80.0 cm. Dry poorly graded coarse sand with densities of D_r = 35.0 % and D_r = 54.0 % were used.

The results of his work deal with the maximum values, the displacement magnitude and the mobilization function characteristic in addition to the point of action for the resultant passive earth pressure.

Furthermore finite element calculations were made with the consideration of the material properties of granular sandy soil. A non-linear Equation was developed by using a hyperbolic mobilization curve for the passive earth pressure.

Laumans developed the following hyperbolic mobilization approach:

$$K_{mob} = K_{ph} \frac{U+V}{U} \qquad [2.17]$$

Where:

K_{mob} The mobilized earth pressure coefficient
K_{ph} The earth pressure coefficient at peak
U The displacement of the top
V The displacement at 50% of the ultimate state (Serviceability)

Figure 2-7 below shows a comparison between the numerical and experimental results by Laumans for the normalized horizontal earth pressure load $\overline{H}$ as a function of the wall top displacement U for two different soil densities γ = 16.0 and 16.5 kN/m^3 with different friction angles.

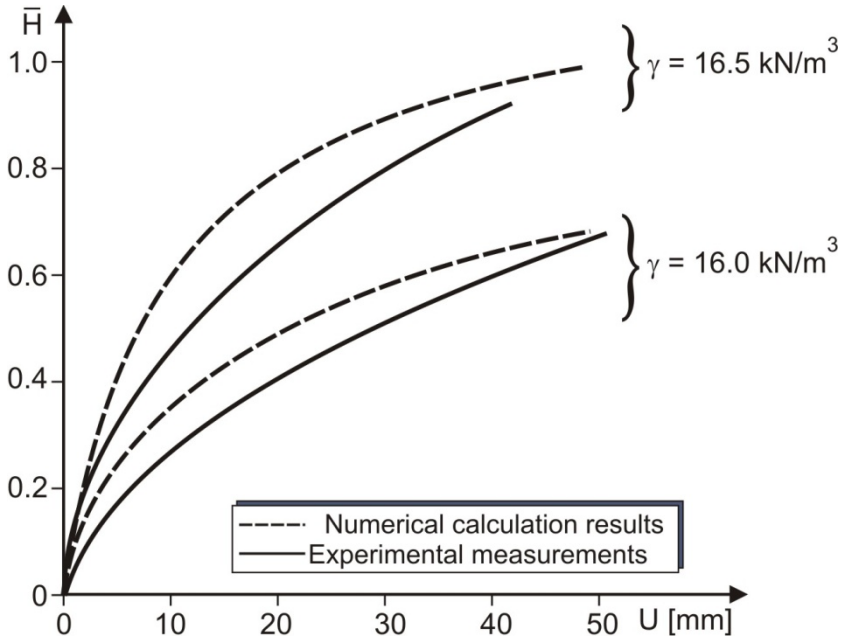

Figure 2-7: Numerical and experimental results for horizontal earth pressure load $\bar{H}$ as a function of the wall displacement U according to [47]

It was observed that the results of the numerical model and the experimental test did not agree well with each other. Laumans attributed this to the accuracy of the laboratory tests used to determine the soil parameters and the assumptions made for the numerical model.

Vogt (1984):

Laumans' Equation was modified by Vogt [90] using finite element calculations and experimental investigations. In his experiments the embedded wall was allowed to rotate around a point in the lower third of the wall as shown in Figure 2-8. Vogt used carbon rods instead of sandy soil in order to visualize the failure mechanism. He applied modified Equation assumptions to other modes of wall movement.

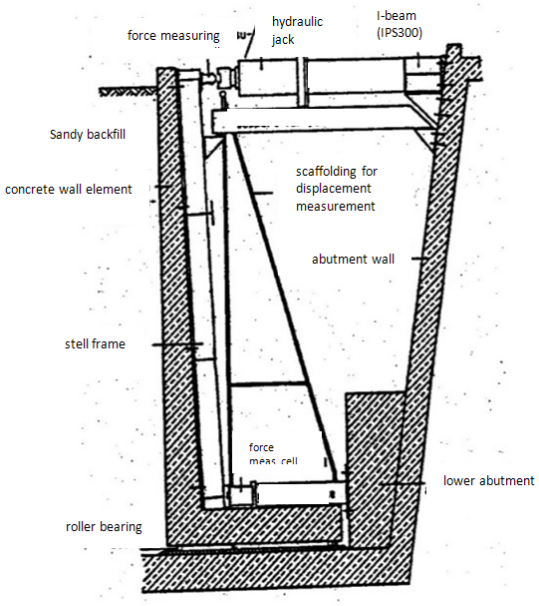

Figure 2-8: Schematic cross section of the model developed by Vogt [90]

Vogt made the following assumptions to develop a mobilization earth pressure function:

- The earth pressure depends on the relative displacement of the wall $\frac{U(Z)}{Z}$.
- The initial soil stress condition of the earth pressure at rest (K_0) is simply added to the soil stress condition developed as a result of the wall displacement.

The following Equation [2.18] describes the mobilization function of the earth pressure coefficient K_{mob}:

$$K_{mob} = K_0 + (K_{ph} - K_0)\left[\frac{(\frac{U(Z)}{Z})}{(a+\frac{U(Z)}{Z})}\right] \quad [2.18]$$

K_o Earth pressure coefficient at rest
a Constant parameter which is determined according to the soil stiffness
K_{ph} Horizontal passive earth pressure coefficient at peak
$\frac{U(Z)}{Z}$ Relative displacement

Figure 2-9 shows a comparison between the mobilization function of the passive earth pressure by Vogt (black line) and the experimental results for the three main wall movement modes at a point with a constant depth.

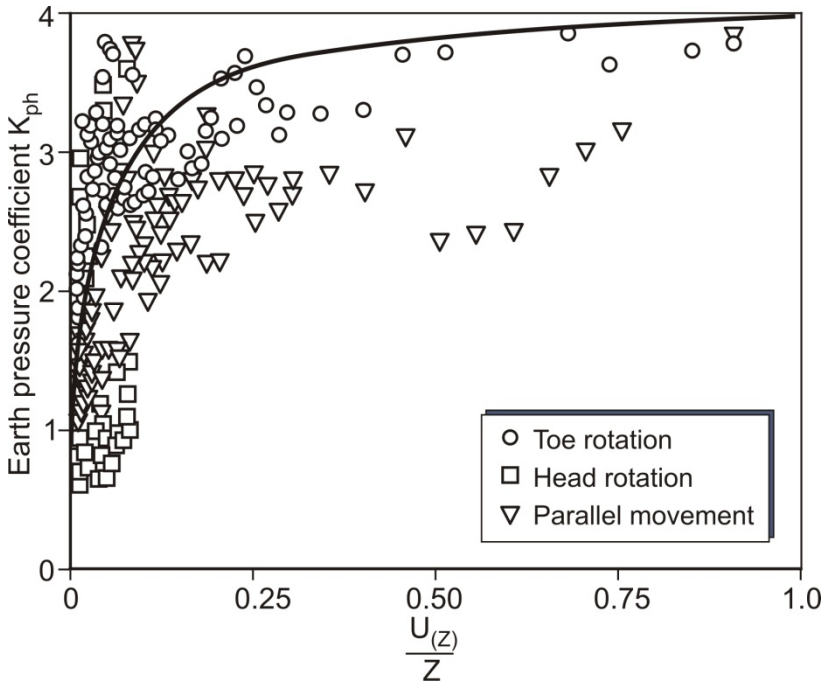

Figure 2-9: Earth pressure coefficient as a function of relative displacement [90]

It is observed from Figure 2-9 that a good agreement between the experimental results and the mobilization function occurs for small mobilized displacements. By increasing the displacement, the mobilization function is in good agreement with the experimental values of passive earth pressure coefficient only for rotation around the toe.

In his experiments Vogt also investigated the development of the earth pressure distribution along the wall depth as a function of the wall displacements for different wall movement modes as shown in Figure 2-10.

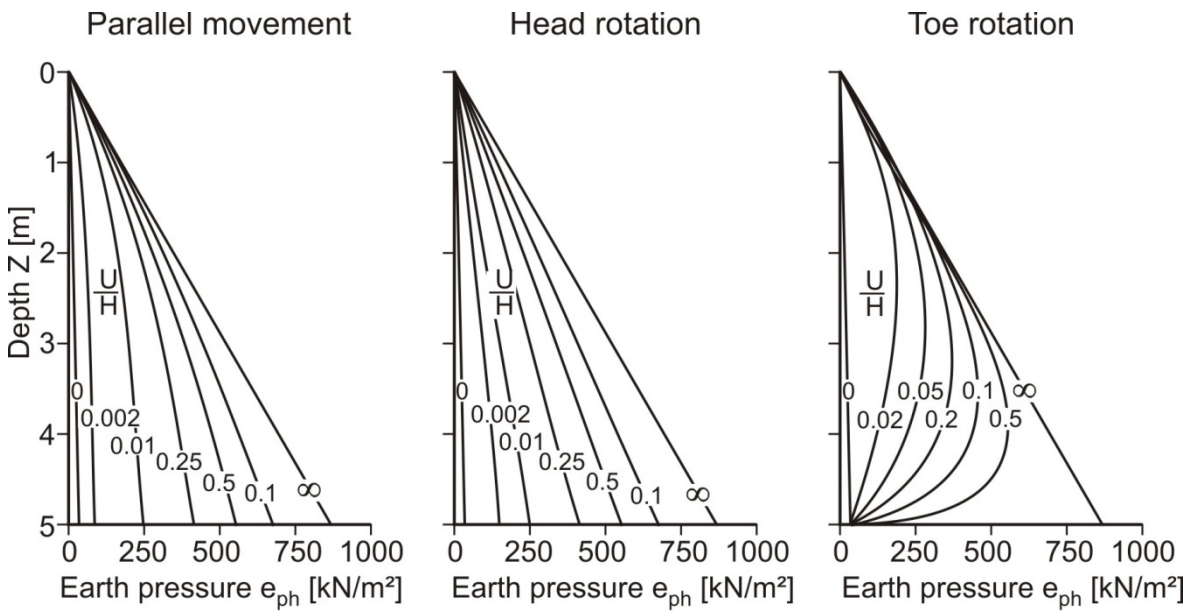

Figure 2-10: The earth pressure distribution along the wall depending on the relative displacements [90]

Mao (1993):

Mao [48] carried out experiments with several models in order to investigate the dependence of passive earth pressure in sandy soil for different modes of wall movement, wall friction angles, degrees of saturation, embedded depths (t) and soil densities. Therefore Karlsruhe coarse sand with relative densities between $D_r = 35$ % to 80 % was used. The height of the model wall was varied between h = 0.10 m and h = 0.25 m. The results of his experiments deal with the maximum passive earth pressure value, the corresponding displacement magnitude and the mobilization function in addition to the position of the resultant force. Figure 2-11 shows results for ratios of the mobilized passive earth pressure load E_{ph} to the maximum passive earth pressure load at peak max E_{ph} (E_{ph}/maxE_{ph}) as a function of displacement for different wall friction angles δ.

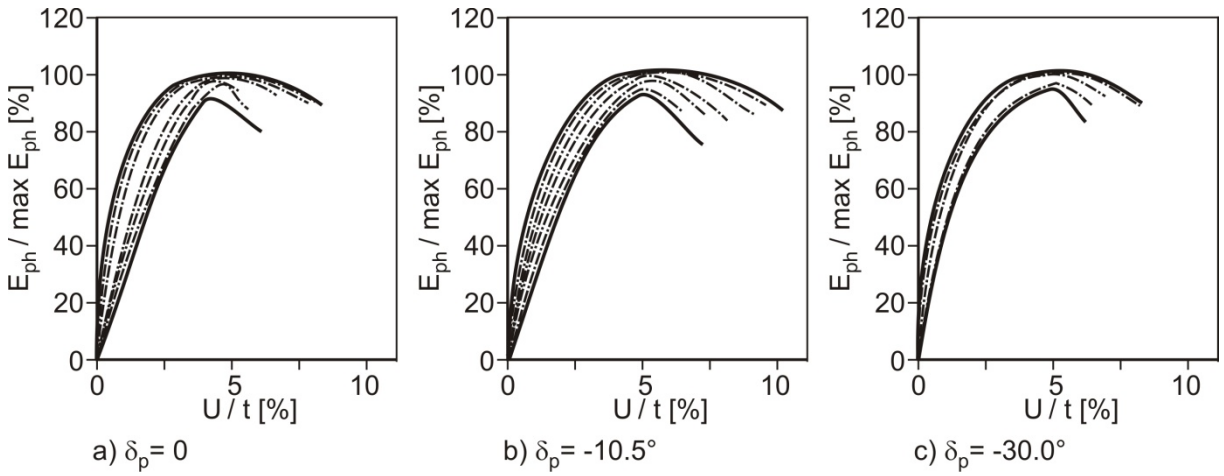

Figure 2-11: Earth pressure coefficient as a function of relative displacement for sandy soil (D = 65 %) with different values of soil-wall friction angle δ [48]

Fang, Chen and Wu (1994):

Fang, Chen and Wu [30], [21] examined different modes of wall movements in their passive earth pressure experiments as shown in Figure 2-12. A rubber layer was used between wall-soil interfaces to reduce friction. Ottawa sand ($e_{max} = 0.76$, $e_{min} = 0.50$, $D_{60} = 0.36$ mm, $D_{10} = 0.23$ mm, $\gamma_s = 26.5$ kN/m^3) was used in the experiment. The initial density of the sand at the beginning of the experiment was 15.5 kN/m^3. The dimensions of the model wall were: Height H = 0.50 m, Width B = 1.0 m and Thickness t = 0.12 m.

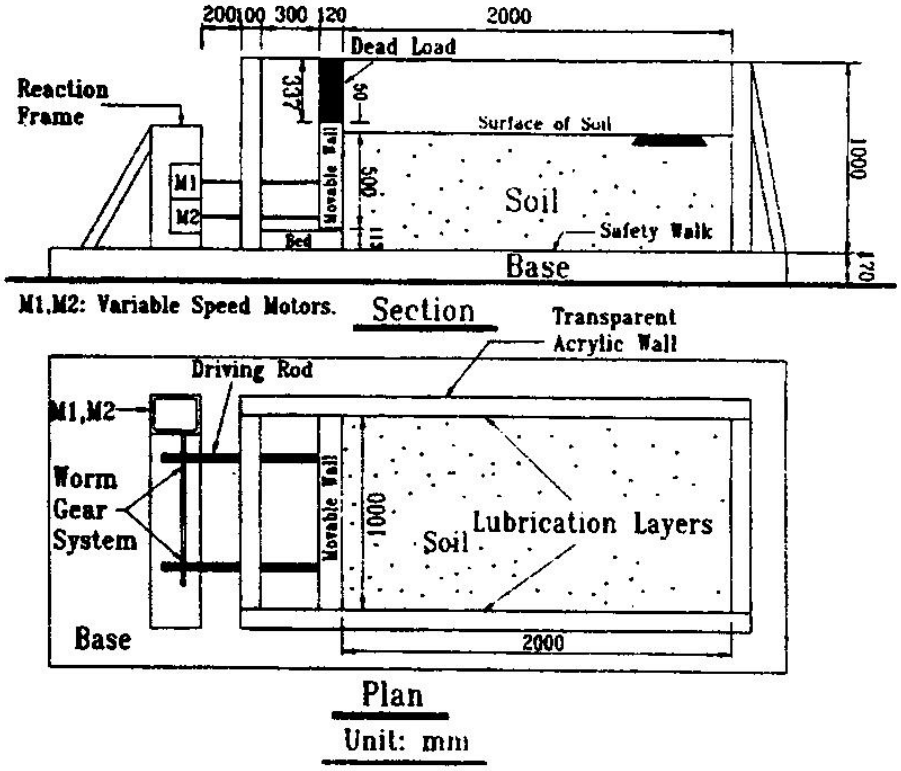

Figure 2-12: Dimensions and the setup of passive earth pressure model [30]

In addition to determining the maximum earth pressures, the displacement magnitudes, the mobilization function and the earth pressure distributions were illustrated at different stages of the wall movement as shown in Figure 2-13. The Figure shows an increase of the earth pressure due to an increase of displacement. A peak pressure was reached at approximately relative displacement $U_p/H = 0.01$, then the pressure decreased with further wall movement because of the soil softening behavior. In Figure 2-13 the earth pressure according to Coulomb's and Terzaghi's theories are also given for comparison.

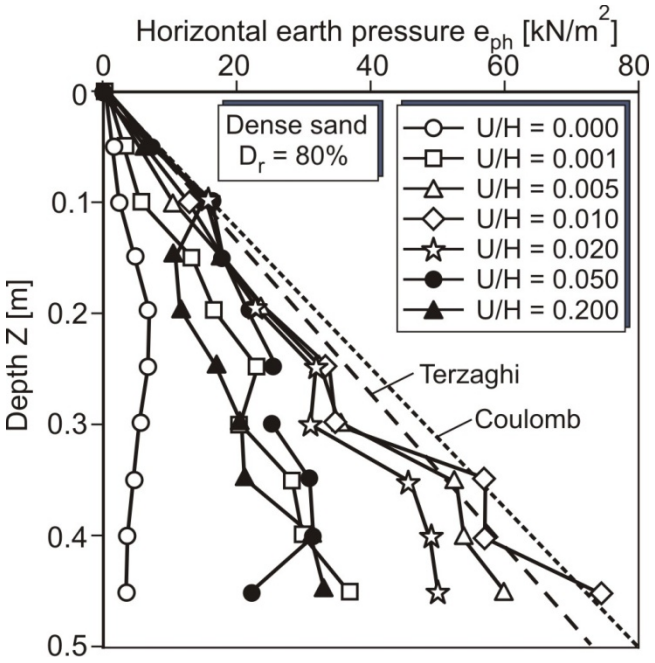

Figure 2-13: Earth pressure distribution measured by Fang et al. [30]

Besler (1997):

Besler [8], [9] developed two non-linear Equations based on the results of Mao's experiments in order to describe the deformation behavior of excavation walls and to verify the validity of the Equations with the deformation of a laboratory scale model. He developed deformation curves of two practically executed excavations using the non-linear Equations and compared these with actual field measurements. Displacements at peak for passive earth pressure were determined by Besler [8] according to the following Equation:

$$U_{G,B} = f_D f_\lambda f_S f_B f_M H \qquad [2.19]$$

Where:

U_G wall displacement at the half amount of the peak
U_B wall displacement at the peak
f_D factor for the density
f_λ factor for the friction of the wall
f_S factor for the degree of saturation
f_B The relative displacement due to the soil limit state
f_M factor for the scale effect
H embedded height of the wall

The values of the previous factors f_D, f_λ, f_S and f_B are published in tables by Besler [8] as functions of the soil density, saturation degree and soil conditions (serviceability or limit state) while the scale effect factor f_M is calculated by using the following Equation [2.20]

$$f_M = \left(\frac{H}{0.175}\right)^B \quad [2.20]$$

Where:

H The wall height in m
B A constant with the value of B = 0.33 for a smooth wall and B = 0.14 for a friction wall

Besler also obtained the following equation [2.21] for the passive earth pressure coefficient mobilization-function:

$$K_{mob}(\xi) = A + \left(\frac{B}{C+\xi}\right) \quad [2.21]$$

Where:

$K_{mob}(\xi)$ Mobilized passive earth pressure.

The other constants are calculated as follows

$$C = \frac{K_{ph}\xi_G}{2(K_{ph}-K_0)\xi_G+2K_0-K_{ph}} \quad [2.22]$$

$$A = K_{ph} + C(K_{ph} - K_0) \quad [2.23]$$

$$B = -(C + C^2)(K_{ph} - K_0) \quad [2.24]$$

Where:

K_o The earth pressure coefficient at rest
K_{ph} The earth pressure coefficient at peak
ξ The relative displacement at peak
ξ_G The relative displacement at the serviceability limit

The following Figure 2-14 shows a result of the mobilized earth pressure approach by Besler compared against measurement values by Mao. The results agree well with each other.

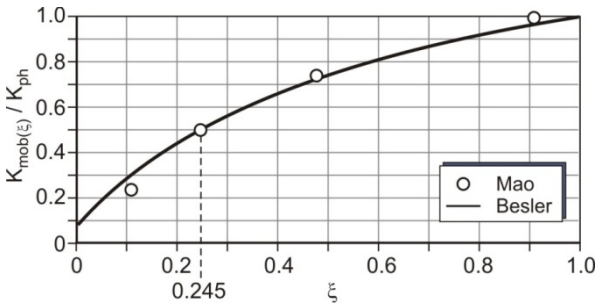

Figure 2-14: Mobilizing approach for passive earth pressure coefficient as a function of relative displacement for medium dense sand (D = 50 %) [8]

Bartl/Franke (1997):

Bartl and Franke [4] carried out centrifugal experimental tests to investigate the passive earth pressure problem. They investigated the mobilized earth pressure as a function of the wall displacement and the effect of the stress level as a function of the depth (scale effect). They used a model wall with a rotational movement around its top. The model consisted of a wall with a height of H = 0.12 m and width B = 0.25 m in a box of length L = 0.46 m. The acceleration due to gravity was varied between 1 g and 35 g. Dry poorly graded fine to coarse grained quartz sand was used. The experimental results clearly showed the dependence of maximum passive earth pressure and the corresponding displacement on the gravitational acceleration and therefore on the stress level as a function of wall height. Bartl also developed the following mobilization approach as shown in Equations [2.25] and [2.26].

$$\chi_{\mathrm{Rn}} = [1 - (1 - (\lambda_R)\,)^b\,]^c \qquad [2.25]$$

Where χ_{Rn} and λ_R are dimensionless factors which are defined according to earth pressure coefficients and relative displacements as follows

$$\chi_{\mathrm{Rn}} = \frac{\mathrm{K_{mob} - K_0}}{\mathrm{K_{Ph} - K_0}}\,,\ \lambda_R = \frac{U_p}{U} \qquad [2.26]$$

Where:

K_o Coefficient of earth pressure at rest
K_{ph} Passive earth pressure coefficient
K_{mob} Mobilized earth pressure coefficient
U_p Maximum wall displacement at peak
U Mobilized wall displacement
b,c constants

Based on his experimental results Bartl recommended a value of 0.7 for the constant c for different wall movement modes and soil density. The constant b on the other hand was recommended to be varied as a function of the wall movement modes and the soil density. Figure 2-15 below shows a comparison between the experimental results and the mobilization

function for passive earth pressure coefficient according to Bartl considering the three main modes of wall movement.

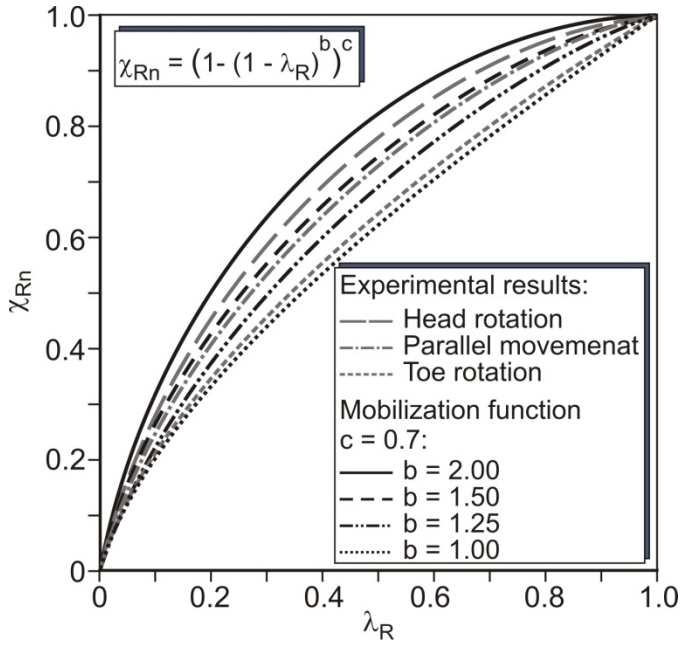

Figure 2-15: Mobilization function for passive earth pressure vs. relative displacement [4]

Bartl also obtained the relative displacement at peak $\frac{U_p}{H}$ as a function of the relative density I_D as follows in equation [2.27]:

$$\frac{U_p}{H} = -0{,}09 I_D + (\frac{U_p}{H})_0 \qquad [2.27]$$

Where $(\frac{U_p}{H})_0$ is the relative displacement at peak for a relative density $I_D = 0$. It is to be varied according to the movement mode.

Bartl also studied the effect of the stress level on the value of the normalized passive earth pressure load K_{rnp} (including passive earth pressure coefficient K_{ph}) and found that the normalized passive earth pressure load K_{rnp} decreases with increasing the stress level as shown in Figure 2-16. The following equation [2.29] was also obtained for dense sand.

$$K_{rnp} = 6.01 \left(\frac{H n_g}{1}\right)^{-0.12} \qquad [2.28]$$

Where:

H The embedded height of the wall
n_g An acceleration scale factor due to the gravity acceleration.

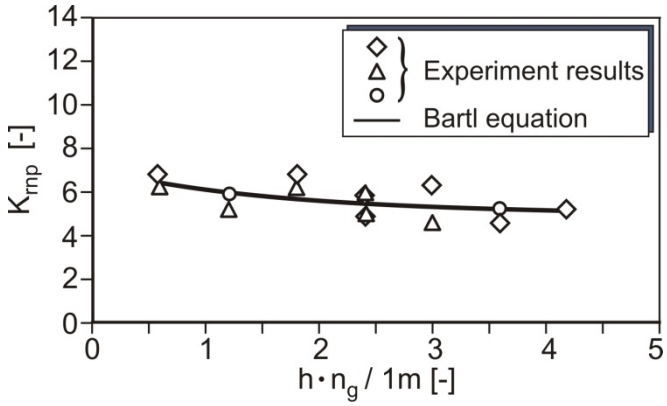

Figure 2-16: Stress level effect on the normalized passive earth pressure load for dense sand [4]

2.1.3 Passive earth pressure approach of German Standard DIN 4085 (2007)

The 2D passive earth pressure coefficient is calculated in the German standard DIN 4085 [31] considering a non-linear failure mechanism. The passive earth pressure coefficient K_{ph} is calculated as shown in Figure 2-17 below as a function of internal soil friction angle φ and soil - wall interface friction angle δ.

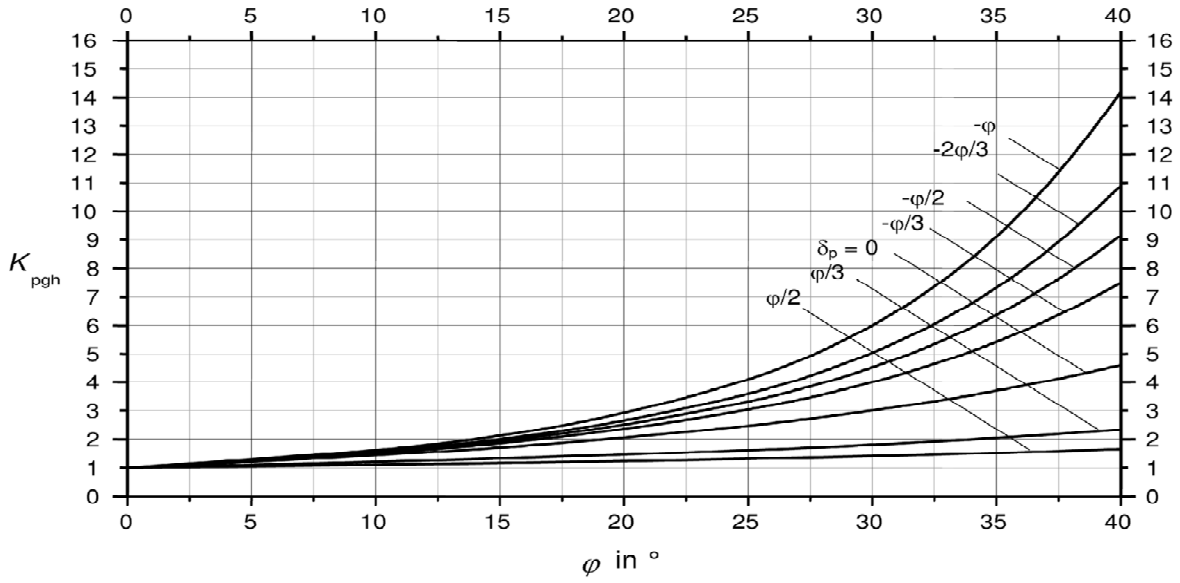

Figure 2-17: 2D passive earth pressure for nonlinear failure curve (vertical wall and horizontal ground surface) [31]

A function of the displacement at the peak is developed in the German standard DIN 4085 as follows:

For rotation around the bottom and parallel movement

$$\frac{U_p}{H} = -0.08D + 0.12 \qquad [2.29]$$

For rotation around the top

$$\frac{U_p}{H} = -0.05D + 0.09 \quad [2.30]$$

Where:

D The relative density
U_p Displacement at peak
H Embedded depth of the wall

A mobilization approach for passive earth pressure as a function of displacement and mode of movement is presented in DIN 4085 as shown in Equation [2.31]

$$\frac{E'_{pgh} - E_{0gh}}{E_{pgh} - E_{0gh}} = \left[1 - \left[1 - \frac{U}{U_p}\right]^b\right]^c \quad [2.31]$$

Where:

E'_{pgh} Mobilized Earth pressure
E_{0gh} Earth pressure at rest
E_{pgh} Earth pressure at peak
U Mobilized displacement at E'_{pgh}
U_p Displacement at peak
b, c Constants defined as in the following Table 2-1

Table 2-1: Constants for the mobilization function in DIN4085

Wall mode of movement	exponent of the mobilization approach	
	b	**c**
rotation around bottom	1.07	0.7
parallel movement	1.45	
rotation around top	1.72	

The previously presented mobilization function is defined only for 2D case. This will be compared later in the thesis with the case of 3D spatial passive earth pressure.

2.1.4 Numerical Simulations for plane strain passive earth pressure

A review of numerical earth pressure simulations previously done for the plane strain conditions is presented in the following paragraphs.

Duncan and Chang [29] developed a hyperbolic constitutive law which was widely used in most of the numerical models. The model described the stress-strain behavior using the following Equation [2.32]:

$$\sigma_1 - \sigma_3 = \frac{\varepsilon}{\frac{1}{E_i} + \frac{\varepsilon R_f}{(\sigma_1 - \sigma_3)_f}} \qquad [2.32]$$

Where:

σ_1 - σ_3 The deviatoric stress
$(\sigma_1$ - $\sigma_3)_f$ The deviatoric stress at failure conditions
R_f The failure ratio between asymptotical and curved value for the deviatoric stress
ε The strain of the soil
E_i The initial tangent modulus

The constitutive law included six parameters which can be determined from triaxial and plane strain compression tests. Duncan and Chang described successfully the stress-strain nonlinear behavior and stress dependency of the stiffness. Laumans [47] added the hardening behavior to the description of the passive earth pressure problem using an elasto-plastic constitutive material law as a function of the stress level. The soil was modeled using 4 node elements. On the contrary, the wall was modeled using disc elements. Laumans considered the nonlinearity in his analysis by using an iterative method to obtain the tangential stiffness of the soil. Figure 2-18 shows the geometry of the model by Laumans.

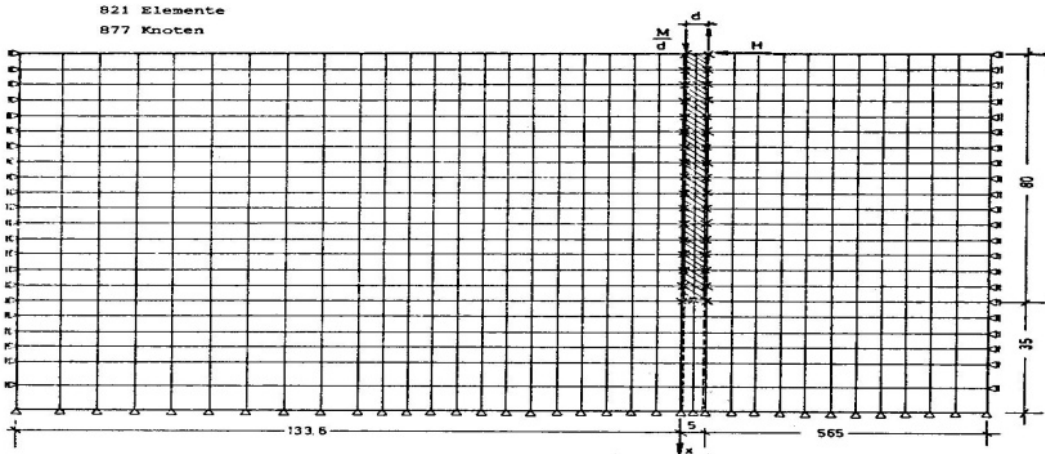

Figure 2-18: The mesh of the FEM model [47]

Christian et al [23] applied three constitutive models which are based on the Mohr-Coulomb constitutive law to establish the relationship between earth pressure mobilization and wall displacement in different movements. He simulated the problem of earth pressure in parallel and rotation around bottom movements for smooth and frictional walls. Christian used his FEM soil model simulations to compare three different constitutive laws namely: an elasto-plastic formulation derived from Mohr Coulomb, a law without plastic dilatancy using a non-symmetric stiffness and finally a strain hardening model with a capped yield criterion. By studying the effect of the mesh Christian noted that very fine element divisions in areas

with high stresses are requested for good results. Figure 2-19 shows the geometry mesh for the simulation of the earth pressure problem and Figure 2-20 shows the results of Christian's model for the non dilatancy model in parallel and rotation around bottom movements.

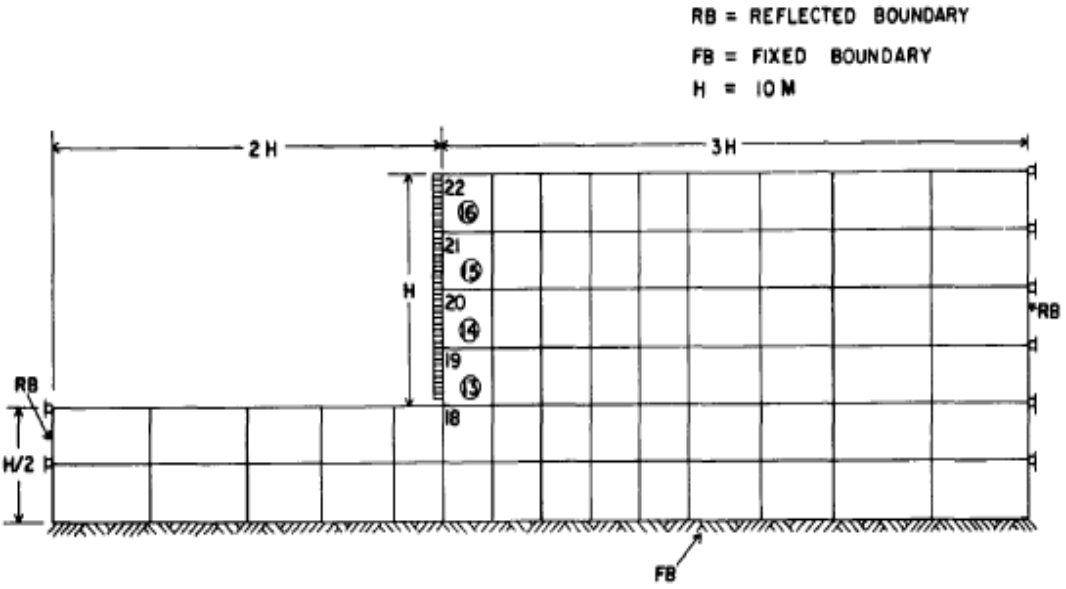

Figure 2-19: Geometrical mesh model used for earth pressure problem [23].

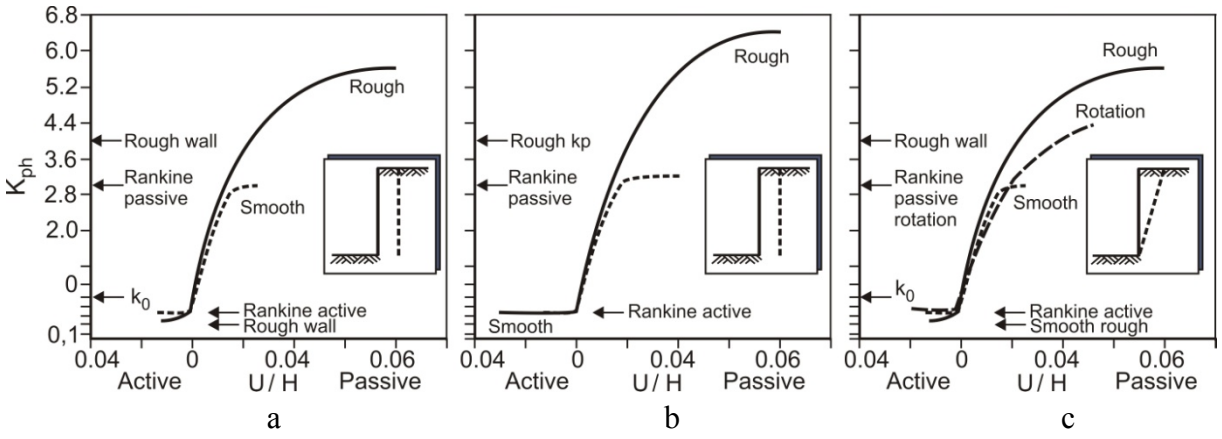

Figure 2-20: Earth pressure using the different constitutive laws a) non-dilatant b) with dilatantcy c) parallel and rotation movement (non-dilatant) by Christian [23]

Nakai [54] used an elasto-plastic constitutive material law with two yield surfaces in a numerical simulation to obtain the mobilized passive earth pressure as a function of the displacement for different modes of wall movement. Potts [63] developed a numerical model for the purpose of numerical investigation of passive earth pressure as a function of the displacement for granular soils with the Mohr-Coulomb constitutive law considering the three main movement modes. Potts also made a parametric study by varying the dilatancy angle, the initial earth pressure coefficient and the soil stiffness. In his study of the mobilization

earth pressure Ugai [87] carried out numerical simulations based on the elasto-plastic constitutive law verified with laboratory experiments.

Schweiger [75] investigated the problem of passive earth pressure as a function of the displacement. He compared the results of his FEM simulations that had been done using several variations of the Drucker-Prager constitutive laws with other results obtained by using the Mohr-Coulomb constitutive law. Schweiger recommended that the Drucker-Prager constitutive law is a poor approximation for the soil passive earth pressure problem in comparison with the Mohr–Coulomb failure criterion for different circular approximations as shown in Figure 2-21. As a result of his study, Schweiger suggested that a proper Mohr-Coulomb failure surface for a numerical solution of the earth pressure problem is to be preferably used. Figure 2-21 shows the results for the 2D passive earth pressure of Schweiger's model as a function of displacement.

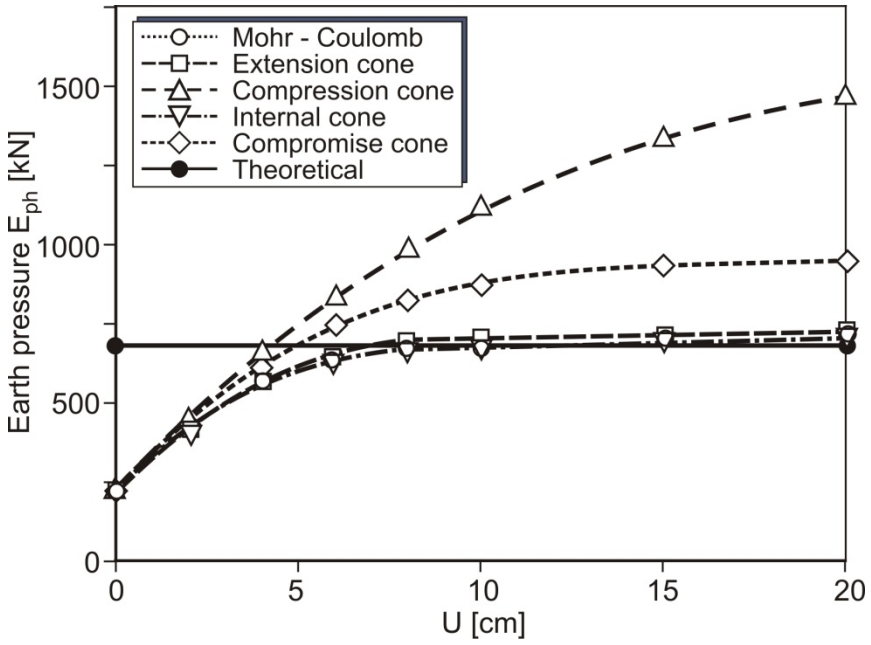

Figure 2-21: Earth pressure results by Schweiger [75].

A Discrete-Element-Method (DEM) was used by Chang [22] to simulate the problem of the passive earth pressure against a gravity retaining wall for the three main wall movement modes.

The soil was modeled as comprising blocks connected to each other using elasto-plastic Winkler-springs, which enabled, to highlight the effect of the shear stresses at the failure plane on the resulting passive earth pressure. Figure 2-22 shows the stress distribution on the wall for the three main movement modes by Chang. The results were compared with other results by Shields and Tolunay.

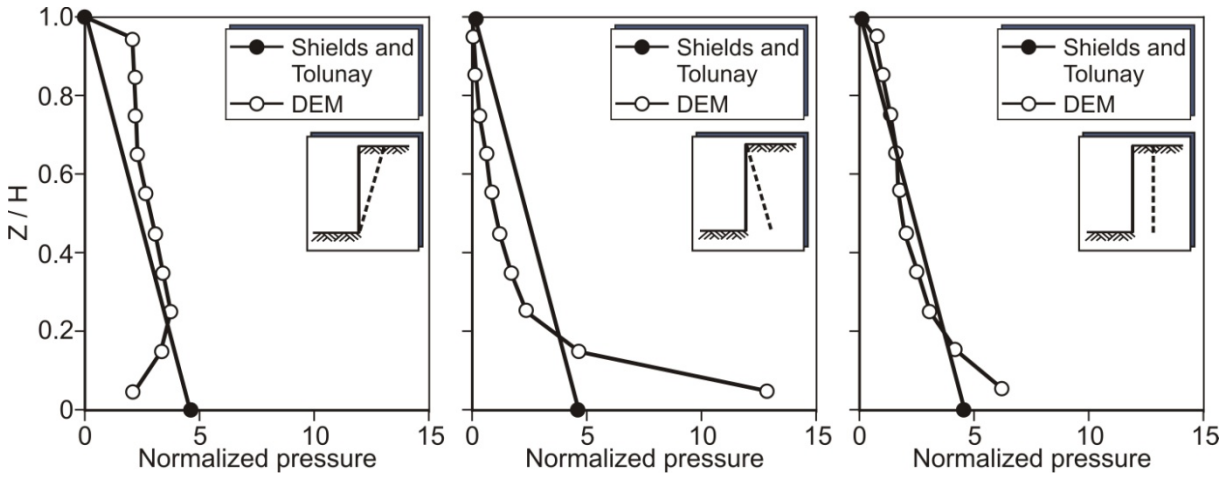

Figure 2-22: A comparison for earth pressure stress distribution results for different modes of movement between Shields with Tolunay and Chang [22].

Shiau [77] modeled the problem of passive earth pressure using FEM formulation of the lower/upper bound theorem (Figure 2-23).

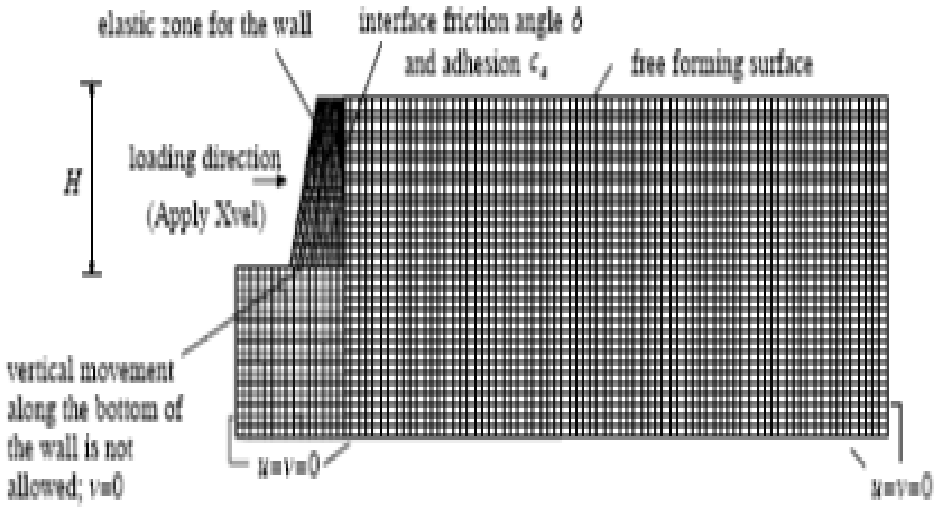

Figure 2-23: FEM mesh for upper-lower bound method for a model of the passive earth pressure for a vertical wall α = 0 with horizontal ground surface β = 0 [77]

The analyses assume associated flow, which restricts the direction of plastic flow. The model consisted of a rigid retaining wall with an inclined back of angle α to the horizontal. The ground surface of the cohesionless soil slope has an angle of β to the horizontal. The passive earth pressure coefficients are found firstly by upper-lower bound theorem equating the energy expended by the external loads to the energy dissipated internally by plastic deformations. On the contrary, the lower-bound theory based on the fact that any equilibrium state of stress can be found, taking the soil conditions into consideration. Figure 2-24 shows

the results of upper-lower bound method for the passive earth pressure coefficient as a function of the soil friction angle φ and the wall-soil friction angle δ.

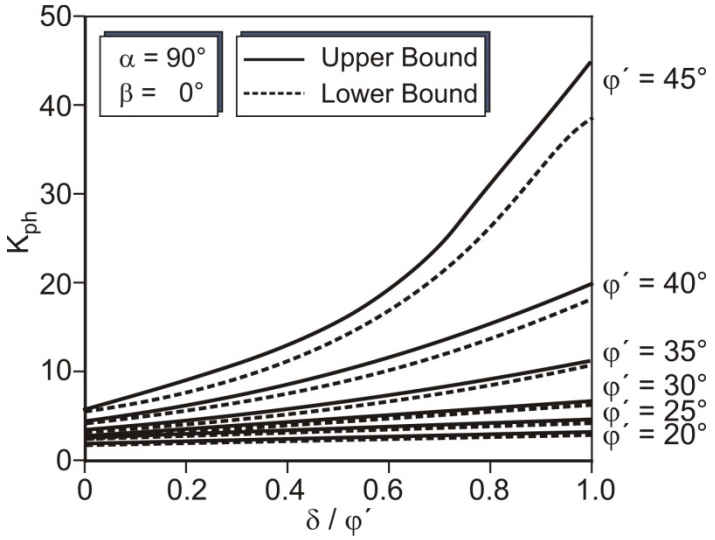

Figure 2-24: Results of upper-lower bound method for the passive earth pressure coefficient as a function of soil friction angle φ and wall-soil friction angle δ [77]

Widuliriski [97] investigated the passive earth pressure problem as a quasi-static model at failure state in dense sand. The problem of earth pressure was simulated by using discrete element method (DEM). The model consisted of a rigid, very rough wall in a Karlsruhe sandy soil that was subjected to parallel and rotation around the bottom movements. The behavior of the Karlsruhe sand was simulated using a three dimensional spherical discrete model, which offered grain rolling resistance. The soil was modeled using the micro-polar hypoplasticity constitutive law, which offered a good description for the non-linearity of the stress strain behavior depending on the void ratio. Figure 2-25 illustrates the results of the passive earth pressure coefficient by Widuliriski for parallel movement (a), rotation around the top (b) and rotation around the toe (c).

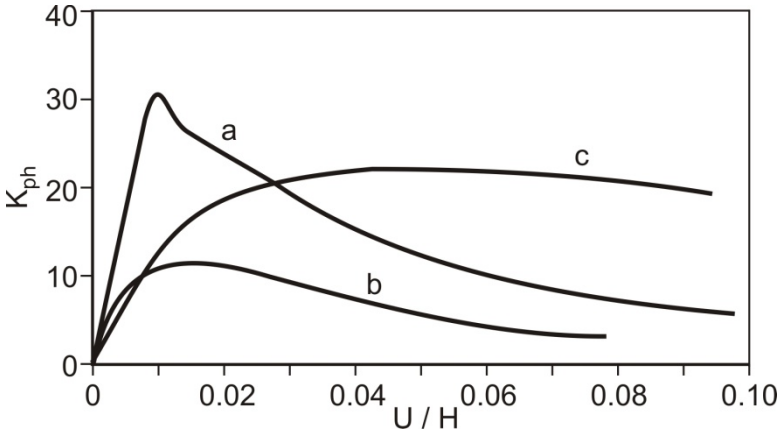

Figure 2-25: Earth pressure coefficient vs. relative displacement by Widuliriski [97]

Al-Jamal [3] also investigated the problem of passive earth pressure using the Plaxis® FEM software. The passive earth pressure problem was simulated in a plane strain FEM model with triangular 15-node elements as shown in Figure 2-26. The soil parameters were specified in laboratory experimental tests and modeled by using the hardening soil constitutive (HSM) law. The FEM simulation was also done for different types of soil such as silty sand (SM), clay sand (SC) and for soil named Test 2. Test 2 was investigated experimentally and also numerically. Passive earth pressure was developed by prescribing a horizontal displacement boundary condition for the wall plate. Free vertical displacements were allowed. The results were compared with an experimental field test result as shown in Figure 2-27.

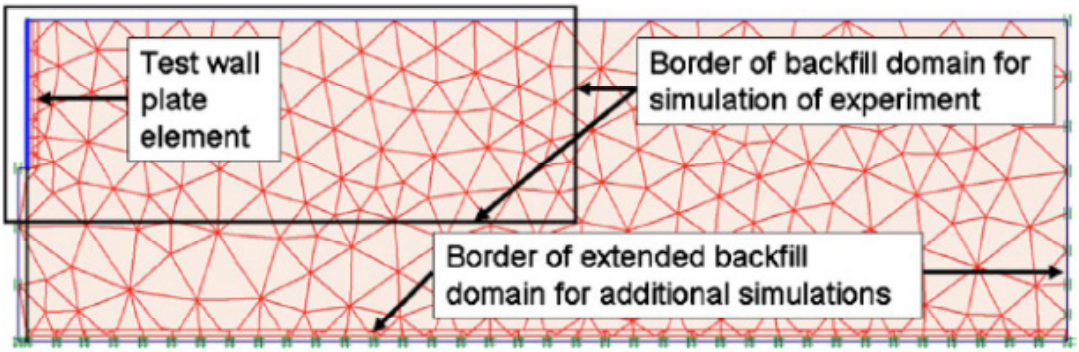

Figure 2-26: Mesh geometry for FEM test [3]

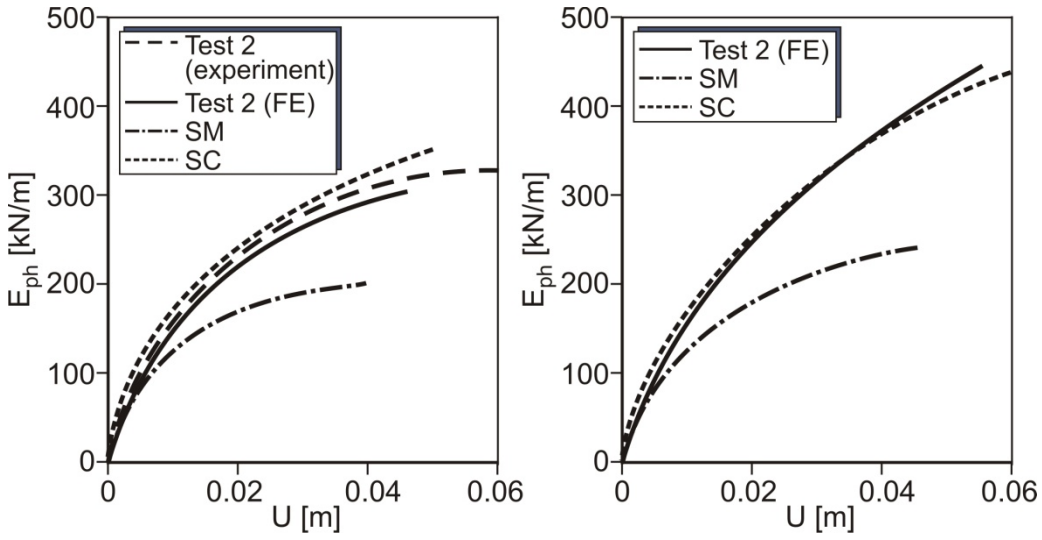

Figure 2-27: Numerical and experimental results [3]

2.2 Spatial Passive earth pressure

Some of the methods for the evaluation of 3D earth pressure that have been developed from previous researches are highlighted below.

2.2.1 Theoretical aspects of spatial passive earth pressure

Blum (1934):

Blum [10] used Coulomb's limit equilibrium theory to develop a failure mechanism by considering a three-dimensional failure surface as illustrated in Figure 2-28.

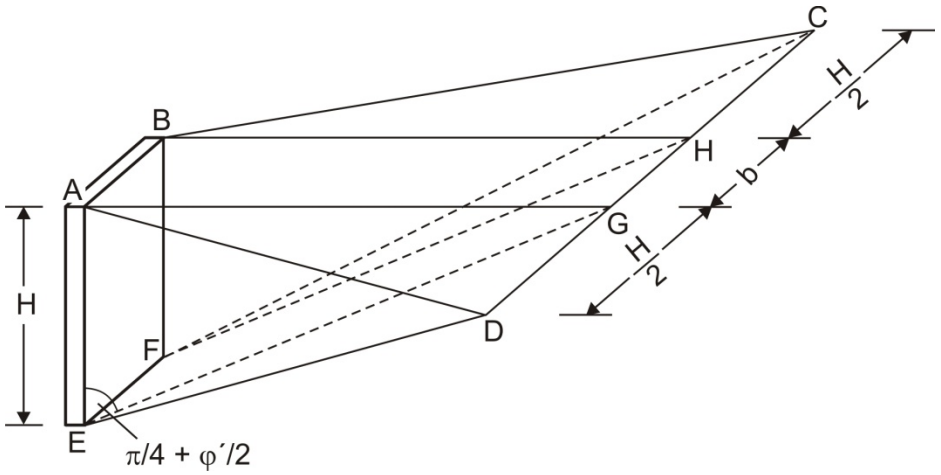

Figure 2-28: Blum's failure surface for spatial passive earth pressure [10]

Within his method Blum ignores the soil-structure friction angle and makes a simplifying assumption for the flat failure surface ($\delta = 0$). The frictional behavior between the failure body and the surrounded soil was also neglected. He accordingly developed the following 3D passive earth force Equation:

$$E_{ph} = \frac{1}{2}\gamma H^2 B \tan^2\left(\frac{\pi}{4}+\frac{\varphi}{2}\right) + \frac{1}{6}\gamma H^3 \tan^2\left(\frac{\pi}{4}+\frac{\varphi}{2}\right) \quad [2.33]$$

Where:

B the width of the wall
H the embedded depth of the wall
γ the soil density
φ the soil friction angle

Duncan and Mokwa (2001):

Duncan and Mokwa [28] developed a program for the numerical calculation of the passive earth pressure as a function of the displacement using the log spiral theory coupled with a hyperbolic load-deflection behavior up to peak resistance. The hyperbolic load behavior is developed similar to the stress-strain constitutive law behavior by Duncan and Chang [29]. It

was obtained using the experimental results for different types of soils as shown in Figure 2-29.

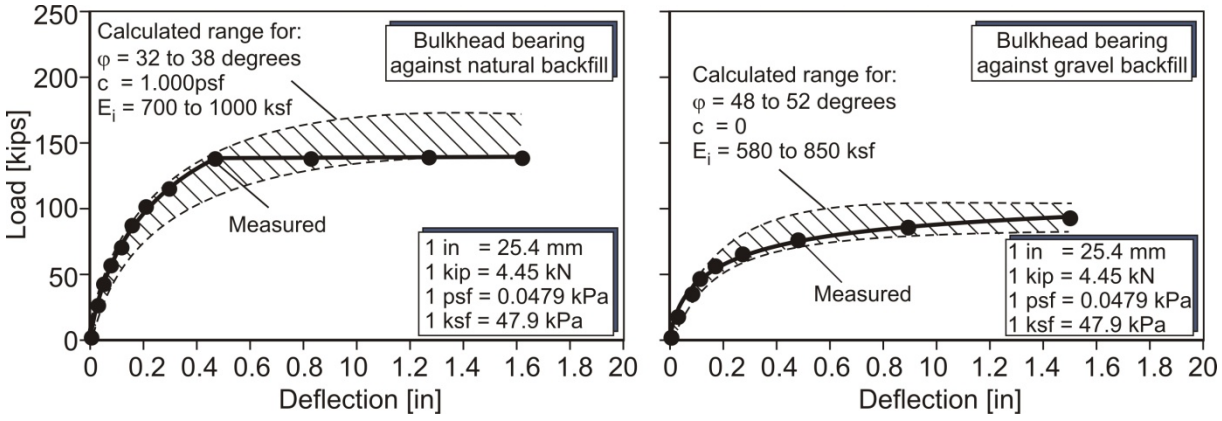

Figure 2-29: Comparisons of measured and computed load deflection curves by Duncan and Mokwa [28]

The nonlinear variation of passive earth pressure resistance with deflection can be approximated by a hyperbolic curve that incorporates the initial elastic stiffness and the ultimate passive resistance in order to compute accurate values of the passive earth pressure value. The solution is solved iteratively by changing the location of the log-spiral center until a minimum passive resistance is found. The program of Duncan and Mokwa includes the Ovesen-Brinch Hansen 3D correction factor to consider the shear plane extending beyond the edge of the wall. Duncan and Mokwa used a model defined by an initial stiffness K_{max}. K_{max} is based on the elastic solution from Douglas and Davis [27]. The hyperbolic load is defined according to Equation [2.34]. A detailed explanation of the constitutive law equation is given in the form of stress-strain behavior in chapter 2.1.4.

$$P = \frac{U}{\frac{1}{K_{max}} + R_f \frac{U}{P_{ult}}} \qquad [2.34]$$

Where:

P Passive earth pressure
U horizontal displacement
P_{ult} Passive earth pressure at the peak
R_f The failure ratio
K_{max} the initial stiffness of the soil deflection load curve
P_{ult} is calculated from the following Equation:

$$P_{ult} = E_p M B \qquad [2.35]$$

M is the Ovesen-Brinch Hansen 3D correction factor based on Ovesen's test for compacted sand obtained by varying φ from 32° to 41°. M according to the measurements is limited to a

maximum value of 2 [28]. E_p is the passive resistance per unit length and B is the structure length perpendicular to the plane of analysis.

The value of R_f in the hyperbolic model is defined as the failure ratio and is equal to the ultimate load divided by the hyperbolic asymptote value of passive resistance. Figure 2-30 shows the form of the hyperbolic model solution.

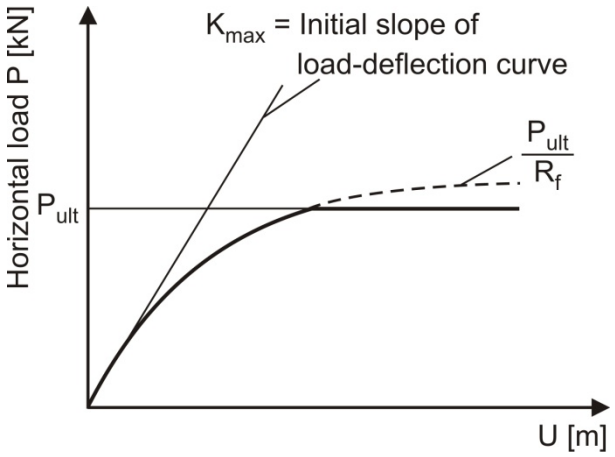

Figure 2-30: Hyperbolic horizontal load deflection relationship used by Duncan and Mokwa [28]

Alternatively Shamsabadi [76] proposed a model that based on the secant stiffness K at $\frac{P_{ult}}{2}$ (serviceability limit) as shown in equation [2.36] below.

$$P(y) = \frac{P_{ult}(2KU_{max} - P_{ult})U}{P_{ult}U_{max} + 2(KU_{max} - P_{ult})U} \quad [2.36]$$

Where:

U_{max} Displacement at peak when $P=P_{ult}$
K_{max} Secant stiffness modulus
U Mobilized displacement

For practical usage hyperbolic model parameters for Equation [2.34] are provided in Table 2-2. The values listed in Table 2-2 produce essentially identical curves using either Equation [2.34] or Equation [2.36]. These models may be limited at appropriate residual levels for displacements beyond the peak by capping the curve and continuing with a constant resistance thereafter.

Table 2-2: Example for hyperbolic model parameters [28]

Backfill soil	φ	c	P_{ult}	K_{max}
	(degree)	kPA	kN/m	kN/cm/m
δ governed by vertical equilibrium requirements (vertical uplift conditions)				
Test	46	14	315	250
Silty sand	34	15	205	220
clayey sand	25	62	400	260
δ = 0.35 φ				
Test	46	14	500	270
Silty sand	34	15	250	250
clayey sand	25	62	270	270

Soubra and Regenass (2001):

Soubra and Regenass [80] developed a method for the calculation of a 3D passive earth pressure coefficient based on the upper-bound method of limit analysis that consisted of three steps.

In the first step an extension of the Coulomb 2D theory was used to consider a one-block simple failure mechanism M_1 as shown in Figure 2-31.

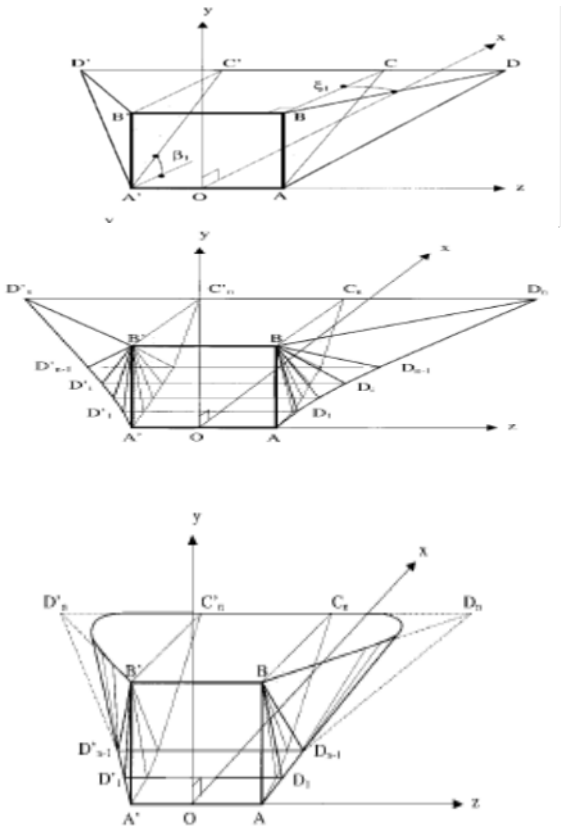

Figure 2-31: Failure mechanism upper-bound method [80]

This mechanism is defined by a single angular parameter B, the dihedral angle between the horizontal plan and the lower plan, where $B \in \left[0\ ,\ (\frac{\pi}{2} - 2\varphi)\right]$ is with the consideration that the lateral planes are at maximum in the plane of the wall as shown in Figure 2-31.

The second step consisted of a multi-block mechanism M_n, composed of n rigid blocks as shown in Figure 2-31. Any number of blocks n is applicable. The horizontal movement of the wall is accommodated by movement of n rigid blocks.

The third and final step comprised of a truncated multi-block mechanism M_{nt} which is obtained by upper-bound solution with a volume reduction of the final block in the M_n mechanism, in which the block M_n is truncated by two portions of circular cones. According to the work theory the sum of the external work on an element is equal to the energy dissipation for the same element. This principle was used to obtain Equation [2.37] to calculate the passive earth pressure load E_{Ptotal} due to the soil weight γ, the cohesion c and a load q.

$$E_{Ptotal} = K_{p\gamma}\gamma\frac{H^2}{2}B + K_{pc}cHB + K_{pq}qHB \quad [2.37]$$

Where:

$K_{p\gamma}$	Passive earth pressure coefficient due to soil weight
K_{pc}	Passive earth pressure coefficient due to cohesion
K_{pq}	Passive earth pressure coefficient due to surcharge loading q
B	The wall width
H	The wall height

All of these coefficients are functions of φ, δ and B/H ratio. This method is inaccurate for big values of φ and δ especially in the case of M_n and M_{nt}. Figure 2-32 shows a comparison between the results of 3D passive earth pressure coefficient for M_1, M_n and M_{nt}.

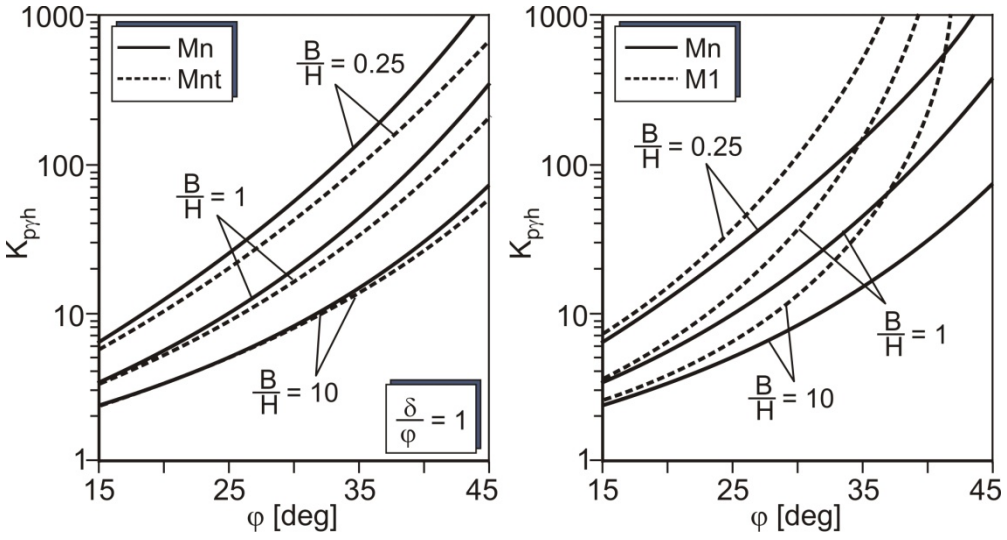

Figure 2-32: Comparison between 3D passive earth pressure coefficients for different blocks M_1, M_n and M_{nt} for different spatial ratios B/H [80]

It is to be noticed that the choice of the number of blocks affects the accuracy of the results. For a rough wall a maximal number of 5 blocks is available. However, for high soil friction angles only one block M_1 is available. The results are also affected by varying the friction angle and so the inclination of the blocks. For a high accuracy and more complex boundary conditions it is always better to use the multi-block mechanism M_{nt}.

2.2.2 Experimental investigations of spatial passive earth pressure

Paul (1955)

Paul [59] carried out extensive experiments to determine the maximum earth pressure on I-profile walls and masts embedded and fixed with different boundary conditions in a sandy

soil with relative density D_r between 30 % and 80 %. As a result of his experiments he proposed a failure mechanism that was composed of two conical failure bodies with elliptical bottom areas as shown in Figure 2-33.

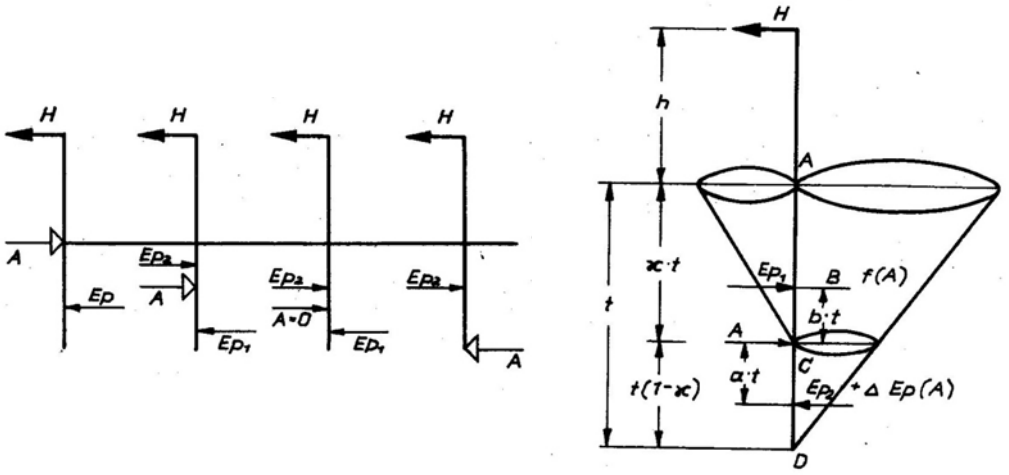

Figure 2-33: Possibility of the boundary conditions for planar failure mechanism by considering active and passive pressure [59]

The surface line of the conical failure body is considered as being almost linear and only shows a slight curve in the bottom area. Paul obtained the following Equation [2.38] to calculate the passive earth pressure of an I-profile wall of width (d) and the embedded depth (t).

$$E_{pgh} = \frac{1}{3}\gamma(t + \frac{b}{4}d)^3 \lambda_{ph} k_1 \qquad [2.38]$$

The λ_{ph} is the passive earth pressure coefficient which Paul indicated in diagrams. The factor k_1 takes into account the position of the rotation axis as well as the point of action of the horizontal force H. He also found out that with a greater slenderness ratio of the I-profile wall a cutting effect occurred and no failure body is formed. Therefore, the use of Paul's method is only permissible when the slenderness ratio (width (d) to thickness (t) of the I-profile) fulfills the following condition: $3 \leq t/d \leq 8$. Additionally, Paul obtained a mobilization function for the passive earth pressure with displacement as follows:

$$y^n = 1 - (1 - x)^n \quad [2.39]$$

Where:

y	Function of the horizontal passive earth pressure load
x	Function of the rotation angle α at the top of the I-profile
n	Constant related to the slenderness ratio t/d

The given calculation method has three limitations. Firstly, Paul neither studied nor took into consideration the effect of sandy soils with small capillary cohesion. Secondly, the distance of the point of action of the horizontal force from the ground level surface must be greater than the embedment depth (h > t). Thirdly, earth pressure inclination angle δ_p is set to φ/3.

Brinch Hansen (1961)

Brinch Hansen [17] introduced a method for the calculation of the spatial passive earth pressure for load bearing capacity of horizontally loaded piles and anchor plates as shown in Figure 2-34. The piles and the anchor plates are considered as rigid.

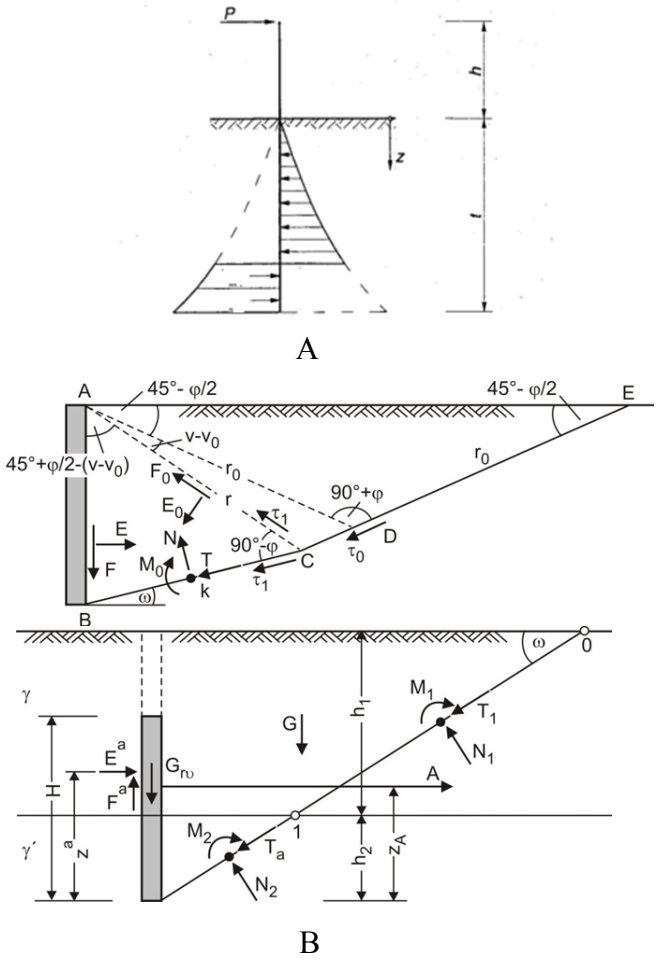

Figure 2-34: (A) Earth pressure distribution (B) Passive earth pressure on anchor plate [17]

The resultant passive earth pressure E_r along the beam can then be determined according to the Equation [2.40] below as shown in Figure 2-34 A.

$$E_r = \frac{1}{2}\gamma H^2 B\, K_{ph3D} = \frac{1}{2}\gamma H^2 B K_{ph2D}\left(1 + \frac{1.1(K_{ph2D})^{\frac{2}{3}}}{1+5\frac{B}{H}}\right) \quad [2.40]$$

Where:

H anchor depth

B width of the anchor plate

K_{ph3D} Spatial Earth pressure coefficient

K_{ph2D} Earth pressure coefficient in 2D case

For the pile case Brinch Hansen considered a 2D earth pressure distribution at the upper third of the embedded depth. Also the frictional shear load on the side surface of the failure body was taken into consideration.

Brinch Hansen [16] [18] also studied the earth pressure on vertical anchor plate in a cohesionless sandy soil, considering the soil in the ultimate state of failure, to produce a state of rupture in the earth around the anchor plate as shown in Figure 2-34. The 3D earth pressure coefficients by Brinch Hansen for piles and anchor plates are to be taken as a function of the friction angle φ and the ratio of depth. He determined these through the assumption that the earth pressure can be calculated by means of the 2D passive earth pressure coefficient K_{ph2D}. On the contrary, for the middle part of the embedded depth, 2D passive earth pressure with a consideration of a friction component on both side surfaces of the failure body was taken into account. This friction component is the magnitude of the earth pressure at rest (E_0) multiplied with a friction factor equal to tan φ.

rinch Hansen obtained an approach, as shown in Equation [2.41], to calculate the ratio between the measured earth pressure (E_{exp}) by his experimental tests to the calculated earth pressure according to his theoretical Equation (E_{th}) [2.40] for I-profile walls as a function of the spatial ratio ($\frac{B}{H}$).

$$\frac{E_{exp}}{E_{th}} = 1.23 + 0.213\ \frac{B}{H} \quad [2.41]$$

Brinch Hansen used Ovesen's [17] experimental results to obtain the following correction factor m:

$$m = 1 + (K_{ph} + K_{ah})^{0.67}\left[1.1E4 + \frac{1.6B}{1+5(\frac{B}{H})} + \frac{0.4(K_{ph}-K_{ah})E^3B^2}{1+0.05(\frac{B}{H})}\right] \quad [2.42]$$

Where:

Constants B and E are calculated as follows: $B = 1 - (\frac{B}{B+s})^2$, $E = 1 - \frac{H}{H+Z}$

B The anchor width
s The distance between two adjacent anchors
Z Depth of the anchor
H The height of the anchor
K_{ph} Horizontal passive earth pressure coefficient
K_{ah} Horizontal active earth pressure coefficient

The previous calculation method is not very accurate for small values of the friction angles.

Weissenbach (1961):

Weissenbach [91] formulated a method for the calculation of 3D earth pressure which has been widely used for the design of I-profile walls till the present day. The calculation method based on experiments which were carried out with I-profile widths varying from 5 cm up to 30 cm and for narrow I-profile walls in which the widths varied between 0.2 cm and 5 cm. Weissenbach determined the spatial passive earth pressure on the I-profile by applying a correction factor to the 2D passive earth pressure coefficient. The 2D passive earth pressure coefficients were correspondingly determined by using Streck's [93] failure line diagram. Streck's results for passive earth pressure coefficient K_{pgh} are given in Table 2-3. His experiments were classified as follows:

1. Without vertical wall movement $\delta > 0$ (between sandy soil and steel $\delta = 27.5°$).
2. With vertical wall movement $\delta = 0$ (measuring the vertical load).

The earth pressure inclination angle δ_p^* must be set according to Equation [2.43] by Weissenbach.

$$\delta_p^* = \begin{cases} -(\varphi - 2{,}5) : \varphi \leq 30^\circ \\ 27.5^\circ : \varphi \geq 30^\circ \end{cases} \quad [2.43]$$

Table 2-3: 2D passive earth pressure coefficients by Streck [93]

φ	45	42.5	40	37.5	35	32.5	30	27.5	25	22.5	20	17.5	15
δ_p	-27.5	-27.5	-27.5	-27.5	-27.5	-27.5	-27.5	-25	-22.5	-20	-17.5	-15	-12.5
K_{pgh}	13.6	11.4	9.64	8.27	7.12	6.15	5.46	4.51	3.81	3.23	2.77	2.38	2.11

Weissenbach obtained Equations [2.44], [2.45] and [2.46] to calculate the passive earth pressure in two components namely the internal frictional component and the cohesion component.

$$E_{ph} = E_{pgh} + E_{pch} \quad [2.44]$$

Where:

$$E_{pgh} = \frac{1}{2}\gamma K_{pgh(\delta_p=\delta_p^*)} t^2 \left(b + b_{s,r}\right) \quad [2.45]$$

$$E_{pch} = 2cK_{pch(\delta_p=\delta_p^*)} t\left(b + b_{s,k}\right) \quad [2.46]$$

Weissenbach defined an imaginary calculative width $b_{s,r}$ for the consideration of internal friction (φ) as well as cohesion $b_{s,k}$ as shown in Equation [2.47] (internal friction) and Equation [2.48] (cohesion) in the case of b > 0.3 t

$$b_{s,r} = 0{,}6\ t\ tan\varphi \quad [2.47]$$

$$b_{s,k} = 0{,}9\ t\ (1 + tan\varphi) \quad [2.48]$$

Weissenbach used his results to define a critical width $b_{kr} = 0.3$ t. It was concluded from the experiments that beyond a certain wall width b_{kr} (normal to the displacement direction often described as critical width b_{kr} in technical literature) a different characteristic failure mechanism was identified, in which no clear failure body occurs and the soil in front of the wall is mainly squeezed sideways. In this case $b_{s,r}$ is calculated as in Equation [2.47] but by multiplying with a decrease Factor F, which is defined as follows:

$$F = \sqrt{\frac{b}{0.3t}} = \sqrt{\frac{b}{b_{kr}}} \text{ for } b < 0.3\ t \quad [2.49]$$

When the width of the wall is bigger than the critical width b_{kr}, a failure body forms against the moved wall and the factor F is equal to 1 as shown in Equation [2.50] and Equations [2.45] and [2.46] are in use.

$$F = 1 \text{ for } b \geq 0.3\ t \quad [2.50]$$

This altered failure characteristic is taken into consideration by using a different mobilization function for the imaginary calculated width, in which an additional decreasing factor F must be introduced. This is because the calculation of the passive earth pressure without the decreasing factor F would yield a resultant $E_{ph} > 0$ for a beam width of b = 0. The factor F rounds off the calculative width of a root function to b (b = 0) = 0. The passive earth pressure is then calculated using Equations [2.51], [2.52] and [2.53] as follows:

$$E_{ph} = E_{pgh} + E_{pch} \quad [2.51]$$

$$E_{pgh} = \frac{1}{2}\gamma K_{pgh(\delta_p=\delta_p^*)} t^2 \left(b + b_{s,r}\right)F \quad [2.52]$$

$$E_{pch} = 2cK_{pch(\delta_p=\delta_p^*)}t(b + b_{s,k})FK_{ai} \quad [2.53]$$

Very high values for passive earth pressures are obtained for predominantly cohesive soils. For this reason in combination with Kaercher's experimental results, Weissenbach recommended the reduction of E_{pch} to half its value by means of a factor K_{ai}. The Equation is valid for non-cohesive soils with capillary cohesion without the reduction of E_{pch}, so K_{ai} can be set to a value of 1.0 in the Equation.

Based on his experimental research results Weissenbach calculated the displacement at limit state (at peak) for parallel movement of a wall in medium dense sand as follows:

$$U_{Bd} = 27.5\frac{t^2}{\sqrt{b}}\,[\text{mm}] \quad [2.54]$$

Where t is the embedded depth in unit of meter and b is the width in m. For dense sand the value of U_{Bd} in the Equation [2.54] decreases by 20 %. On the other hand for loose sand the value of U_{Bd} increases by 20 %.

Also for the displacement at half the failure load (serviceability), Weissenbach obtained the following Equation:

$$U_{Gb} = 1.65\sqrt{\frac{t^3}{b}}\,[\text{mm}] \quad [2.55]$$

The following Equation for passive earth pressure was also developed by Weissenbach.

$$E_{ph}^* = 1.25\,\gamma\,\omega_R\,Z^2 \quad [2.56]$$

Where:

Z Coordinate of the depth starting from the surface of the excavation
γ the soil density
ω_R is defined in Figure 2-35 below:

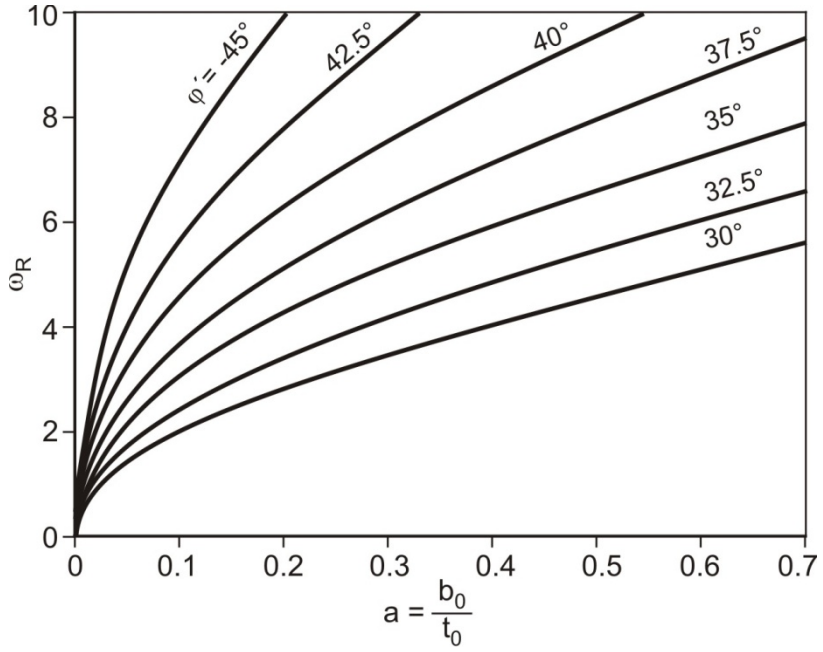

Figure 2-35: Factor ω_R [91]

Colling (1962)

Colling based his researches on the experimental results of Biarez [25] in which the true soil particles-motion conditions for an I-profile were made visible. It was found out that the soil particles at the I-profile bottom move in a rotationally manner around the bottom forming a lock as shown in Figure 2-36 below. He developed a calculation model which additionally considered the mode of the movement and total deformation.

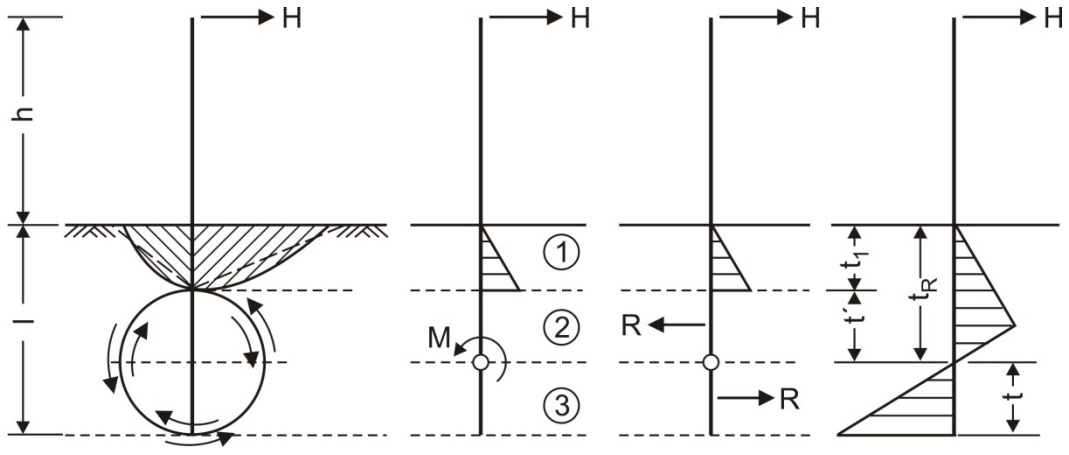

Figure 2-36: Geometry and load in the failure body [25]

The failure mechanism was idealized such that for the top third of the embedment depth in area ①. Passive earth pressure is mobilized in front of the I-profile by moving it horizontally against the soil while active earth pressure was mobilized behind the I-profile. The magnitude of the active and passive earth pressures increased linearly as a function of the depth

according to Coulomb's theory. The distribution of the failure body is illustrated in Figure 2-37 below.

The soil in the other two thirds was replaced with a force pair arising from linear stress distribution over the entire height of the soil cylinder. This force pair acts around a pivoting point and is equal to the soil reaction against the moment of rotation M. The depth of the pivoting point t_R by Colling is almost between 0.69l and 0.72l depending on the ratio t/h.

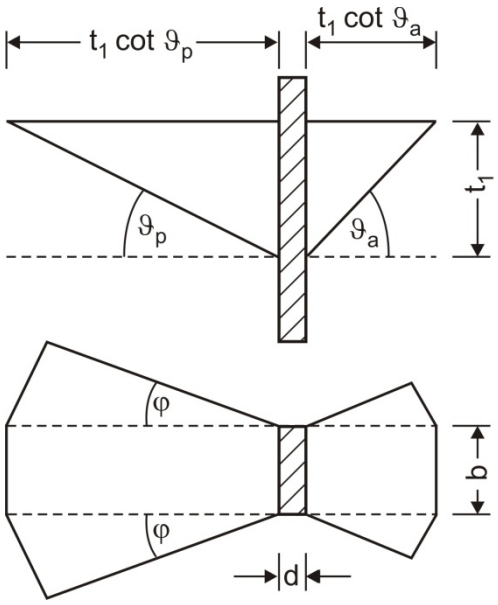

Figure 2-37: Ideal failure body at the upper face surface by Colling [25]

Colling defined the spatial earth pressure coefficient K_{ph} according to Equation [2.57] below.

$$K_{ph} = \gamma\left(K_{ph2D} - K_{ah2D}\right)b_0 = \gamma\left(K_{ph2D} - K_{ah2D}\right)b(1+\nu) \qquad [2.57]$$

Where:

K_{ph2D} 2D Horizontal passive earth pressure coefficient
K_{ah2D} 2D Horizontal active earth pressure coefficient
b Width of the I-profile
ν Constant defining the spatial shape of the failure body
b_0 The imaginary effective width($b_0 = b(1+\nu)$)

The constant ν depends on the soil and parameters , the ratio $\frac{t}{h}$ and on the wall friction angle. In contrast to other methods, Colling did not neglect the 3D active earth pressure behind the embedded I-profile. The imaginary effective width b_0 as a result of 3D failure process is determined by failure wedge dispersion with the factor ν which is related to the soil friction angle φ and the geometrical dimensions b and h of the I-profile.

Ovesen (1964)

Ovesen [58] conducted an extensive series of tests on passive earth pressure against anchor slabs to investigate the 3D effects. His tests were performed on compacted sand with friction angles ranging from 32.7° to 41.7°. Ovesen developed a test model as shown in Figure 2-38. The model included anchor plates, on which a passive earth pressure is mobilized after a movement of the anchors towards soil. The maximum difference between the passive and the active earth pressure coefficients in the test was 5.7 and the correction factor for the 3D effects did not exceed a value of about 2.

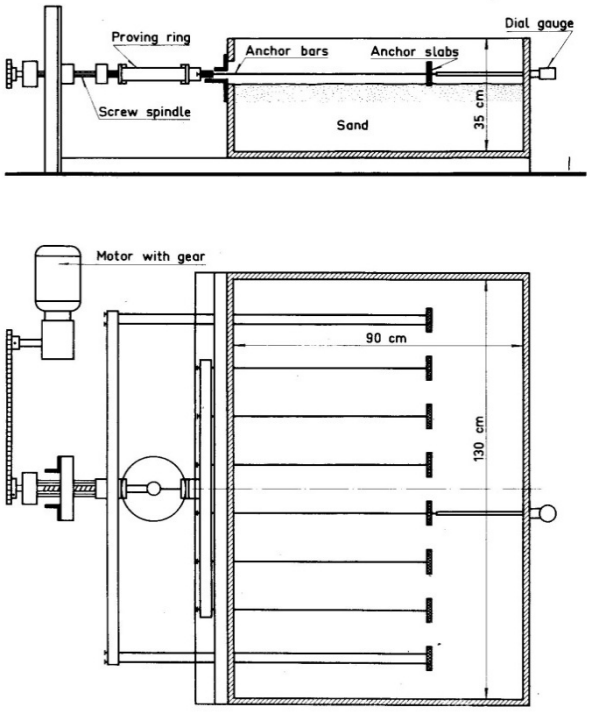

Figure 2-38: Experimental apparatus made by Ovesen [58]

The results in Table 2-4 for dense sand with a void ratio $e_0 \approx 0.55$ show the value of the correction factor M. The correction factor M is defined as the ratio of the spatial anchor pressure (A_{3D}) to the anchor pressure in the 2D case (A_{2D}). The spatial anchor pressure is considered to occur when earth pressure acts against an anchor slab with a limited width and height. On other hand, the anchor pressure in the 2D case results from having earth pressure against an anchor slab with unlimited width and height as shown in Figure 2-39.

Table 2-4: Results of Ovesen for infinite anchor at ground surface

h/H	l/L	e_0	$M=A_{3D}/A_{2D}$
1.0	1	0.549	1
1.0	0.5	0.549	0.948
1.0	0.25	0.548	0.803
0.5	1	0.548	1.007
0.5	0.5	0.547	0.81
0.5	0.25	0.552	0.688
0.25	1	0.536	0.913
0.25	0.5	0.542	0.736
0.25	0.25	0.544	0.609
0.1	1	0.545	0.642
0.1	0.5	0.553	0.599
0.1	0.25	0.548	0.431

Where: H, h, l and L are explained in the following Figure 2-39.

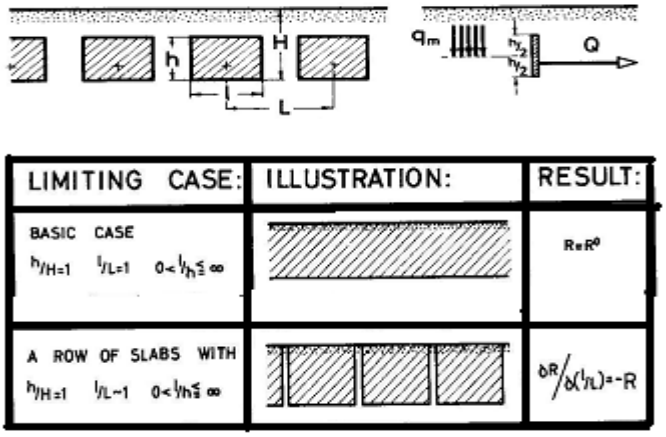

Figure 2-39: Geometrical parameters for anchor slab with limited height and limited length [58]

Zweck (1953 - 1964)

An experimental test was developed by Zweck [103] to investigate the passive earth pressure problem from a spatial perspective. The experiment consisted of two different tests using wooden smooth walls. The experimental set up parameters are summarized in Table 2-5 below.

Table 2-5: Experimental set up parameters

	Experimental box Dimension			Wall Dimension	
	Length L (m)	Width B (m)	Height H (m)	b (cm)	h (cm)
Experiment 1	1.5	0.7	1.0	38	30
Experiment 2	3.2	3.2	1.4	50	50

The dimensions of the wall were chosen such that a failure body will be formed during the movement without exceeding the boundary condition. Sandy soils with different relative densities were tested. Both of vertical and horizontal displacements were measured. Zweck illustrated the results of the spatial passive earth pressure load as a function of the embedded depth for different widths as shown in Figure 2-40. A mobilization function for passive earth pressure load and displacement U was obtained as shown in following Equation [2.58]:

$$P = d(1 - e^{-bU}) \qquad [2.58]$$

Where:

P Measured Passive earth pressure load.
d, b Constants are calculated according to the soil physical properties
U Displacement of the wall

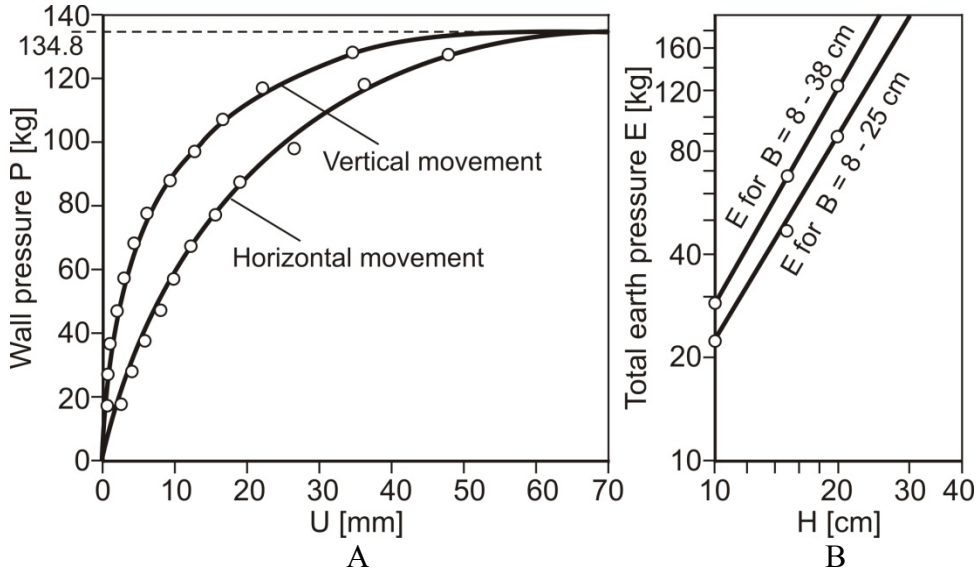

Figure 2-40: (A) Vertical and horizontal movement related to the measured load
(B) Passive earth pressure load as function of the wall dimensions [103] [104]

An important conclusion by Zweck is that the volume of the failure body increases by increasing the wall dimensions or by increasing the soil friction angle. A big field test was also carried out by Zweck and Kölnmonheimer Bridges Company in 1953 within the

framework of his research on the spatial passive earth pressure problem. An I-profile wall with section dimensions of 3 m height and 5.6 m width was moved in a sandy silty soil with 2.2 m embedded depth. The value of the measured load reached 392 t. The load calculated using Coulomb's Equation equaled to 326 t. The difference in loads (measured and calculated) was related to the difference in the failure body volume between reality and Coulomb assumptions.

Zweck carried out further experiments [104] investigating the passive pressure on narrow walls embedded in sandy soils. He found out that the width $b_{s.r}$ of the soil failure body, on both sides of the wall, is independent from the depth of the wall t_0, therefore he did not define the relation between the depth of the wall t_0 and the equivalent width of the failure body at both sides of the wall. The major limitation of Zweck's method is, that no considerations of the soil-wall interface friction angle δ were made in the calculations. Furthermore, his assumptions of an inclined resultant earth pressure force on the wall and a planar failure surface do not correspond to actual field conditions. A curved slope surface would better correspond to actual field conditions for such angular load.

Kaercher (1968 - 1980)

Kaercher [43] made comprehensive model experiments as shown in Figure 2-41 in order to investigate the passive earth pressure problem in cohesive soils with parallel movement. Medium plastic clay was used for the experiments. The water content of the soil in the experiments lay between 24 % and 48 % corresponding to the ratio of the soft particles. The soil was placed in layers in the test box. The pile in the prototype was moved during the test in a small velocity, in order to ensure that no extra effect on the passive earth pressure will be developed. The width b and thickness t of the I-profile sections used in the tests were b = 0.7, 1.0 and 2.9 cm and with thicknesses t = 1.5, 2.0, 4.0 cm, respectively.

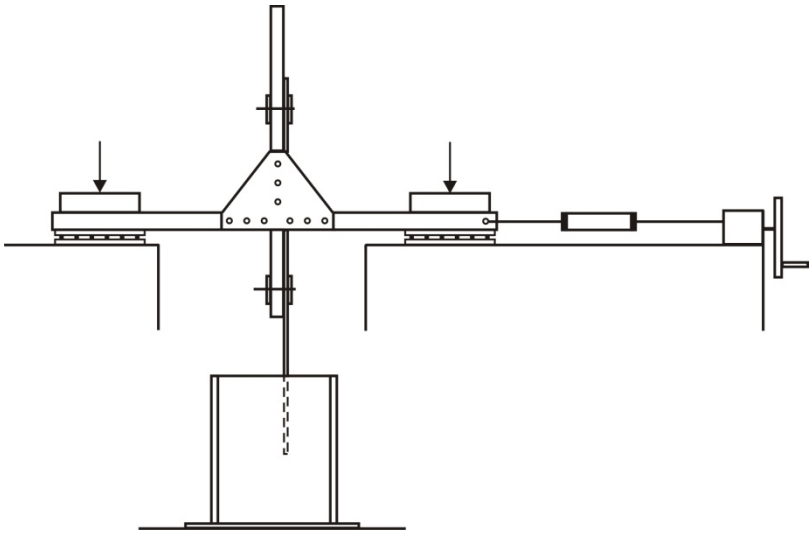

Figure 2-41: Experimental apparatus for passive earth pressure problem [43].

As a result of his experiments, Kaercher proposed the predominant use of the Brinch Hansen method for earth pressure problem calculations, with the inclusion of a modification factor f

to take into account the load resulting from the friction at the failure body sides. Kaercher defined the correction factor f as a function of the I-profile thickness t and width b as shown in Equation [2.59]. The Brinch Hansen theoretical earth pressure force E_{th} is corrected by multiplication with the factor f as shown in Equation [2.60].

$$f = 1 + 0{,}213\frac{t}{b} \qquad [2.59]$$

$$E = E_{th}\left(1 + 0{,}213\frac{t}{b}\right) \qquad [2.60]$$

In an extension of these experiments Kaercher [44] also examined the effect of inclined ground surfaces on the horizontal loading. Basing upon his proposal that the horizontal earth pressure $H_{b,h}$ of the I-profile is uninfluenced by the ground inclination, Kaercher calculated the earth pressure coefficients by setting the earth pressure inclination angle δ_p to zero. For this reason, the calculation results always lie on the safe side in comparison to the experimental results. He validated his assumption making calculations with the earth pressure inclination not set to zero.

Kaercher [44] also investigated the stability of horizontal loaded piles with horizontal and inclined ground surfaces. For this purpose an experimental apparatus was developed as shown in Figure 2-42 with a different section pile using Karlsruhe sand. For an inclined ground surface a correction factor is defined as a function of the inclination angle and the soil friction angle.

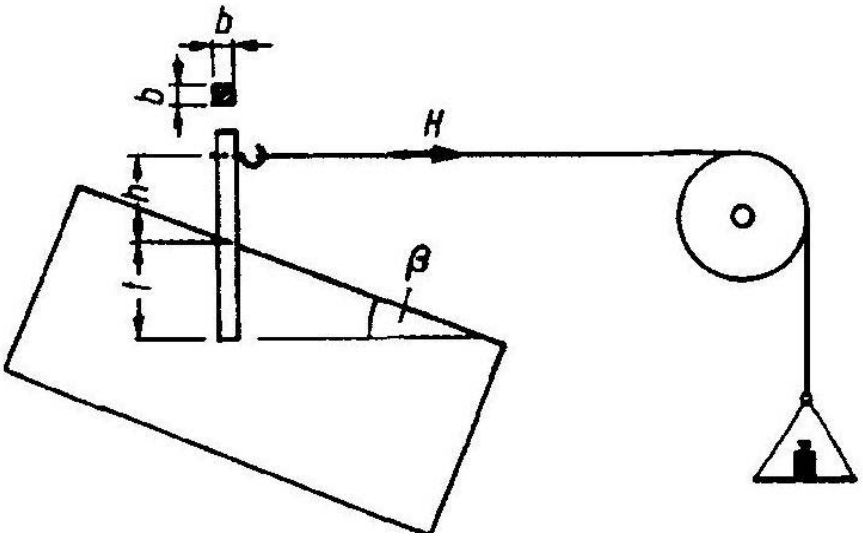

Figure 2-42: Experimental apparatus for passive earth pressure problem [44]

Figure 2-43 shows a comparison between the approach of Weissenbach and Brinch Hansen to the results of Kaercher's tests for different I-profiles. For both, smooth walls w_c and frictional walls w_0 of different profile sections (I or U section) with different ratios t/b, it was observed that Kaercher's results are in a better agreement with Brinch Hansen's than with

Weissenbach's approach. Kaercher found out that the values of Weissenbach are higher than his values.

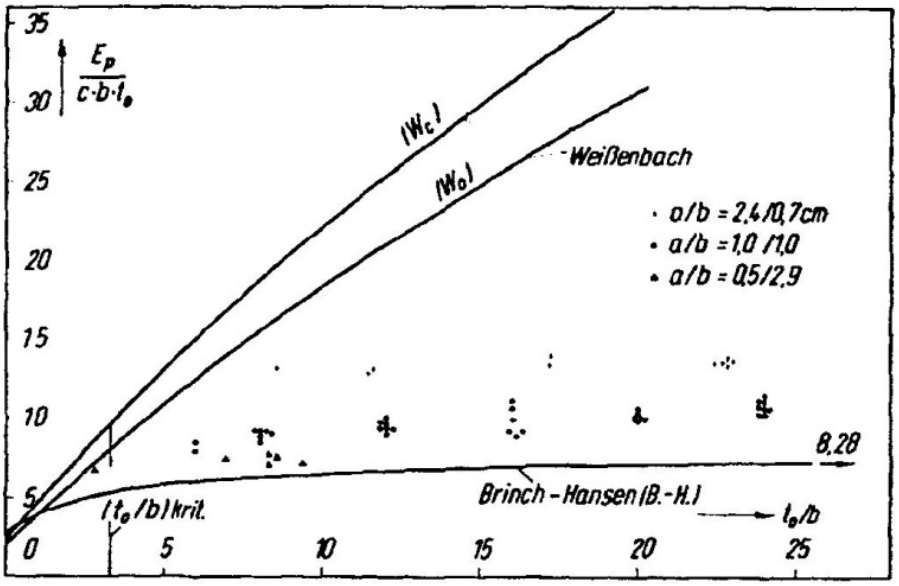

Figure 2-43: Comparisons between approaches of Weissenbach, Brinch Hansen and Kaercher [43]

Horn (1970)

Horn [39] carried out both, laboratory and field tests, in order to investigate the mobilized spatial passive earth pressure against embedded walls of different dimensions (B/H). In the experiments he used retaining walls that consist of I-profile sections with timber planks between them. He used a wall of width B and varied the penetration depth t between 0.5 m and 3.0 m without permitting the wall to move vertically. A wet sandy soil was used in the experiments. In each test, the wall was displaced using parallel movement mode till the peak at the soil limit state conditions was reached.

The spatial passive earth pressure at peak is defined in Equation [2.61] below:

$$E_{ph}^{*} = \frac{1}{2}\gamma H^2 B K_{ph2D} A \left(1 + C\frac{H}{B}\right) \qquad [2.61]$$

The Constant A is defined as the ratio of the earth pressure coefficient calculated from Horn's results to the 2D theoretical earth pressure coefficient $A=\frac{K_{ph2D_{Horn}}}{K_{ph2D}}$.

The experimental constant C is a function of the soil friction angle φ. For a soil friction angle $\varphi = 30°$ is $C = 0.3$. A simplification of Equation [2.61] with the assumption that $\omega_\varphi = 0.5AK_{ph2D}$ yields Equation [2.62] below:

$$E_{ph}^{*} = \frac{1}{2}\gamma H^2 B K_{ph2d} + \frac{1}{3}\gamma H^3 \omega_\varphi \qquad [2.62]$$

Where:

K_{ph2D} Earth pressure coefficient for 2D case

ω_{φ} Frictional spatial passive earth pressure coefficient as a function of soil friction angle φ

The mobilized earth pressure E_{ph} is related to the spatial earth pressures at peak E^*_{ph} with the mobilized displacement function W_e as follows:

$$\frac{E_{ph}}{E^*_{ph}} = W_e \qquad [2.63]$$

The spatial Earth pressure at peak

$$E^*_{ph} = \frac{1}{2}\gamma H^2 B K_{ph2D} A\left(1 + C\frac{H}{B}\right) = \frac{1}{2}\gamma H^2 B K_{ph2DHorn}\left(1 + c\frac{H}{B}\right) \qquad [2.64]$$

With:

$$W_e = \frac{\frac{\Delta l}{\Delta l_{Br}}}{0.12+0.88\frac{\Delta l}{\Delta l_{Br}}} \qquad [2.65]$$

W_e Mobilization function of displacement

Δl Mobilized displacement

Δl_{Br} Displacement at peak

$$\Delta l_{Br} = 10.4H^{1.5}(1 - 0.625D) \qquad [2.66]$$

Where:

D The relative density

H The embedded depth of the wall

Horn also investigated the stress distribution along a rigid wall in both conditions of soil limiting state, firstly at the peak ultimate state conditions and secondly at soil serviceability conditions. The stress distribution was calculated along the width at different wall sections namely at the corners and the middle of the wall. He found that the stress value is higher at the corner of the wall than in the middle of the wall as illustrated in Figure 2-44.

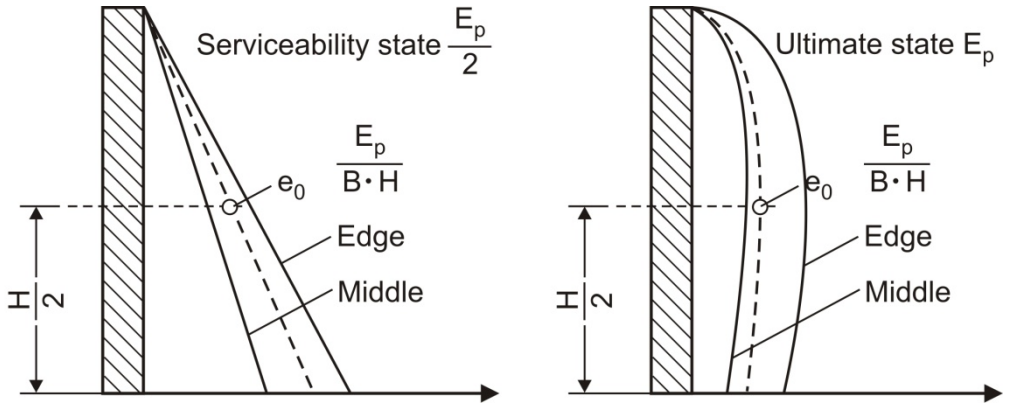

Figure 2-44: Stress distribution for earth pressure at peak along the wall at corner and middle [39]

Horn also investigated the problem of the neighboring I-profile overlapping pressure and its dependence on the distance between the I-profiles. His analyses showed a very high dispersion of the results, which is related to the difference in the material natures, the laboratory deficiency in the properties data and the scale effects according to the size of the experimental models.

Al - Diban (1999)

Al – Diban [2] carried out numerous experimental model tests with fixed embedded I-profiles between the years 1995 to 1999 at the TU Dresden institute for Geotechnics. The profile was moved in a 1.5·0.5·0.8 m glass box to make the visualization of the moving soil particles possible. He tested a sandy soil with relative soil densities of 26 %< D_r < 83%. In the process, he examined the influence of inclined ground surfaces and stepped ground surfaces on the failure force of horizontally loaded I-profiles as shown in Figure 2-45.

Al-Diban calculated the effect of the spatial passive earth pressure on an I-profile wall by considering two areas. Firstly substituted width $\bar{b_1}$ above the pivoting point and secondly $\bar{b_2}$ for the spatial effect below the pivoting point. The effective I-profile width $\bar{b_1}$ and $\bar{b_2}$ are obtained as follows:

$$\bar{b_1}(\varphi) = \begin{cases} b + \eta_{pv}\, tan\varphi \sqrt{\frac{bt}{0{,}3}} : b < 0{,}3t \\ b + 0.6 tan\varphi . t : b \geq 0.3t \end{cases} \text{[mm]} \qquad [2.67]$$

$$\overline{b_2}(\varphi) = \begin{cases} b + \eta_{pv} tan\varphi \sqrt{\frac{b(t_0 + 0{,}5t_2)}{0{,}3}} : b < 0{,}3t \\ b + \eta_{pv}(t_0 + 0{,}5t_2) tan\varphi : b \geq 0.3t \end{cases} \text{[mm]} \qquad [2.68]$$

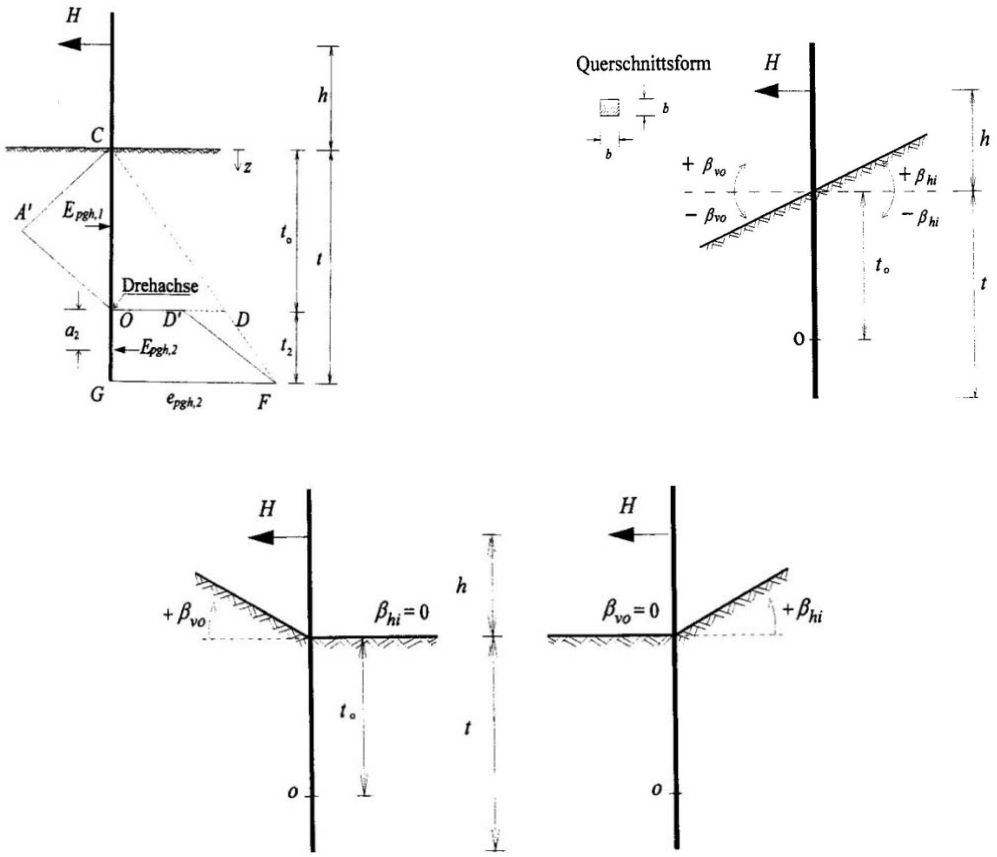

Figure 2-45: Description and Mechanism of experimental model by Al Diban [2]

The factor η_{pv} is for the consideration of a better conformity between the previous theoretical Equation and the experimental results and it is calculated as follows:

$$\eta_{pv} = n_p 1.6 \tan(\varphi) \qquad [2.69]$$

Constant n_p is calculated according to TGL Standard 11464/03 as a function of the relative density I_D [2].

Neuberg (2002)

Neuberg [56] studied the spatial passive earth pressure effect by establishing an experimental model of a retaining wall that consisted of I-profile sections with timber planks between them as shown in Figure 2-46. He also performed numerical simulations using a discrete element model. From the results of both the experimental and the numerical analysis, he proposed a mobilization function for the dependence of passive earth pressure on the corresponding wall displacement, which will be discussed later in section 2.2.4.

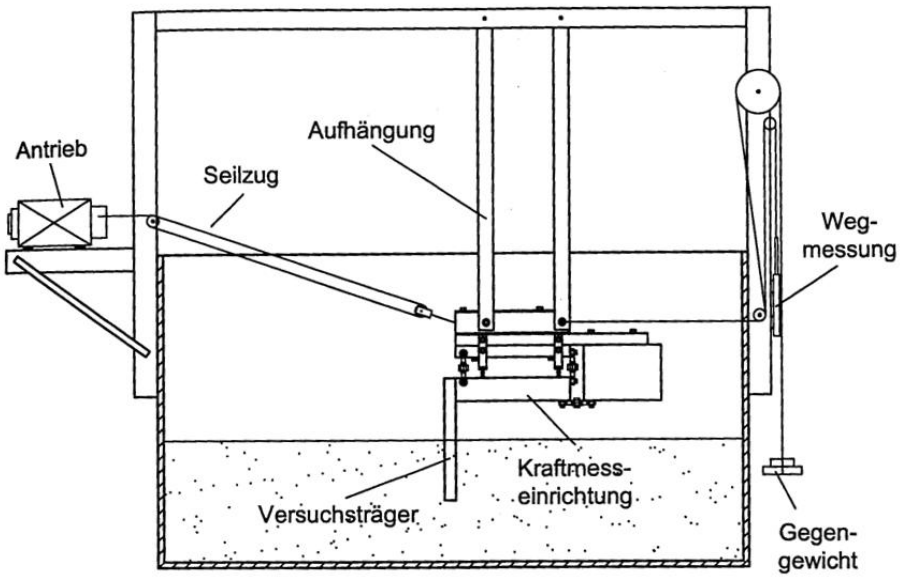

Figure 2-46: Neuberg experimental apparatus [56]

Arnold and Herle (2005):

Herle [53] carried out a research on a new type of a tunnel drilling machine that had been developed and patented by Hoch Tief construction AG which was designed to be supported by rigid plates that are laterally pressed into the soil. These plates are used as supports or abutments in tunneling and pipeline construction as seen in Figure 2-47.

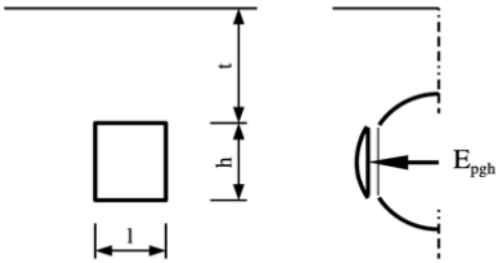

Figure 2-47: Plate laterally pressed into the tunnel side. Left: side view; Right: cross section [53]

The load-displacement behavior of these structures is of particular importance for their design. The horizontal displacement of the supporting plates against the soil generated a special case of spatial earth pressure problem that was investigated experimentally for dry sand at different relative densities. Additionally a 3D Numerical simulation of this special earth pressure problem was made using the Finite Element Code TOCHNOG. Moreover a mobilization function between the earth pressure coefficient and the corresponding displacement was obtained taking into consideration the plate dimensions (width and height) and the overburden depth. In a first step experiments with dry sand of different densities were performed. These tests were subsequently used to validate the numerical simulations of this boundary value problem. In the second step, the numerical model included a parametric study.

This study was carried out using field values in order to investigate the influence of stress level, density and overburden for only the parallel wall movement mode. The test consisted of a box with dimensions of length 3 m, width 1 m and height 1.5 m, which included a wall with a varied height from 0.6 m to 1.2 m. The wall was displaced using the parallel movement mode without reaching the peak at the ultimate state. Two types of sand, Dresdner sand (DDS) and Ottendorf-Okrillaer sand (OOS), were used. The wall had a coarse aluminum surface with protrusions to develop a frictional wall-soil interface behavior at request. As a general result, it was observed by Arnold and Herle that the passive earth pressure on a supporting plate under an overburdened soil is mobilized similar to a wall in 2D case for small displacement. Figure 2-48 shows the FEM mesh of the model used in the numerical calculations to serve scope of the research. The soil was modeled using the hypoplasticity constitutive law to simulate the scale effect. The results were then compared with the previous test result as shown in Figure 2-49.

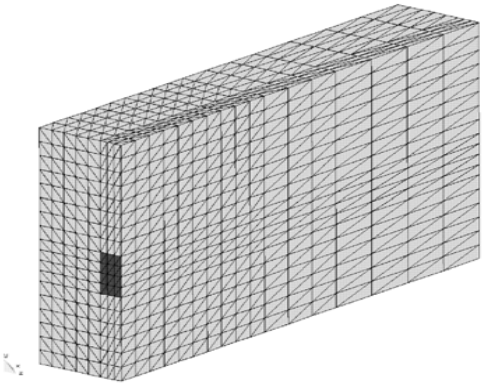

Figure 2-48: Finite element mesh used in the simulations of the model [53]

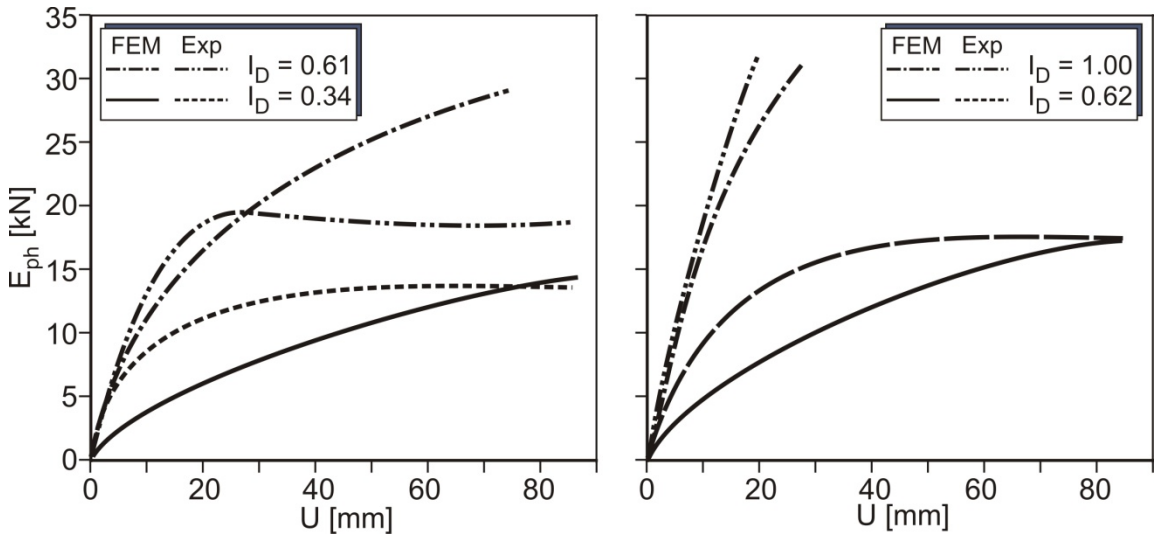

Figure 2-49: Experimental and FEM results a) for DD sand b) for OO sand [53]

The FEM results are in fairly acceptable agreements with the experimental test, which means that FEM has the capability to simulate the behavior of soil induced contractancy and dilatancy with an overestimation of the deformation values in some complicated cases.

Bilina (1998):

An experimental work was carried out by Bilina [65] [66] to investigate the problem of the spatial passive earth pressure. The experimental model, which was used, consisted of a box with dimensions of 21 cm depth, 28 cm width and 56 cm length filled with sandy soil as shown in Figure 2-50. A pile embedded in the soil was moved horizontally, using three load cells at different heights, in order to generate a 3D passive earth pressure. The weight of the pile was modeled by adding a mass on the pile head with the restriction of vertical I-profile pile movement. The applied forces and the pile horizontal displacement were measured. The experimental results were then used to derive an Equation for 3D passive earth pressure as a difference between active and passive pressure on both sides of the pile.

$$E_{ph}{}^{*} = \Delta E + E_{ah}{}^{*} \qquad [2.70]$$

Where:

E_{ph}^{*} The 3D horizontal passive earth pressure load
E_{ah}^{*} The 3D horizontal active earth pressure load
ΔE The difference between passive and active

The earth pressure coefficient is calculated:

$$\Delta K_{\gamma h} = \frac{2\Delta E}{\gamma h^2 B} \qquad [2.71]$$

Where:

γ The soil density
h The embedded depth of the pile
B The width of the I-profile pile perpendicular to the displacement direction.

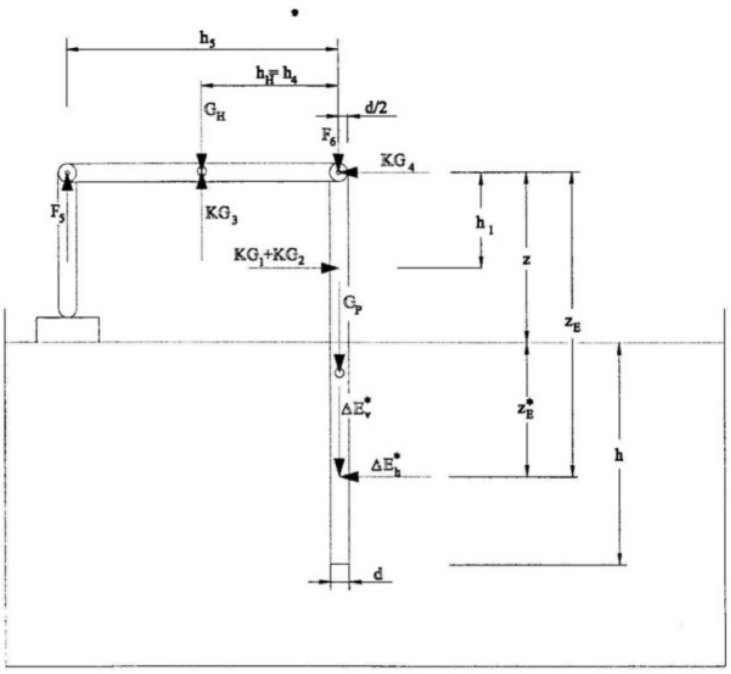

Figure 2-50: Earth pressure experimental test [65].

The mobilization curves of the passive earth pressure dependent on relative displacement during the advance of the experiment in medium dense fine sand and medium dense coarse sand were also recorded by varying the spatial ratio B/H (between 8.30 to 7.88) and for different embedded depths (between 20.7 to 19.7). The results are illustrated in Figure 2-51.

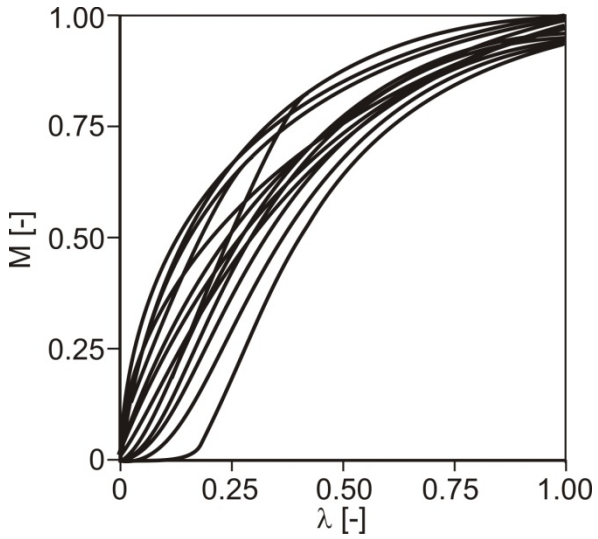

Figure 2-51: Experimental Mobilization approaches for the passive earth pressure (M) due to relative displacement (λ) [65]

While M and λ are defined in the following Equations:

$$M = \frac{\Delta E^*_h - \Delta E^*_{h.o}}{\Delta E^*_{h,f} - \Delta E^*_{h,o}} \quad [2.72]$$

$$\lambda = \frac{U}{U_p} \quad [2.73]$$

Where:

ΔE^*_h The mobilized result of passive earth pressure load obtained from the experimental results of the test.

ΔE^*_{h0} The earth pressure at rest load derived from the experimental results of the test.

$\Delta E^*_{h,f}$ Passive earth pressure load at peak due to DIN 4085

U The mobilized displacement

U_p The displacement at peak

2.2.3 The German Standard DIN 4085 / OE – Standard B 4434

The calculations of the spatial passive earth pressure according to the German Standard DIN 4085 [31] bases on the experimental results of many researchers. The spatial 3D earth pressure against a moved wall must be calculated using an imaginary calculative width for the friction and cohesion parts as shown respectively in Equations [2.74] and [2.75].

$$b_{s,r} = \mu_{pgh} b \quad [2.74]$$

$$b_{s,k} = \mu_{pch} b \quad [2.75]$$

In the process, the shape coefficients μ_{pgh} and μ_{pch} are determined according to the following Equations [2.76] and [2.77]:

$$\mu_{pgh} = \begin{cases} 1 + 0.6 \tan\varphi \frac{H}{b} : \frac{H}{b} < 3.333 \\ 0.55(1 + 2\tan\varphi)\sqrt{Hb} : \frac{H}{b} \geq 3.333 \end{cases} \quad [2.76]$$

$$\mu_{pch} = \begin{cases} \left(1 + 0.3\frac{H}{b}\right)(1 + 1.5\tan\varphi) : \frac{H}{b} < 3.333 \\ 1.1(1 + 0.75\tan\varphi)\sqrt{Hb} : \frac{H}{b} \geq 3.333 \end{cases} \quad [2.77]$$

The total sum of the earth pressures due to self weight and cohesion are calculated as follows:

$$E_{ph=}\frac{1}{2}\gamma H^2 b_{s,r} K_{pgh} + cHb_{s,k}K_{pch} = \frac{1}{2}\gamma H^2 b\mu_{pgh}K_{pgh} + cHb\mu_{pch}K_{pch} \quad [2.78]$$

The passive earth pressure coefficients in the 2D case for self weight K_{pgh} and cohesion K_{pch} in the DIN 4085 are determined according to curved failure surfaces. According to the OE-Standard B4434 [57] the coefficients can be determined with plane as well as curved failure surfaces, taking into consideration that Coulomb's theory delivers too high values for friction angles $\varphi > 35°$ or higher earth pressure inclination angles.

The displacement at the ultimate limit state (failure condition) in German standard DIN 4085 is calculated as follows:

For thin walls when $\frac{B}{H} < 0.333 \Longrightarrow U_{Bd} = 40\frac{1}{1+0.5D}\frac{H^2}{\sqrt{B}}$ [2.79]

For broad walls when $\frac{B}{H} \geq 0.333 \Longrightarrow U_{Bd} = 100(1-0.6D)\sqrt{H^3}$ [2.80]

Where:

D The relative density of the soil

U_{Bd} The displacement at failure conditions in (mm)

H The embedded depth in (m)

B The wall width in (m)

And the displacement at half limit load (Serviceability) is defined as follows in Equations [2.81] and [2.82]:

$$U_{Gd} = 2\frac{1}{1+0.5D}\sqrt{\frac{H^3}{B}} \text{ [mm] for thin walls } \frac{B}{H} < 0.333 \quad [2.81]$$

$$U_{Gd} = 10(1-0.6D)\sqrt{H^3} \text{ [mm] for wide walls } \frac{B}{H} \geq 0.333 \quad [2.82]$$

2.2.4 Numerical modeling of spatial passive earth pressure

A number of numerical models developed by many researchers are presented in the following section.

Neuberg (2002)

Neuberg (2002) [56] modeled the spatial passive earth pressure problem by carrying out an experimental model of a retaining wall that consisted of I-profile sections and timber planks between them. He also used the Distinct Element Method (DEM) with the Particle Flow Code (PFC) software. The DEM model is illustrated in Figure 2-52.

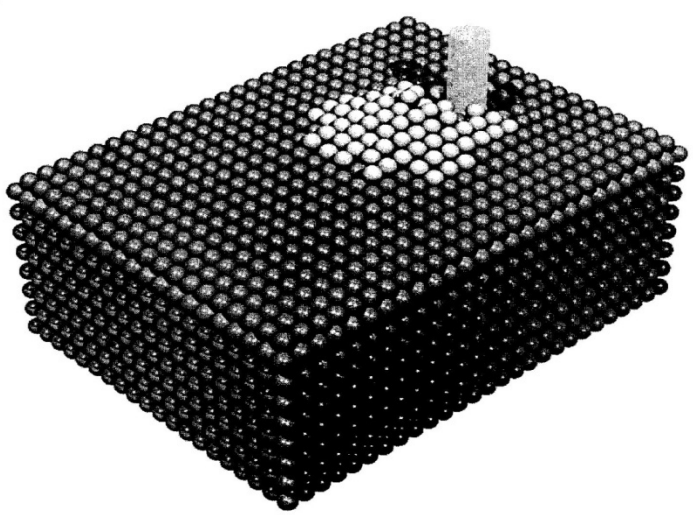

Figure 2-52: DEM model [56]

Neuberg made a model of a cylinder body surrounded by the soil particles taking into consideration the soil and the wall properties. Based on his numerical and experimental results, he obtained a mobilization approach for the spatial passive earth pressure by parallel movement as a function of the corresponding displacement. The approach is illustrated in Equation [2.83]. The Distinct Element Method was extended and improved to enable the numerical simulation of load tests. Based on this knowledge, conditions, which were not covered by experiments, were simulated by means of the DEM. The test matrix could be accordingly extended. With the results of these simulations a new calculation method for parallel movement was derived in the frame of the subgrade reaction method.

$$e'_p = \frac{mE_p}{tb}\left(\frac{-4m^2-59}{4m^2-31}\right)\bar{Z}^{\left(\frac{-8m^2-28}{4m^2-31}\right)} \qquad [2.83]$$

The mobilization degree of the passive earth pressure (m) is defined as follows:

$$m = \frac{E'_p}{E_p} = (1-(1-\bar{U})^2)^{1.55I_D} \qquad [2.84]$$

Where:

$$\bar{U} = \frac{U}{U_B} \qquad [2.85]$$

I_D The relative density

U The moblized of the displacement

U_B The displacement at the peak

E'_p The mobilized passive earth pressure force

E_p The passive earth pressure force at peak

$\bar{Z}$ The geometrical depth according to the coordinate system of the model

t The total embedded depth of the I-profile wall

b The width of the I-profile wall normally to the load direction

Figure 2-53 shows the results of Neuberg's mobilization function for different soil densities. It is to be noticed that according to his mathimatical function when I_D=0, the earth pressure mobilization function is a straight line equal to one.

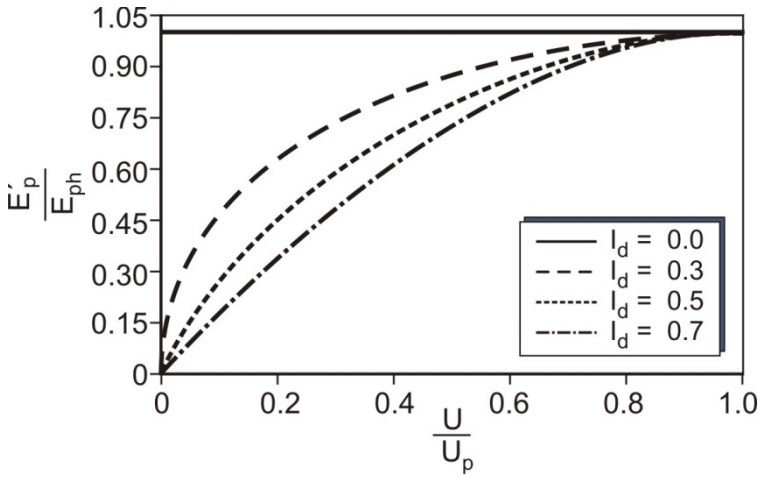

Figure 2-53: Mobilization functions in relation to the compactness of the packing [56]

The following Figure 2-54 shows horizontal stress distributions at different values of displacement for an I-profile wall with 2 m embedded depth.

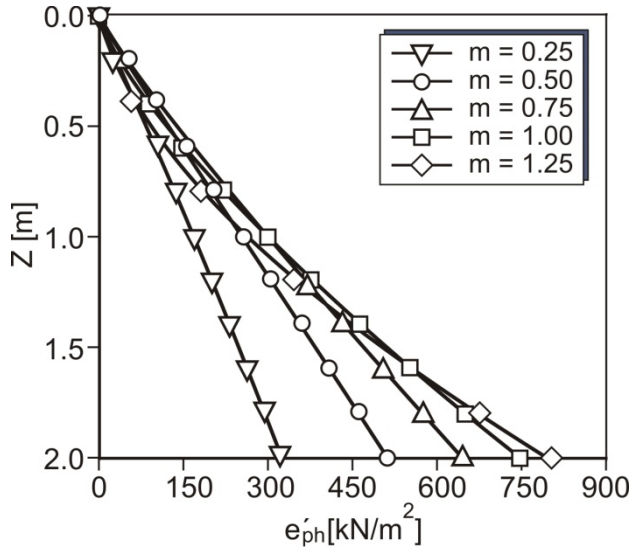

Figure 2-54: Stress distribution at different displacement [56]

The displacement at failure conditions in a parallel movement was determined by Neuberg according to his result as follows:

$$U_B = \frac{0.03t}{I_D} \text{ [m]} \qquad [2.86]$$

Where:

U_B The displacement at failure

t The embedded depth of the I-profile wall

I_D The relative density

The displacement at failure by Neuberg according to his experimental results, is in the range of 10 – 20 % of the embedded depth and is about 50 % away from Weissenbach's experimental results. From other side the displacement at serviceability ultimate $U_{B,50\%}$ by Neuberg is defined depending on his results as in the following Equation:

$$U_{B,50\%} = \left[1 - \sqrt{1 - 0.5^{\left(\frac{1}{1.55 I_D}\right)}}\right] \frac{0.03t}{I_D} \text{ [m]} \qquad [2.87]$$

This is in the range of 2 – 4 % of the embedded depth t, which is also far from Weissenbach's results and DIN 4085.

Jung (2007):

Jung [42] used a finite element simulation to investigate the behavior of I-profile walls with the application of an elasto-plastic material model for sand. His numerical results were calibrated with in-situ measurements of a large scale model carried out at the University of Texas [13].

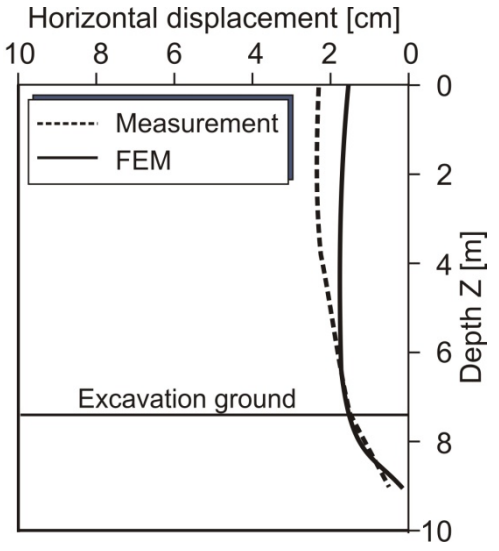

Figure 2-55: FEM and experimental measurement results for the wall horizontal movement along the total height of the excavation's wall [42].

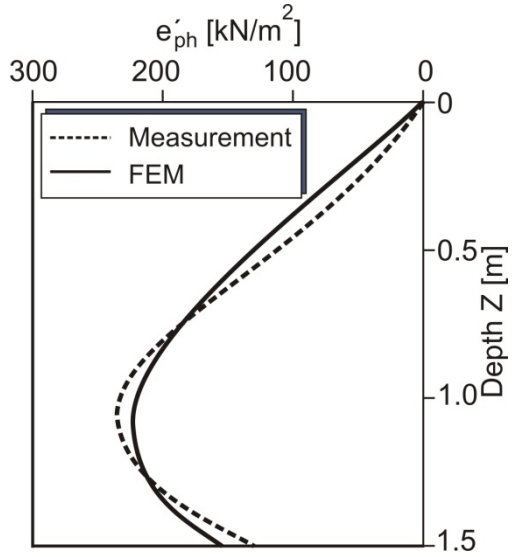

Figure 2-56: FEM and experimental results for the passive earth pressure distribution along the embedded depth [42]

The curves in Figure 2-55 and 2-56 show a good agreement between the distributions for both of FEM and the experimental results. As a result of his study, a mobilization approach for the passive earth pressure as a function of the relative displacement was obtained as shown in Equation [2.88]

$$m = \frac{E'ph}{E_{ph}} = \left[1 - \left[1 - \frac{U}{U_B}\right]^2\right]^{C_E} \qquad [2.88]$$

The value of the displacement at failure by parallel movement is defined using the previous Neuberg's Equation [2.88]. The constant C_E ($C_E = 2.44\ I_D$) is also defined using previous Neuberg's results as a function of relative density I_D.

Figure 2-57 shows a comparison of the mobilization approach of the passive earth pressure between Besler in 2D case on one hand and Jung and Neuberg in 3D case on the other hand. The curves show a good agreement.

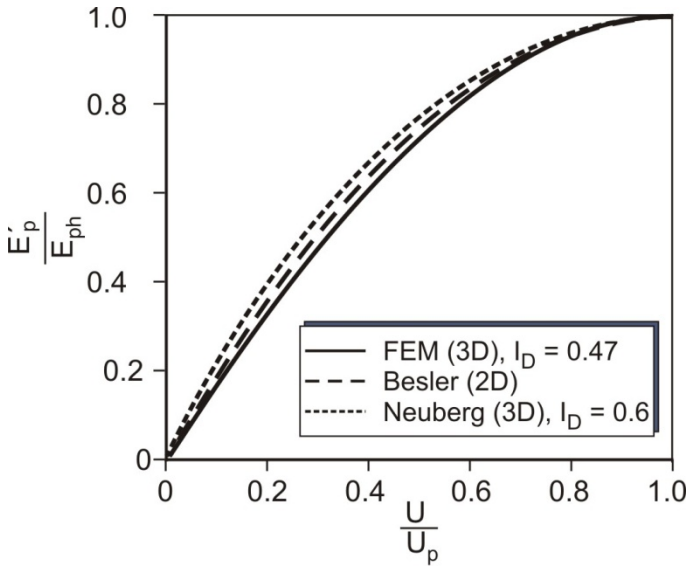

Figure 2-57: Comparison of the passive earth pressure mobilization approach as a function of relative displacement between Besler, Neuberg and Jung [42]

Jung [42] calculated the coefficient of subgrade reaction as a function of many parameters $K_{sh} = \frac{e'_{ph}(Z,B,t,a,H,EI)}{U(Z,B,t,a,H,EI)}$ namely embedded depth t [m], the bending stiffness EI of I-profile [KN/m^2], width of the I-profile B [m], depth of the excavation H [m], the distance between two I-profiles a [m] and the coordinate in the depth direction Z [m].

Figure 2-58 below shows results of the mobilization function for the earth pressure by Jung due to the subgrade reaction method at different depths Z.

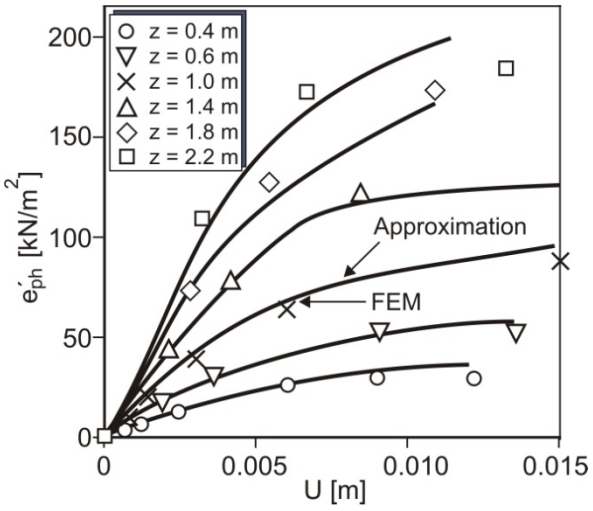

Figure 2-58: Mobilization function of Subgrade coefficient and earth pressure distribution [42]

In his thesis Jung studied the passive earth pressure on I-profile wall in a general mode of movement, but he did not take the soil density and mode of movement into account.

Benmebarek (2008):

Benmebarek [7] carried out a numerical study of 3D passive earth pressure for parallel movement of rigid walls by means of a finite element simulation as shown in Figure 2-59.

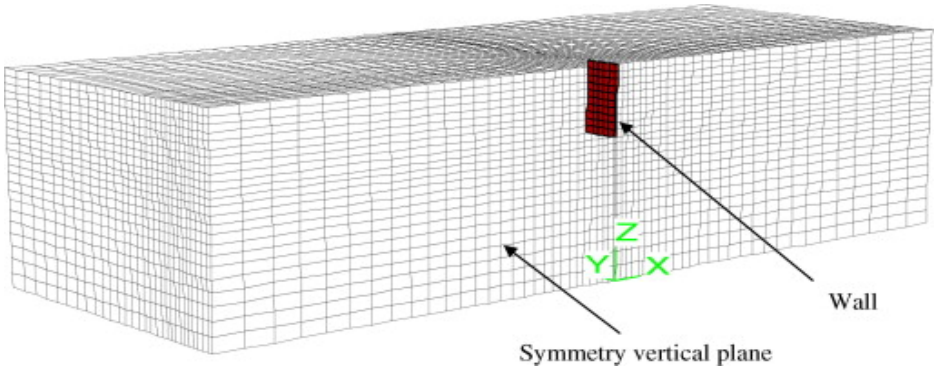

Figure 2-59: FEM Model using FLAC software [7]

He used a linear elastic-ideal-plastic constitutive model with Mohr-Coulomb failure criterion and an associated flow rule. His results were presented in design tables that show the relationship between different geometrical input parameters and spatial passive earth pressure coefficients. Figure 2-60 summarizes the numerical results showing the decay of the spatial passive earth pressure correction factor μ ($\mu = K_{ph3D}/K_{ph2D}$) with increasing spatial ratio until it reaches the 2D passive earth pressure conditions.

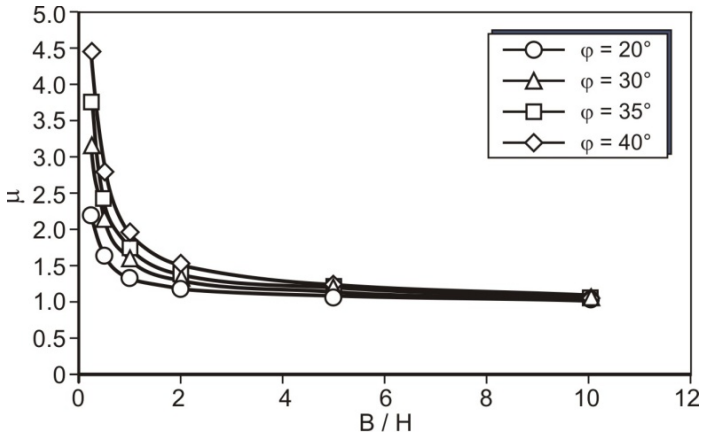

Figure 2-60: Spatial passive earth pressure for different friction angles [7]

Benmebarek showed the effect of the friction angle on the distribution of the failure body and on the spatial passive earth pressure coefficient. The results show an increase of the failure body volume by increasing the soil friction angle. It also shows that for the same soil friction angle φ, the failure body volume is shaped differently for different soil wall interface friction angles φ. The results are illustrated in Figure 2-61.

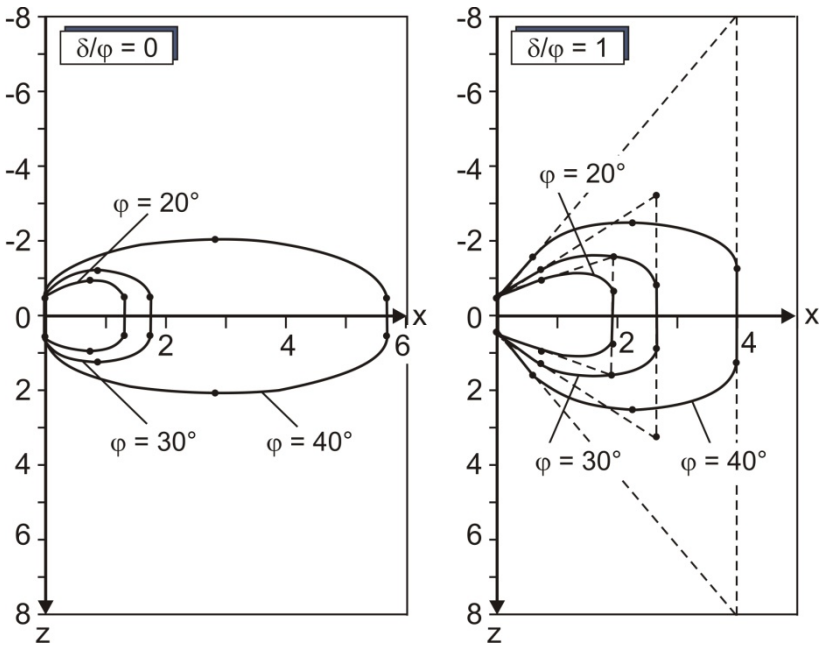

Figure 2-61: Surface plane of the failure body at peak as a function of the friction angle φ [7]

Benmebarek concentrated in his researches on the passive earth pressure at peak for a parallel movement without considering the development of the passive earth pressure with increase of the displacement till the peak or for other modes of wall movement.

Rmanso and Antäo (2010):

A three dimensional FEM model of the limit analysis upper-lower bound theorem using 3D SUBLIME software was done by Rmanso and Antäo [89] to determine the horizontal passive earth pressure coefficient. The software 3D SUBLIME was developed by a research group at university NOVA de Lisbon. It solves large scale problems using parallel computing techniques by scaling the mechanism and setting the external forces work rate to minimize the difference between the plasticity dissipated work rate and the work rate of the fixed external forces. The geometry of the model consists of a symmetrical vertical rigid wall with width B and height H. The analysis was done using the following wall dimensions ratio n=$\frac{B}{H}$= 0.25, 0.5, 1.0, 2.0, 5.0, 7.0 and ∞ during the analysis. The soil surface is horizontal. A Mohr-Coulomb yield criterion with cohesionless sand and different friction angles was used. The angle of the soil-wall interface friction angle δ was also varied to calculate the passive earth pressure for frictional wall.

Figure 2-62 shows the results of Rmanso and Antäo for the passive earth pressure coefficient as a function of spatial ratio for a smooth wall and soil with three different friction angles (30°, 35° and 40°).

It is to be noticed that the correction factor μ decreases by increasing spatial ratio n till an almost constant value is reached at $n = \infty$ (2D case). Also the correction factor increases by increasing the friction angle φ.

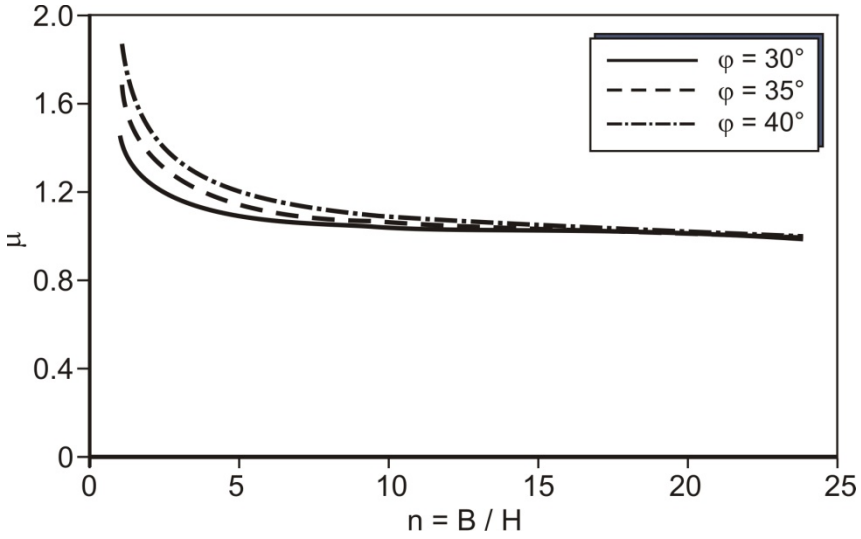

Figure 2-62: Correction factor μ for passive earth pressure [89]

As a result of the investigation the correction factor μ is also defined as a function of the spatial ratio multiplied with a constant m_α which is a function of the Rankine passive earth pressure coefficient in 2D case. The function is defined as follows:

$$\frac{K_{ph}}{K_{kph,2D}} = 1 + m_\alpha \frac{B}{H} \qquad [2.89]$$

The following Equation gives the values of the constant m_α as a function of Rankine passive earth pressure coefficient in 2D case.

$$m_\alpha = 0.36 + 0{,}36\left(K_p^{Rankine}\right)^{0.75} \qquad [2.90]$$

Where $K_p^{Rankine}$ is Rankine's passive earth-pressure coefficient which is given as follows:

$$K_p^{Rankine} = \frac{1+\sin\varphi}{1-\sin\varphi}. \qquad [2.91]$$

The effect of the wall-soil friction angle was also investigated and the following results were obtained as shown in Figure 2-63.

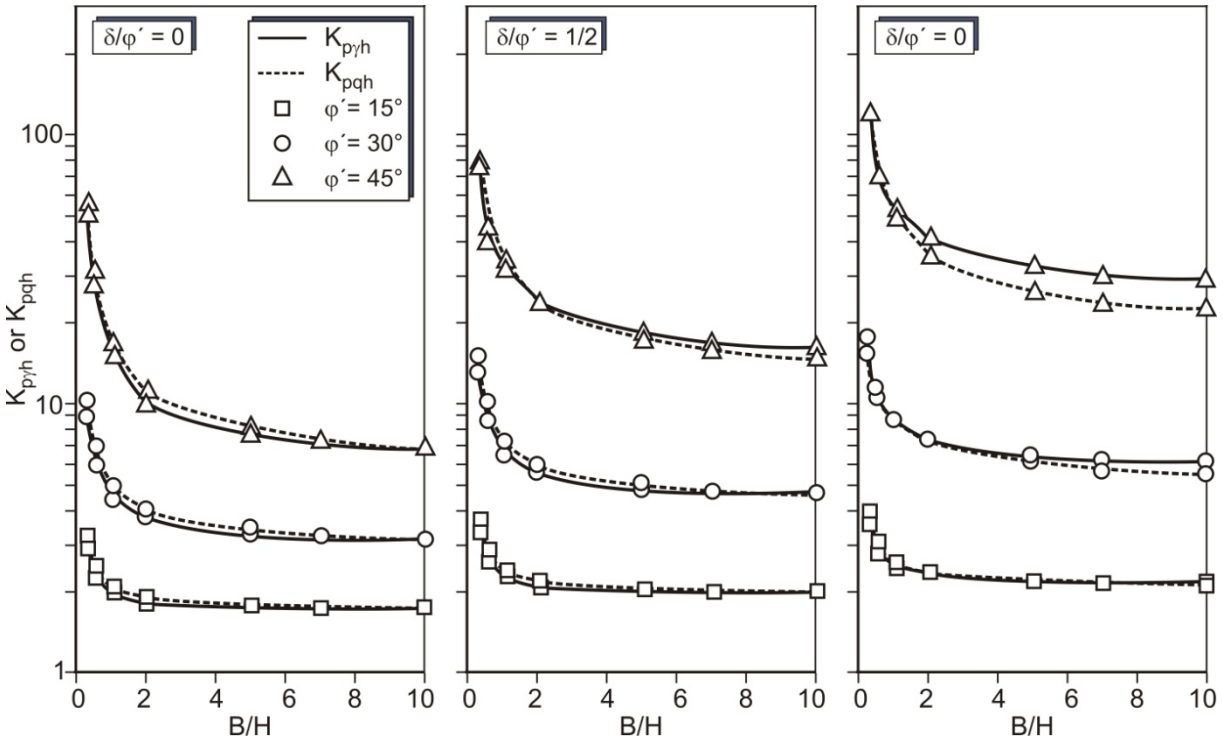

Figure 2-63: Correction factor of the spatial passive earth pressure coefficient K_{p3D}/K_{p2D} as a function of the spatiality ratio B/H [89].

Earth pressure coefficient increases by increasing soil-wall interface friction angle δ. This increase was related by Rmanso and Antäo to the increase of the failure body volume. They noticed that the failure body volume increases by increasing wall soil interface friction angle δ as shown in Figure 2-64. The passive earth pressure by Rmanso and Antäo was investigated only for parallel movement.

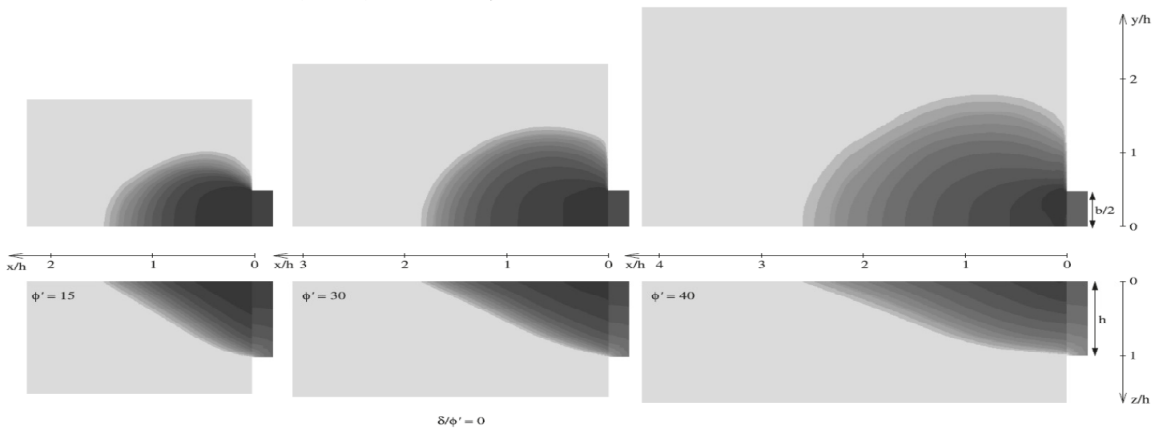

Figure 2-64: Representation of the relative magnitude of the velocity fields obtained in determining soil weight passive earth pressure coefficients for B/H=1 for φ = 15°, 30°and 40° [89].

3 Finite Element Modeling

3.1 Introduction

Recent advances in computers and calculation algorithms have made finite element analysis a viable tool for assessing the internal mechanics of soil structures and the interaction in between. Finite element models consist of many single elements connected to each other at nodes. The simulations are carried out by calculating the displacements or the stress in these nodes according to defined mathematical functions. The calculations are done for each element and thereafter assembled together globally according to certain equations. The displacement within a single element may lead to its deformation. The deformation in turn results to internal forces within the element. The magnitude of the internal forces essentially depends on the relation between the material properties and the element deformation. This relation implies on the constitutive material law and element type in use. The Finite element method (FEM) offers the most powerful analytical approach which enables the simulation of user defined parameters and boundary conditions. Examples of such user defined parameters and boundary conditions may include: non-linear soil behavior, soil homogeneity, different boundary conditions and the contact types between the soil and the structure. The accuracy of numerical modeling results significantly depends on the proper definition of the studied case and a careful control of some critical parameters such as rupture criteria, non-linearity, element types, friction coefficients and mesh fineness. Most of soil-structure interaction models are made using the non-linear finite element method. This is done in order to account the non-linear stress-strain analysis and the geometrical non-linear behavior of the model.

Two types of FEM methodologies are relevant, namely the implicit and the explicit techniques. Implicit methodologies obtain solution by simultaneous solving systems of equations. Therefore a frequent updating of the stiffness matrix for nonlinear FEM analysis is needed which is used in the following thesis. The explicit method however needs smaller time steps to comply with stability requirement for solving the equation, but this technique will not be used in the thesis.

In general, FEM models are conceptual descriptions or approximations that describe physical systems using mathematical equations. They are not exact descriptions of physical systems or processes. The usefulness of a model depends on how closely the mathematical equations approximate the physical system which is modeled. In order to evaluate the applicability of a model, it is necessary to understand the physical system and the assumptions embedded in the derivation of the mathematical equations.

Other important parameters are the geometrical discretization, the size of the model and the time of the step used in the incremental calculation that each step in an Abaqus analysis is divided into multiple increments.

The finite element method (FEM) enables the examination of the force - deformation behavior of complex geometrical structures with different material properties. An attempt to explain the continuum mechanism basic principle completely is outside the scope of this chapter. The

major principle of the FEM, depends on the theory that energy is neither created nor destroyed as shown in the following equation.

$$\Pi = \Pi_i + \Pi_a = \sum_e \Pi_i^e + \sum_e \Pi_a^e \qquad [3.1]$$

With:

Π The total potential energy of the system

Π_i The potential internal energy of the system

Π_a The potential outer energy of the system

$\sum_e \Pi_i^e$ Sum of the potential internal energy over all elements e

$\sum_e \Pi_a^e$ Sum of the potential outer energy over all elements e

The determination of the values of loads such as Gravitation using the energy theory is done by calculating the difference between outer and inner energy.

The FEM calculation is executed according to the steps shown below:

1. Discretization of the system into a suitable number of finite elements
2. Determination of an element stiffness, element plasticity or mixed element matrix
3. Transformation of each element relationship into the global coordinate system.
4. Integration of all boundary conditions
5. Determination of the unknown variables through the implementation of the equation systems
6. Determination of the magnitude of stresses, deformation and other output parameters from the global variables

Using the constitutive non-linear model laws, the solution is obtained iteratively through repetition of the steps above with the adjustment of the element stiffness in dependence of the stresses or expansions.

In general the strain is defined as follows: $\varepsilon_{ij} = \frac{1}{2}(u_{i,j} + u_{j,i})$

Obtaining the strains according to the displacement direction in a 3D space can be done in major axis or any other x, y and z coordinate. By this the following strain matrix results.

$$\varepsilon_{ij} = \begin{bmatrix} \varepsilon_{11} & \varepsilon_{12} & \varepsilon_{13} \\ \varepsilon_{21} & \varepsilon_{22} & \varepsilon_{23} \\ \varepsilon_{31} & \varepsilon_{32} & \varepsilon_{33} \end{bmatrix} = \frac{1}{2} \begin{bmatrix} 2\varepsilon_x & \gamma_{xy} & \gamma_{xz} \\ \gamma_{yx} & 2\varepsilon_y & \gamma_{yz} \\ \gamma_{zx} & \gamma_{zy} & 2\varepsilon_z \end{bmatrix} \qquad [3.2]$$

Where:

$\varepsilon_{i,j}$ The element axial strain vector

$\gamma_{i,j}$ the element shear strain

i and j are defined according to the strain coordinate direction. By taking both of the symmetrical behavior of the strain matrix $\varepsilon_{ij} = \varepsilon_{ji}$ and also the following definition of the

volumetric difference by strain $\varepsilon_v = \frac{\Delta v}{v} = \varepsilon_1 + \varepsilon_2 + \varepsilon_3 = 3\varepsilon_m$ into consideration, the following matrix is obtained

$$\begin{bmatrix} \varepsilon_{11} & \varepsilon_{12} & \varepsilon_{13} \\ \varepsilon_{21} & \varepsilon_{22} & \varepsilon_{23} \\ \varepsilon_{31} & \varepsilon_{32} & \varepsilon_{33} \end{bmatrix} = \begin{bmatrix} \varepsilon_m & 0 & 0 \\ 0 & \varepsilon_m & 0 \\ 0 & 0 & \varepsilon_m \end{bmatrix} + \begin{bmatrix} \varepsilon_{11-}\varepsilon_m & \varepsilon_{12} & \varepsilon_{13} \\ \varepsilon_{21} & \varepsilon_{22-}\varepsilon_m & \varepsilon_{23} \\ \varepsilon_{31} & \varepsilon_{32} & \varepsilon_{33-}\varepsilon_m \end{bmatrix}$$

$$= \qquad [3.3]$$

$$\begin{bmatrix} \varepsilon_m & 0 & 0 \\ 0 & \varepsilon_m & 0 \\ 0 & 0 & \varepsilon_m \end{bmatrix} + \begin{bmatrix} e_{11} & e_{12} & e_{13} \\ e_{21} & e_{22} & e_{23} \\ e_{31} & e_{32} & e_{33} \end{bmatrix}$$

This is simplified as follow in Equation [3.4]

$$\varepsilon_{ij} = \varepsilon_m \delta_{ij} + e_{ij} \qquad [3.4]$$

Where:

ε_m The volumetric strain
δ_{ij} The unit tensor
e_{ij} The deviator matrix which describes the strain by a constant volume (shear strain)

The stress tensor is to be defined similar to the previous description of the strain tensor, considering the major axis in the 3D space where there are only major normal stresses. According to Cauchy tensor, the following Equation is defined $(\sigma_{ij} - \sigma\delta_{ij})n_j = 0$. The solution of the previous Equation in the major stresses is the normal stresses $\sigma_3 < \sigma_2 < \sigma_1$.

Where the isotropic stress $\sigma_m = \frac{\sigma_1+\sigma_2+\sigma_3}{3}$. After some mathematical simplifying the following formulations in Equation [3.5] in general case are obtained

$$\begin{bmatrix} \sigma_{11} & \sigma_{12} & \sigma_{13} \\ \sigma_{21} & \sigma_{22} & \sigma_{23} \\ \sigma_{31} & \sigma_{32} & \sigma_{33} \end{bmatrix} = \begin{bmatrix} \sigma_m & 0 & 0 \\ 0 & \sigma_m & 0 \\ 0 & 0 & \sigma_m \end{bmatrix} + \begin{bmatrix} \sigma_{11-}\sigma_m & \sigma_{12} & \sigma_{13} \\ \sigma_{21} & \sigma_{22-}\sigma_m & \sigma_{23} \\ \sigma_{31} & \sigma_{32} & \sigma_{33-}\sigma_m \end{bmatrix}$$

$$= \qquad [3.5]$$

$$\begin{bmatrix} \sigma_m & 0 & 0 \\ 0 & \sigma_m & 0 \\ 0 & 0 & \sigma_m \end{bmatrix} + \begin{bmatrix} s_{11} & s_{12} & s_{13} \\ s_{21} & s_{22} & s_{23} \\ s_{31} & se_{32} & s_{33} \end{bmatrix}$$

The first part describes the hydrostatic behavior of the hydrostatic stresses σ_m. The second part describes the difference in stresses in the different directions which is called deviator stress tensor s_{ij}.

The mechanical behavior of the soil is to be described by a constitutive law that defines the strain-stress relation using the previous mathematical equations. The constitutive law Equations are obtained according to an experimental work and then to be described mathematical and numerically in a FEM program, such as in this thesis the use of the hypoplasticity constitutive law in the FEM ABAQUS software.

The use of the finite element method for the calculation of earth pressure in failure condition implies difficulties because of the big deformations that occur. Some of the difficulties are based in the right selection of the model parameters, the constitutive laws and boundary conditions, which adequately represent the physical behavior of the model.

3.2 Finite Element Program ABAQUS

The CAE ABAQUS FEM program is often applied to solve geotechnical problems. ABAQUS CAE enables a wide range of geotechnical simulations. For soil-structure-interaction problems, the soil is often modeled as a single, two or three phase material depending on its constituent's volume fractions. 3D models of geotechnical structures embedded in soil are commonly characterized by ratio of mesh element's length to smallest structure dimensions. This makes the three-dimensional models rather complex. ABAQUS offers a wide range of soil mechanics simulation possibilities and can be extended using several user subroutines. Some of the possibilities offered by the FEM-program ABAQUS are:

- Simulations of advanced models with the inclusion of several finite elements, deformations, pore-water pressure, temperature, degrees of freedom, the soil body for one-, two- and three-dimensional stress-deformation, seepage, heat transfer and diffusion problems.
- Use of constitutive models for soils such as, Mohr Coulomb plasticity, Drucker Prager plasticity models or hypoplasticity in the form of a subroutine
- Definition of the initial values for effective stresses, void ratio, pore pressure or the degree of saturation, which can be done within element and node groups

3.2.1 Constitutive material law "Hypoplasticity" implemented in ABAQUS

A constitutive law for the soil (Hypoplasticity) is executed in ABAQUS with the help of a user subroutine (umat.f). This ABAQUS subroutine capability displays results using the following parameters out of the ABAQUS input file: user defined boundary conditions, initial conditions and non-uniform boundary conditions for all degrees of freedom. They can depend on time, coordinates and element number. Non-linear distributed initial values of state

variables can be defined for effective stresses with void ratio and for pore water pressure, as required. Furthermore, the use of the subroutine in ABAQUS offers the following possibilities:

- It can be used to define the mechanical constitutive behavior of a material;
- It will be called at all material calculation points of elements for which the material definition includes a user-defined material behavior;
- It can be used with any procedure that includes mechanical behavior;
- It can use solution-dependent state variables;
- It updates the stresses and solution-dependent state variables to their values at the end of the increment for which it is called;
- It provides the material Jacobian matrix $\Delta\sigma/\Delta\varepsilon$ for the mechanical constitutive model;
- It can be used in conjunction with other user subroutine to redefine any field variables.

More details for the Hypoplasticity constitutive law will be later explained in chapter 4.

3.2.2 Simulation of the contact surface in ABAQUS

This option is used to create a definition of the surface interaction. It defines contact surface simulations between two different elements such as soil and wall by tie constraints. The surface interaction behavior is governed by its input properties. The contact surface is an important tool in the special earth pressure problem as it describes the relative behavior between the soil and the wall during the analysis. The soil–wall interaction is a major factor in almost all geotechnical structural problems. This is because all stresses and strains are dependent upon the nature of this interaction. The contact surface tool has the ability to simulate the stresses, shear stresses and relative displacements between the wall and the soil. It is also able to describe the transfer of the resulting stresses thereby generally describing the real soil behavior.

A certain kind of contact element is used (interface element) to define the soil-wall interaction behavior.

ABAQUS also offers the ability to simulate the contact between a rigid surface and a deformable body. The rigid structures can be either two- or three-dimensional or they can undergo either small or finite sliding. For the both methods, the contact pair or contact element, the program ABAQUS offers the use of two contact discretization options: “node-to-surface” and “surface-to-surface:

- Node-to-surface contact discretization: By node-to-surface the contact conditions are made such that every single node of the contact interface slave surface side effectively interacts with a point of projection on the contact interface master surface on the opposite side. This means, that by every contact condition a single slave node involves with a group of nearby master nodes from which values are interpolated to the projection. The nodes of the master surface can penetrate into the slave surface, but the slave nodes are constrained not to penetrate into the master surface. By node-to-surface, the contact direction is based on the normal of the master surface.

- Surface-to-surface contact discretization: By Surface-to-surface contact the slave and master surfaces are in the region of contact constraints. The contact direction is based on an average normal of the slave surface in the region surrounding a slave node. The contact regions by surface-to-surface contact are approximately centered on slave nodes, so each contact constraint will predominantly consider one slave node but will also consider adjacent slave nodes. Some penetration may be observed at individual nodes; however, large, undetected penetrations of master nodes into the slave surface do not occur by surface to surface contact.

Program ABAQUS also offers the use of small or finite sliding to describe the behavior of the contact interaction between the two bodies. Both small and finite sliding can be either two- or three-dimensional or only small relative displacements between nodes are allowed.

In the simulation, Coulomb's friction model was used for the frictional behavior. The basic concept of the Coulomb friction model is to relate the maximum allowable frictional (shear) stress across an interface to the contact pressure between the contacting bodies. In its basic form, two contacting surfaces can carry shear stresses up to a certain magnitude across their interface before they start sliding relative to one another. The Coulomb friction model defines this critical shear stress T_{crit} at which sliding of the surfaces starts as a fraction of the contact pressure p between the surfaces ($T_{crit}=\mu p$). The friction factor μ is known as the coefficient of friction. Key factor to be determined when creating a contact formulation is the assignment of "master" and "slave" roles to the respective surfaces.

The program ABAQUS uses the concept of slave master interaction surface to define the contact area between different bodies. The rigid area is defined as the master surface while the deformable surface is defined as slave surface. The ABAQUS master-slave algorithm permits the master surface nodes to penetrate the slave surface without resistance. If the refinement technique does not work or is not practical, a symmetric master-slave method can be used. However, the condition that both surfaces are element-based surfaces with deformable or deformable-made-rigid parent elements has to be fulfilled. The symmetric master-slave method defines two contact pairs using the same surfaces. The master and slave surfaces are defined for the initial contact surface. This results in additional computation because contact searches must be conducted twice for the same contact pair. The contact pair method is used in the thesis simulations because of the high accuracy it provides.

4 Numerical Modeling

4.1 Introduction

Different simplified assumptions are made for numerical modeling. It is very important to ensure that the constitutive law is a good approximation of the physical behavior in reality. Conditions for the application of suitable constitutive laws in the model have to be provided to allow a certain degree of accuracy. These considerations are taken into account using the continuum mechanics laws. For example the dimensions of the model are very big compared with dimensions of the element and the soil is a homogenous single phase system. The stress-strain behavior is considered as a pure mechanical process. Only a static load was considered during the analysis by avoiding a quick load or displacement during short time. This implies that no dynamic effect is taken into consideration.

4.2 The Constitutive Model

The modeling of the soil material behavior using the suitable constitutive law according to the studied case is of crucial importance for the quality and accuracy of the computation results. The hypoplasticity constitutive model was used in this thesis to study the earth pressure in relation to the stress levels. The computations were executed for each movement mode (parallel, rotation around top or bottom) using the hypoplastic material law developed for sandy soil. It describes the stress-strain behavior including the nonlinearity and inelasticity without using the prevailing concepts in other constitutive laws. It describes the soil behavior by loading and unloading in a unique equation which expresses the stress increment as a function of a given strain increment, the actual stress and void ratio without a priori distinguishing between elastic and plastic deformations. A furthermore feature of Hypoplasticity is the description of the soil behavior with special emphasis on barotropy and pycnotropy. Barotropy means the influence of the stress level on the friction angle φ and on the stress-strain tangential stiffness while pycnotropy is defined as the effect of soil density including the behaviour of the dilatancy and contractancy. Hypoplasticity expresses the stress increment as a function of a given strain increment due to the current void ratio. The hypoplasticity equation includes many parameters through which the stress conditions into the soil are to be calculated considering the fact of the fading influence of the initial state with increasing length of the history. The constitutive Equation has eight constants, which are stress independent, at least in a particular pressure range, thus enabling the application of the hypoplastic Equation in boundary value problems with pressure and density variation. The parameters are measured in a simple way from standard tests in soil mechanics and are illustrated as follows:

The angle φ_c is a fundamental soil parameter representing the friction angle in the critical state. It is not influenced by the level of normal effective stress or drainage conditions and can be obtained in a simple estimation from the angle of repose for a dry non-cohesive granular material. This angle of repose is defined for a sand as the maximum angle of sand at which

the sand can rest on an inclined plane under its self weight without sliding down. The granulate hardness h_s is a constant used as a reference pressure and it is influenced with the size and form of grains as well as the grain size distribution. The exponent n allows a non-proportional increase of the incremental stiffness with increasing mean granulate pressure p_s. Both constants h_s and n can be obtained from the oedometric compression test. The constants e_{d0} ,e_{c0} and e_{i0} are the minimum, the critical and the maximum void ratio at zero pressure, respectively. The minimum void ratio at zero pressure e_{d0} is approximately determined from the related index test. It can be taken equal to e_{min}. The critical void ratio at zero pressure e_{c0} is approximated with the maximum void ratio e_{max} obtained from the index test. The maximum void ratio at zero pressure e_{i0} can be estimated from e_{max}. The maximum void ratio at zero pressure e_{i0} can be also estimated from e_{max}. In theory e_{i0} can be reached during an isotropic consolidation of a grain suspension in a gravity free space. $e_{d0} \approx e_{min}$, $e_{c0} \approx e_{max}$ and for sand it is supposed that $e_{i0} \approx 1.2e_{max}$. Those (the void ratios) e_{min} and e_{max} are pressure-dependent.

The exponent α controls the influence of density on the peak shear strength (peak friction angle) and is obtained from triaxial tests. The exponent ß takes into consideration the influence of density on the compressibility. It considers the stiffness increases consecutive to a soil densification and can be determined by two different compression tests at different densities (loose to dense).

Hypoplasticity was first developed at university of Karlsruhe. The numerical modeling was done using Karlsruhe sandy soil, which consists mainly of sub round quartz grains. The hypoplasticity Equation for sands is rate independent and it is also allowed for the application of large strain problems. The sand index properties determined from the experiments are given in Table 4-1.

Table 4-1: Index properties of Karlsruhe medium sand [37] [38]

Unit weight of the grains, kN/m3	26.5
D_{10}, mm	0.240
D_{60}, mm	0.443
Uniformity coefficient, Cu	1.85
Min. void ratio, e_{min}	0.53
Max. void ratio, e_{max}	0.84

The behavior of Karlsruhe sand in triaxial tests and other laboratory experiment was also investigated by Kolymbas & Wu [46]. Figure 4-1 shows the result of triaxial tests for dense sand samples ($e_0 = 0.53$) at different confining pressures (σ_3).

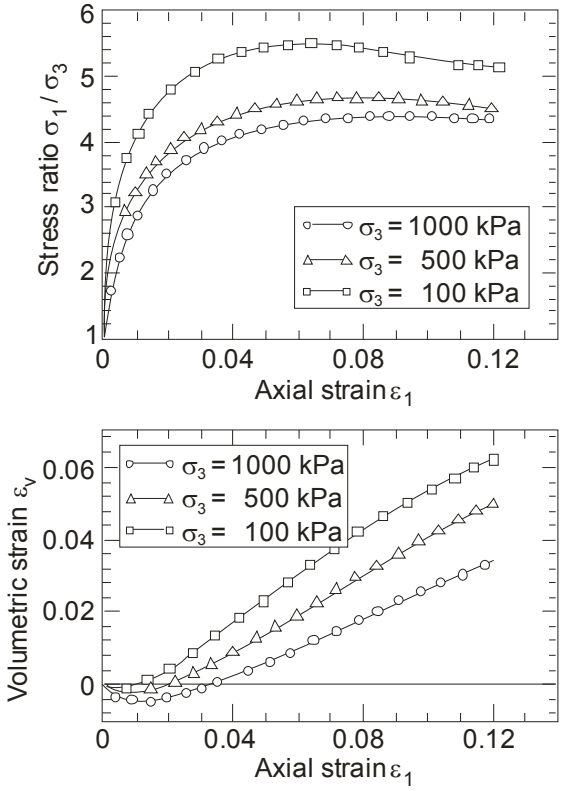

Figure 4-1: Experimental triaxial test results for dense Karlsruhe sand [46]

They also determined the eight material parameters required for the hypoplasticity constitutive law for this sand as shown in Table 4-2.

Table 4-2: Input Parameters for Hypoplastic material law, Karlsruhe Sand [37] [38]

ϕ_c	grain stiffness (h_s)	e_{d0}	e_{c0}	n	e_{i0}	α	β
30.0°	5800.0 MN/m^2	0.53	0.84	0.25	1.00	0.13	1.05

In the frame of the hypoplasticity constitutive law, many versions for the hypoplastic Equation were developed by Kolymbas, Wu and Bauer [46] The constitutive parameters however do not have a recognizable relation to the granulometric properties. The determination of these parameters should as far as possible be performed on the basis of granulometric soil properties and can therefore hardly be interpreted physically. The hypoplasticity equation was also extended later with a scalar factor considering the pycnotropy (influence of density on the constitutive law). Moreover, considering the critical void ratio e_{crit} depends on the stress level and barotropy.

The numerical modeling in this thesis is based on the version developed by von Wolffersdorf [98] [99] in the following tensorial Equation [4.1]

$$T_j = f_b f_e \frac{1}{t_r(\dot{T}\dot{T})}\left[F^2 D + a^2 \dot{T} t_r(\dot{T} D) + f_d a F(\dot{T} + \dot{T}^*)\|D\|\right] \quad [4.1]$$

Where:

T_j Jaumman tensor rate

D The symmetrical stretching tensor

T Cauchy stress tensor rate

$\dot{T}$ an abbreviation defined as follows $\dot{T} = \frac{T}{\mathrm{tr}\, T}$

$\dot{T}^*$ is the normalized Cauchy stress tensor rate using the trace of tensor T that $\dot{T}^* = \dot{T} - \frac{1}{3}I$

The dimensionless functions f_e and f_d describe the influence of pycnotropy (density dependency) and the transition to the critical state. The peak friction angle and the dilatant behavior is included in function f_d. The function f_d is defined as follows in Equation [4.2]

$$f_d = \left(\frac{e - e_c}{e_c - e_d}\right)^{\alpha} \text{ with } 0.1 < \alpha < 0.3 \quad [4.2]$$

Where:

α constant parameter that describes the effect of the soil density on the frictional angle at peak as shown before.

The function f_e includes the effect of the void ratio on the incremental stiffness (the stiffness increases when void ratio decreases) as shown in Equation [4.3]

$$f_e = \left(\frac{e_c}{e}\right)^{\beta} \text{ with } 1 < \beta < 1.1 \quad [4.3]$$

f_e in Equation [4.3] allows the stress rate tensor to be equal to zero, the critical state is reached when factor f_d is equal to 1

β constant parameter that describes the effect of the stress level

e_c void ratio at the critical state

The previous void ratios are related to the isotropic pressure p_s which is defined as follows in Equation [4.4]

$$p_s = \frac{-(\sigma_1 + \sigma_2 + \sigma_3)}{3} \quad [4.4]$$

$\sigma_{1,2,3}$: the three major stresses in the stress plane

The relation between the void ratio and the isotropic pressure p_s is defined in consideration of the fact that the ratios e_i and e_d bound the admissible states in the plane e vs. p_s = -trT/3 as

shown in Equation [4.5] below. It describes the critical void ratio $\frac{e_c}{e_{c0}}$ for high and low pressures, with the corresponding critical value for zero pressure e_{c0}.

$$\frac{e_i}{e_{i0}} = \frac{e_c}{e_{c0}} = \frac{e_d}{e_{d0}} = exp\left[-\left(\frac{3p_s}{h_s}\right)^n\right] \quad [4.5]$$

Where:

h_s stiffness of the granular soil particles

n constant parameter related to the soil particles stiffness

e_{d0} void ration at a maximum compaction at p_s=0

e_{i0} void ratio at isotropic compression at p_s=0

e_{c0} void ratio at critic state at p_s=0

e_i void ratio at isotropic compression

e_d void ratio at a maximum compaction using small shear cycles

e_c void ratio at the critical state

The barotropy function f_b (pressure dependency) depends only on the void ratio e_i as shown in Equation [4.6]. It considers the increase of the stiffness consecutive to an increase of the mean stress. f_b is related to the fact that a perfect isotropic compression must provide the same exponential relationship between the void ratio e_i and the mean pressure p=-trT/3.

$$f_b = \frac{h_s}{n}\left(\frac{1+e_i}{e_i}\right)\left(\frac{e_{i0}}{e_{c0}}\right)^{\beta}\left(\frac{3p_s}{h_s}\right)^{1-n}\left[3 + a^2 - a\sqrt{3}\left(\frac{e_{i0} - e_{d0}}{e_{c0} - e_{d0}}\right)^{\alpha}\right]^{-1} \quad [4.6]$$

The normal void ratio e is limited as shown in the following Equation [4.7]:

$$e_d < e < e_i \quad [4.7]$$

The factor a is defined as follows:

$$a = \frac{\sqrt{3}(3-\sin\varphi_c)}{2\sqrt{2}\sin\varphi_c} \quad [4.8]$$

Factor a is determined by the critical friction angle φ_c.

The limiting conditions proposed by Matsouka and Nakai were incorporated by Von Wolffersdorf as the stress conditions for the critical conditions in the hypoplastic law.

The following stress function is contained therein. Factor F in Equation [4.9] is a function of the deviatoric stress ratio tensor $\dot{T}^*$ and it is calculated as shown in the following Equations

$$F = \sqrt{\left(\frac{1}{8}tan^2\psi + \frac{2 - tan^2\psi}{2 + \sqrt{2}tan^2\psi cos3\theta}\right)} - \frac{1}{2\sqrt{2}}tan\psi \qquad [4.9]$$

$$tan\psi = \sqrt{3}\left\|\dot{T}^*\right\|, \cos 3\theta = -\sqrt{6}\frac{tr\dot{T}^{*3}}{(tr\dot{T}^{*2})^{\frac{3}{2}}} \qquad [4.10]$$

Where:

θ, ψ Angles in the deviatoric plane which describe the stress state.

4.3 Estimation of the internal soil friction angle

In the hypoplastic formulation the shear strength is stress-dependent and is not described by an explicit parameter (such as the friction angle) that the soil friction angle φ is not an input parameter in the constitutive hypoplasticity law. Thus, the friction angles given were derived by numerical simulation of a direct shear test under vertical stresses in order to compare the corresponding earth pressure coefficients with its values from the results according to other researchers. A FEM model for direct shear test was simulated and the soil was simulated as a rectangular 2D body with a width of 10 cm and height of 3 cm surrounded with rigid surfaces as shown in Figure 4-2.

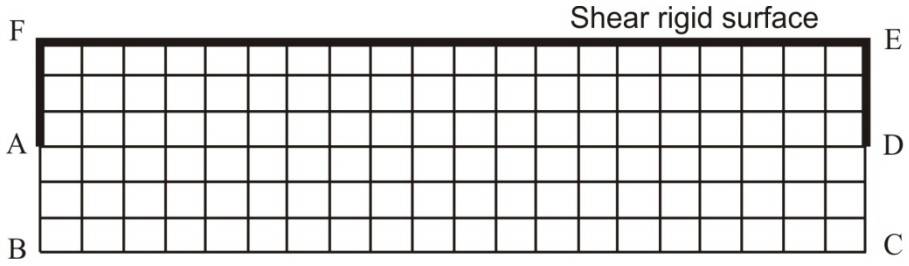

Figure 4-2: Mesh element for the numerical model of the soil direct shear test

The boundaries at AB and CD were simulated as being fixed in the horizontal direction allowing only movements in vertical direction. Boundaries at BC were simulated as being fixed in both the horizontal and vertical directions, while at the boundaries AFED, the movement were prescribed by the movement of the adjacent rigid surface.

The shear test of the rectangular 2D body was simulated by introducing a rigid surface enclosing AFED outer surfaces using the surface to surface contact tool in the program ABAQUS neglecting the soil self weight. The contact surface to surface in ABAQUS offered the possibility of using an option called Equation which was used to define the behavior between the introduced outer rigid surface at the top and the corresponding soil surface (AFED) as a single unit that moves together without any relative displacement between them, thereby generating a shear failure surface at AD as shown in Figure 4-3.

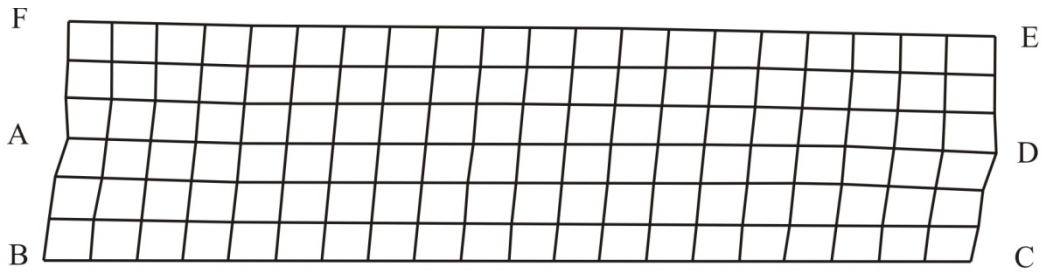

Figure 4-3: Mesh element at the failure step after shearing

The simulation was done by applying a predetermined horizontal displacement and a fixed vertical stress to the introduced upper rigid surface. The vertical load is applied on surface FE in the first step then the part AFED was moved horizontally in the second step. The resulting shear forces R_f during the displacement are shown in Figure 4-4 below. The shear stresses were calculated by the resulting peak shear forces R_f from the actual shearing surface. The relative displacements between the rigid surface and the adjacent soil are equal to zero so no shear strengths will be generated. The actual shear surface is considered automatically in ABAQUS software. Shear stress is calculated as follows in Equation [4.20]:

$$\tau = \frac{R_f}{active\ surface} \qquad [4.20]$$

The test was done for three different vertical stresses 100, 200 and 400 kN/m^2 with three different soil densities $e_0 = 0.55$, $e_0 = 0.65$ and $e_0 = 0.75$. The vertical stress 400 kN/m^2 was chosen to clearly show the behavior of the dense sand under large vertical stresses. The results of the peak shear force R_f as a function of the horizontal displacement U_1 are shown in the following Figure 4-4, 4-5 and 4-6. The friction angles given were derived under vertical stresses of 100, 200 and 400 kN/m^2. These values were used for the conventional calculation of earth pressures with regard to Equation [2.8] in the German Standard DIN 4085 [31].

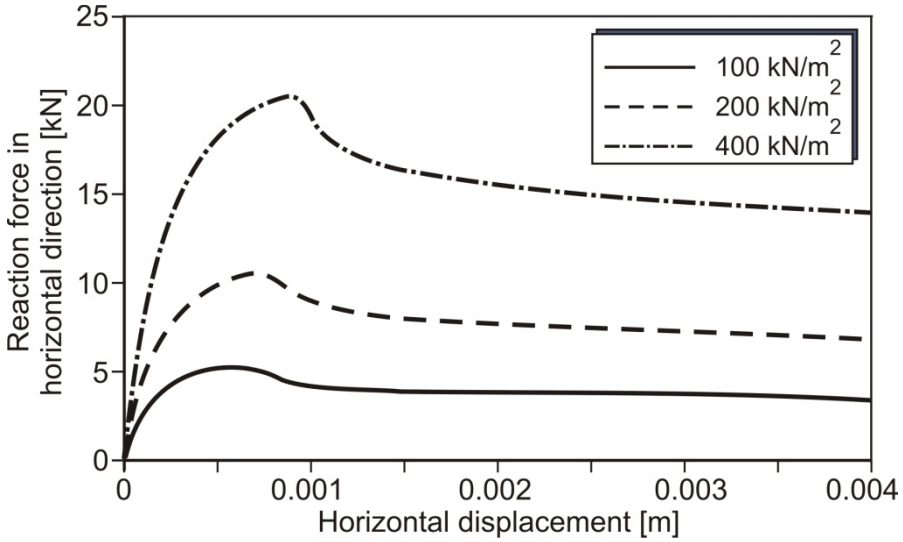

Figure 4-4: Reaction Force in the horizontal direction for dense sand ($e_0 = 0.55$) by different vertical stresses ($\sigma_v = 100$, 200 and 400 kN/m^2)

Figure 4-4 for a dense sand ($e_0 = 0.55$) above, shows an increase in the reaction force in the horizontal direction by increasing the horizontal displacement in the direct shear test until a maximum value which defines the shear resistance of the soil. After this maximum peak, the horizontal reaction force decreases suddenly and after a large displacement it is nearly constant, implying that the soil in the direct shear test has got its residual strength and the test is complete. It is also observed that an increase in the vertical stress leads to an increase in the maximum peak.

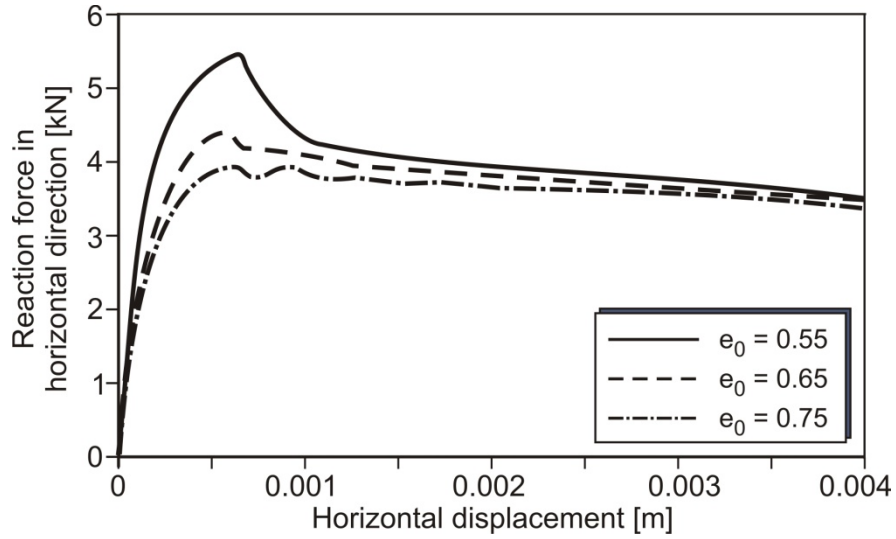

Figure 4-5: Reaction Force in the horizontal direction for vertical stress $\sigma_2 = 100$ kN/m^2

Figure 4-5 above shows the effect of the initial void ratio e_0 (soil relative density) on the shear strength for a constant vertical stress of 100 kN/m². The peak value of horizontal reaction force increases with increasing soil density as was to be expected. The diagrams for other results are presented in the annex.

Mohr Coulomb graphs of shear stress against vertical stress were plotted for the three different soil densities as shown in Figure 4-6.

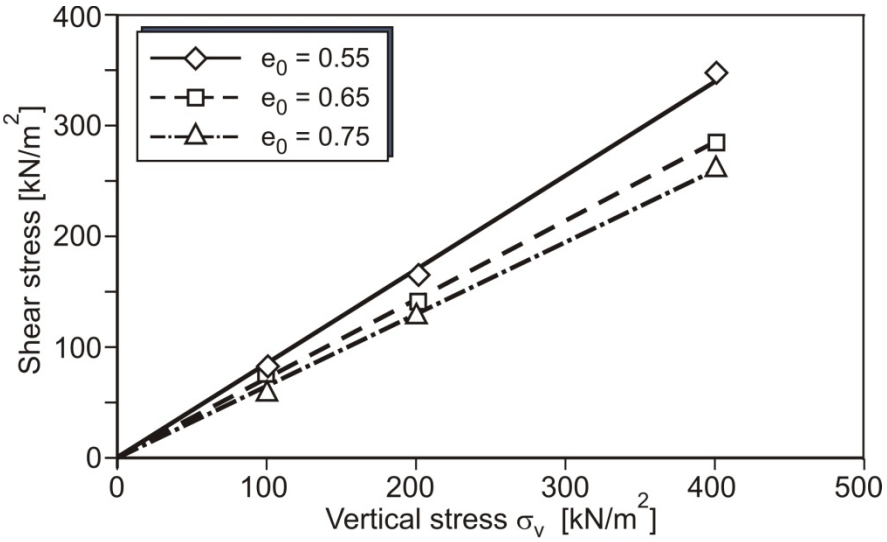

Figure 4-6: Mohr Shear stress envelope for three different initial void ratios (e_0 = 0.55, 0.65, 0.75)

The values of the friction angle φ as a function of the initial void ratio e_0 are illustrated in Table 4-3 below. These values of the friction angle φ presents its initial values for the stresses at 100, 200 and 400 kN/m^2 but it is to be noticed that in the spatial case by using hypoplasticity φ is related to the stress level.

Table 4-3: Soil friction angle φ as function of the soil densities

Initial void ratio (e_0)	Relative Density (D)	Peak friction angle (φ)
0.55	92.0%	40.0°
0.65	57.0%	36.0°
0.75	26.0%	33.0°

4.4 Verification of the initial stress condition

In order to verify the initial stresses of the analyses, which affects the result of the calculation for the passive earth pressure problem, a compression test (Oedometer test) with the purpose of calculating the earth pressure coefficient at rest K_0 was simulated. The K_0-values given were derived by a numerical simulation of the stress state under the own weight of the soil using the hypoplastic material law. By considering, that the FEM simulation is a reflection of the reality in field, a higher accuracy of the result requires a good definition of the initial soil parameters such as initial void ratio and the corresponding initial earth pressure coefficient K_0. K_0 is defined as the ratio between the horizontal earth pressure σ_h to the vertical stress σ_v as shown in Figure 4-7 below.

The stress in the initial vertical and horizontal stress condition is related linearly to each other as follows $\sigma_h = K_0 \cdot \sigma_v$. The oedometer test was simulated as one element with 0.1 m diameter and 0.02 m height.

The first step includes the application of the soil weight, the setting of the initial void ratio and the corresponding soil parameters. In the next step the pressure is increased gradually to a value of 500 kN/m^2.

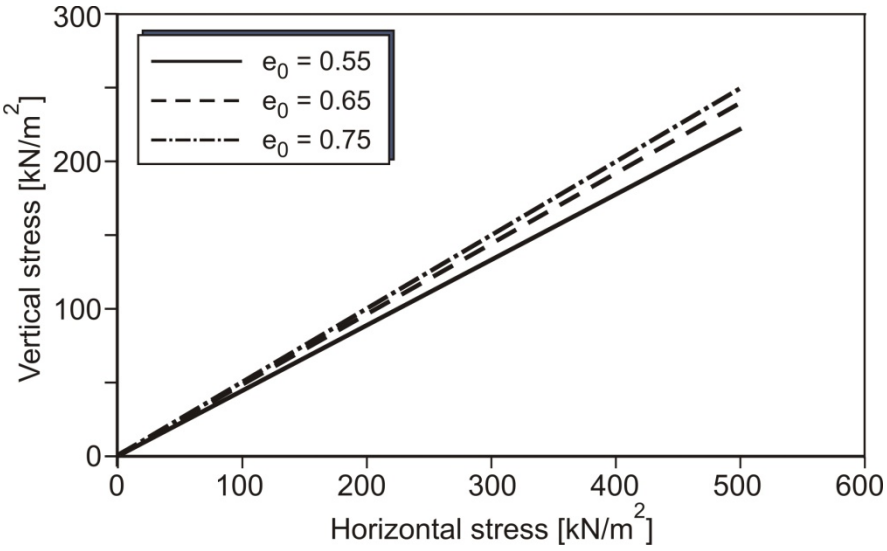

Figure 4-7: The result of the vertical and horizontal stresses due to the FEM oedometer compression test

The values of K_0 in Figure 4-7 are listed in Table 4-4.

Table 4-4: Earth pressure at rest vs. initial void ratio

e_0	0.55	0.65	0.75
K_0	0.46	0.48	0.5

Figure 4-8 shows the distribution of the vertical strain ε_z according to the vertical stresses σ_v by loading and unloading showing the non-linearity of the soil behavior with a good agreement with the general soil behavior in oedometer compression test.

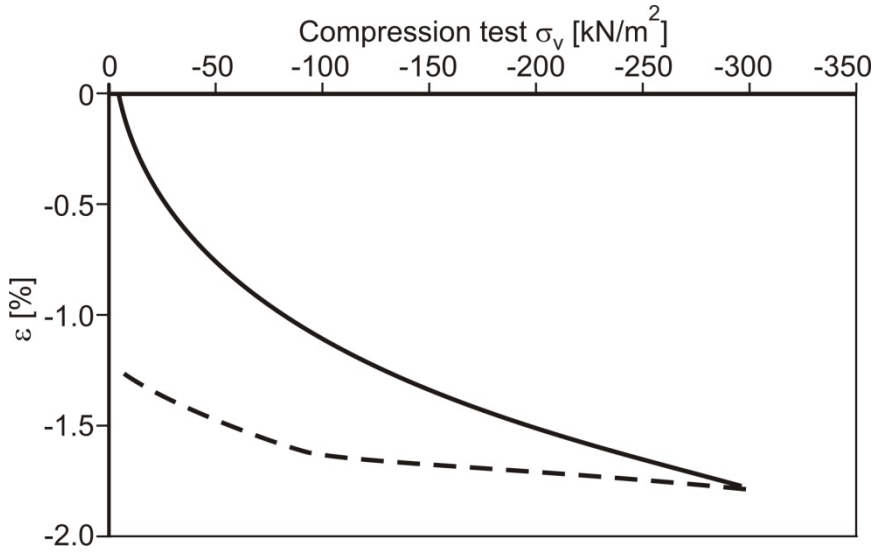

Figure 4-8: Oedometer compression test results for the strain as a function of the vertical stresses σ_v

Table 4-5 shows the initial conditions used in the numerical simulations (including input parameters such as e_0 and the corresponding parameters such as K_0), including average friction angles for peak states φ of the sand, the value of the initial earth pressure coefficient K_0 according to oedometric compression test.

Table 4-5: Input parameters for primary stress state

e_o void ratio	n_o porosity	D relative density	φ (°) friction angle	γ (kN/m³) unit weight	K_o earth press.
0.55	0.355	92.00%	40	17.1	0.46
0.65	0.394	56.80%	36	16.1	0.48
0.75	0.428	26.00%	33	15.1	0.50

4.5 Modeling Procedure

The main aspects of the FEM numerical investigations that were done using ABAQUS are listed below:

- Due to symmetry, only the half of the model was discretized.
- The dimensions of the three-dimensional model area were varied in order to fit different wall dimensions (breadth/height). As an example: a model with a wall of width B = 10.0 m and height H = 10.0 m was set to the following dimensions: length in X direction is L_x = 130.0 m. Length in y direction is L_y = 100.0 m. The total depth H_{total} = 20.0 m. The geometrical model is shown in Figure 4-9. With these model dimensions the behavior of the wall is not influenced by the boundary conditions as shown below in section 4.6.

- The soil was modeled with 8-noded solid elements as shown in Figure 4-10. The interaction behavior in the boundary surface between wall and soil was modeled using interface elements. Relative displacements occur, if the relationship between shearing and normal stresses exceeds a defined limit value μ.
- In the front surface of the model area many different smooth rigid walls (Wall ① to Wall ⓘ) were specified as shown in Figure 4-9. According to the embedded depth that will be investigated, one or more of the walls are moved while the other walls remain unmoved during the modeling process. The earth pressure on the movable wall was calculated by integrating the horizontal soil stresses behind the wall. The wall movement modes, parallel movement, rotation around the toe of the wall and rotation around the top of the wall were examined.
- Geometrical non-linearity was also implemented which considers the changes in geometry during the analysis and this is significant in a large deformation analysis as in passive earth pressure problem.
- The simulation was made for three different initial void ratios (e_0 = 0.55, 0.65, 0.75), which means three different relative densities.

The modeling process is executed in two steps. In the first step, the primary stress state using self weight of the soil medium is generated for different initial void ratios and the corresponding parameters for this stage such as the friction angle and the earth pressure at rest K_0. In the second step the rigid walls were moved according to the three previously defined wall movements.

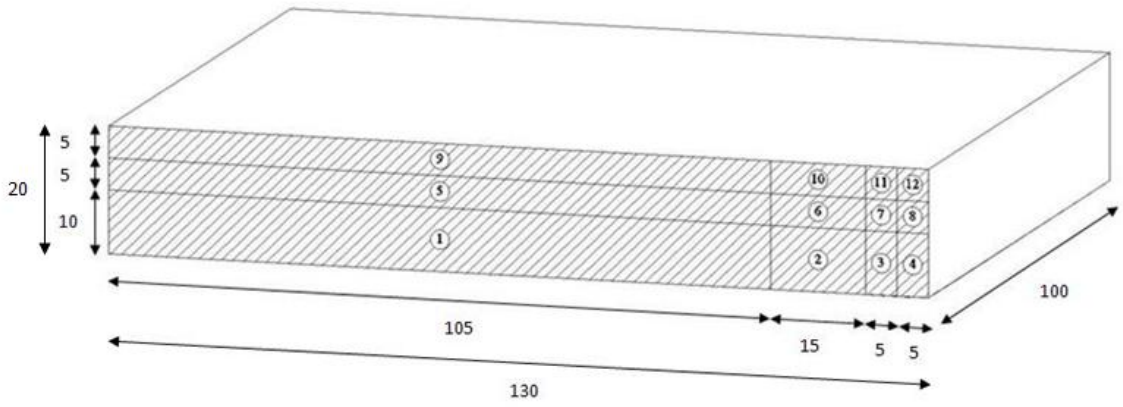

Figure 4-9: Geometrical model for spatial passive earth pressure

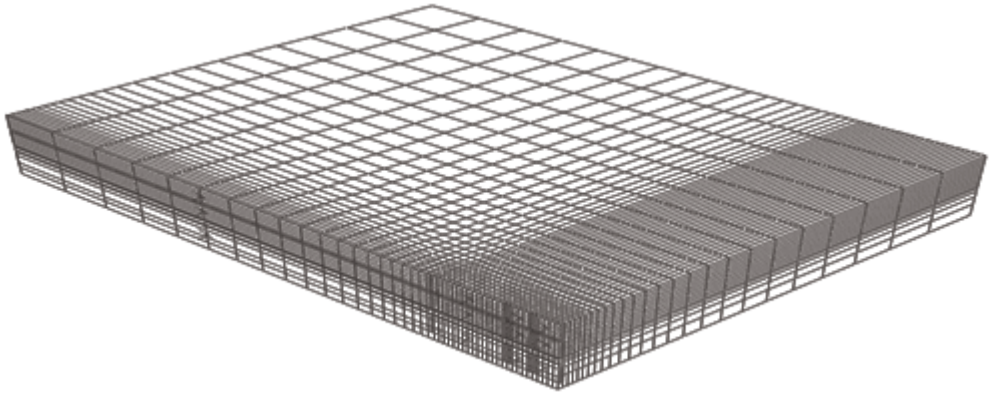

Figure 4-10: Finite element mesh for spatial passive earth pressure

4.6 The effect of the mesh density and the size of the discretized regions

In the following chapter a study of the mesh dimensions was carried out. First of all the effect of the boundary conditions was tested in the verification of the model by studying the effect of the model length L_y and the model depth H_{Total} as shown in Figure 4-11. Three values for the lengths namely L_{y1} = 80 m, L_{y2} = 100 m and L_{y3} = 120 m and two values for the depth with H_{total} = 20 m and Htotal = 25 m were used in order to check the effect of the boundary conditions on the results.

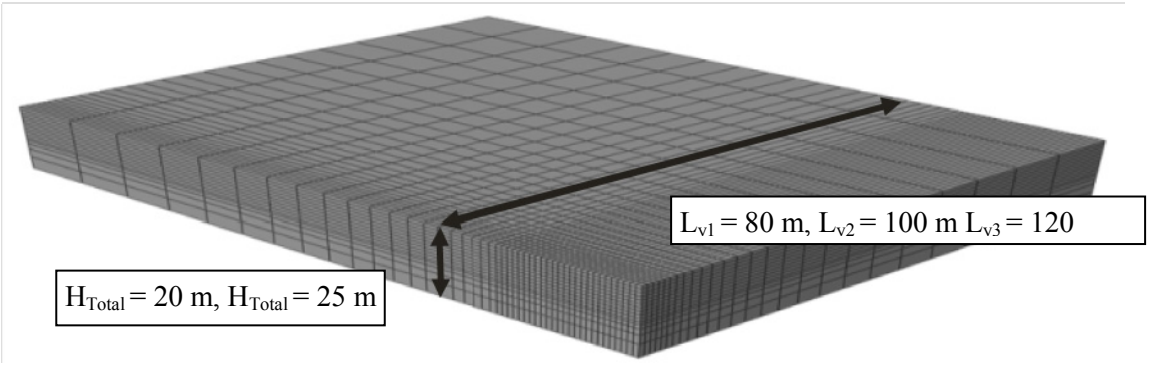

Figure 4-11: The model with the different lengths the heights which are defined in displacement directions

The results are illustrated in Figure 4-12 below. The earth pressure coefficient K_{ph} versus relative displacement U/H shows that no effect of the boundary conditions is noticed. The length L_{y1}=100 m thus was considered in the model as sufficient.

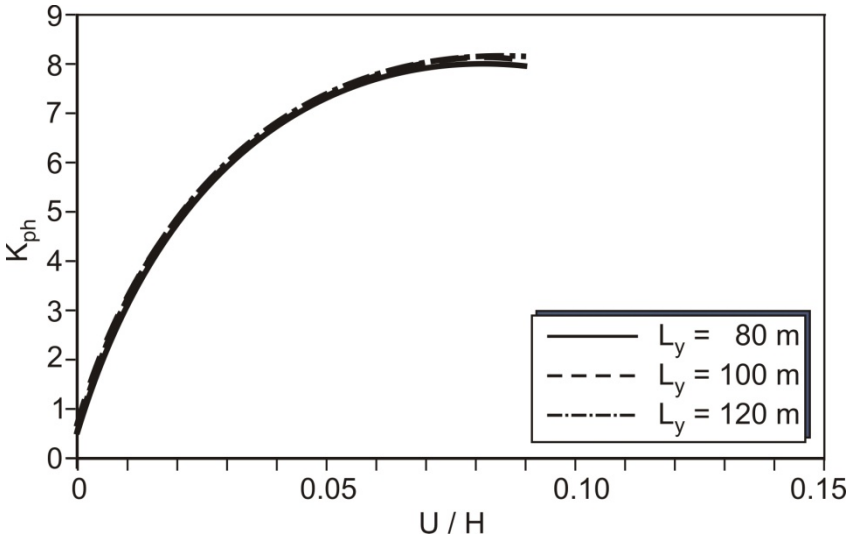

Figure 4-12: Earth pressure coefficient K_{ph} for three different models with mesh lengths by 80 m, 100 m and 120 m

On the other hand the results show that both models with $H_{total} = 20$ m and $H_{total} = 25$ m have the same earth pressure coefficient curves. In both cases by changing the boundary condition, no effect is noticed as long as the displacement spectrums or the elements in motion are far away from the boundary. When a failure body cuts the boundary it will lose a part of its volume which causes a loss of accuracy in the results.

An important step in the finite element analysis is to study the effect of the coarseness and the size of the discretized regions on the accuracy of the results. For this purpose, three different models with different meshes were developed for different values of the soil initial void ratio, namely $e_0 = 0.55$ and 0.65. Figure 4-13 below illustrates the three models with different meshes.

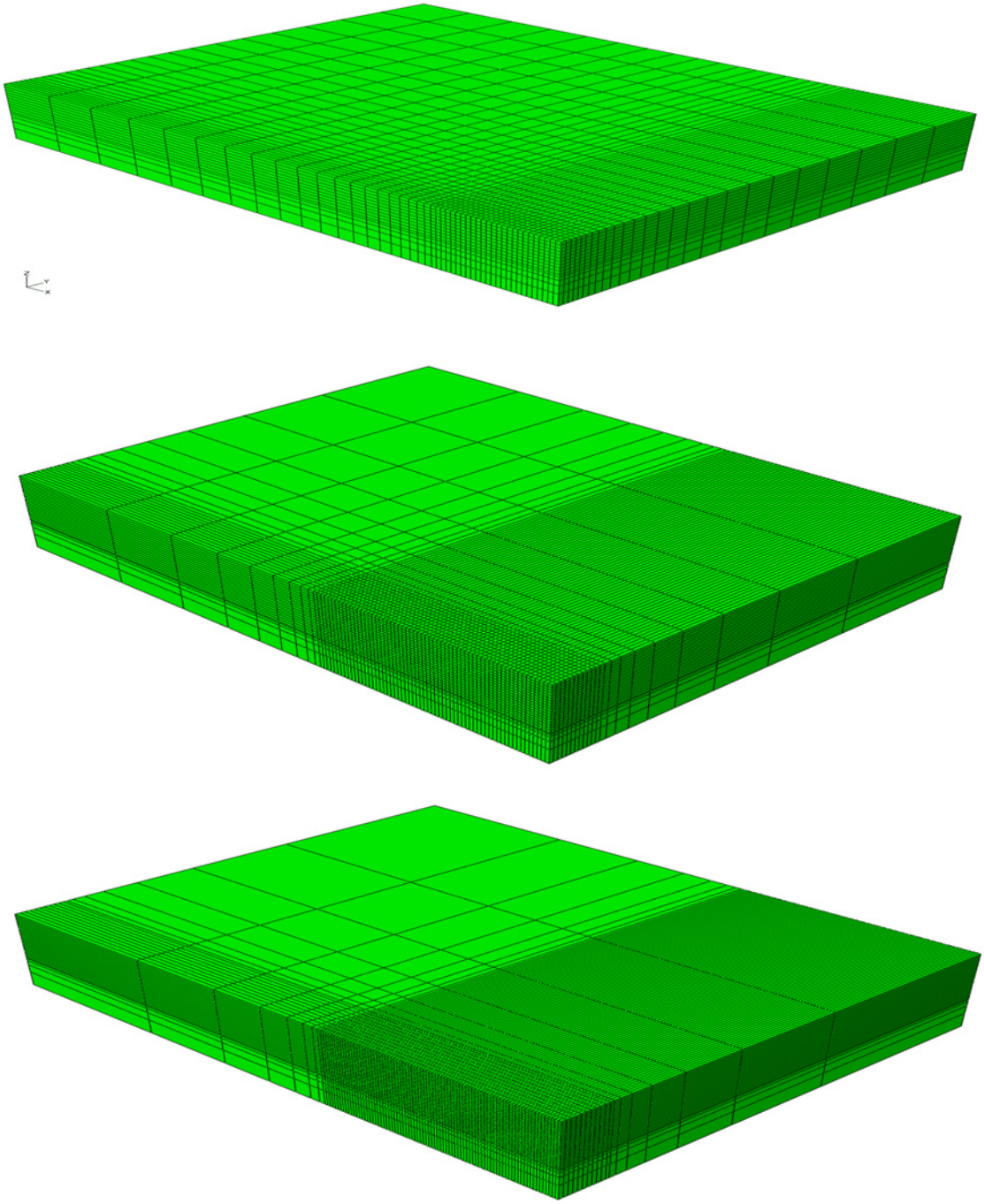

Figure 4-13: Finite element model using the three different meshes. Respectively from the top; medium, fine and very fine mesh.

The first mesh is a medium mesh with 19136 nodes and 57408 degrees of freedom while the second is a fine mesh with 37488 nodes and 112464 degrees of freedom and the third one is finest one with 46860 nodes and 140580 degrees of freedom. Two cases of a wall having a width (B) of 20 m and 10 m and depth (H) of 10 m embedded in dense sand ($e_0 = 0.55$) and medium dense sand ($e_0 = 0.65$) respectively were considered. Figure 4-14 and 4-15 show the passive earth pressure coefficient K_{ph} which will be defined in section 5.1 plotted on the y

axis, as a result of moving the wall towards the soil. The results of the three models for the three different meshes are shown in Table 4-6.

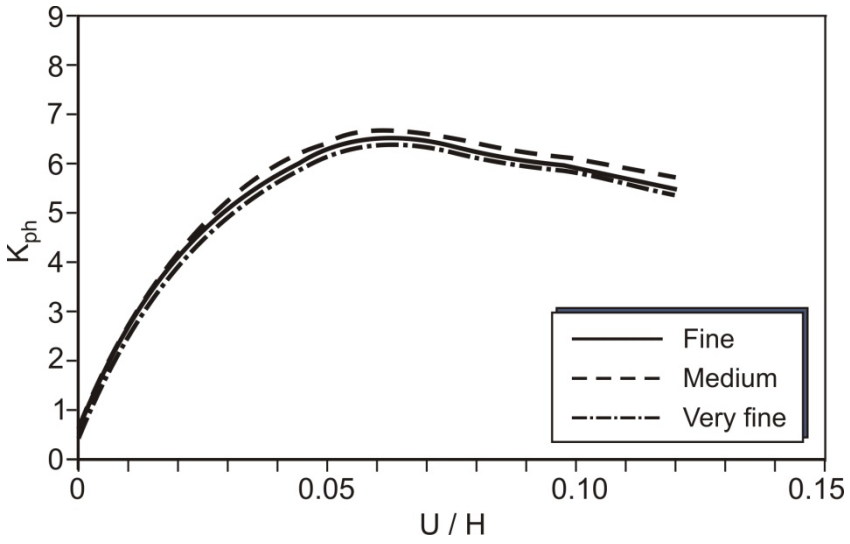

Figure 4-14: Passive earth pressure coefficient of a wall with B = 20 m and H = 10 m for dense sand

It can be observed from the Figure 4-14 and Table 4-6 that for a wall with B = 10.0 m and H = 10.0 m in dense sand, there is almost no difference in the results obtained under the three different meshes used. The same conclusion is also observed for a wall having a width (B) of 20 m and depth (H) of 10 m and the medium dense sand (e_0=0.65) as shown in Figure 4-15 and in Table 4-7 below.

Table 4-6: Passive earth pressure for three different meshes with (B = 20 m, H = 10 m, e_o = 0.55)

Mesh	K_{ph}	U_p (m)	U_p/H
Medium	6.624	0.63	0.063
Fine	6.549	0.608	0.0608
Very fine	6.412	0.607	0.0607

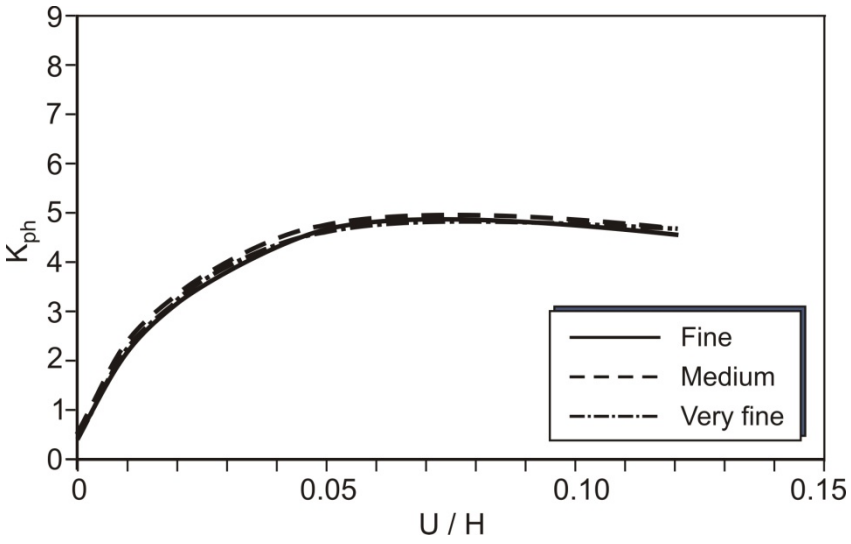

Figure 4-15: Passive earth pressure coefficient for a wall B = 20 m H = 10 m in medium dens sand

Table 4-7: Passive earth pressure for three different meshes (B = 20 m, H = 10 m, e_o = 0.65)

Mesh	K_{ph}	U_p (m)	U_p/H
Medium	4.95	0.75	0.075
Fine	4.91	0.73	0.073
Very fine	4.90	0.70	0.0702

It can be concluded from the above mesh gradation study, that the mesh refinement made by increasing the number of elements, has a negligible influence on the results. Hence, the first mesh one gradation proposed in Figure 4-10 is adopted in the further analyses carried out in this thesis. Many previous analyses were also made to study the effect of the element type on the results. It was concluded, that the biquadratic element (element C3D8 in ABAQUS) is very suitable for the case of spatial passive earth pressure. This is because this element resulted in accurate results with reasonable computation time as compared to the other investigated element types and it also does not affect the distribution of the failure surface inside the soil block.

4.7 Effect of contact algorithm

Furthermore, two soil-wall interface contact conditions were examined under separate analyses, namely, the node to surface contact condition and the surface to surface contact condition. Such analyses were carried out for a wall having a width (B) of 50 m and depth (H) of 10 m and dense sand (e_0 = 0.55). The results of the analyses are shown in Figure 4-16 and Table 4-8. It can be noticed from the Figure 4-16 that both contact conditions produce similar results. The node to surface contact interface is adopted in this thesis.

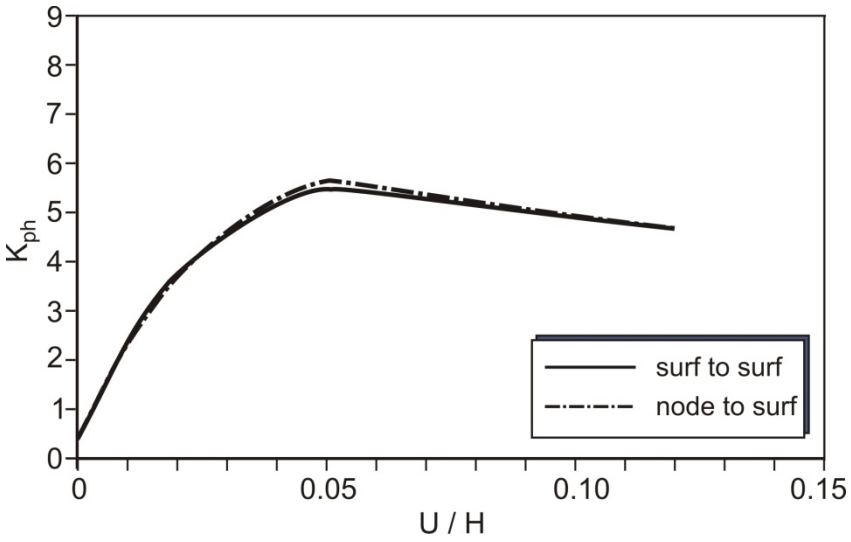

Figure 4-16: Passive earth pressure for two different interface approaches (node to surface and surface to surface, n=5, H = 10 m, e_o = 0.55, parallel movement)

Table 4-8: Passive earth pressure for two models (n = 5, H = 10 m, e_o = 0.55, parallel movement)

Contact	K_{ph}	U_p	U_p/H
Node to surf	5.013	0.47	0.047
Surf to surf	5.061	0.486	0.049

4.8 Model Verification

The reference wall examined with the finite element method (FEM) exhibits a height (*H*) of 10 m and a breadth (*B*) of 10 m (*B/H* = 1) considering a smooth wall δ = 0. Figure 4-17 shows the relationship between the passive earth pressure coefficient (K_{ph}) and the normalized displacement (*U/H*) under parallel movement.

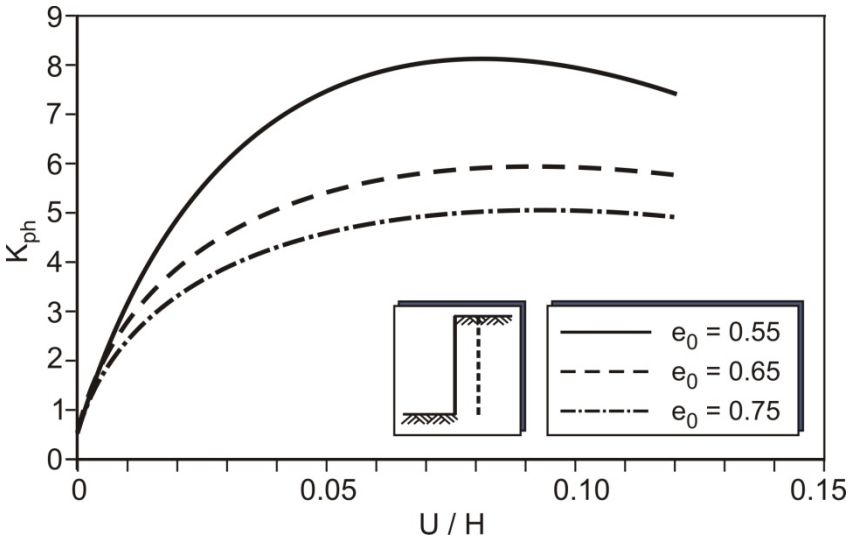

Figure 4-17: Passive earth pressure coefficient as a function of the wall displacement for parallel movement (H = 10 m, n = 1).

The earth pressure coefficient at peak (K_{p3D}^{fem}) ranges from 8.0 for dense sand ($e_0 = 0.55$) to 5.0 for loose sand ($e_0 = 0.75$). The passive earth pressure for plane strain conditions (K_{p2D}^{fem}) was calculated from the model with $B = 260$ m (i.e. $B/H = 26$). The results were compared to the Equations given in the German Standard DIN 4085. According to this standard, the earth pressure coefficient calculated for plane strain conditions should be multiplied by a correction factor (μ_{DIN}) to calculate the spatial passive earth coefficient as shown in Equation [4.21]:

$$\mu_{DIN} = 1 + 0.6 \tan(\varphi) \left(\frac{H}{B}\right) \qquad [4.21]$$

The obtained results are summarized in Table 4-9. Evidently, for the investigated case of parallel movement of a smooth rigid wall the agreement of the numerical results with the DIN 4085 [31] approach is rather good. The coefficients for plane strain conditions obtained from the numerical simulation are slightly higher than the coefficients obtained from German Standard DIN 4085 in Equation [4.21], which of course is a result of the different assumptions regarding the material behavior. However, the μ factors of both methods coincide very well, with deviations of less than 4%.

Table 4-9: Comparison of earth pressure coefficients from numerical simulation and from the German Standard DIN 4085.

initial void ratio	friction angle φ (°)	(K_{p2D}^{DIN})	μ_{DIN}	K_{p2D}^{fem}	K_{p3D}^{fem}	$\mu = K_{p3D}^{fem} / K_{p2D}^{fem}$
0.75	33.0	3.39	1.39	3.55	5.01	1.41
0.65	36.0	3.85	1.44	3.98	5.98	1.50
0.55	40.0	4.60	1.50	5.01	8.085	1.61

5 Numerical modeling results

5.1 Introduction

The results of the numerical passive earth pressure modeling for the three main wall movement modes in the ultimate limit state as well as the serviceability state are presented in this chapter. In general the case of a smooth wall (δ=0) is considered. However, in order to show the effect of wall roughness, exemplary results for a wall with δ>0 are presented in section 5.5.

According to the analysis, the stresses in the model experience two equilibrium conditions namely, the soil stress conditions under its self weight and the soil stress conditions under the effect of the wall movement. The existing stress conditions in the soil before any construction interventions are referred to the initial stress conditions. The equilibrium condition calculations were done using the nonlinear hypoplastic constitutive material law. The results are presented in tables and figures which give the magnitude of the passive earth pressure as a function of the following parameters, spatial ratio n=B/H, initial void ratio e_0 and the wall movement mode. The maximum passive earth pressure E_{ph} or the earth pressure coefficient K_{ph} and the relative displacement at the limiting conditions can be extracted from the force - displacement diagrams derived with ABAQUS.

The following terms, which are used in the presentation of the results, are defined below:

- The resultant horizontal passive earth pressure E_{ph} was calculated and normalized by using Equation [5.1]

$$E_{ph} = \frac{\gamma H^2 B K_{ph}}{2} \qquad [5.1]$$

Where:

B is the wall width in (m)
H the wall embedded height(m)
γ the soil density (kN/m^3)
K_{ph} the horizontal passive earth pressure coefficient which is calculated by rearranging Equation [5.1] as follows in Equation [5.2]:

$$K_{ph} = \frac{2E_{ph}}{\gamma H^2 B} \qquad [5.2]$$

The resultant earth pressure has been calculated by integrating the horizontal stresses at the centers of gravity of the interfacing soil elements on the moved wall.

- The horizontal mobilized displacement U during the movement, which reaches a value U_p at the peak state. The ratio of the wall displacement (during an analysis) to its

embedded height H is termed as the relative displacement U/H, so the relative displacement at peak is U_p/H.

In the cases of rotation of the wall around the top or the toe, the displacement U denotes the maximum displacement occurring at the toe or the top of the wall, respectively.

- The spatial ratio n of the wall width B to wall height H ($n = \frac{B}{H}$). When $n \rightarrow \infty$ (infinite width) the passive earth pressure coefficient is then equal to K_{ph2D}.
- The correction factor μ which is defined in the following equation [5.3]

$$\mu = \frac{K_{ph3D}}{K_{ph2D}} \qquad [5.3]$$

Here μ is used to determine the 3D earth pressure coefficient from any given 2D earth pressure coefficient for the same wall embedded height H.

The main findings and results will be illustrated in the following sections. Additional calculation results will be illustrated in the annex.

5.2 Parallel movement

In this mode of movement the whole wall displaced parallel with the same value towards the soil. As a result of pushing the wall towards the soil, a passive earth pressure is produced. Parallel wall movement was started from the initial stress conditions with an earth pressure coefficient at rest K_0. The maximum K_{ph} at the peak requires a displacement value U_p that depends on the soil type and density. For example, the German Standard DIN 4085 gives a displacement value in the 2D case for dense sand of approximately 3 – 5 % of the wall embedded height.

5.2.1 Passive earth pressure at peak

Figure 5-1 shows the distribution of the passive earth pressure coefficient K_{ph} as a function of the relative displacement (U/H) for three initial soil densities (e_0 = 0.55, 0.65 and 0.75). The spatial ratio of the wall equals to n = 1 with an embedded height of H = 10 m.

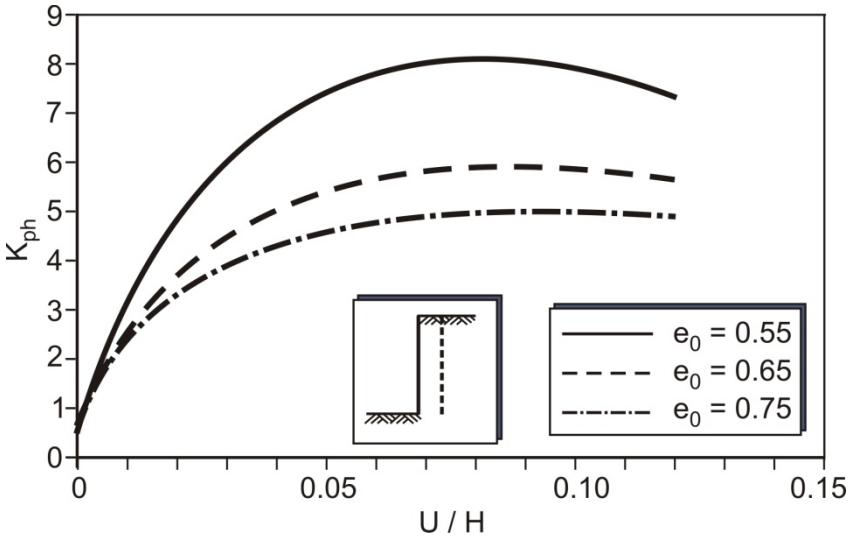

Figure 5-1: Passive earth pressure coefficient as function of the relative displacement (n = 1, B = 10 m, H = 10 m)

The following observations can be obtained from this figure:

- The curve of the earth pressure coefficient with relative displacement shows a non-linear increase till a maximum peak value before decreasing as a result of softening. The peak value of the earth pressure coefficient K_{ph} increases with increasing soil density (e_0 = 0.55, 0.65, 0.75). The peak value appears distinctively in dense sand and indistinctively for medium and loose sand. This enables an accurate relative displacement determination for dense sand. On the other hand, the relative displacements at peak state for medium dense and loose sand cannot be easily determined. The reason is the clear behavior of dilatancy and softening of dense sand.

Figure 5-2 shows the passive earth pressure coefficient K_{ph} as a function of the relative displacement (U/H) by varying the spatial ratio n. When the spatial ratio $n \rightarrow \infty$, it means that the passive earth pressure coefficient is equal to (K_{ph2D}).

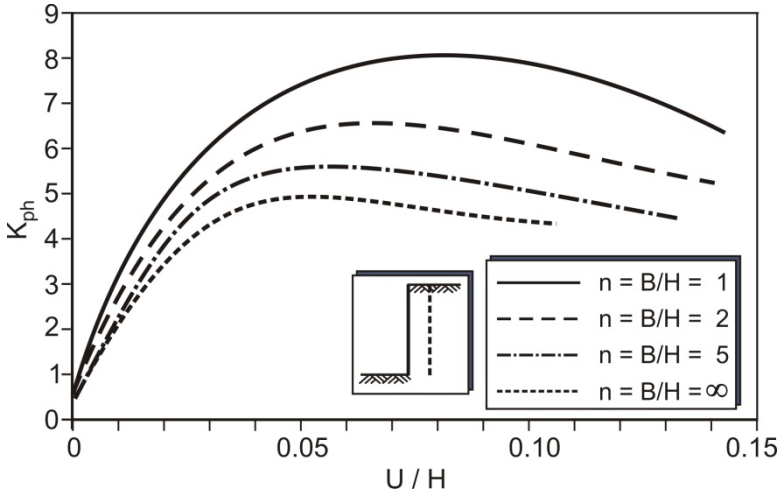

Figure 5-2: Passive earth pressure coefficient as function of the relative displacement U/H (H = 10 m, e_0 = 0.55)

This figure shows that the value of the passive earth pressure coefficient K_{ph} decreases with increasing the spatial ratio n of the wall dimensions. It decreases from $K_{ph} \approx 8$ at n = 1 till $K_{ph} \approx 5$ in the 2D case.

The progression of the correction factor μ for three soil densities (e_0 = 0.55, 0.65 and 0.75), namely dense sand, medium dense and loose sand, respectively as a function of the spatial ratios n are shown in Figure 5-3.

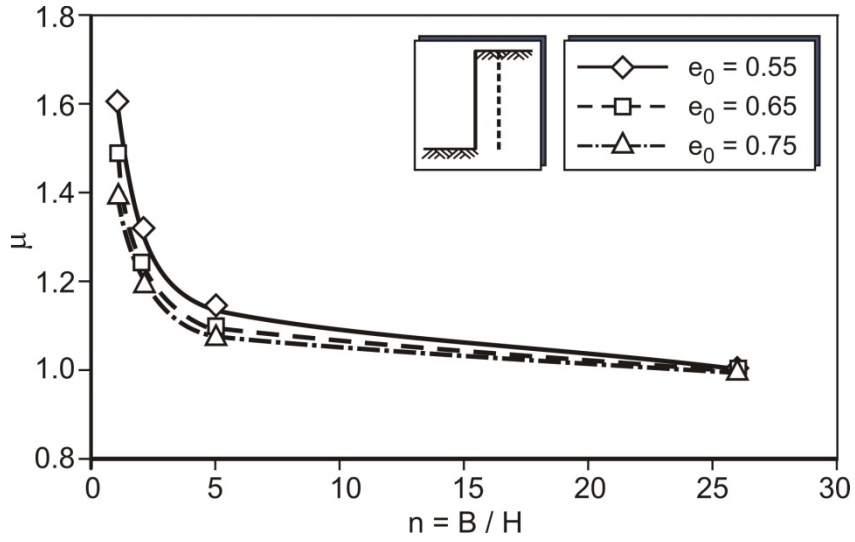

Figure 5-3: Correction factor μ as function of spatial ratio n=B/H (H = 10m)

The following can be concluded:

- The curves progressions show a non-linear decrease of the correction factor μ by increasing spatial ratio n.
- The correction factor curve μ varies with the respective soil density as shown in Figure 5-3. The effect of the soil density on the correction factor μ decreases with

increasing spatial ratio n. For small spatial ratios within the 3D range, a distinctive difference between the curves was observed for the three soil densities. By increasing the spatial ratio n, the difference between the curves of the correction factor μ for the three soil densities decrease progressively until the curves converge at very large spatial ratio n = ∞.

As conclusion for the case of parallel movement, the spatial ratio range for the steep curve gradient increases by decreasing the embedded height. Table 5-1, 5-2 and 5-3 present the numerical results including the correction factor μ and the passive earth pressure coefficient as functions of soil initial density and spatial ratio B/H for three different wall heights.

Table 5-1: Numerical simulation results for parallel movement (H = 5.0 m)

e_0	H(m)	B(m)	n	K_{ph}	μ	U_p(m)	U_p/H
0.55	5	5	1	8.62	1.61	0.43	0.09
		10	2	7.36	1.37	0.40	0.08
		20	4	6.4	1.19	0.34	0.07
		25	5	6.04	1.12	0.32	0.064
		50	10	5.83	1.09	0.30	0.06
		2D	52	5.37	1	0.27	0.05
0.65	5	5	1	6.4	1.53	0.48	0.10
		10	2	5.31	1.27	4.55	0.91
		20	4	4.74	1.13	0.42	0.08
		25	5	4.49	1.07	0.41	0.08
		50	10	4.42	1.05	0.39	0.08
		2D	52	4.19	1	0.36	0.07
0.75	5	5	1	5.35	1.45	0.60	0.12
		10	2	4.54	1.23	0.58	0.12
		20	4	4.11	1.11	0.05	0.01
		25	5	4.02	1.09	0.06	0.01
		50	10	3.86	1.05	0.49	0.10
		2D	52	3.69	1	0.46	0.09

Table 5-2: Numerical simulation results for parallel movement (H = 10.0 m)

e_0	H(m)	B(m)	n	K_{ph}	μ	U_p(m)	U_p/H
0.55	10.00	10.00	1.00	8.085	1.61	0.8	0.08
		20.00	2.00	6.624	1.32	0.63	0.063
		40.00	4.00	5.566	1.11	0.53	0.053
		50.00	5.00	5.707	1.14	0.52	0.05
		2D	26.00	5.013	1.00	0.47	0.05
0.65	10.00	10.00	1.00	5.98	1.50	0.91	0.091
		20.00	2.00	4.957	1.24	0.75	0.075
		40.00	4.00	4.406	1.11	0.59	0.059
		50.00	5.00	4.357	1.09	0.57	0.057
		2D	26.00	3.983	1.00	0.56	0.056
0.75	10.00	10.00	1.00	5.018	1.41	0.97	0.097
		20.00	2.00	4.282	1.21	0.81	0.081
		40.00	4.00	3.855	1.09	0.63	0.063
		50.00	5.00	3.834	1.08	0.61	0.061
		2D	26.00	3.547	1.00	0.61	0.061

Table 5-3: Numerical simulation results for parallel movement (H = 15.0 m)

e_0	H(m)	B(m)	n	K_{ph}	μ	U_p(m)	U_p/H
0.55	15	10	0.67	8.62	1.84	1.14	0.076
		15	1	7.47	1.6	1.08	0.072
		30	2	6.23	1.33	0.93	0.062
		45	3	5.77	1.23	0.855	0.057
		60	4	5.53	1.18	0.825	0.055
		75	5	5.37	1.15	0.81	0.054
		2D	17.33	4.68	1	0.795	0.053
0.65	15	10	0.67	6.24	1.65	1.26	0.084
		15	1	5.55	1.46	1.2	0.08
		30	2	4.75	1.25	1.02	0.068
		45	3	4.45	1.17	0.945	0.063
		60	4	4.3	1.13	0.93	0.062
		75	5	4.21	1.11	0.915	0.061
		2D	17.33	3.79	1	0.8985	0.0599
0.75	15	10	0.67	5.12	1.5	1.365	0.091
		15	1	4.64	1.36	1.32	0.088
		30	2	4.09	1.2	1.14	0.076
		45	3	3.79	1.11	1.05	0.07
		60	4	3.68	1.08	1.035	0.069
		75	5	3.63	1.06	1.02	0.068
		2D	17.33	3.41	1	0.975	0.065

The following remarks can be drawn from the previous tables:

- The correction factor μ is a function of the spatial ratio n as shown before. For a constant height H, the correction factor μ decreases with increasing wall width B, while for a constant width B, the correction factor μ increases with increasing wall height H.
- For a constant spatial ratio, the correction factor μ remains constant with increasing wall dimensions. It is to be noticed that for a constant spatial ratio n, the spatial passive earth pressure coefficient K_{ph3D} decreases with increasing wall dimensions as presented before. This is referred to the scale effect and will be discussed later.

5.2.2 Wall displacement at peak

A failure body is formed by pushing the wall towards the soil as shown in Figure 5-4. The boundaries of this failure body depend on the type of soil, soil relative density, mode of movement and the wall dimensions. The soil reaches its maximum passive earth pressure value at a certain displacement U_p named displacement at the peak or relative displacement at peak $\frac{U_p}{H}$. The boundary of the failure body in the thesis is defined using the maximum width ($B + 2*B_0$) and height ($H + 2*H_0$) of the failure body. Therefore the imaginary width B_0 is defined as the maximum extension of the failure body width parallel to the wall width at the soil surface. Similarly, the imaginary depth H_0 is defined as the maximum extension of the failure body depth parallel to the wall height H as shown in Figure 5-4.

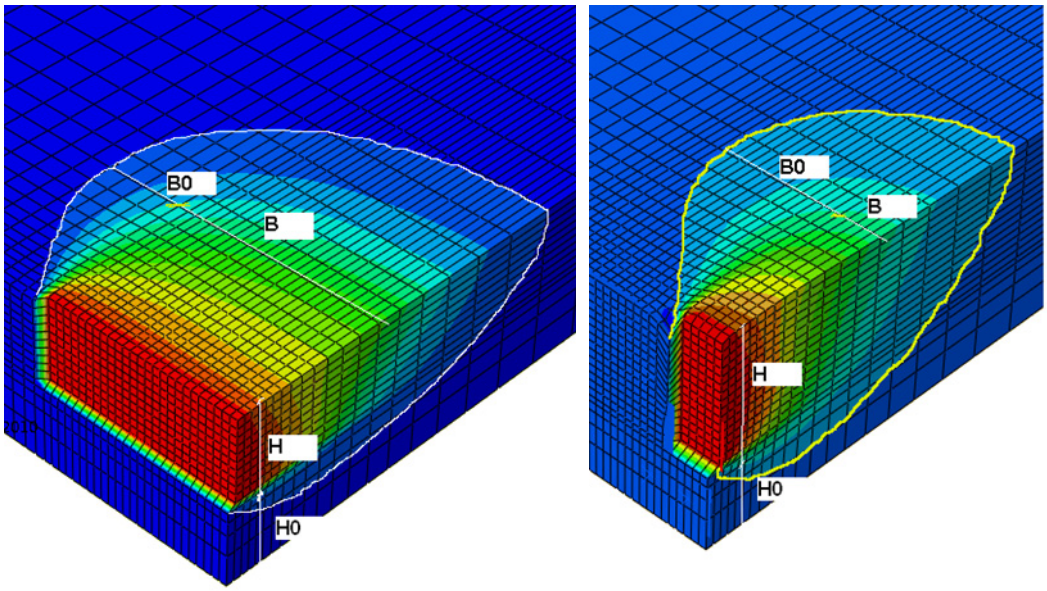

Figure 5-4: Definition of the imaginary width B_0 and height H_0 with respect to the dimensions of the failure body

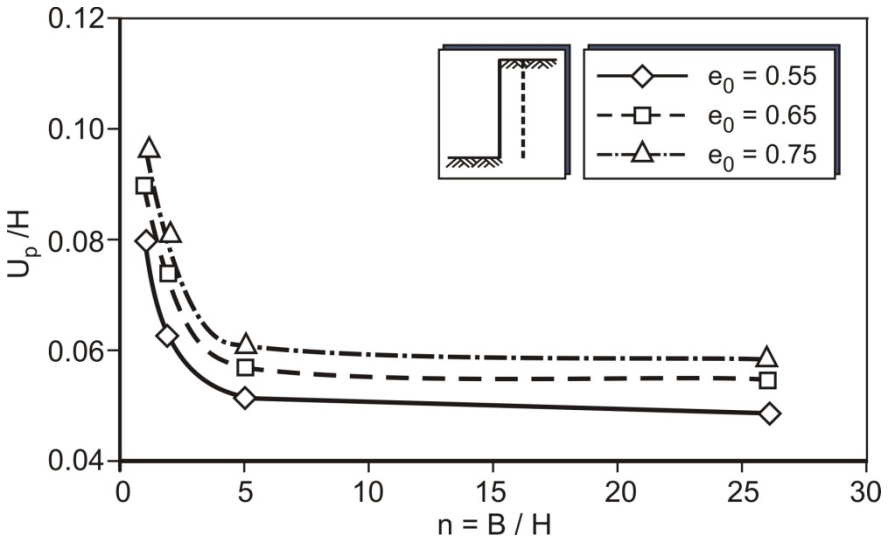

Figure 5-5: Relative displacement of the maximum value at the peak U_p/H as a function of the spatial ratio n = B/H (wall height H = 10 m)

Figure 5-5 illustrates the variation of the relative displacement at peak as a function of the spatial ratio n for a wall with an embedded height of H = 10 m and for different initial densities of soil. The figure shows a non-linear decrease of the relative displacement with increasing the spatial ratio n until it reaches its minimum value by 2D. Specifically, a smaller spatial ratio (thin wall) generates a big relative failure body volume compared with the wall dimensions (Figure 5-4). So that, the wider the wall (higher B/H), the smaller the failure body volume relative to the wall dimensions. The decrease of the wall width B causes the ratio of the imaginary width B_0 to the wall width B ($\frac{2B_0}{B}$) to increase and the failure volume relative to the wall dimensions to increase which leads to a big relative displacement necessary to develop the failure body.

For parallel movement of a wall with a constant spatial ratio (n=constant), the relative displacements at peak for medium dense sand ($e_0 = 0.65$) are smaller than for loose sand ($e_0 = 0.75$) as was expected. The annex gives more results and curves of the relative displacement at peak as a function of the spatial ratio for different soil densities and wall heights.

Table 5-1, 5-2 and 5-3 show the effect of varying the width (B) on the relative displacement at peak for a constant soil density. It is to be noticed that the displacement U_p at the peak increases by decreasing the width (B), which means by decreasing the spatial ratio n.

5.2.3 Passive earth pressure distribution

As a result of the modeling of spatial passive earth pressure, the distribution of the stress with depth z was calculated as shown in the figures below for a wall with a height of H = 10 m. The stress was determined by defining a path of elements along the contact soil surface. The path is defined at the symmetric face of the element adjacent to the moving wall at x = 0.5 m as to be shown later in Figure 5-9. The horizontal stresses e_{ph} were defined by taking the sum

of the whole integral of the horizontal stresses in every single element at its center of gravity. The stress distributions are presented in Figure 5-6 and 5-7.

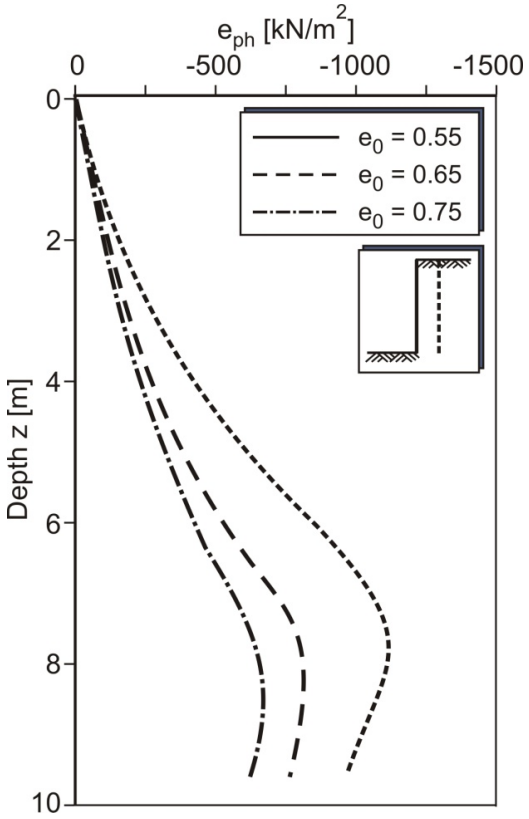

Figure 5-6: Horizontal passive stress distributions at peak state in the symmetric plane (x = 0.5 m) for a wall with H = 10 m and B = 10 m (n = 1)

The distribution of the horizontal stresses by parallel movement show a non-linear increase of the stress till a maximum value is reached approximately at z = 0.8H. After that the stress decreases till a small value is accomplished at the wall toe. These result is fully compliant to the general stress distribution mentioned in the German standard 4085[31].

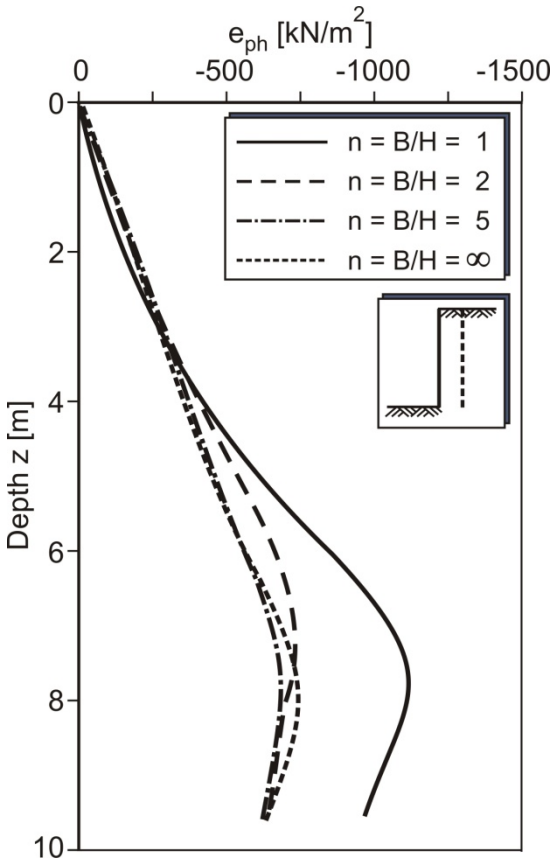

Figure 5-7: Stress distributions at peak state in the symmetric plane (x = 0.5 m) for different spatial ratios n (e_0 = 0.55)

By varying the spatial ratio n of the wall dimensions, it is observed, that the curves are similar for the approximate upper third of the wall as shown in Figure 5-7. This conforms to the Brinch Hansen [17] assumption which is also equal to the distribution of a 2D case. For the last two thirds the curves show that the smaller the spatial ratio n of the wall dimensions is, the greater is the stress value.

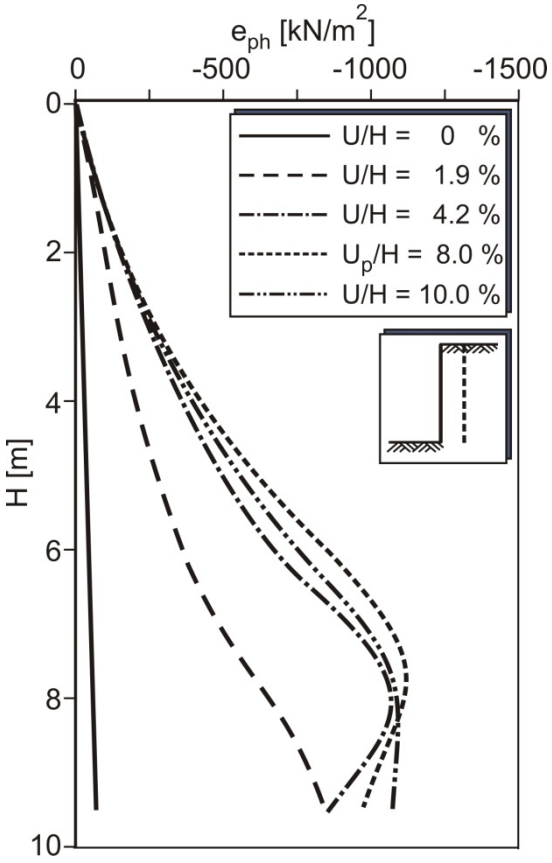

Figure 5-8: Stress distributions in the symmetric plane at different displacements for a wall of spatial ratio n=1 (x = 0.5 m, e_0 = 0.55)

For the case with n = 1 and e_0 = 0.55, horizontal stress distributions at different displacement values were calculated. The curves in Figure 5-8 show that the horizontal stresses increase till a maximum value at the relative displacement at peak U_p/H, subsequently the depth corresponding to the maximum horizontal stress value decreases with increasing relative displacement till the peak is reached.

During the wall movement, the horizontal stresses against the wall and the shear stresses at certain areas in the soil body increase. When the peak is reached, the horizontal stresses are at their maximum value and the shear stresses at the failure surface approach the soil resistance which leads to the generation of the failure body.

Studying the stress conditions at the peak, it was observed that the curves tend to small values of stresses at the wall toe. This is attributed to the arching of the soil particles which causes a redistribution of the internal stress and a stress relaxation at the wall toe. Further displacements beyond the peak displacement ($U > U_p$) reduce the horizontal stresses. This is due to the softening behavior.

In order to get an accurate description of the spatial stresses along the whole wall, many element paths were considered along the width at different positions starting from the symmetric plane at x = 0.5 m to other positions at x = 10, 15, 20 and 25 m on the wall width as shown in Figure 5-9 for a wall of B = 50 m and H = 20 m.

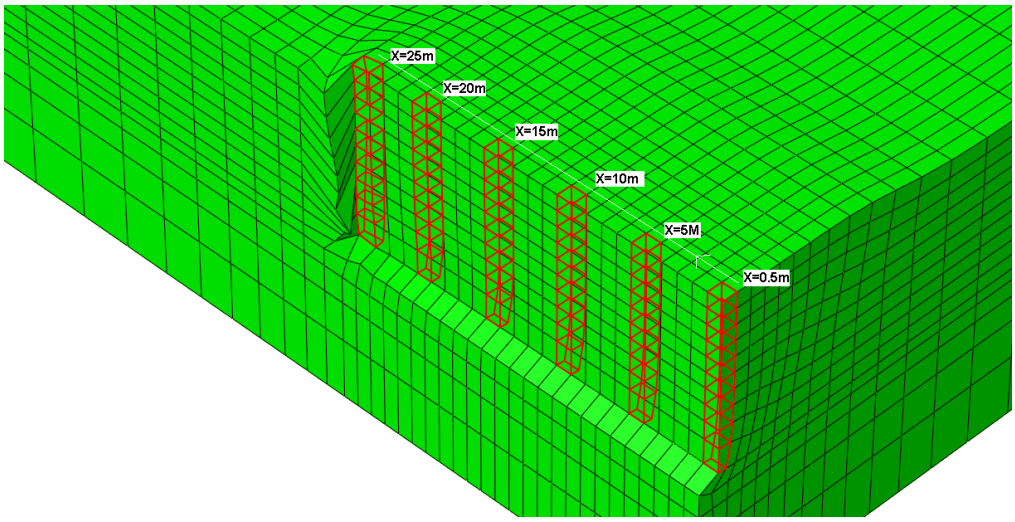

Figure 5-9: Path geometry along the wall with width B = 50 m and height H = 10 m (x denotes the horizontal distance of the path from the plane of symmetry)

The stress distribution is calculated by considering the path of an element along the depth z. Figure 5-10 shows the results of stress distributions for all paths along the width B.

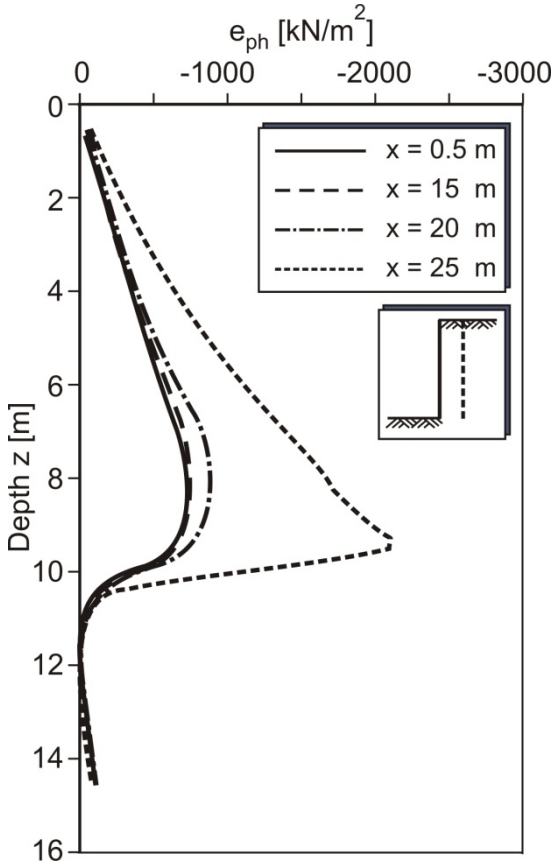

Figure 5-10: Horizontal stress distributions by peak state eph at different distances x of symmetric plane at x = 0.5 (B = 50 m, H = 10 m,e_0 = 0.55)

The distribution curves are similar to those at the symmetric plane as was expected. By going far away from the symmetric plane which is at x = 0.5 m, it is observed that the stress increases. As shown above in Figure 5-10 the stress distributions for the paths at x = 0.5, 10 and 15 m are almost equal. The stress is however slightly higher at x = 20 m and has the maximum value at x = 25 m which is the outer edge of the wall.

The results are attributed to the following reason that by rigid constructions such as plate or walls the stresses concentrate at the edges and decrease at the middle. Also the stress distribution at the wall edge is affected by the spatial shape of the failure body. As shown in section 5.2.2, the failure body will be generated with a total width ($B_{Total} = B + 2B_0$) and this extra volume of the soil affects the stresses at the wall edge.

5.2.4 Failure mechanisms

As a result of the wall displacement against the soil, a failure body forms. It is to be noted that the dimension of this failure body is affected by many parameters such as the soil friction angle φ, the wall soil friction δ and the spatial ratio n. The problem of the failure mechanisms is studied in the following chapter for parallel movement mode by presenting the results in form of vector plots, displacement contours and void ratio distributions.

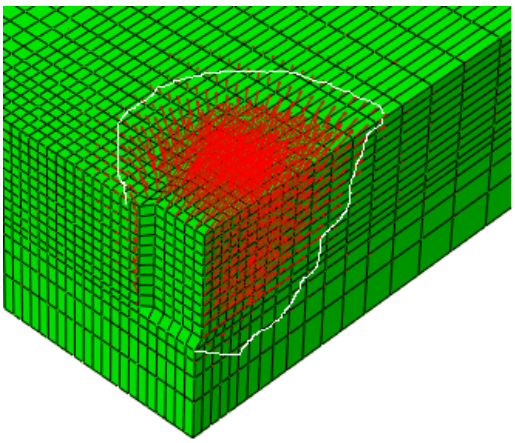

Figure 5-11: Vector plot of displacements at peak state for parallel movement (H = 10.0 m, n = 1, e_o = 0.55)

Figure 5-11 shows the vector plot field at the peak state behind a wall with a spatial ratio n = 1 in dense sand (e_o = 0.55) which illustrates the movement of the soil particles behind the wall. The soil particles within the failure volume move in different values and directions towards the top surface of the soil forming a failure body of a wedge form.

The model shows a non-linear slip line of the failure body with a slip zone that begins from the wall toe and develops towards the upper soil surface. These results show that Blum's assumption extending Coulomb's theory to 3D conditions is in general valid for the spatial failure body shape. The differences are the non-linearity of the failure surface and the different stress conditions inside the failure body.

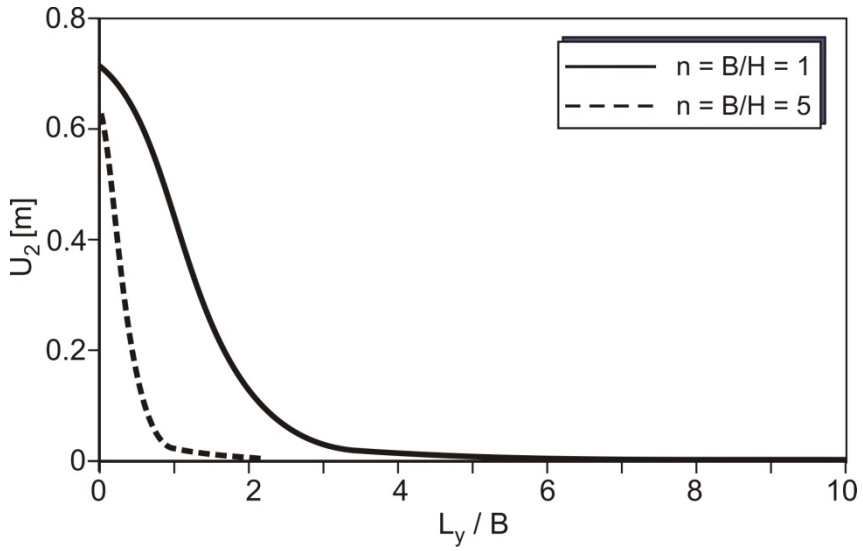

Figure 5-12: Distribution of horizontal displacements (U_2) at peak state along a line at ground surface perpendicular to the moved wall for parallel movement (n = 1 and 5, e_0 = 0.55)

Figure 5-12 shows that the magnitude of the displacement along the symmetrical plane at the top surface of the soil perpendicular to the moved wall decreases with increasing distance from the wall till the zero value displacement is reached at a certain distance from the wall. The distribution is dependent on the value of the spatial ratio n, so that the wider the wall (greater n), the smaller the relative failure body volume to the wall dimensions. It is to be noticed that the boundary of the failure body for a wall of a spatial ratio n = 1 is reached at about five to six times the width while for a spatial ratio n = 5 it is reached at about one to two times the width. The absolute breadth of the failure body is thus affected by the spatial ratio n.

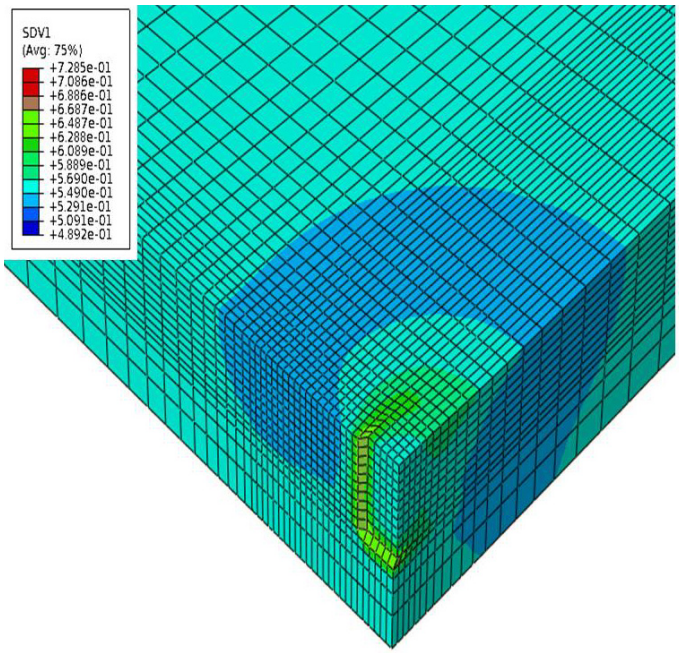

Figure 5-13: Void ratio e of the soil at the peak state for parallel movement (n = 1, e_0 = 0.55)

Figure 5-13 shows the void ratio distribution at peak state for a wall of n = 1 in dense sand (e_0 = 0.55). By comparing the void ratio and the vector plot illustrations (Figure 5-11), it is to be noticed that they determine approximately the same boundary of the failure body volume at peak state.

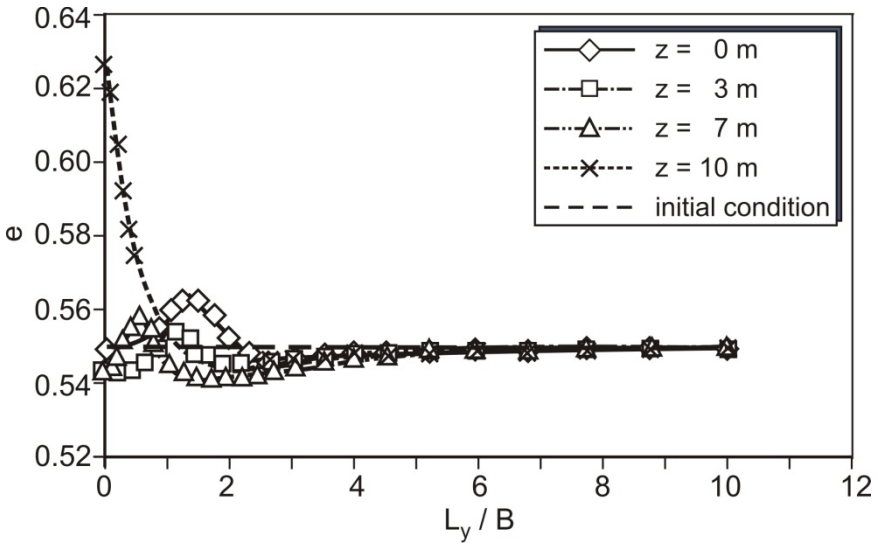

Figure 5-14: Void ratio e along lines perpendicular to the moved wall with different depths at the peak state for parallel movement (n = 1, e_0 = 0.55)

Excepting the values at the wall toe (z = 10 m), the void ratio at peak varies approximately between 0.54 and 0.57 as shown in Figure 5-14. A part of the failure body is under dilatancy effect while the contractancy condition affects the other part. At the beginning of the displacement, the soil particles interlock initially with each other leading to volume reduction (contractancy). By developing the wall displacement till the peak is reached, a part of the particles, which are located at a certain distance from the wall, related to depth z, are moved out of their interlocking position leading to volume increase (dilatancy). At the same time another part is still under contractancy conditions. It is not possible to estimate the soil areas which are in a plastic or in elasto-plastic states.

The following Figures 5-15 and 5-16 show a comparison of the development of the failure body at peak in plane and side view between two walls of two different spatial ratios n = 1 and 5.

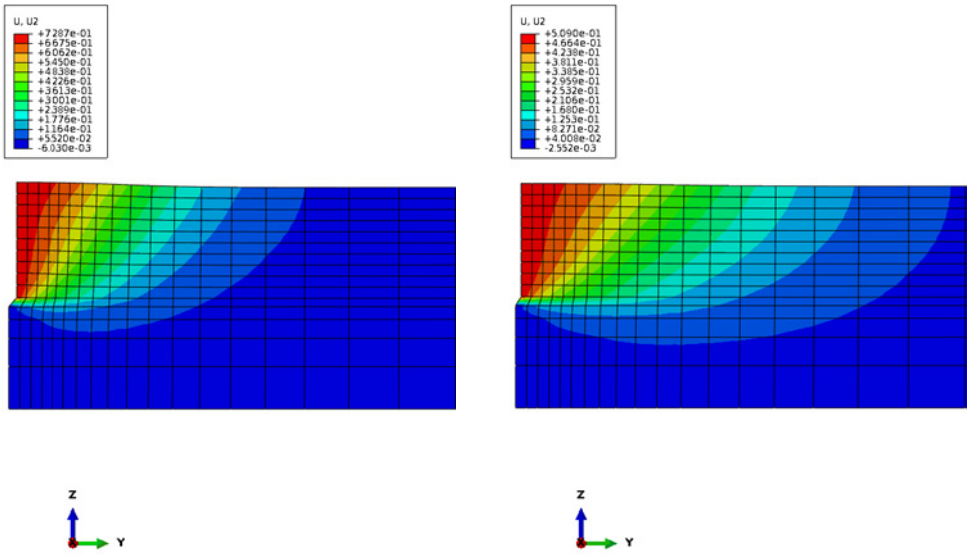

Figure 5-15: Side view of failure body approximately at peak state for two different walls (n = 1 and 5, e_0 = 0.55)

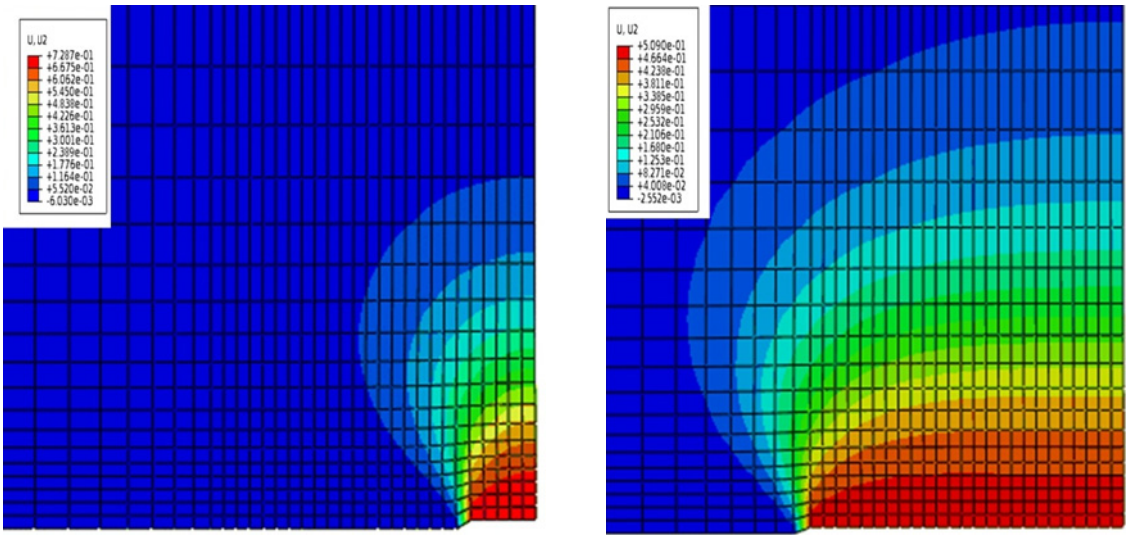

Figure 5-16: Plan view of failure body approximately at peak state for two different walls (n = 1 and 5, e_0 = 0.55)

It is to be distinguished between two concepts, on one hand the total failure body volume and on the other hand the relative failure body volume in relationship to the wall dimensions. The wider the wall, the bigger the total failure body volume but the smaller the relative failure body volume with respect to the wall dimensions. This leads to a greater value of the spatial passive earth pressure by a wall of a smaller spatial ratio n.

Figure 5-17 and Figure 5-18 show the effect of the soil density (e_0 = 0.55, 0.65 and 0.75) for a smooth wall $\delta = 0$ on the failure mechanism. It is to be noticed that the denser the soil, the bigger the failure body volume.

The failure body volume increases by increasing soil density. This is due to the differences in the shear strengths and shear dilatancy according to the soil density and the initial void ratio e_0. As a result, the area, which is influenced by the wall displacement, increases.

As it was expected the presented results regarding the failure mechanism by parallel movement show that the failure body has a spatial form of a shell. The dimensions of the failure body and the form of the failure surface depend on many factors some of which are wall dimensions (spatial ratio n) and the initial condition of the soil (void ratio e_0).

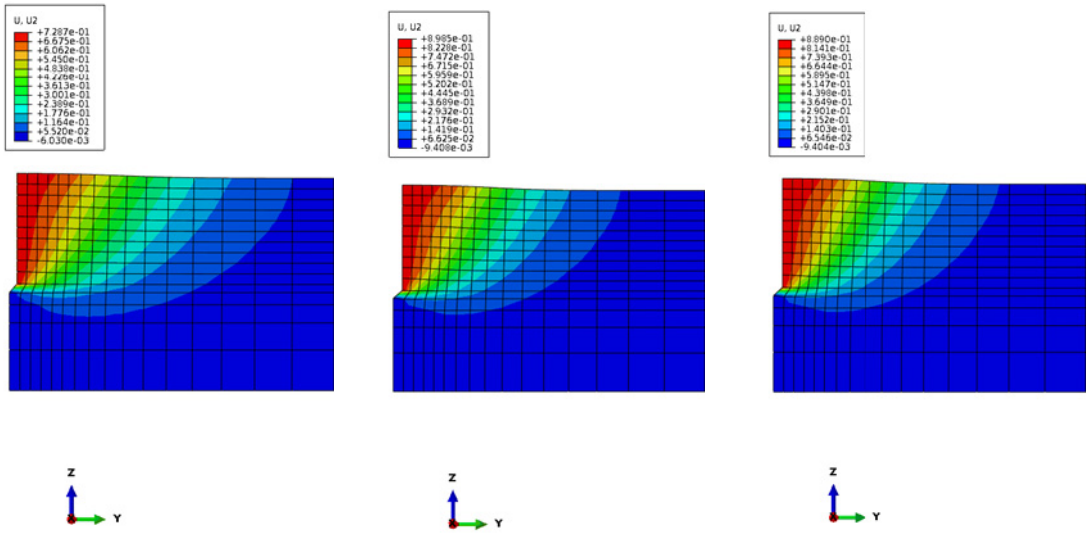

Figure 5-17: Side view of failure body at the peak state for a wall of n = 1 and different soil densities respectively from left to right: dense sand $e_0 = 0.55$, medium sand $e_0 = 0.65$ and loose sand $e_0 = 0.75$

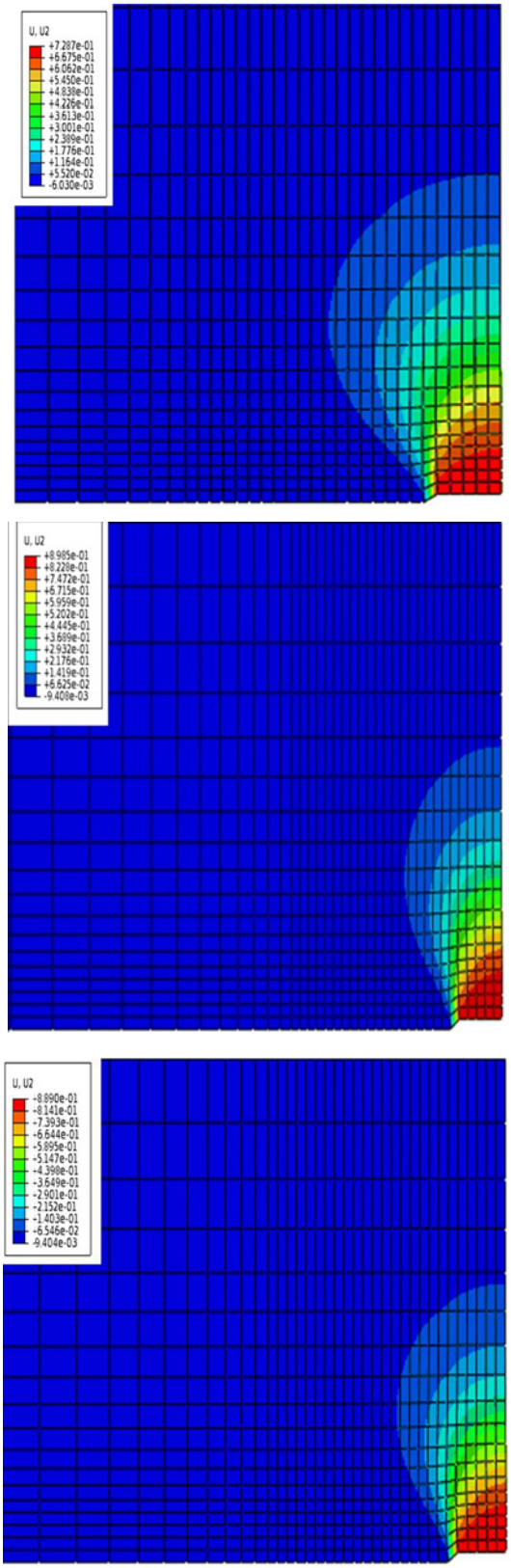

Figure 5-18: Plan view of failure body at peak state for a wall of n = 1 and different soil densities respectively from top to bottom: dense sand $e_0 = 0.55$, medium dense sand $e_0 = 0.65$ and loose sand $e_0 = 0.75$

5.3 Rotation around the top

The mode of wall movement has a main effect on the spatial earth pressure. The numerical modeling results for rotation around the top are presented in the following chapter. This mode of movement occurs frequently in the practice, where the top of the wall is fixed while the toe moves horizontally.

5.3.1 Passive earth pressure at peak

Figure 5-19 and Figure 5-20 show the relation between the spatial passive earth pressure coefficient K_{ph} and the relative displacement (U/H) for different soil densities and various wall spatial ratios n.

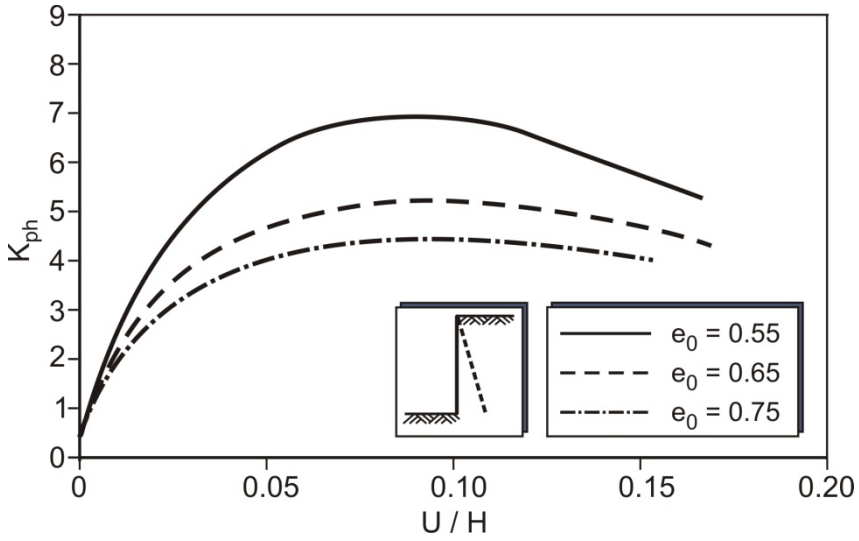

Figure 5-19: Passive earth pressure coefficient as function of relative displacement (n = 1, B = 10 m / H = 10 m)

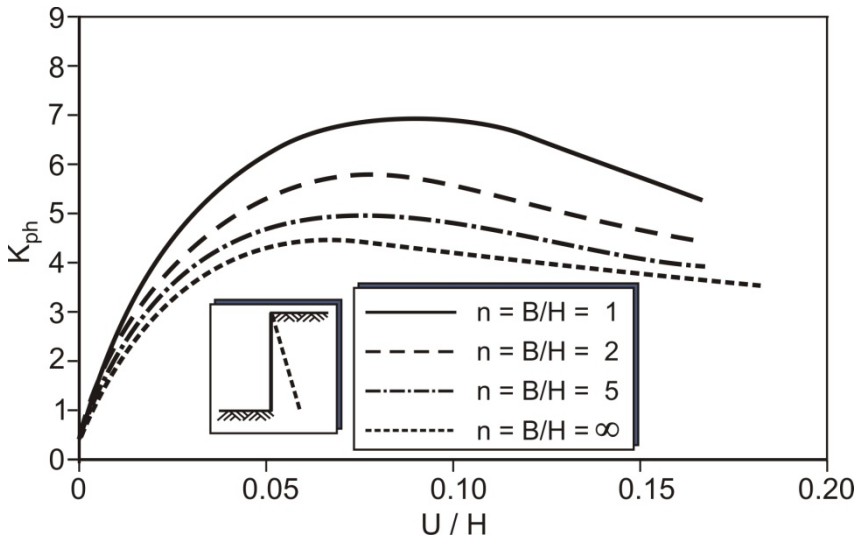

Figure 5-20: Passive earth pressure coefficient as function of relative displacement U/H (H = 10 m, e_0 = 0.55)

The following observations can be noticed:

- Increasing the relative displacement ($\frac{U}{H}$) results in a non-linear increase of the earth pressure coefficient until the peak state is reached, beyond which a decrease is observed due to the softening effect.
- The distribution varies for the respective soil densities. The peak is more clearly to distinguish for dense sand than for medium dense and loose sand.
- Considering other Figures in the annex, for a constant soil density, the required peak displacement ($\frac{U_p}{H}$) is related majorly to the wall height. Also for a constant wall height, the value of the passive earth pressure coefficient decreases with increasing the wall width, which means with increasing the spatial ratio n.

The distributions of the correction factor μ as a function of the spatial ratio n for different soil densities are illustrated in Figure 5-21. Figures for other wall heights and parameters are presented in the annex.

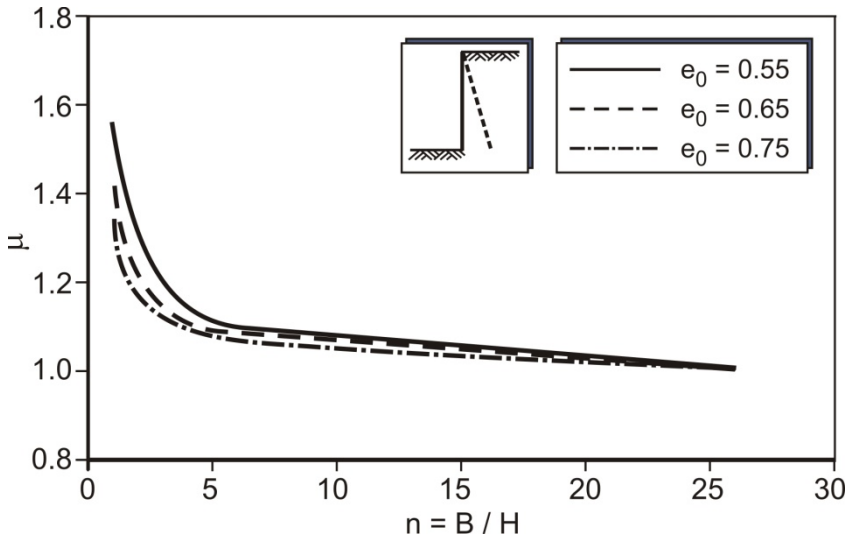

Figure 5-21: Correction factor μ as function of spatial ratio n=B/H (H = 10 m)

The following observations can be stated:

- The curves progressions show a non-linear decrease of the correction factor μ with increasing spatial ratio n.
- The correction factor μ varies with the respective soil density. The correction factor μ decreases with increasing spatial ratios until the curves converge to μ = 1 at very large spatial ratio n = ∞ (2D case).
- Each correction factor curve of a certain soil density shows a sharp gradient for a limited spatial ratio range, beyond which the curves vary gently to converge to μ = 1 at a very large spatial ratio value.
- Considering the Figures (Figure 5-21 for H = 10 m, n = 1 and other similar Figures for H = 5 m and 15 m, n = 1 in the annex) of the correction factor μ as a function of the spatial ratio n for different embedded heights, it is to be noticed that, in the same manner to the parallel movement mode, the spatial ratio range n, in which the curves have a steep gradient, is affected by the value of the embedded height H.

As conclusion in the mode of rotation around the top, the spatial ratio range for the steep curve gradient increases by decreasing the embedded height which means by increasing the spatial ratio n. Also the range between 2D and 3D case for mode of rotation around the top is smaller than its value in the parallel movement mode.

The following Tables 5-4, 5-5 and 5-6 include the correction factor μ and the passive earth pressure coefficient as functions of the initial void ratio e_0 and spatial ratio n for three different wall heights.

Table 5-4: Numerical simulation results for rotation around the top (H = 5.0 m)

e_0	H	B	B/H	K_{ph}	μ	U_p	U_p/H
0.55	5	5	1	7.33	1.6	0.41	0.082
		10	2	6.14	1.34	0.37	0.074
		20	4	5.37	1.17	0.36	0.072
		50	10	4.87	1.07	0.35	0.07
		260	52	4.57	1	0.35	0.07
0.65	5	5	1	5.3	1.43	0.43	0.086
		10	2	4.55	1.23	0.38	0.076
		20	4	4.13	1.12	0.38	0.076
		50	10	3.87	1.04	0.37	0.074
		260	52	3.71	1	0.38	0.076
0.75	5	5	1	4.49	1.37	0.42	0.084
		10	2	3.88	1.18	0.5	0.1
		20	4	3.6	1.09	0.42	0.084
		50	10	3.4	1.03	0.41	0.082
		260	52	3.29	1	0.39	0.078

Table 5-5: Numerical simulation results for rotation around the top (H = 10.0 m)

e_0	H	B	n=B/H	K_{ph}	μ	U_p	U_p/H
0.55	10	10	1	6.897	1.563	0.87	0.087
		20	2	5.777	1.309	0.8	0.08
		50	5	4.921	1.115	0.71	0.071
		260	26	4.413	1	0.65	0.065
0.65	10	10	1	5.167	1.416	0.97	0.097
		20	2	4.445	1.218	0.85	0.085
		50	5	3.974	1.089	0.77	0.077
		260	26	3.648	1	0.7	0.07
0.75	10	10	1	4.395	1.343	1	0.1
		20	2	3.856	1.179	0.87	0.087
		50	5	3.524	1.077	0.79	0.079
		260	26	3.272	1	0.75	0.075

Table 5-6: Numerical simulation results for rotation around the top (H = 15.0 m)

e_0	B	H	n=B/H	K_{ph}	μ	U_p	U_p/H
0.55	10	15	0.67	6.98	1.69	1.21	0.08
	20	15	1.33	6.07	1.47	1.25	0.08
	50	15	3.33	5.06	1.23	1.19	0.08
	260	15	17.33	4.12	1.00	1	0.07
0.65	10	15	0.67	5.46	1.57	1.27	0.08
	20	15	1.33	4.61	1.33	1.21	0.08
	50	15	3.33	4.04	1.16	1.14	0.08
	260	15	17.33	3.47	1.00	0.97	0.06
0.75	10	15	0.67	4.55	1.44	1.29	0.09
	20	15	1.33	3.95	1.25	1.14	0.08
	50	15	3.33	3.33	1.06	1.08	0.07
	260	15	17.33	3.15	1.00	0.95	0.06

The following remarks can be derived from the previous tables:

- For a constant height H, the correction factor μ decreases with increasing width B, while for a constant width B, the correction factor μ increases with increasing wall height H. This means that the correction factor decreases with increasing the spatial ratio n.
- For a constant spatial ratio n, the coefficient of passive earth pressure at peak decreases by increasing the wall dimensions, while the correction factor μ remains almost constant. An example is illustrated in the following Table 5-7 (it is to be noticed that μ and K_{ph3D} for H = 15 m was interpolated between n = 1.33 and n = 3.33 for a value of n = 2).

Table 5-7: Dependence of the correction factor μ and the passive earth pressure coefficient K_{ph} on the absolute height H of the wall (for a spatial ratio n = 2)

e_0	B/H	H	μ	K_{ph3D}
0.55	2	5	1.34	6.14
		10	1.31	5.77
		15	1.389	5.731

5.3.2 Wall Displacement at the peak

The following section presents the numerical modeling results, showing the relative displacement at peak state $\frac{U_p}{H}$ and its relation to the spatial ratio n and initial soil density for a rotation around the top movement.

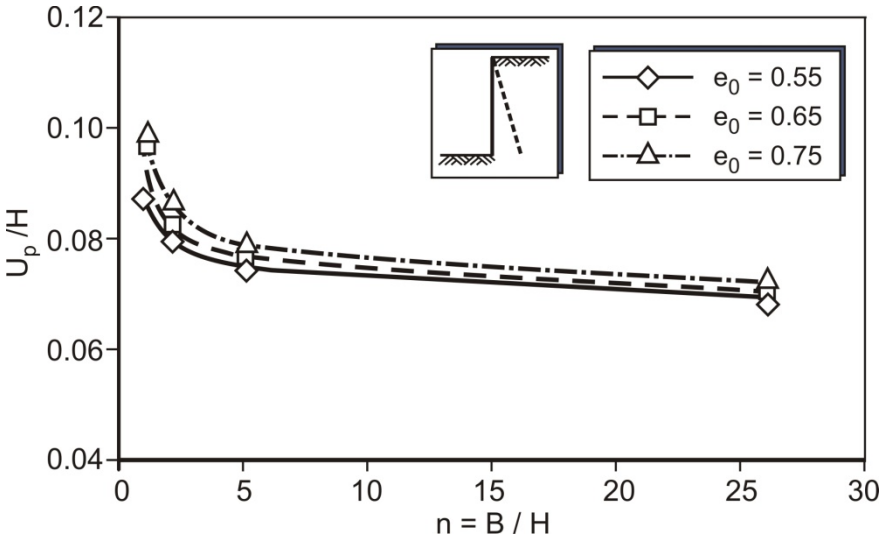

Figure 5-22: Relative displacement of the maximum value at the peak U_p/H as a function of the spatial ratio n (wall height H = 10 m)

Figure 5-22 shows the relative displacement at peak $\frac{U_p}{H}$, as a function of the spatial ratio n for different soil densities. The following observations were made:

- The curves of the relative displacement at peak state as function of the spatial ratio for defined embedded height H show non-linear distribution for small spatial ratio, beyond which the curves display gentle gradients.
- The relative displacements at peak decrease with increasing the spatial ratio n. Specifically a smaller spatial ratio n generates a larger relative failure body volume compared with the wall dimensions, which in turn requires a larger relative displacement.
- Considering the Figures for other embedded heights in the annex, the spatial ratio range n, in which the curves of the relative displacements at peak state have a steep gradient, is affected by the value of the embedded height H.

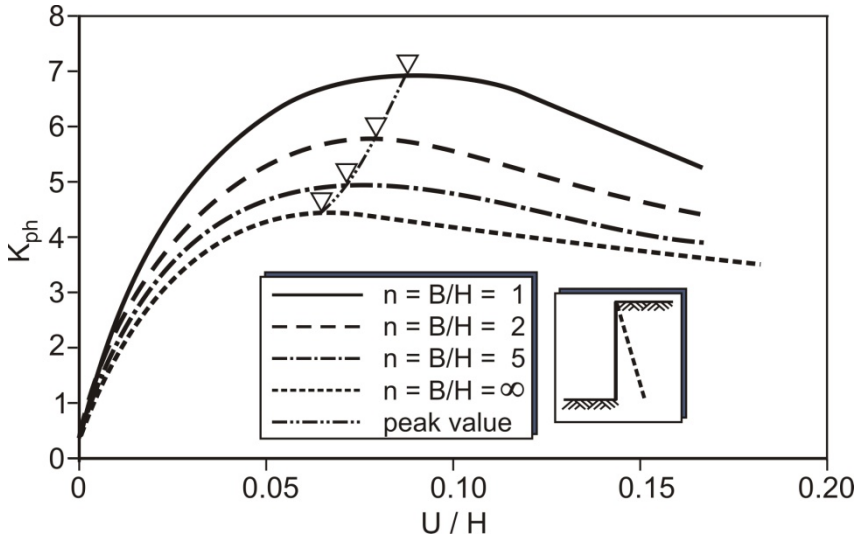

Figure 5-23: Distribution pf passive earth pressure coefficient K_{ph} as a function of relative displacement (n = 1, e_0 = 0.55)

Figure 5-23 shows the effect of varying the width B (the spatial ratio n) on the value of the relative displacement at peak in dense sand (e_0 = 0.55). It is to be noticed that the relative displacement at peak decreases with increasing the wall width B (increasing the spatial ratio n). The reason is that, the ratio of imaginary width to wall width ($\frac{2 \cdot B_0}{B}$) increases with decreasing the width B in a similar way to the parallel movement.

5.3.3 Passive earth pressure distribution

As a result of the passive earth pressure analysis, the stress distribution as a function of the depth z for rotation around the top was calculated as shown in Figure 5-24 and Figure 5-25. Similar to parallel movement, the path is defined at the symmetric face of the element adjacent to the middle of the moving wall at the symmetric plane at x = 0.5 m.

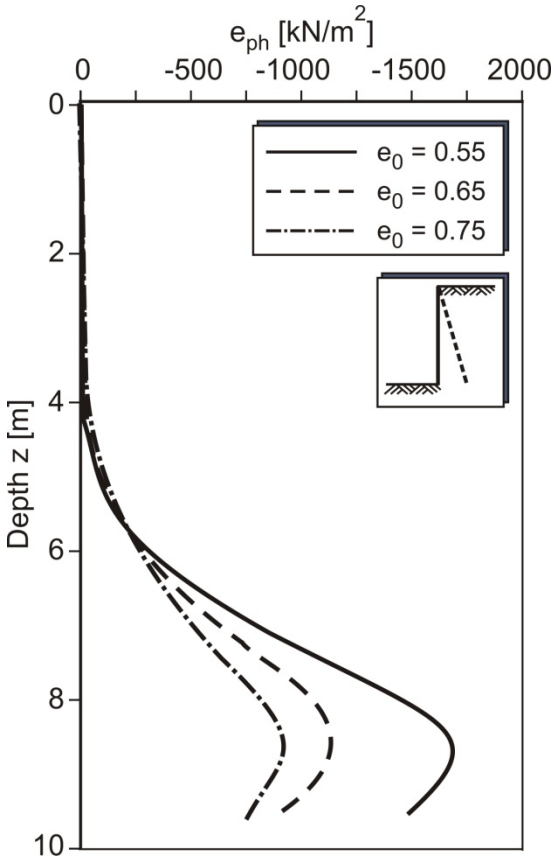

Figure 5-24: Horizontal passive stress distributions at peak state in the symmetric plane (x = 0.5 m, n = 1)

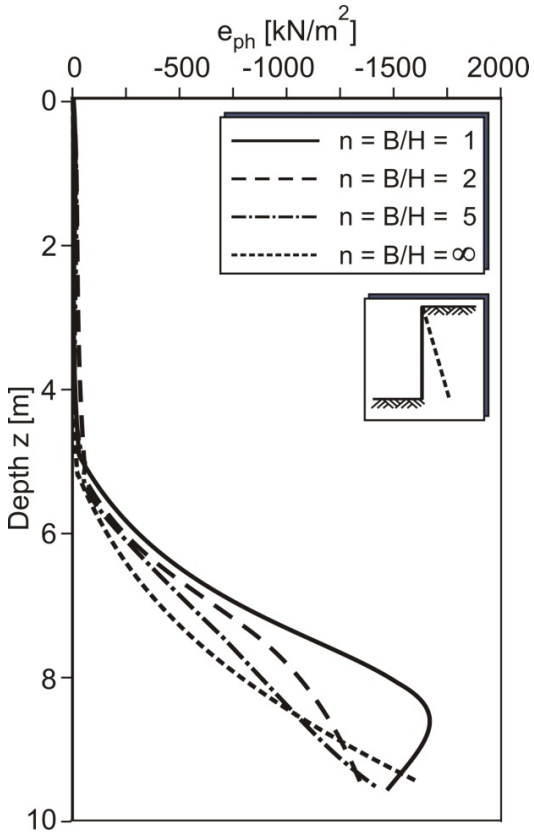

Figure 5-25: Stress distributions at peak state in the symmetric plane for different spatial ratios n ($x = 0.5$ m, $e_0 = 0.55$)

The curves show a non-linear increase of the horizontal stresses e_{ph} with increasing the depth z until a maximum value at the wall toe is reached. By varying the spatial ratio n with a constant wall height H, it was observed that the curves have a small value nearly to zero till half of the wall height. The top edge of the wall remains immobile in the horizontal and vertical direction. Therefore, the passive earth pressure in the top area of the wall is almost not mobilized. Furthermore, the distributions of the horizontal stresses vary linearly with increasing embedded depth z starting from the middle part of the wall. In the bottom part however, the variation is a non-linear curve with a maximum value at the toe for all walls with different spatial ratios. Only for a wall of small spatial ratio (n = 1), the stresses decrease after the maximum value to a smaller value at the wall toe as shown in Figure 5-25. The passive earth pressure indicated by the passive earth pressure coefficient K_{ph} for rotation around the top mode is in general smaller than its value in parallel movement. This result is compliant to the general stress distribution given in the German standard 4085 [31].

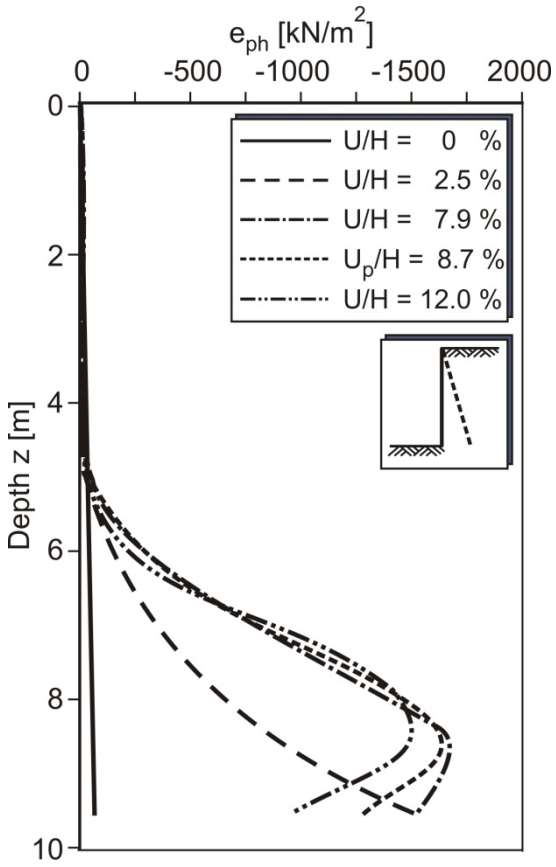

Figure 5-26: Stress distributions in the symmetric plane at different displacements for a wall of spatial ratios n = 1 (x = 0.5 m, e_0 = 0.55)

By calculating the horizontal stresses at different displacement values as shown in Figure 5-26, the curves show that a peak stress value is generated after a certain displacement value U_p is reached. Further displacements beyond the peak displacement do not generate higher stresses.

5.3.4 Failure mechanism by rotation around the top

To investigate the effect of the mode of movement on the form of the failure body a study of the failure mechanism is done in the following section. Figure 5-27 below shows a vector plot for the failure body at peak during a rotation around the top movement.

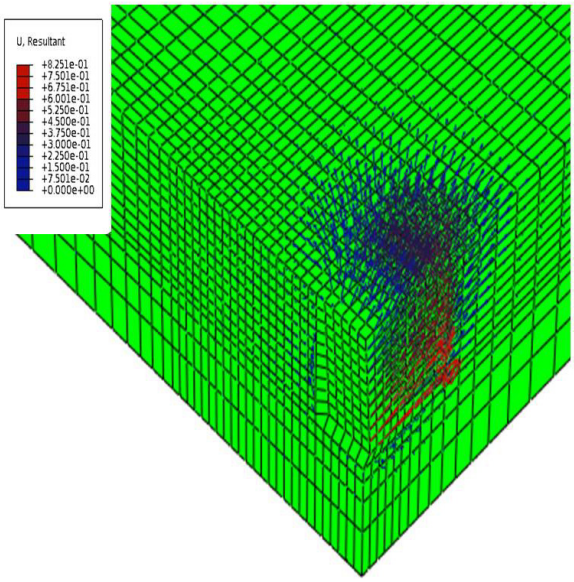

Figure 5-27: Vector plot at the failure state for rotation around the top (H = 10.0m, n = 1, e_0 = 0.55)

Figure 5-27 shows the vector plot field at the peak state behind a wall of a spatial ratio n = 1 in dense sand (e_o = 0.55). The soil particles within the failure volume move in different directions and values forming a failure body of a wedge form. The model shows a non-linear 3D failure body with a slip zone that begins from the wall toe and develops until the upper soil surface.

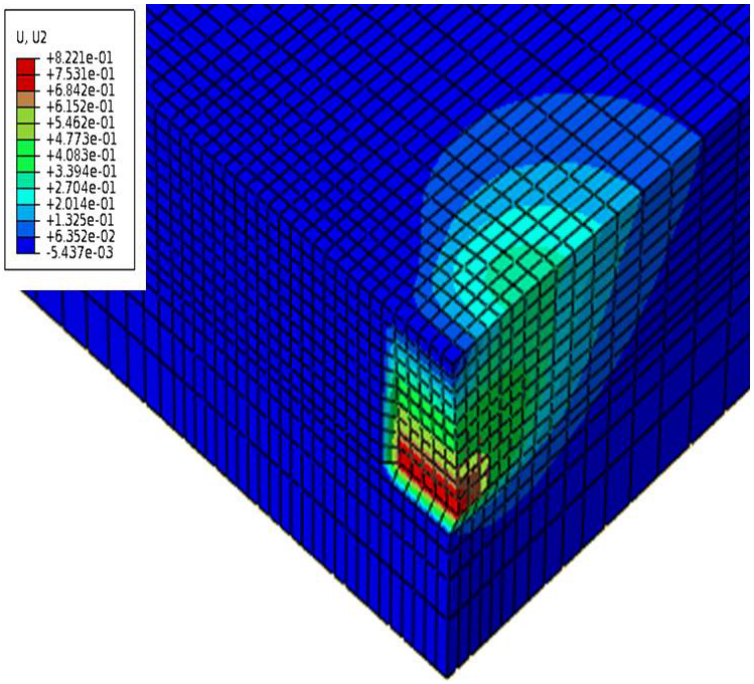

Figure 5-28: Horizontal displacement distribution at the failure state by peak state for rotation around the top movement (H = 10.0m, n = 1,e_0= 0.55)

The distributions of the horizontal displacement behind the wall are shown in Figure 5-28. The magnitude of the displacement decreases with increasing distance from the wall till the zero value displacement is reached at a certain distance from the wall which is related to the spatial ratio n, so that the wider the wall (higher B/H), the smaller the relative failure body volume to the wall dimensions.

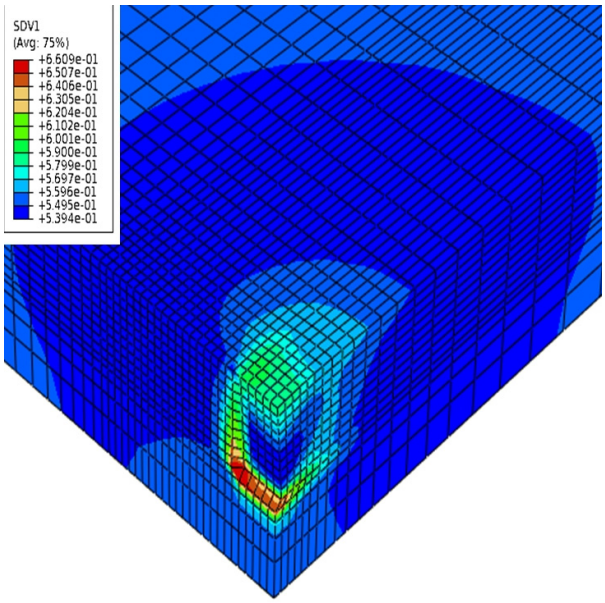

Figure 5-29: Void ratio e of the soil at the peak state for rotation around the top (n = 1, e_0 = 0.55)

Excepting the values at the wall toe, Figure 5-29 shows that the void ratio at peak varies approximately between 0.54 and 0.59. A part of the failure body is under dilatancy effect while the contractancy condition affects the other part.

By comparing Figure 5-11 with Figure 5-29 it is to be noticed that, the mechanism of the rotation movement limits the volume of the failure body. The mode of rotation around the top generates a failure mechanism similar to the parallel movement mode with a smaller failure body. The reason is that during the movement around the top, the wall acts in a manner similar to lifting soil with a fully embedded shovel. This also causes a reduction in the value of the spatial passive earth pressure coefficient K_{ph3D} comparing with its value in the parallel mode.

5.4 Rotation around the toe

5.4.1 Passive earth pressure at peak

In this mode of movement, the bottom edge of the wall remains immobile in both horizontal and vertical direction, while the top of the wall moves horizontally. The numerical modeling results given in Figure 5-30 show that the earth pressure coefficient K_{ph} increases continuously with increasing the relative displacement, showing a hardening behavior without forming a peak or showing a softening behavior. As a result, a clear peak state cannot be

formed, therefore, a displacement criterion was used. The peak state was defined at a relative displacement U = 0.2H, considering the real measurements in situ and the serviceability limit state. The earth pressure increases initially non-linear with increasing the rotation.

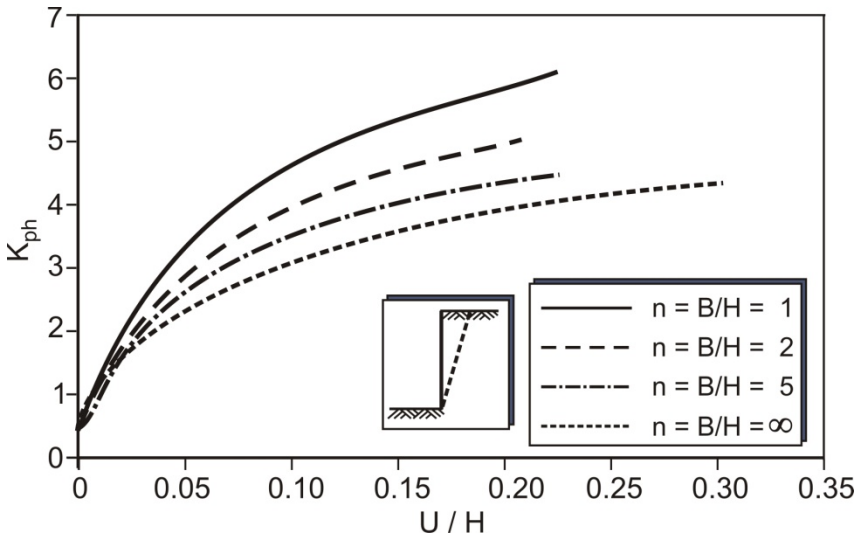

Figure 5-30: Passive earth pressure coefficient as function of relative displacement U/H (H = 10 m,e_0 = 0.55)

Figure 5-31 shows the distributions of the spatial passive earth pressure correction factor μ with different spatial ratios n for various soil densities. As mentioned above, the U_p value at U/H = 0.2 were used to define the values of the correction factor μ.

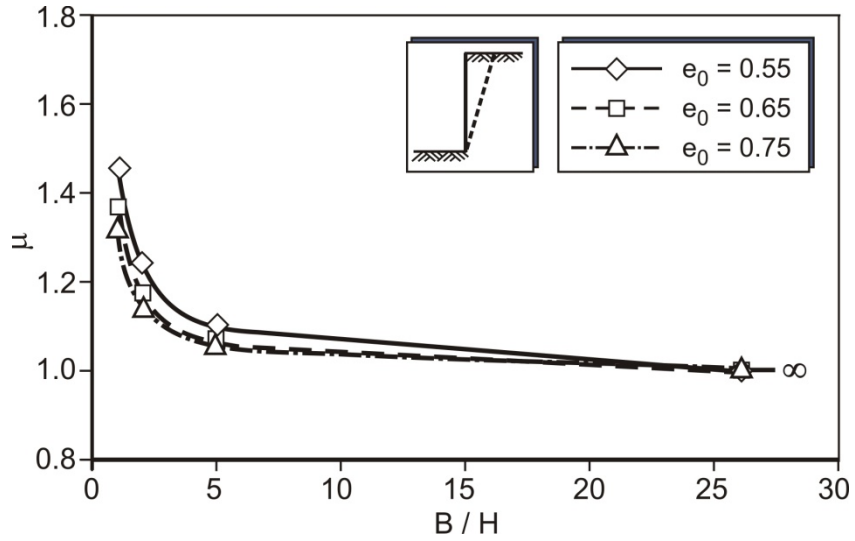

Figure 5-31: Correction factor μ as function of spatial ratio n (H = 10 m)

The following can be observed:

- The curve shows a non-linear decrease of the correction factor μ with increasing the spatial ratio.

- The correction factor μ varies for the respective soil densities. The difference between the curves decreases with increasing the spatial ratio n until the curves converge to μ= 1 at a very large spatial ratio n = ∞.
- Considering the Figures of the correction factors μ for different embedded heights (Figure 5-31 for H = 10 m and other Figures for H = 5 m and 15 m in the annex), the spatial ratio range n, in which the curves have a steep gradient, is affected by the value of the embedded height H.

Table 5-8, 5-9 and 5-10 include the correction factor μ and the passive earth pressure coefficient as functions of soil initial density and spatial ratio B/H for three different wall heights. As mentioned before, the values of the passive earth pressure coefficient are taken at relative displacements approximately equal to U/H = 0.2.

Table 5-8: Numerical simulation results for rotation around the toe (H = 5.0 m, U/H = 0.2)

e_0	H	B	n	K_{ph}	μ
0.55	5.00	5.00	1.00	5.95	1.59
	5.00	10.00	2.00	4.78	1.28
	5.00	20.00	4.00	4.32	1.15
	5.00	50.00	10.00	3.96	1.05
	5.00	260.00	52.00	3.75	1.00
0.65	5.00	5.00	1.00	4.42	1.42
	5.00	10.00	2.00	3.61	1.17
	5.00	20.00	4.00	3.31	1.07
	5.00	50.00	10.00	3.19	1.03
	5.00	260.00	52.00	3.10	1.00
0.75	5.00	5.00	1.00	3.69	1.29
	5.00	10.00	2.00	3.20	1.11
	5.00	20.00	4.00	2.99	1.04
	5.00	50.00	10.00	2.89	1.01
	5.00	260.00	52.00	2.87	1.00

Table 5-9: Numerical simulation results for rotation around the toe (H = 10.0 m, U/H = 0.2)

e_0	H	B	n	K_{ph}	μ
0.55	10.00	10.00	1.00	5.58	1.46
	10.00	20.00	2.00	4.75	1.24
	10.00	50.00	5.00	4.20	1.10
	10.00	260.00	26.00	3.82	1.00
0.65	10.00	10.00	1.00	4.16	1.37
	10.00	20.00	2.00	3.56	1.17
	10.00	50.00	5.00	3.22	1.06
	10.00	260.00	26.00	3.02	0.99
0.75	10.00	10.00	1.00	3.65	1.32
	10.00	20.00	2.00	3.13	1.13
	10.00	50.00	5.00	2.92	1.05
	10.00	260.00	26.00	2.77	1.00

Table 5-10: Numerical simulation results for rotation around the toe (H = 15.0 m, U/H = 0.2)

e_0	H	B	n	K_{ph}	μ
0.55	15.00	10.00	0.67	5.85	1.64
	15.00	20.00	1.33	4.80	1.35
	15.00	50.00	3.33	4.12	1.16
	15.00	260.00	17.33	3.56	1.00
0.65	15.00	10.00	0.67	4.30	1.50
	15.00	20.00	1.33	3.70	1.29
	15.00	50.00	3.33	3.28	1.14
	15.00	260.00	17.33	2.87	1.00
0.75	15.00	10.00	0.67	3.68	1.36
	15.00	20.00	1.33	3.16	1.17
	15.00	50.00	3.33	2.74	1.01
	15.00	260.00	17.33	2.70	1.00

The tables show that for a constant spatial ratio n, the correction factor μ decreases with increasing the wall dimensions. This will be discussed later. Also the passive earth pressure coefficient at peak K_{ph} decreases with increasing the wall width B when the wall height H is constant.

5.4.2 Passive earth pressure distribution

As a result of the spatial passive earth pressure numerical simulation, the stress distribution as a function of the depth z was calculated as shown in Figure 5-32 below. The stress was determined similar to parallel movement, the path is defined near to the symmetric plane at x = 0.5 m.

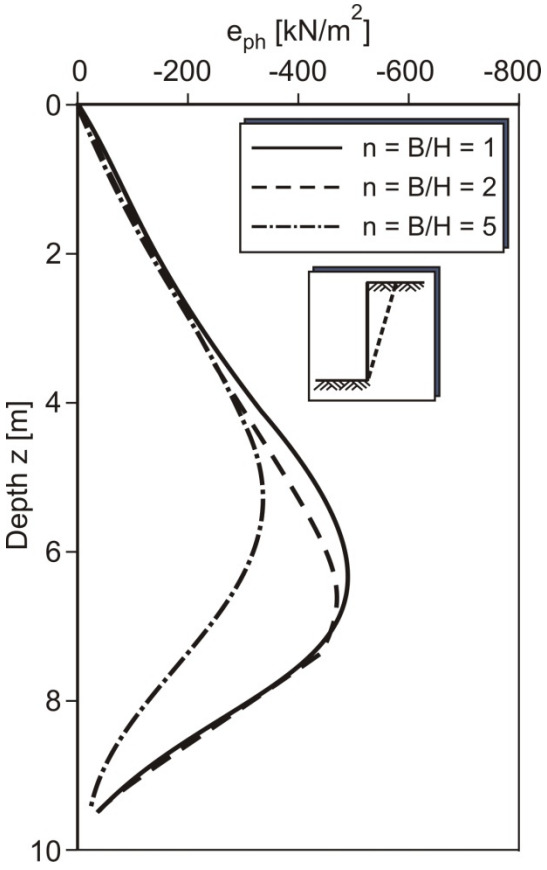

Figure 5-32: Stress distributions at peak state in the symmetric plane (x = 0.5 m) for different spatial ratios n (e_0 = 0.65)

The distribution of the horizontal stresses with increasing embedded depth z varies almost linearly in the upper part of the wall. In the lower part however, the distribution of the horizontal stresses at peak show a non-linear accretion of the stress till a maximum value at about two thirds of the wall height (starting from the ground surface) is reached. Beyond the peak value, the stress decreases to a small value, smaller than the horizontal initial stresses $e_{0h} = \gamma \cdot H \cdot K_0$, at the wall toe due to the arching of the soil which causes a stress decrease at the bottom.

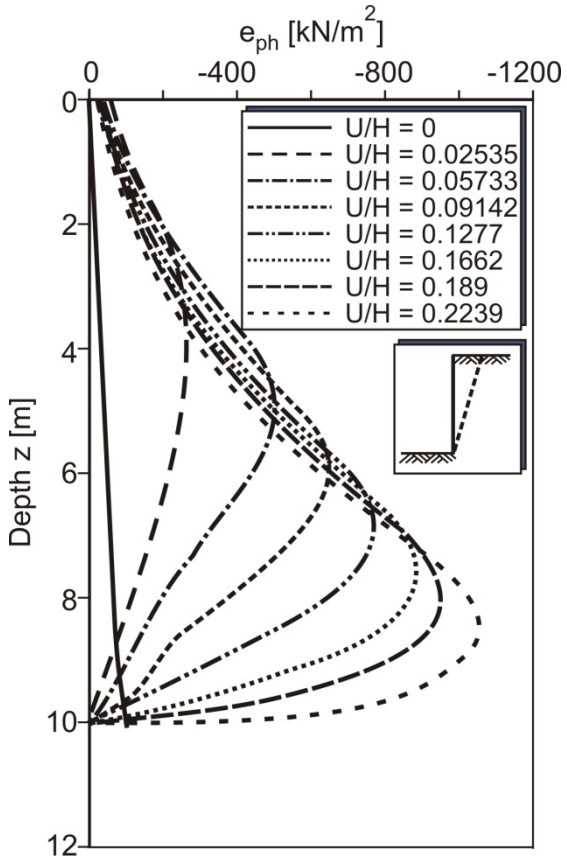

Figure 5-33: Stress distributions in the symmetric plane at different displacements for a wall of spatial ratios n = 1 (x = 0.5 m, e_0 = 0.55)

By the advance of the displacement, the depth z_{peak} corresponding to the maximum horizontal stress value location increases. z_{peak} varies from half of the wall height at U/H = 5 % till 90 % of the wall height at U/H = 22 % as shown in Figure 5-33. The influence of the wall movement extends in the soil deeply (greater $H_{Total} = H+H_0$). This causes a move of the peak value towards the bottom.

5.4.3 Failure mechanism by rotation around the toe mode

The following Figure 5-34 shows the void ratio for the rotation around the toe mode.

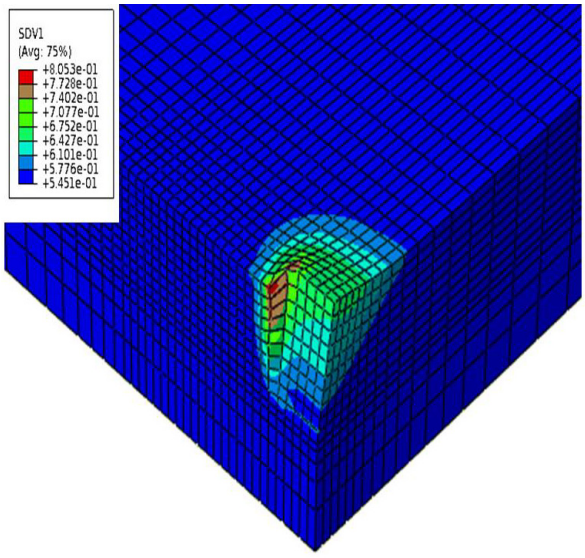

Figure 5-34: Void ratio e of the soil at the peak state for rotation around the toe (n=1, e_0=0.55)

During the wall displacement, the affected soil area starts from the top of the wall and extends in vertical and horizontal directions. As shown in Figure 5-34 the soil particles inside this area are with a void ratio e greater than the initial void ratio e_0 (dilatancy condition). Increasing the displacement increases the volume of the affected area continuously without forming a limited failure volume as in parallel movement or rotation around the top.

5.5 Frictional wall

The calculations of the earth pressure coefficient on a frictional wall were done exemplarily in this chapter for parallel movement mode only. This mode of movement activates more friction, due to greater relative displacement between the wall and the soil, than the other movement modes. The value of the friction angle δ was added in the model by using the interface element, in which the maximum shear stress was limited to $\tau_{max} = \tau_h.\tan\delta$. δ is expressed here as a ratio of the soil friction angle φ. It is to be noticed that the friction angle φ and its related wall-soil friction angle δ are determined according to the value of the initial void ratio as shown in section 4-3 before. Figure 5-35 illustrates the graph of the spatial passive earth pressure coefficient K_{ph} as a function of the relative displacement U/H for various values of δ (0, $\frac{\varphi}{3}$, $\frac{2\varphi}{3}$ and φ) and different initial void ratios (e_0=0.65 and 0.55) and wall dimensions (n = 1 and n = ∞).

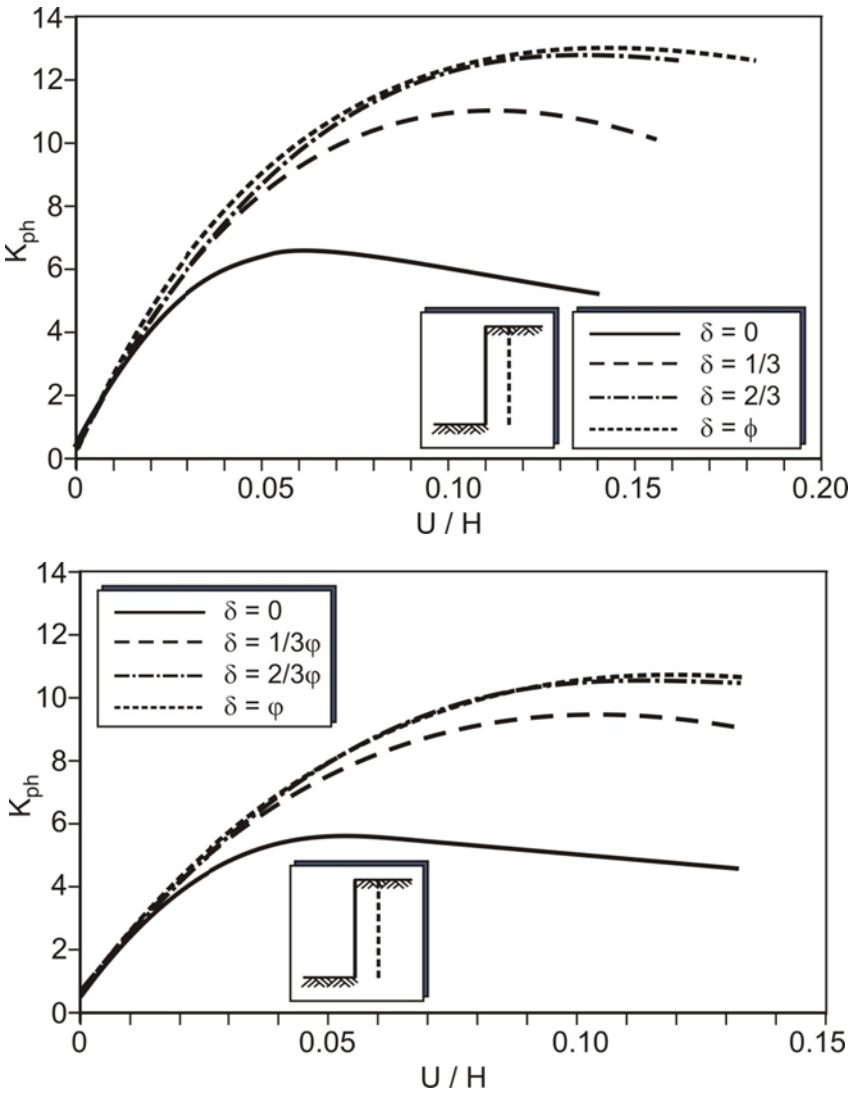

Figure 5-35: Passive earth pressure coefficient as function of relative displacement for different soil-wall friction angles δ (e_0 = 0.65 for n = 1 and e_0 = 0.55 for n = ∞, H = 10 m)

The results in Figure 5-35 show that the horizontal passive earth pressure coefficient increases with increasing the wall friction angle δ as was to be expected. By increasing the value of the wall friction angle δ to $\frac{2\varphi}{3}$ and φ, it was noticed that the generated friction stresses were limited to the value of $\delta = \frac{2\varphi}{3}$. The reason for that is not totally clear. According to the classical theories and to German standard DIN 4085 [31] the earth pressure must increase with increasing wall friction angle. However, the numerical model gives no further mobilization of wall friction for $\delta > \frac{2\varphi}{3}$.

In order to check whether this is induced by the used hypoplastic material law, additional earth pressure simulations have been carried out with an elasto-plastic material law (hardening soil) using the PLAXIS 2D software as shown in Figure 5-36.

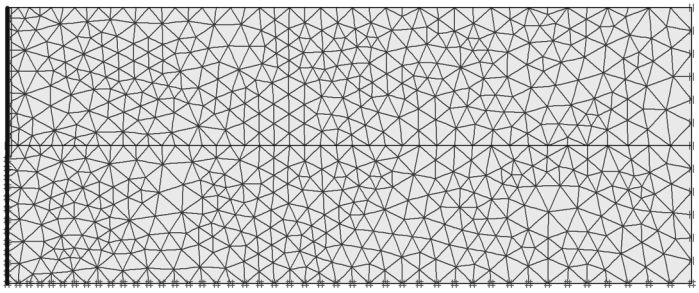

Figure 5-36: FEM Mesh for2D passive earth pressure using PLAXIS

The wall was modeled as a rigid plate and the soil was modeled with the hardening soil constitutive law with soil parameters included in Table 5-11. More details about the hardening soil constitutive law and about the soil parameters are in [74]. The constant R_{inter} was varied according to the value of angle δ.

Table 5-11: The soil parameters in the PLAXIS 2D model by using hardening soil constitutive model

γ (kN/m³)	E^{ref}_{50} (kN/m²)	E^{ref}_{oed} (kN/m²)	E^{ref}_{u} (kN/m²)	power (m)	(°)	C (kN/m²)	Ψ (°)	R_{inter} (for $\delta_=$
17.1	80000	80000	329000	0.5	40	0.1	8	1

The passive earth pressure coefficient K_{ph} is calculated for different values of the soil-wall friction angle δ and the results were compared with the values of K_{ph} in ABAQUS and in the German standard DIN 4085 [31]. It is to be noticed that this comparison was done just to identify the behavior of the earth pressure coefficient by varying the angle δ and not to compare the value of K_{ph} or to identify the constitutive laws hypoplasticity and hardening soil parameters. The results are presented in Figure 5-37.

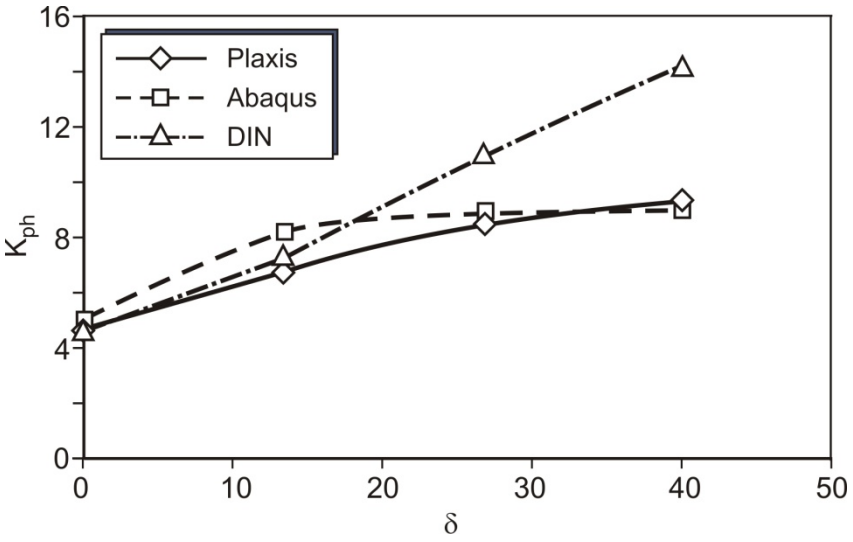

Figure 5-37 Passive earth pressure coefficient as a function of soil wall friction angle δ for PLAXIS and ABAQUS and German standard 4085 [31].

It is to be noticed that the value of K_{ph} increases in PLAXIS with increasing the value of δ. On the contrary the value of K_{ph} increases in ABAQUS with increasing δ till $\delta = \frac{2\varphi}{3}$ then the value of K_{ph} is almost constant which is obviously related to the subroutine of the hypoplasticity. An additional frictional subroutine in hypoplasticity must be developed in the future so that the values of the shear stresses for high values of δ ($\delta > \frac{2\varphi}{3}$) increase with increasing the value of angle δ in the recent hypoplasticity form. This problem will not be discussed in this thesis.

Figure 5-37 shows also the increase of K_{ph} with increasing angle δ according to the German standard DIN 4085 [31] in comparison with FEM results in ABAQUS and PLAXIS. The curves show an obvious difference that the linear increase of K_{ph} values in DIN 4085 is higher than in PLAXIS and ABAQUS.

The results were also illustrated for the correction factor μ as a function of the spatial ratio by varying the soil wall friction angle δ as shown in Figure 5-38.

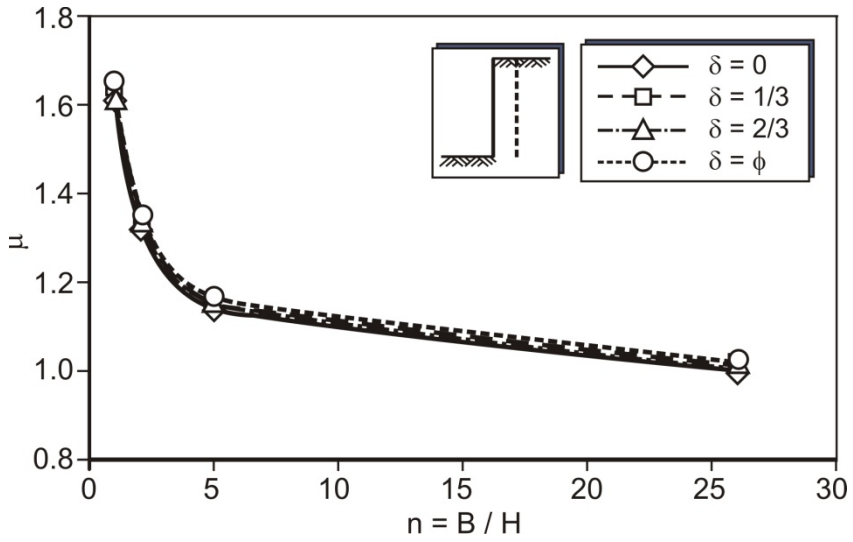

Figure 5-38 Correction factor μ as function of spatial ratio n (e_0 = 0.55, H = 10 m) for different wall friction angles

The correction factor $\mu = \frac{K_{ph3D}}{K_{ph2D}}$ is not affected by the values of the earth pressure coefficient K_{ph} as a function of δ. This an important result, indicating that the effect of the wall friction angle δ on the magnitude of the passive earth pressure is fully covered by the differences in the respective K_{ph} values for the 2D case.

Figure 5-39 and Figure 5-40 show the effect of the wall soil friction angle δ on the distribution of the failure body volume. It is to be noticed that the higher the soil wall friction angle δ, the bigger the failure body volume.

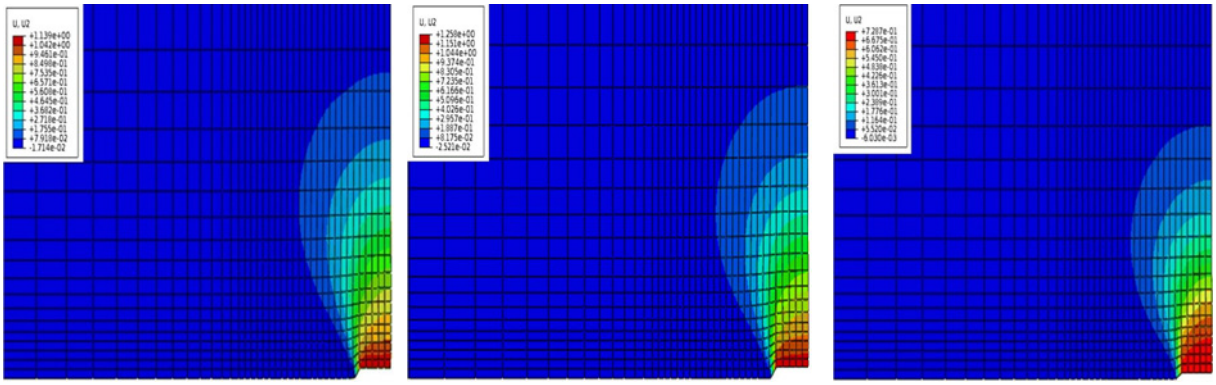

Figure 5-39: Top view for the failure body volume at peak state for different soil wall friction angles for dense sand (e_0 = 0.55)

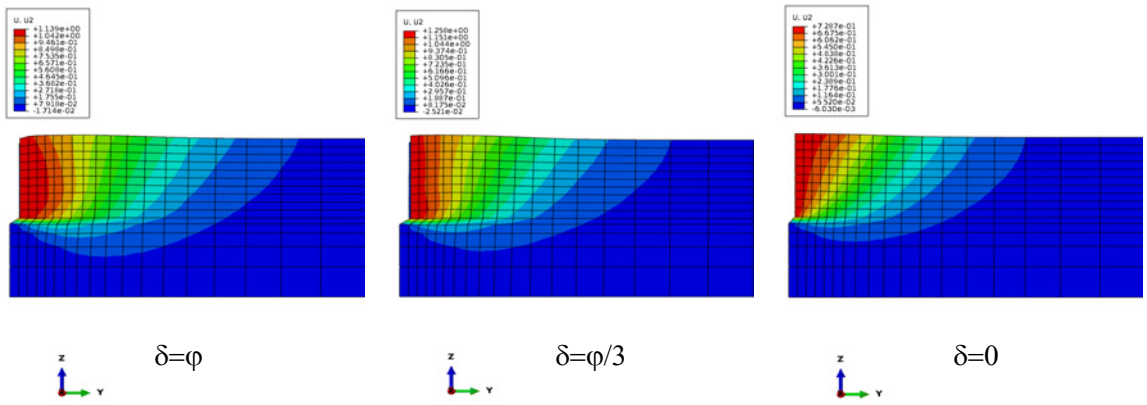

Figure 5-40: Side view for the failure body volume at peak state for different the soil wall friction angles for dense sand (e_0 = 0.55)

It is to be concluded that, the value of E_{ph} for frictional wall is bigger than its value for smooth wall $\delta = 0$. This is due to the expected fact that the earth pressure coefficient increases by increasing the value of δ. On the contrary the correction factor μ is not affected by the value of δ. Also a frictional wall develops a non-linear failure body.

6 Evaluation of the numerical results

6.1 Introduction

The global understanding of all aspects associated with the spatial passive earth pressure problem requires a practical illustration of the results placing all the interacting factors and variables under the spot light. This enables good analysis, high evaluation degree and practical solutions to be achieved. The following chapter presents an analysis and discussion of the thesis results with particular emphasis on the factors affecting the 3D passive earth pressure in general. These also include aspects such as the comparison of the three modes of wall movement, the effect of the soil wall friction angles and the scale effect related to the absolute height of the wall. Descriptions of the spatial passive earth pressure problem by analytical mobilization functions were made. These functions consider various parameters such as relative displacement, the mobilized displacement ratio $\frac{U}{U_p}$, the initial soil densities and the spatial ratios $n = \frac{B}{H}$.

6.2 Comparison of the three types of movement

In the following section 6.2 the effect of the mode of wall movement and soil density will be discussed. The graphs in Figure 6-1 to 6-4 illustrate the passive earth pressure coefficient as a function of the initial void ratio and movement mode for varied spatial ratios n. The spatial ratio n was varied between n = 1, 2, 5 and ∞. The results for H = 5 m, 10 m and 15 m show evidently, that the earth pressure coefficient is smaller, the greater the wall height is. This scale effect is discussed in section 6.5.

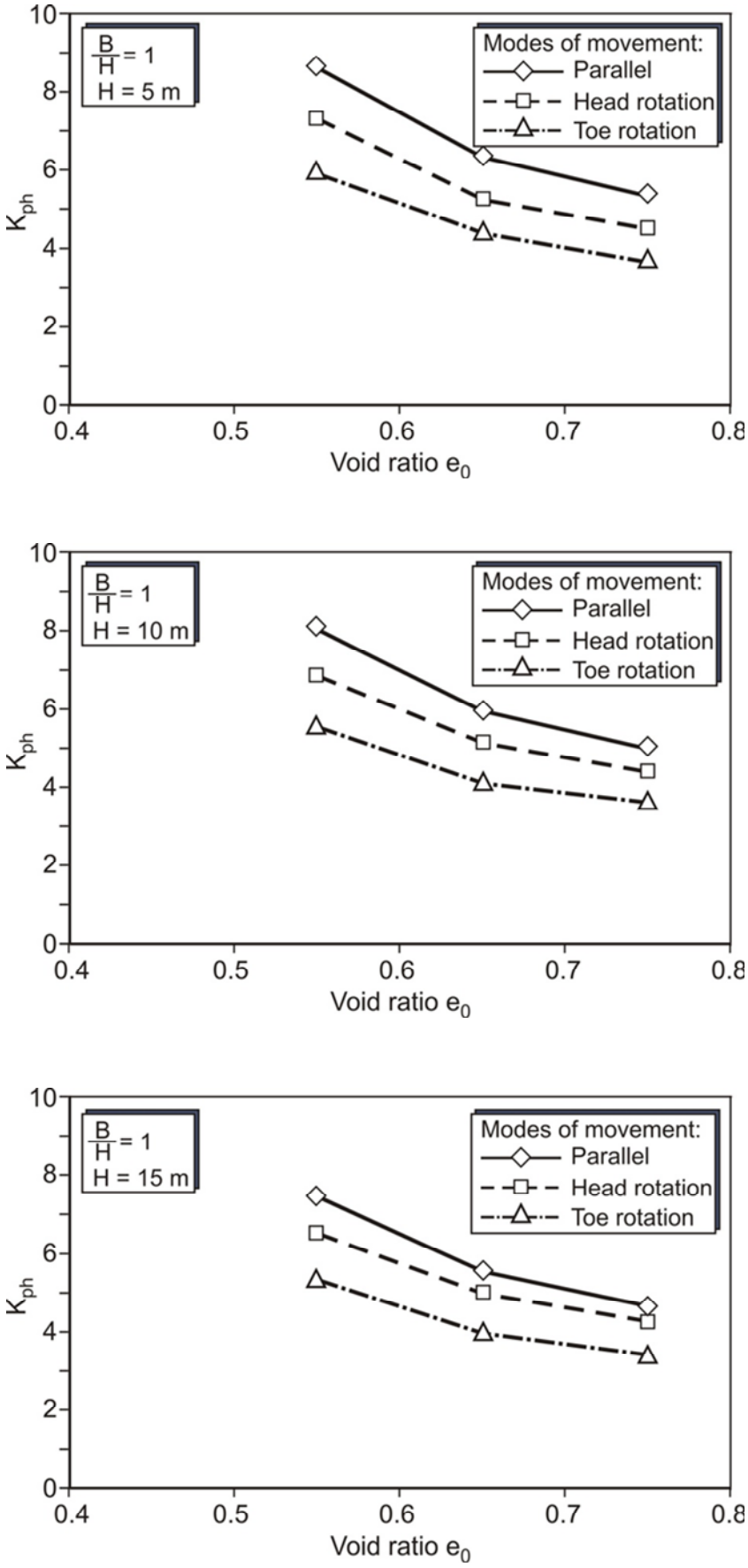

Figure 6-1: K_{ph} as a function of the initial void ratio e_0 (n= 1)

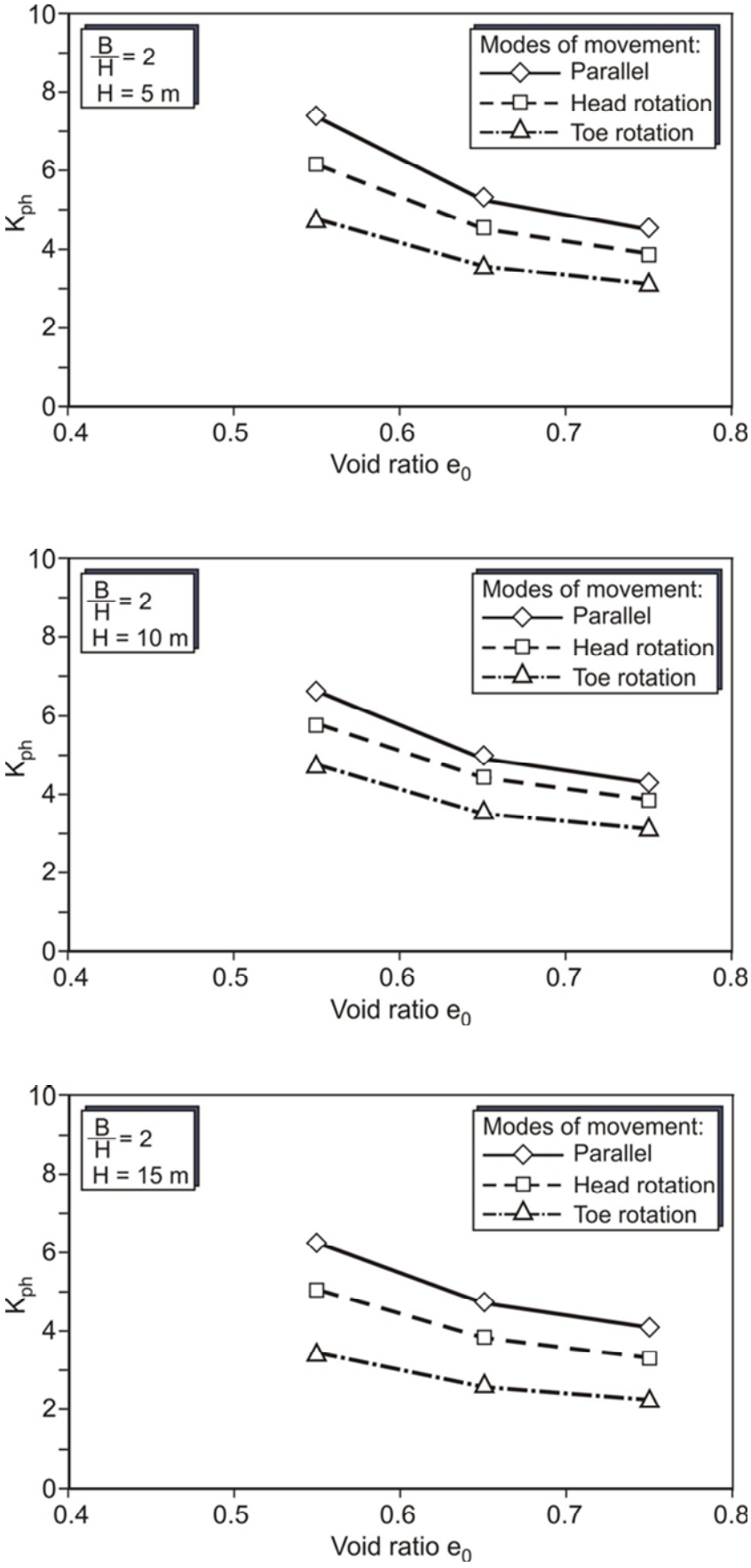

Figure 6-2: K_{ph} as a function of the initial void ratio e_0 (n= 2)

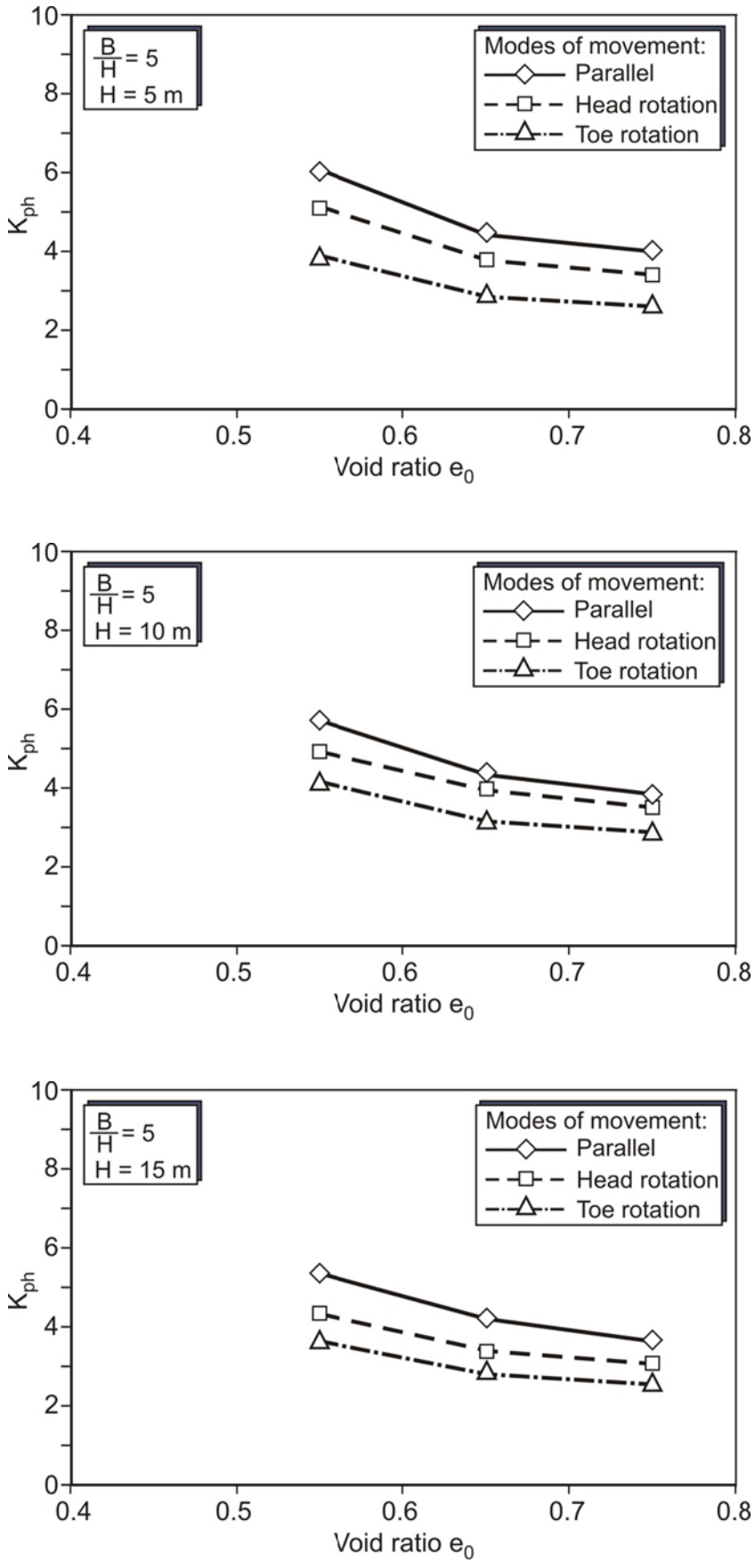

Figure 6-3: K_{ph} **as a function of the initial void ratio** e_0 **(n= 5)**

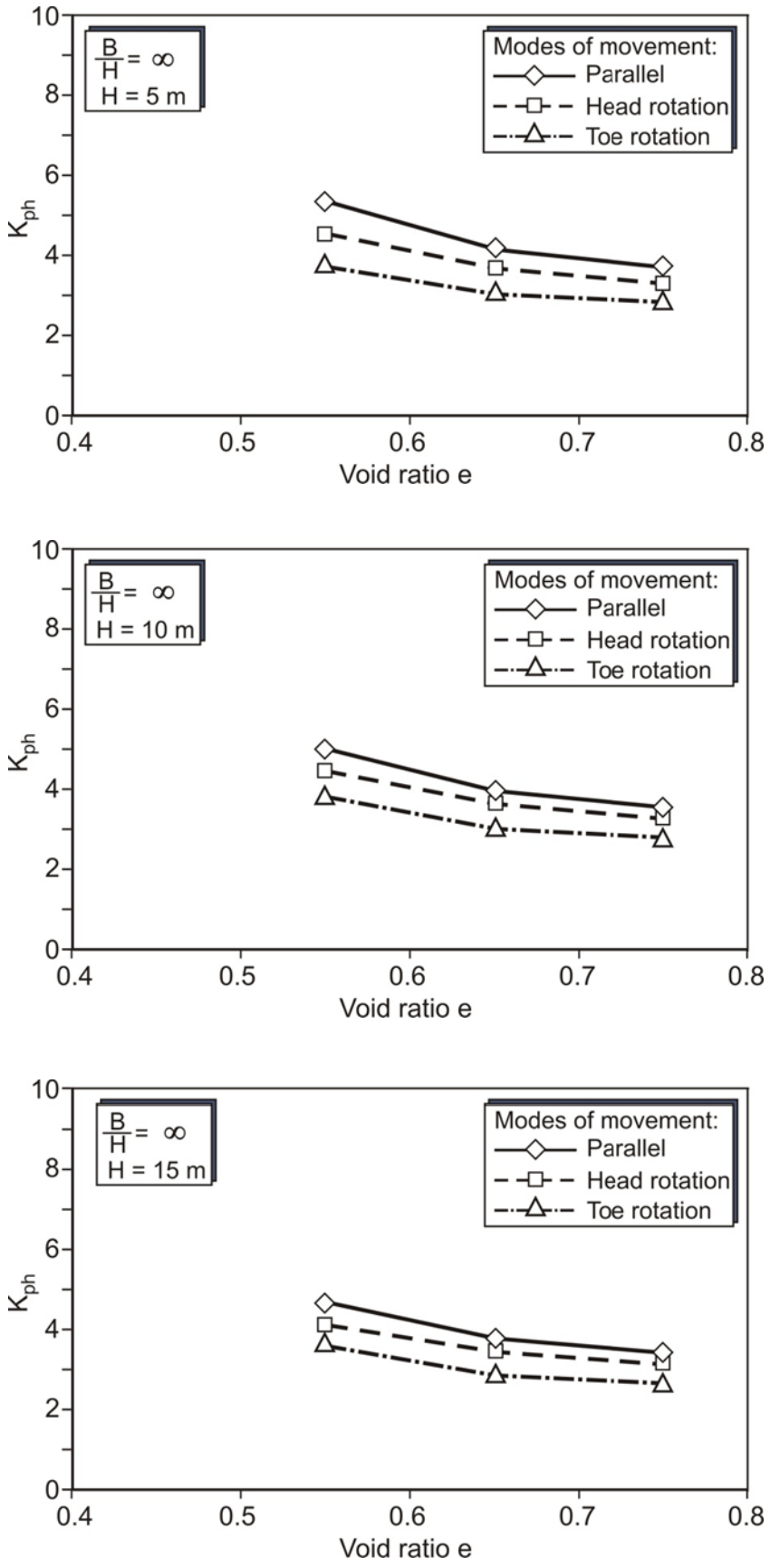

Figure 6-4: K_{ph} **as a function of the initial void ratio** e_0 **(n= ∞)**

It is observed in the Figures above that the passive earth pressure coefficient K_{ph} decreases non-linearly with increasing the void ratio e (which means decreasing the soil density) as it is to be expected. This is attributed to the fact that the denser the soil is, the greater is the soil shear strength. Another effect which is also shown in Figure 6-5 is the mode of movement effect. The value of the horizontal passive earth pressure coefficient K_{ph} at the peak has the highest value for parallel movement and the lowest one for rotation around the toe. The K_{ph} value for rotation around the top lies between the previously mentioned movement modes. This may be explained by the different failure mechanisms for the respective wall movement modes. The failure volume formed during parallel wall movement is greater than that formed during rotational movements. This is due to the upward movement of the wall bottom during rotation around the top which decreases the horizontal spread of the failure body and thus leads to limit its volume. During this mode of movement, the wall acts in a manner similar to jacking soil up with a fully embedded shovel. For rotation around the toe, the toe remains fixed. This means that full slip which is necessary to mobilize the ultimate shear strength is hindered in the soil near to the toe. The stresses are also smaller than the generated stresses for other modes of rotation.

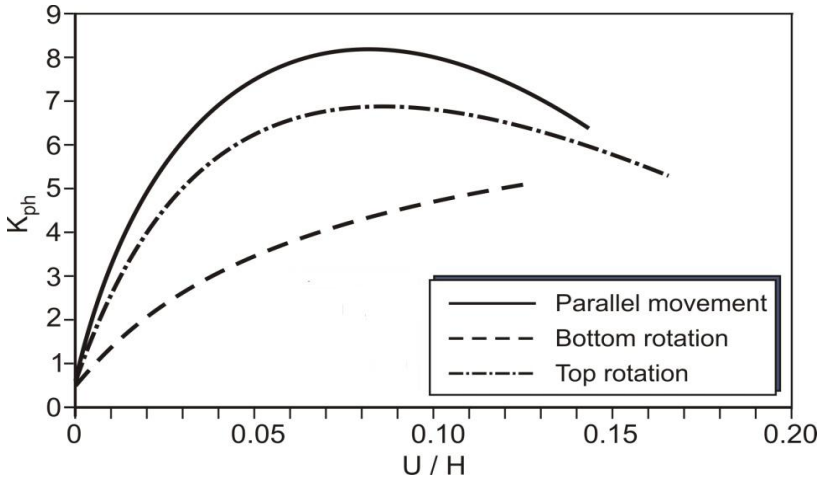

Figure 6-5: Passive earth pressure coefficient K_{ph} as function of the relative displacement by different modes of movement (n = 1, B = 10 m / H = 10 m, e_0 = 0.55)

Another effect is shown in Figure 6-5 which illustrates the curves for horizontal passive earth pressure coefficient as a function of relative displacement for different modes of movement. It is to be noticed that the mode of movement also affects the initial stiffness of the load – deflection curves. This in turn affects the value of the horizontal earth pressure coefficient at the peak state.

A comparison of top rotation and parallel movement mode can be done by illustrating the ratio of the respective earth pressure coefficients F_{top} as shown in Equation [6.1]:

$$F_{top} = \frac{K_{ph,top\,rot}}{K_{ph,par}} \qquad [6.1]$$

Figure 6-6 shows this ratio for all parameters variations considered in this study, i.e. for different spatial ratios, embedded wall heights and relative soil densities.

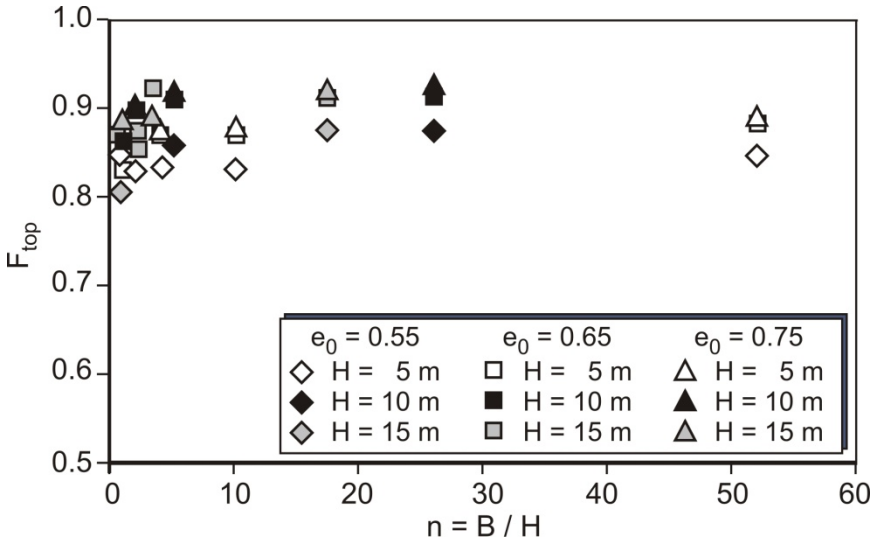

Figure 6-6: Factor F_{top} as a function of the spatial ratio n

All the numerically obtained values lie in a range between $F_{top} = 0.8$ and $F_{top} = 0.92$. Tendentially, the values are the smaller, the larger the relative density is, therefore, as a suitable approximation an average value of $F_{top} = 0.85$ can be used for all considered parameter calculations. According to Weissenbach's experimental results [91], the passive earth pressure coefficient K_{ph} for rotation around the top shows a constant percentage of about 85 % of the passive earth pressure coefficient K_{ph} for parallel movement. The thesis FEM results agree reasonably well with Weissenbach's experimental results [91]. On the contrary, according to German standard DIN 4085 [31], the passive earth pressure coefficient K_{ph} for rotation around the top shall be taken as 67 % of the passive earth pressure coefficient K_{ph} for parallel movement. According to the results presented here, the German standard DIN 4085 approach lies on the safe side for walls in sand soils.

No peak state occurs during rotation around the toe movement mode, so the value of the passive earth pressure coefficient was taken at $U_P = 20$ % of the embedded height as stated before. Although the K_{ph}-values given for this case are thus to a certain extent arbitrary, a comparison of toe rotation and parallel movement mode is done by illustrating the ratio of the respective earth pressure coefficients as shown in Equation [6.2].

$$F_{toe} = \frac{K_{ph,toe\,rot}}{K_{ph,par}} \qquad [6.2]$$

Figure 6-7 shows the ratio F_{toe} for all parameters variations considered in this study.

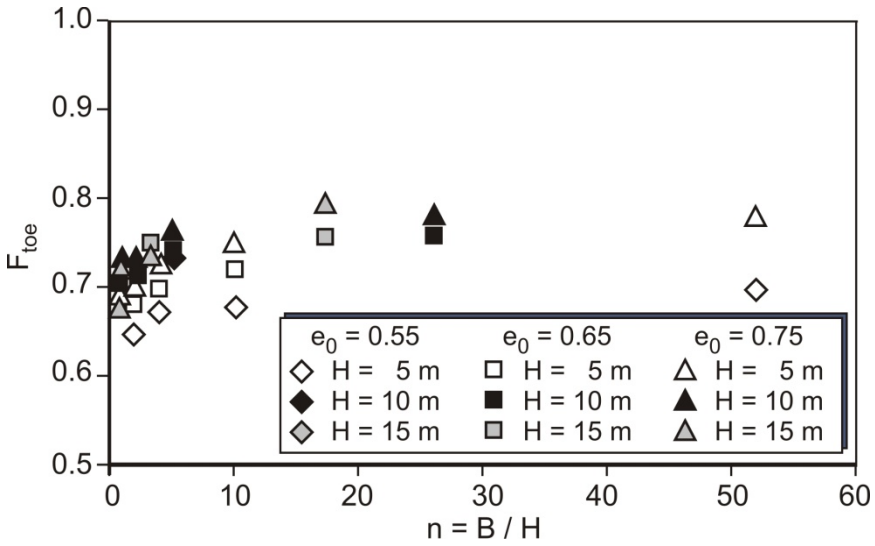

Figure 6-7: Factor F_{toe} as a function of the spatial ratio

All the values lie in a range between $F_{toe} = 0.64$ and $F_{toe} = 0.77$. According to German standard DIN 4085 [31], the passive earth pressure coefficient K_{ph} for rotation around the toe shall be taken between 50 % and 67 % of the passive earth pressure coefficient K_{ph} for parallel movement. The results presented here show that the German standard DIN 4085 approach lays also on the safe side for walls in sand soils. For the considered failure state, i.e. $U_p/H = 0.2$ and in most cases conservative value for F_{toe} would be $F_{toe} = 0.67$.

6.3 Displacement at peak

The magnitude of the required displacement to reach the peak is defined in the German Standard DIN4085 [31] for the 2D case as a function of the relative densities D and the mode of movement as shown in Equations [2.29] and [2.30] before. For the 3D case however, the relative displacement at the peak state is calculated as a function of the wall dimensions and the relative density as shown in Equations [2.79] and [2.80] before.

In this section, the FEM results for the relative displacement at the peak state in relation to the spatial ratio and mode of movement are analyzed. This also includes a comparison between the FEM results and the German Standard DIN4085 [31] approach for both 2D and 3D cases.

Figure 6-8 shows an increase of the relative displacement at peak state $\frac{U_P}{H}$ with decreasing the spatial ratio n. The greater the spatial ratio n is the smaller is the failure body volume relative to the wall dimensions. This in turn requires a greater magnitude for the relative displacement at peak $\frac{U_P}{H}$.

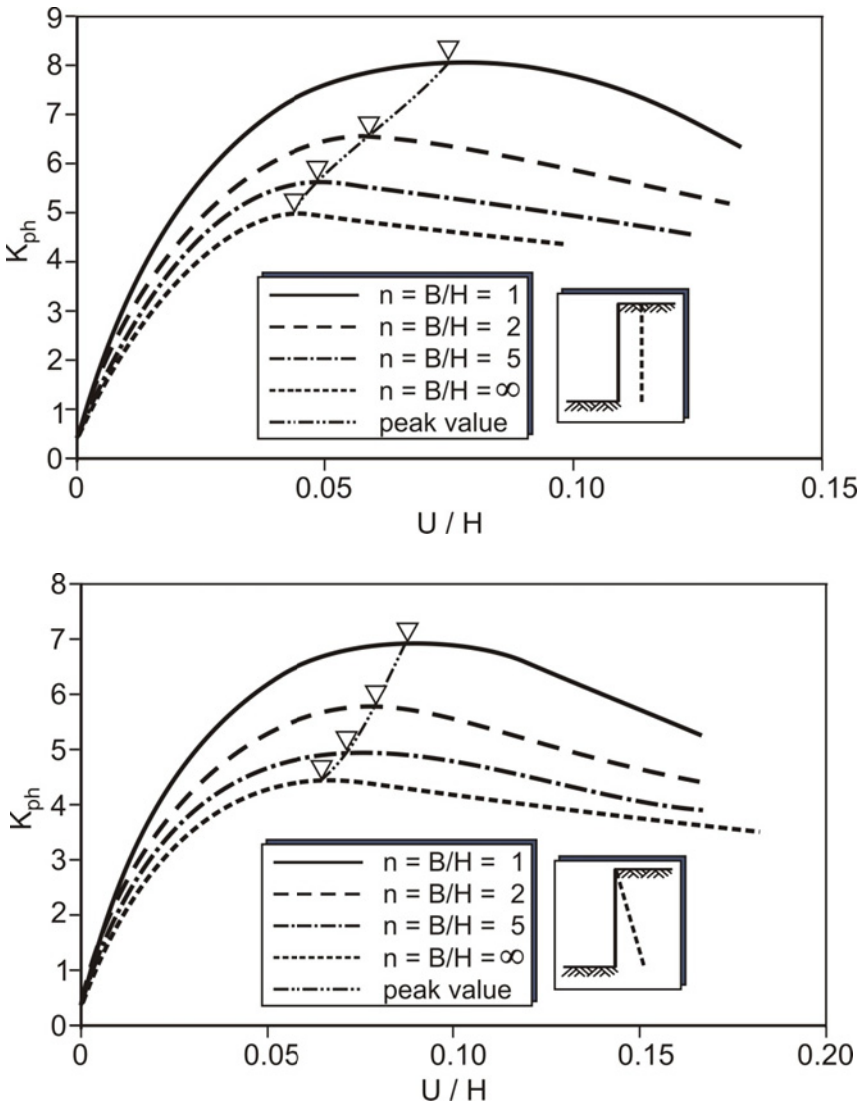

Figure 6-8: An illustration of relative peak displacement Up/H as a function of spatial ratio (H = 10 m, e_0 = 0.55)

Figure 6-9 shows a non-linear decrease for the relative displacement at peak by increasing the spatial ratio n for parallel movement. The curves exhibit a very sharp variation corresponding to smaller values of the spatial ratios (up to n = 5). Beyond this area the curves vary almost gradually. The denser the soil is, the smaller is the value of the relative peak displacement. Medium dense and loose sand require more movement to generate high shear strength.

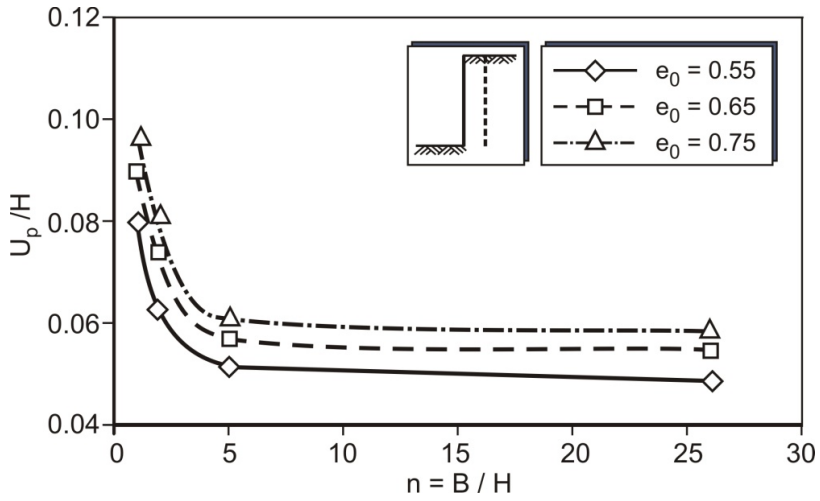

Figure 6-9: Relative displacement at the peak Up/H as a function of the spatial ratio n (H = 10 m)

The effect of the movement mode on the values of the relative peak displacement was studied by defining the ratio $F_{U\text{-}top}$ between the relative displacement at peak for both rotation around the top to its value by parallel movement as shown in Equation [6.3]:

$$F_{U-top} = \frac{U_{p,top\,rot}}{U_{p,par}} \qquad [6.3]$$

Figure 6-10 shows the ratio $F_{U\text{-}top}$ for all parameter variations considered in this study, i.e. for different spatial ratios, embedded wall heights and relative soil densities.

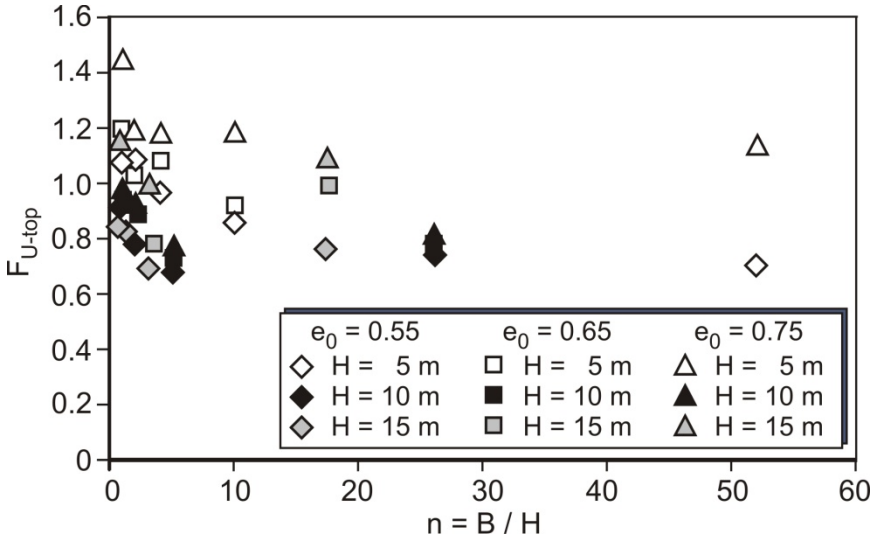

Figure 6-10: Factor $F_{U\text{-}top}$ as a function of the spatial ratio n

As shown in Figure 6-10, the peak by rotation around the top mode requires in most cases higher value of peak relative displacement than by parallel movement. This was expected due to the mechanism of the movement mode, that during a rotation around the top the maximum

displacement at peak occurs only at the toe of the wall. On the other hand Figure 6-10 shows also unexpected results in which the displacements for both parallel and top rotation modes are almost equal. The relative displacement at peak for parallel movement is in average about $0.8 - 1.2$ of its values for rotation around the top movement. As a suitable approximation an average range value of F_{top} = 0.9 - 1.1 can be used for all considered parameter calculations as shown in Equation [6.4]

$$(\frac{U_p}{H})_{par} = (0.9 - 1.1)\,(\frac{U_p}{H})_{topR} \qquad [6.4]$$

A comparison between the numerical results and the previously mentioned approach in German Standard DIN4085[31] was also made for both cases 2D and 3D.

The comparison for the 3D case is done using Equations [2.79] and [2.80] in German Standard DIN 4085-Blatt1 [31] for different soil densities and spatial ratios n. The relative displacement at peak state in German Standard DIN 4085 [31] Equations [2.79] for thin walls (n < 0.333) is a function of the relative density D and wall dimensions H and B. On the contrary in Equations [2.80] (n > 0.333), the relative displacement at peak state is a function of the relative density D and the wall embedded height H only.

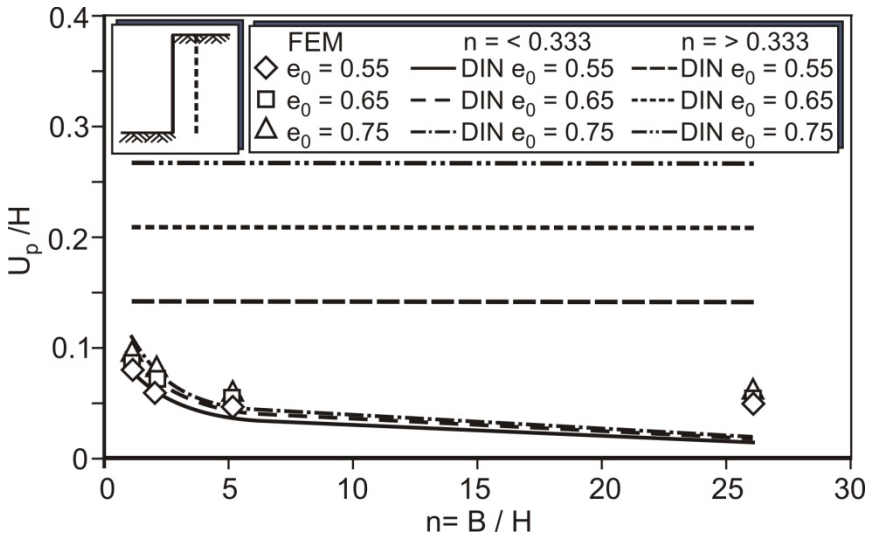

Figure 6-11: Comparison of relative displacement at peak Up/H (n = 1, H = 10 m) between FEM results and the German standard DIN4085

Figure 6-11 shows that the curves of FEM results and German Standard DIN 4085 [31] are very different. The results of the German standard Equation [2.86] for wide wall (n > 0.333) are higher than the FEM results and constant for different spatial ratio values n.

The German Standard Equation [2.79] for thin walls (n < 0.333) was used to compare the FEM results even for a spatial ratio n range > 0.333. The comparison shows a good agreement till a spatial value of almost n = 5 although that the approach is valid for n < 0.333 only. The denser the sand is, the better is the agreement. The results for other wall embedded heights H = 5 and 15 m are presented in the annex.

Figure 6-12 illustrates the relative displacement at peak in the 2D case as a function of the soil relative density for various embedded wall heights H = 5, 10 and 15 m for parallel and rotation around the top mode according to the FEM results and the German standard DIN 4085 Equations [2.29] and [2.30].

The relative displacement values using German standard DIN 4085 for top rotation at peak are smaller than the value for parallel movement, while in FEM the values with top rotation at peak are higher than its value for parallel movement. The result of the German standard for parallel movement agree very good with the FEM results for a wall of embedded height H = 5 m, but do not agree with the results for H = 10 and 15 m. It is here to be noticed that the scale effect is not considered in the German standard DIN 4085 [31].

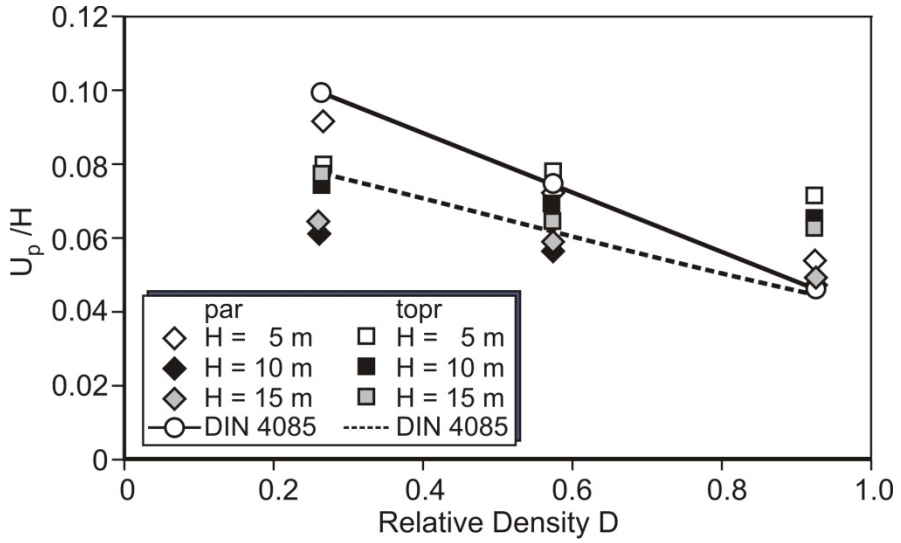

Figure 6-12: The relative displacement as a function of relative density according to the German standard DIN 4085 and FEM results (e_0 = 0.55, 2D case)

For a constant spatial ratio n, the relative displacement at peak $\frac{U_P}{H}$ decreases with increasing the wall dimensions as shown in Table 6-1. This is related to the failure body volume increase. This also confirms the effect of the scale effect on the magnitudes of the relative displacement at peak state for different spatial ratios n.

Table 6-1: Relative displacement as a function of the embedded depth H for (e_0 = 0.55) and spatial ratio n = 1 and n = 2.

n	H (m)	U_P/H
1	5	0.086
	10	0.08
	15	0.072
2	5	0.08
	10	0.063
	15	0.0613

In order to study the relative displacement at peak state in the spatial case in relation to the relative displacement in 2D case a factor ξ is defined as follows: $\xi = \frac{U_{p3D}}{U_{p2D}}$.

Figure 6-13 shows that the curve of ξ as a function of the spatial ratio n is independent of the soil density. The effect of the soil density on the relative peak displacement is included simultaneously in both 2D and 3D cases with the same magnitude, hence they cancel each other out. An analytical approach for factor ξ as a function of the spatial ratio n is obtained as shown in equation [6.5]:

$$\xi = \frac{U_{3D}}{U_{2D}} = 0.7 * (\frac{B}{H})^{-a} + 1 \qquad [6.5]$$

The approach shows a good agreement with the FEM results as shown in Figure 6-13.

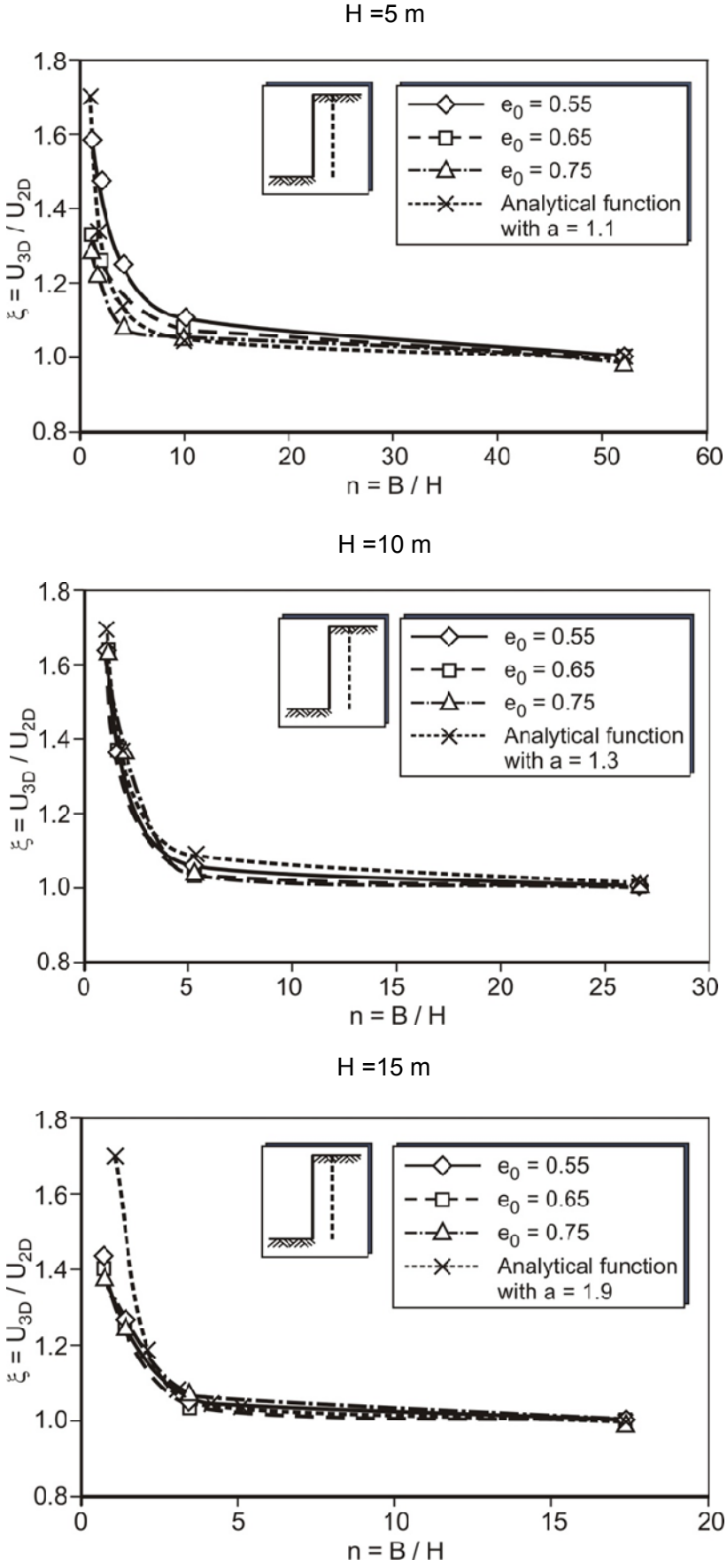

Figure 6-13: FEM results and analytical function of Equation [6.5] as function of spatial ratio n

The value of the exponent a is a function of the embedded height H and has to be varied as follows: a = 1.1 for H = 5 m , a = 1.3 for H = 10 m and a = 1.9 for H = 15 m.

6.4 Correction factor μ

Figure 6-14 and Figure 6-15 show the correction factor μ as a function of the spatial ratio for parallel and top rotation movement for different embedded heights (H = 5 m, 10 m and 15 m). It was observed that the curves are not affected by the variation of the embedded height H, implying that the scale effect disappears in the correction factor results. This is due to the fact that the effect of the embedded height on the correction factor μ is included simultaneously in both 2D and 3D cases with the same magnitude; hence they cancel each other out.

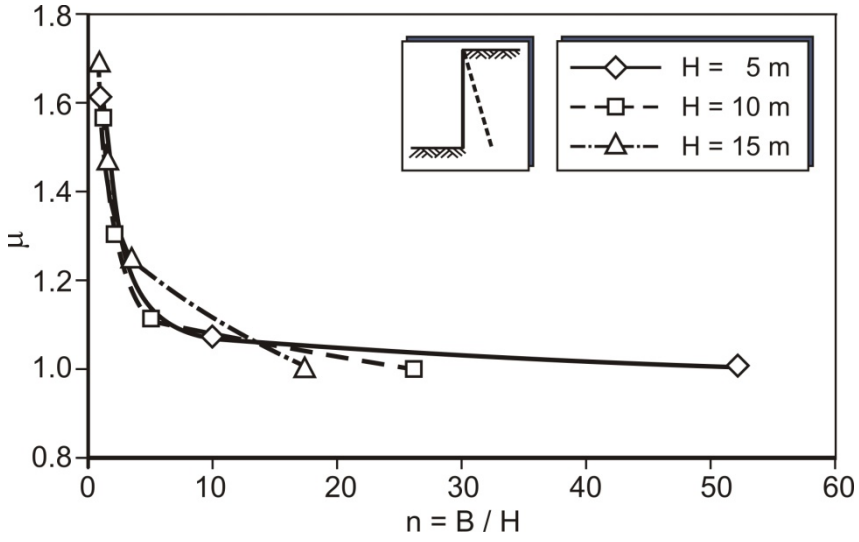

Figure 6-14: Correction factor μ as function of spatial ratio n (e_0 = 0.55) – rotation around top

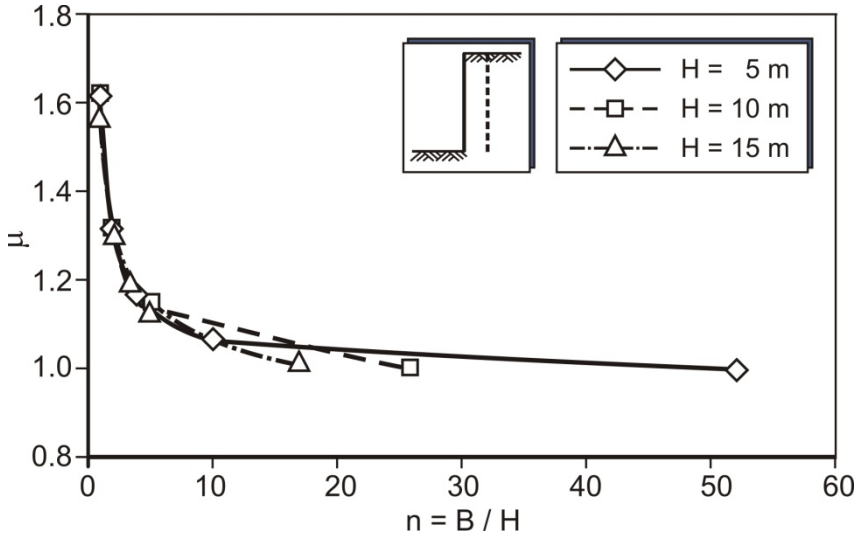

Figure 6-15: Correction factor μ as function of spatial ratio n (e_0 = 0.55) – parallel movement

The results in the previous section 5.5 showed that the 3D horizontal passive earth pressure coefficient K_{ph} increases with increasing the soil-wall interface friction angle δ. The shear strength between the wall and the soil is generated by using a wall with a friction angle δ. This causes a change of the stress conditions into the soil adjacent to the wall, which in turn leads to a non-linear failure surface.

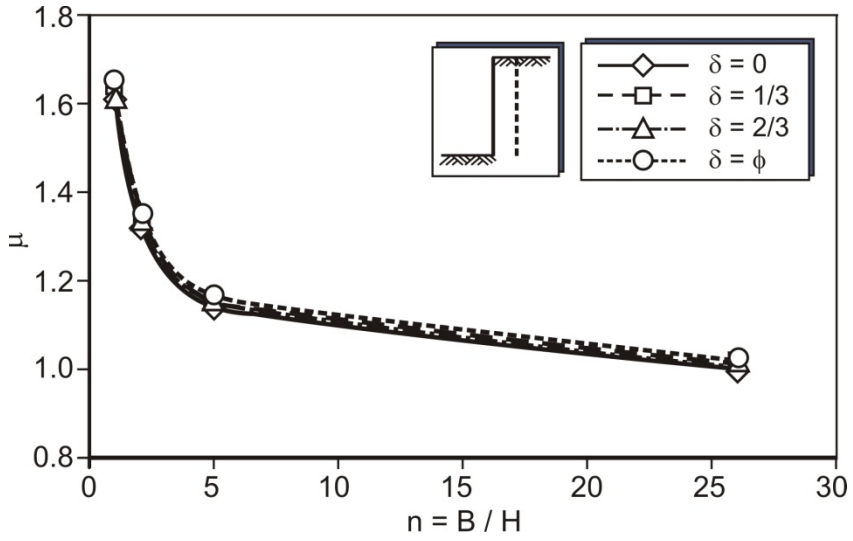

Figure 6-16: Correction factor μ as function of spatial ratio n (e_0 = 0.55, H = 10 m) for different wall friction angles – parallel movement

From Figure 6-16 it is evident that the soil-wall interface frictional angle increase has no effect on the correction factor μ. A possible explanation is that the effect of the wall friction angle δ is included in both 2D and 3D cases. The increase of the passive earth pressure coefficient K_{ph} is the same for both 2D and 3D cases and the effect thus disappears in the correction factor μ.

Figure 6-17 shows a comparison for the correction factor μ between the FEM results, Ramanso and Antäo [89] and the results of Benmebarek [7]. The curves show a good agreement with a small deviation in the spatial range (small values for n). It is to be noticed that by Ramanso and Antäo [89] and also by Benmebarek [7] different constitutive laws were used by them as shown in section 2.2.4 before. The curves refer to a good validity for the values of the correction factor μ by using FEM.

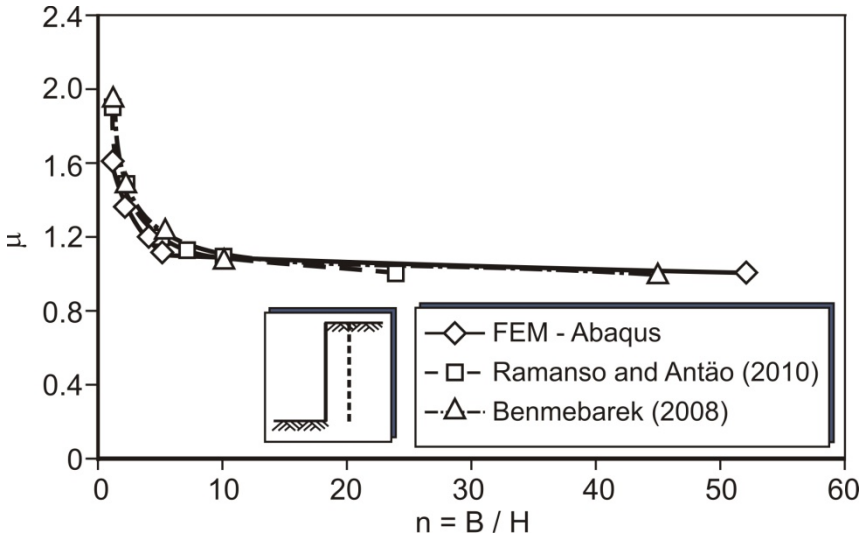

Figure 6-17: Correction factor μ by FEM-ABAQUS, Ramanso and Antäo [89] and by Benmebarek [7]

An analytical function f is obtained to simplify the calculation of the correction factor μ as a function of the spatial ratio n. Equation [6.11] was derived using the regression method on the FEM results with all soil densities.

$$\mu = D * (\frac{B}{H})^{-F} + 1 \qquad [6.11]$$

The constants D and F were varied as functions of the soil densities as shown in Figure 6-18

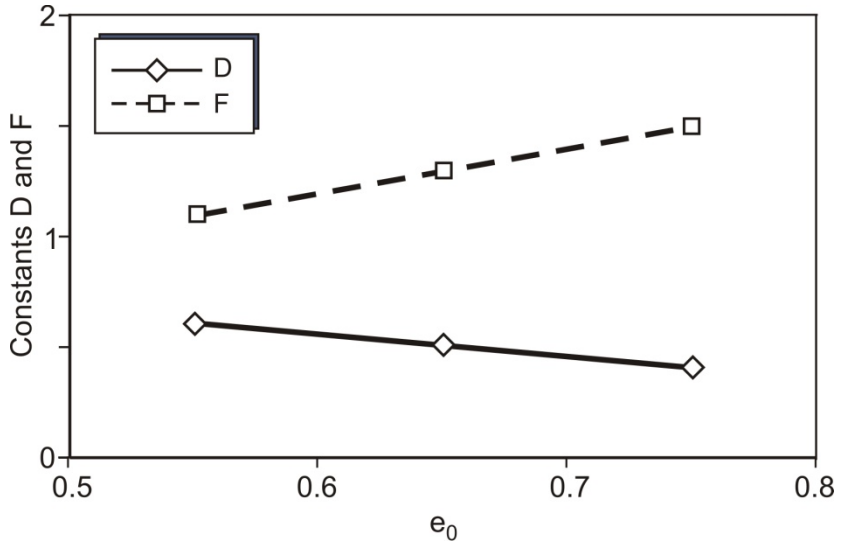

Figure 6-18: Constants D and F as function of the void ratio

The following equations were derived to calculate the value of both constants D and F

$$F = 2 * e_0 \qquad [6.12]$$

$$D = 0.99 * e_0 + 1.152 \quad [6.13]$$

The equations [6.12] and [6.13] were used to generate standardized values for the constant D as shown in Table 6-2 below.

Table 6-2: Values of the constants D and F for the correction factor function.

e_0	D	F
0.55	0.61	1.1
0.65	0.50	1.3
0.75	0.41	1.5

Figure 6-19 illustrates the curves of FEM results for different soil densities and the corresponding analytical functions.

The derived equation shows a very good agreement with the FEM analysis results for dense and medium dense sand with a small deviation in the values for loose sand as shown in Figure 6-19. It can be used for different soil-wall friction angles δ and different wall dimensions. This simplifies the calculation of the spatial earth pressure coefficient using the 2D case as a reference.

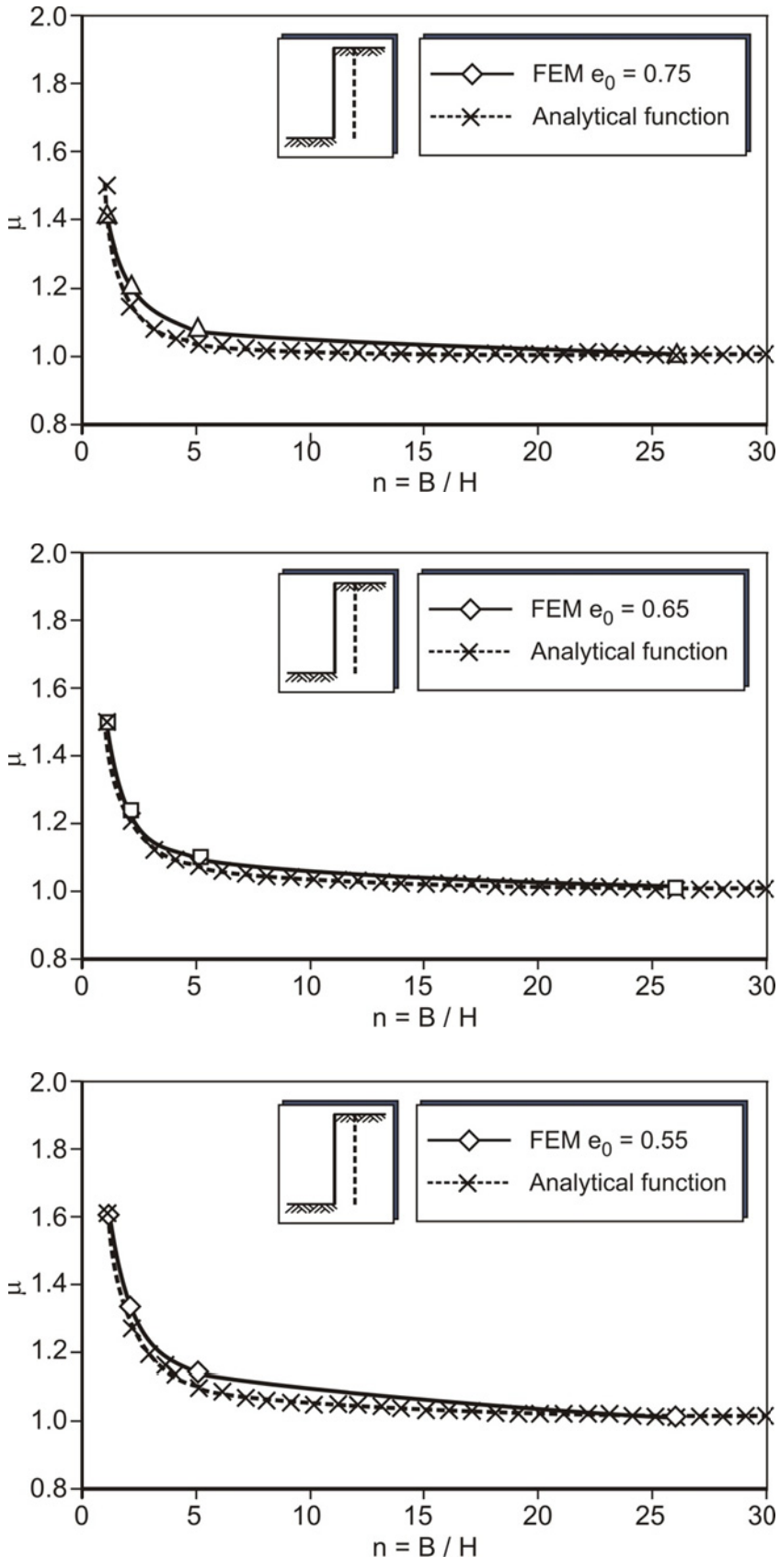

Figure 6-19: Correction factor μ as function of spatial ratio n for FEM results and analytical function of Equation [6.11] (H=10m)

6.5 The scale effect

Previous studies showed that for the 2D case, the earth pressure coefficient is a function of the wall embedded depth. The larger the embedded depth, the smaller is the earth pressure coefficient. Abdel-Rahman [1] found by using the hypoplasticity constitutive law that the earth pressure coefficient is affected by the stress level which is not included in Mohr-Coulomb's theory. Hypoplasticity constitutive law is adopted in the most of modeling to study the scale effect problem. This is due to the fact that hypoplasticity includes the scale effect by the dependency of the friction angle on the stress level, which means shear strengths of the soil are functions of the stresses considering the non-linearity in the shear strength envelope which affects the mobilization friction angle value. The scale effect is also expected in the spatial case in relation to the spatial ratio n. It appears by varying the wall dimensions B and H with a constant spatial ratio (n = constant) as shown in Figure 6-20.

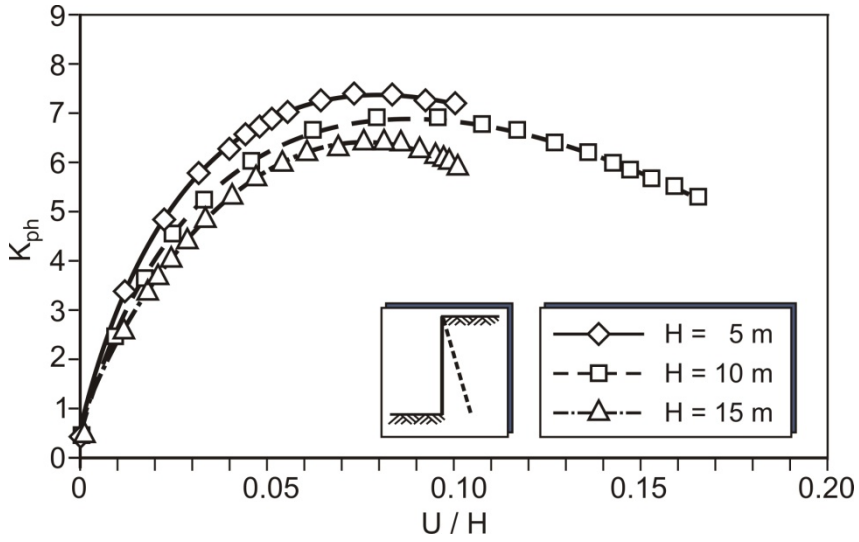

Figure 6-20: Passive earth pressure coefficient K_{ph} as function of the relative displacement for different wall dimensions (n = 1, e_0 = 0.55)

Figure 6-20 above shows the results of the passive earth pressure coefficient in rotation around the top for walls with a constant spatial ratio n = 1 and various embedded heights H = 5.0 m, 10.0 m and 15.0 m. It is to be noticed that the earth pressure coefficient K_{ph} decreases with increasing the wall dimensions for a constant spatial ratio n. A clear distinction between the curves is observed after a certain relative displacement. The difference between the curves increases by increasing the relative displacement till it reaches its maximum value at the peak.

For a further study of the scale effect problem the results of the passive earth pressure are illustrated as a function of the embedded height H. The results are shown in Figure 6-21and Figure 6-22 for different spatial ratios n and void ratios e_0.

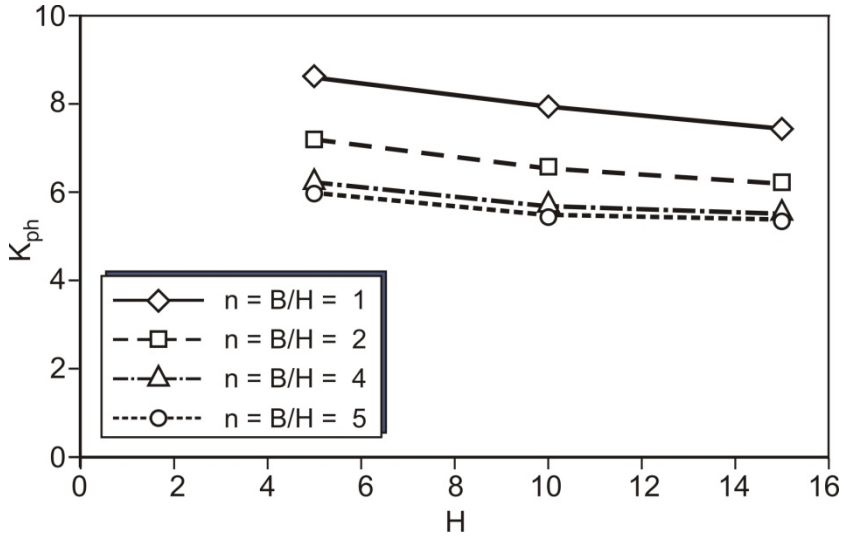

Figure 6-21: Passive earth pressure coefficient K_{ph} as function of the embedded height H (e_0=0.55)

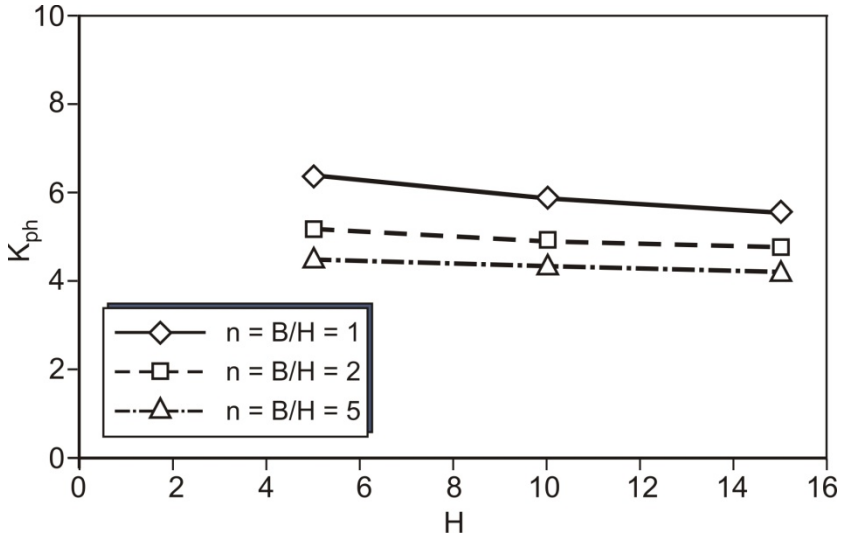

Figure 6-22: Passive earth pressure coefficient K_{ph} as function of the embedded height H (e_0=0.65)

The curves show a decrease of the passive earth pressure coefficient K_{ph} with increasing the embedded height H. The passive earth pressure coefficient decreases almost steadily according to the scale effect for different spatial ratios n. A factor F_H is defined as in Equation [6.14] for a further study of this decrease:

$$F_H = \frac{K_{ph,H_1}}{K_{ph,H_2}} \qquad [6.14]$$

Where:

$K_{ph,H(1\text{-}2)}$ is the earth pressure coefficient corresponding to embedded heights H_1 and H_2, respectively

According to this definition the following values of the factor F_H were calculated for different embedded heights H=5m, 10m and 15m as follows $F_5=\frac{K_{ph,H=5m}}{K_{ph,H=10m}}$, $F_{15}=\frac{K_{ph,H=15m}}{K_{ph,H=10m}}$. The results are presented in Figure 6-23 as a function of the spatial ratio n for different soil densities.

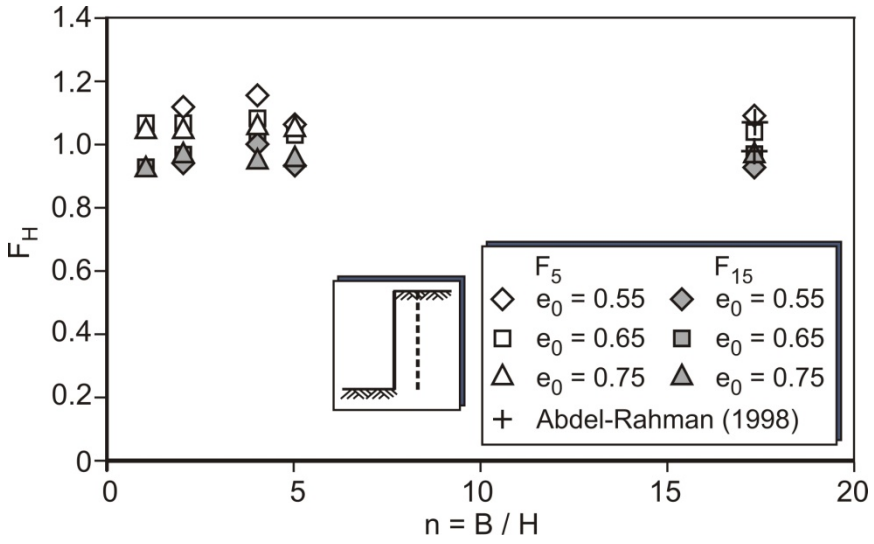

Figure 6-23: Factor F_H as function of the spatial ratio n (F_5, F_{15})

It is to be noticed that the results are almost centered about the value 1 and the passive earth pressure coefficient decreases steadily as a function of H which is also can be seen by Abed-Rahman in Figure 6-23 also as a scale effect by for the 2D case. This leads to an analytical function for the passive earth pressure K_{ph} in relation to the embedded height H as shown in Equation [6.15] below, which was obtained by using the regression method.

$$K_{ph} = J \cdot H^{(-G)} \qquad [6.15]$$

Where:

G and J constants related to the void ratio e_0 and spatial ratio n

Equation [6.15] is valid for a range of embedded height between 5 and 15 m, which is related to the range of the investigated wall dimensions in the analysis model. The values of constants G and J are illustrated in Table 6-3 as a function of e_0 for spatial ratios of n=1, 2 and 5 . The denser the soil, the higher is the value of both constants G and J. For a spatial ratio of larger than 4 till 2D case, it is possible to use the same values of J and G for n=5 because K_{ph} as a function of H is almost equal as shown in Figure 6-21 before.

The following Table 6-3 shows an example for a wall of n = 1 with different soil densities.

Table 6-3: The constants G and J as functions of the initial void ratio e_0.

B/H	e_0	G	J
1	0.55	10	0.1
	0.65	7.7	0.07
	0.75	6.3	0.06
2	0.55	8.1	0.09
	0.65	5.7	0.07
	0.75	5	0.065
5	0.55	6.5	0.07
	0.65	5	0.065
	0.75	5	0.065

A very good agreement between the curves resulting from the function and the curves resulting from the FEM results is obtained as shown in Figure 6-24 below:

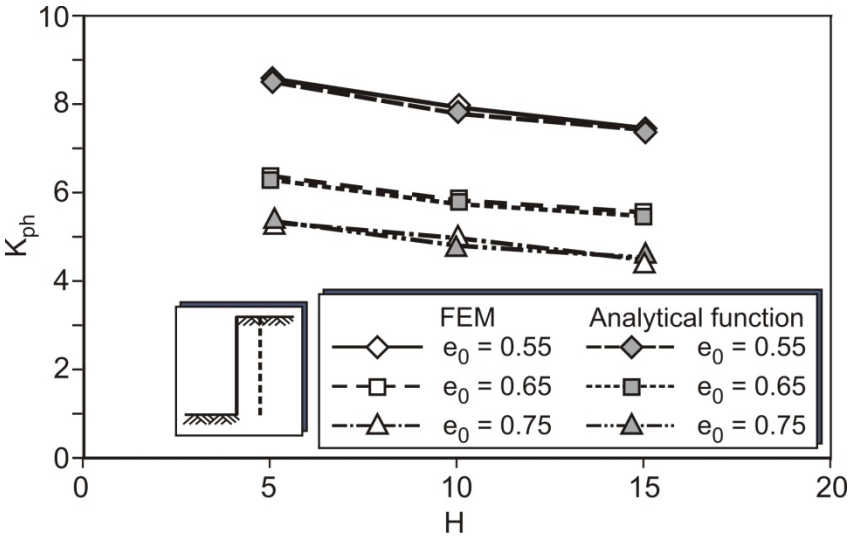

Figure 6-24: Passive earth pressure coefficient as function of the embedded depth H (FEM results and mobilized function, n = 1)

Further experiments and investigations are required to prove the validity of equation [6.15] for wall heights out of the previously mentioned range.

6.6 Mobilization function for the passive earth pressure

The earth pressure behind the wall increases during the development of the relative displacement i.e., the value of the generated earth pressure load E_{ph} is a function of the magnitude of the mobilized displacement U. To estimate the stress conditions and so the value of passive earth pressure during a construction movement, a mobilization approach for

the passive earth pressure coefficient as a function of the displacement is required. The analytical approach is obtained using regression method on the results of many parameter variations such as soil density and spatial ratio and was compared with the different modes of movement. Many researchers obtained similar equations using semi empirical relationships such as Weißenbach [91] and Bartl [4], which have also been used in the German standard DIN 4085 [31] for the 2D case. In most of the equations, the forms of the mobilization functions are similar to the curves described by the function of parabolic or circle quadrants. The previous methods in 2D were used to develop an analytical approach for K_{ph} as a function of the displacement ratio $\frac{U}{U_P}$. A reference dimensionless factor λ is defined as follows in Equation [6.6]:

$$\lambda = \frac{(K_{mob} - K_0)}{(K_{ph} - K_0)} \qquad [6.6]$$

Where:

K_{mob}: The mobilized passive earth pressure coefficient corresponding to the relative displacement $\frac{U}{H}$.

K_0: Passive earth pressure coefficient at rest

K_{ph}: The maximum spatial passive earth pressure at peak.

During the movement the value of K_{mob} increases from K_0 at the initial condition till a maximum value K_{ph} at the peak. The corresponding values of factor λ are (0) at the initial condition (corresponding to K_0) and (1) at the peak (corresponding to K_{ph}) as shown in Figure 6-25.

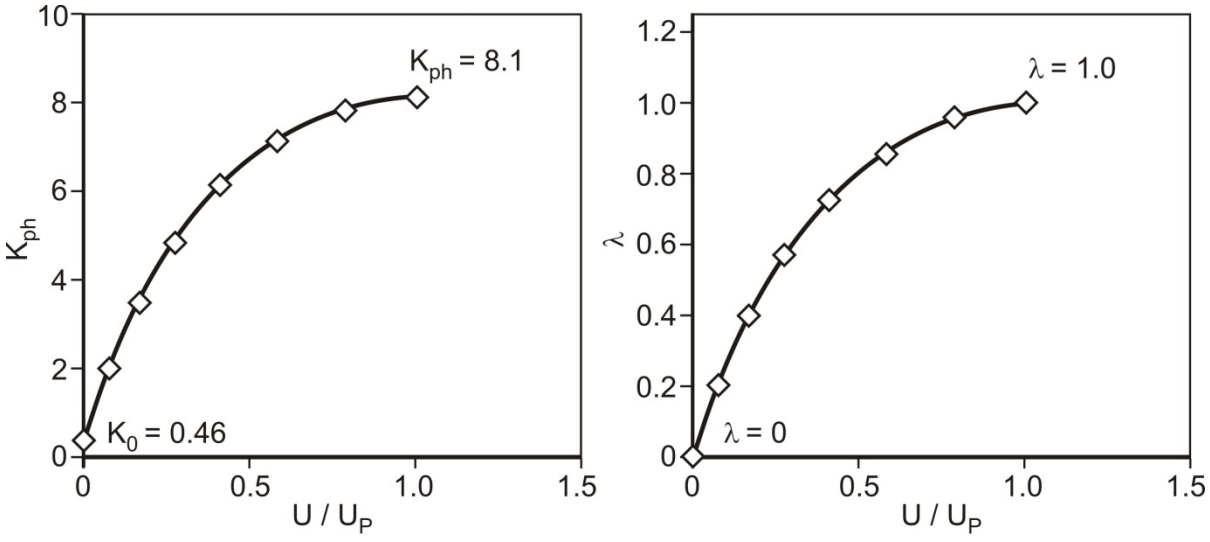

Figure 6-25: Factor λ and the passive earth pressure coefficient K_{ph} as a function of U/U_P (n=1, e_0=0.55)

Figure 6-26 and 6-27 show the value of factor λ as a function of U/U_p. It is to be noticed that the functions develop non-linearly during the displacement up to a maximum value equal to (1). Varying the spatial ratio or the soil density has the effect of distinguishing the curves from each other. The boundary curves are the curves which are corresponding to spatial ratios

n = 1 and n = ∞. All other curves for n = 2 and 5 are in between them. This means that the mobilization curve radius is a function of the soil density and the spatial ratio. By increase either of the spatial ratio n or the soil density, the mobilization curve radius decreases.

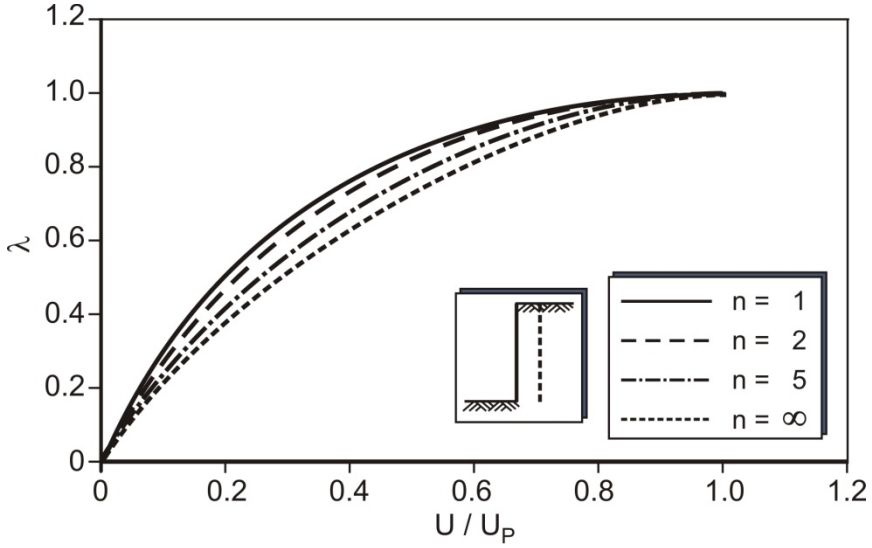

Figure 6-26: Factor λ as a function of U/U_p (n = 1, H = 10 m, e_0 = 0.55)

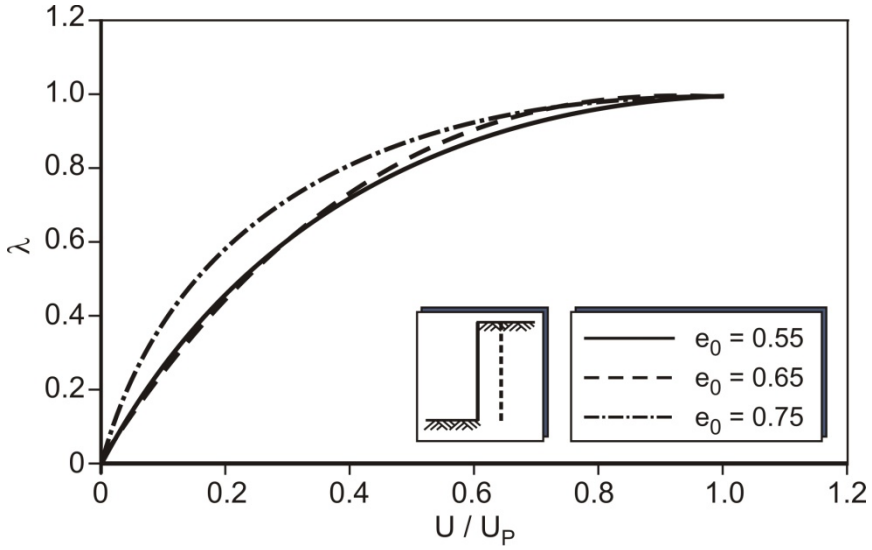

Figure 6-27: Factor λ as a function of U/U_p (n = 1, H = 10 m)

Figure 6-28 shows the courses of the functions λ for a constant spatial ratio (n = 1) with different wall dimensions B and H as a function of $\frac{U}{U_p}$ in dense sand. The curves are almost identical, which means that with regard to λ there is no scale effect.

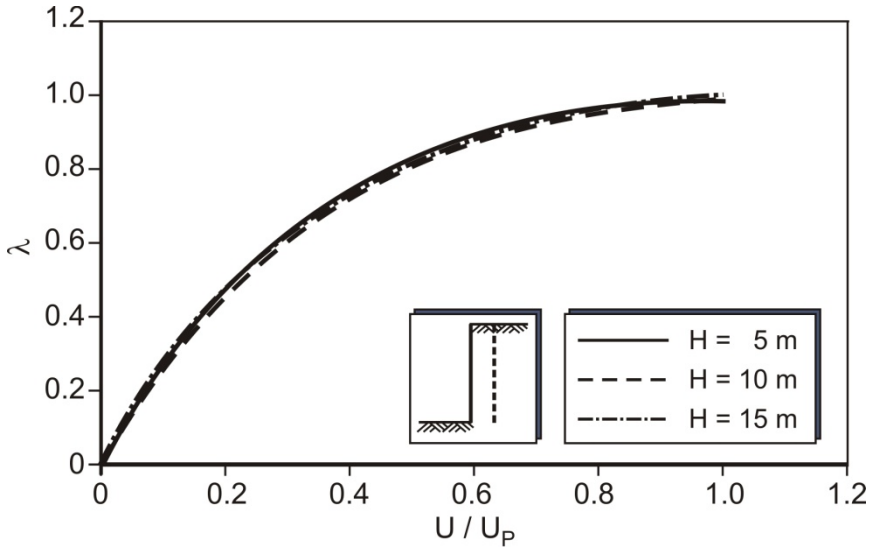

Figure 6-28: Factor λ as a function of U/U_p (n = 1, e_0 = 0.55) parallel movement

The function in Equation [6.7] for λ was obtained using regression methods for the FEM results.

$$\lambda = -e^{-A\left(\frac{U}{U_P}\right)} + 1 \qquad [6.7]$$

The constant A in equation [6.5] was obtained for the parallel movement mode with respect to the soil density and the spatial ratio n as shown in Figure 6-29.

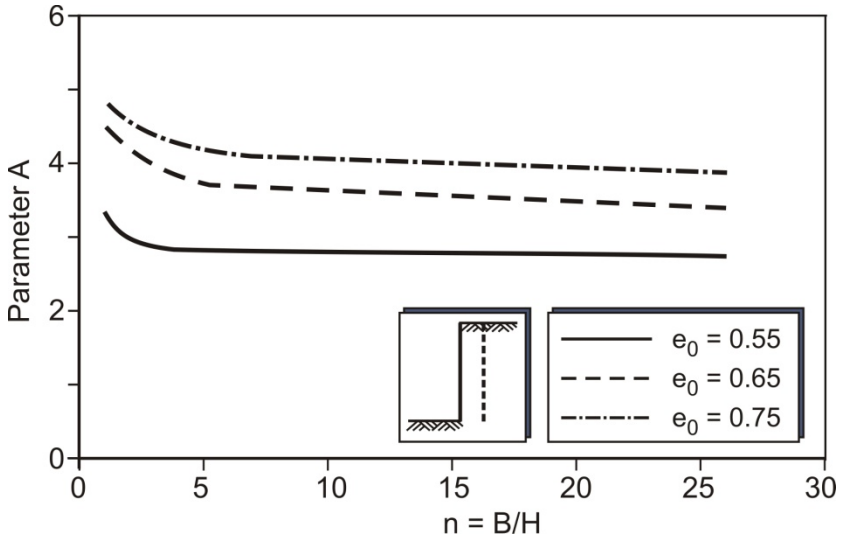

Figure 6-29: Calculated constant A as function of the spatial ratio n

The relation between the constant A and the spatial ratio n and initial void ratio e_0 is illustrated in the following equation:

$$A = K\left(\frac{B}{H}\right)^{-p} \qquad [6.8]$$

The parameters K and p were derived from the numerical simulation results which are presented in tables 6-4 and 6-5 below. For constant K it was found that it depends on the spatial ratio n and the initial void ratio e_0. The exponent p was found to depend only on e_0.

Table 6-4: Constant K for different spatial ratios (parallel movement)

B/H	Dense Sand (e_0=0.55)	Medium dense (e_0=0.65)	Loose Sand (e_0=0.75)
1	3.21	4.47	4.75
2	3.09	4.20	4.53
5	2.93	3.87	4.24
26	2.67	3.33	3.78

Table 6-5: The value of the exponent p depends on the void ratio e_0.

e_0	0.55	0.65	0.75
Power p	0.057	0.09	0.07

Figure 6-30 shows a comparison between the above derived mobilization function and the FEM results

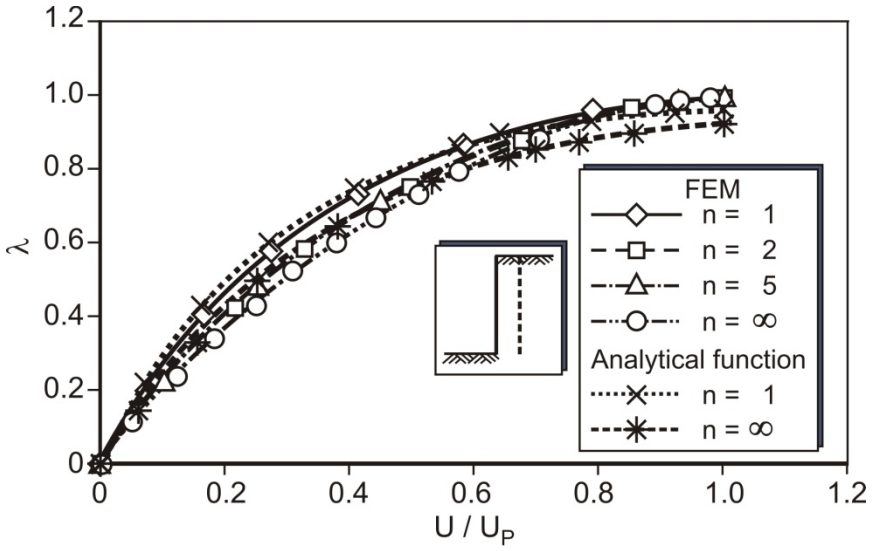

Figure 6-30: Factor λ as a function of U/Up from FEM results and from the analytical function of Equation [6.7] (e_0 = 0.55)

The curves show a good agreement between the FEM results and the function f in equation [6.7] till about 70 % of U/U_p, after which a small neglected difference occurs. This means that the function is in a good agreement at least to the serviceability limit state.

Interpolation should be done for other soil densities using Table 6-4 and 6-5 or Figure 6-29 to calculate the value of the constant A.

Neuberg [56] obtained a mobilization function for the spatial passive earth pressure as shown in section 2.2.4 before. For a further verifying of the analytical model a comparison between the FEM results, the function of approval in equation [6.7] and the mobilization function of Neuberg is done as shown in Figure 6-31.

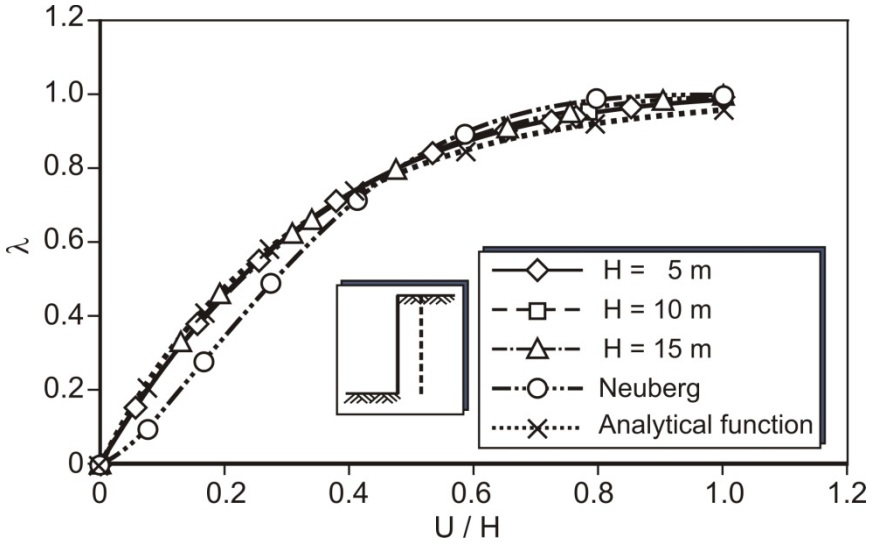

Figure 6-31: Factor λ as a function of U/U_p from FEM results, after Neuberg and from the analytical function ($e_0 = 0.55$)

However function l did not agree well with Neuberg's mobilization function. The curves distinct from each other obviously especially in the service limit range. It is observed that Neuberg's mobilization function alters its direction from convex to concave while the other curves including the analytical function f remain concave.

The same study is also made for the rotation around the top in order to proof the validity of the analytical function for other modes of movement. The distributions of the FEM result curves in the form of λ and U/U_p for the rotation around the top are similar to the curves for the parallel movement as shown in Figure 6-32 and 6-33 below.

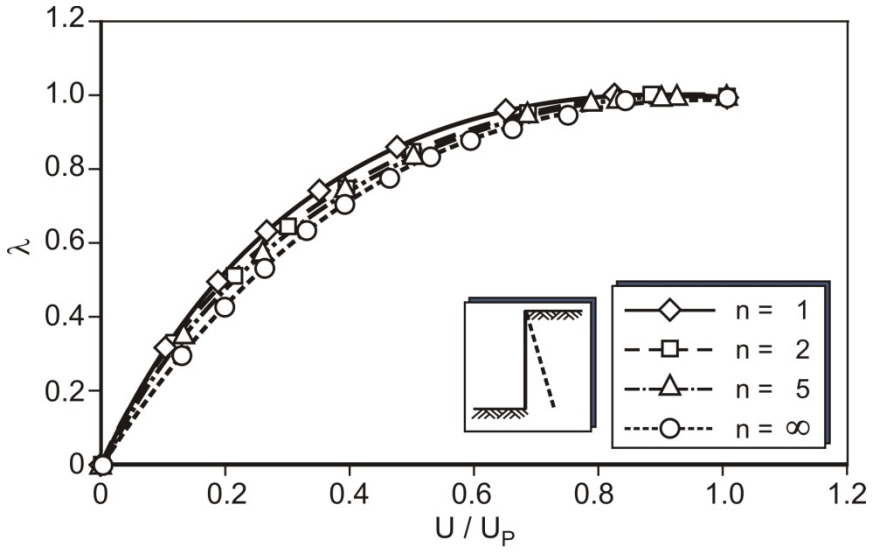

Figure 6-32: Factor λ as a function of U/U_p ($e_0 = 0.55$)

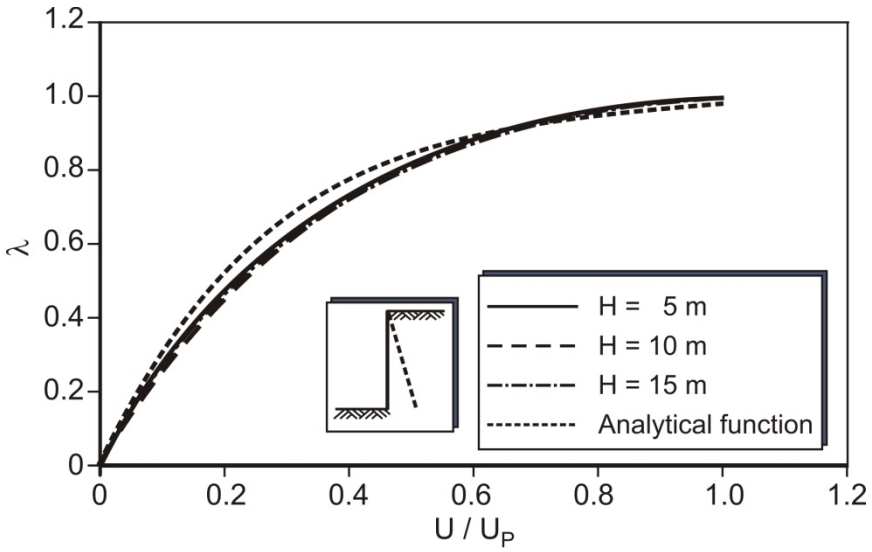

Figure 6-33: Factor λ as a function of U/U_p for FEM results and analytical function ($n = 1$, $e_0 = 0.55$)

The regression method was also used and the values of the constant K are illustrated in the following table

Table 6-6: Constants K by different spatial void ratio (rotation around the top)

B/H	Dense Sand (e_0=0.55)	Medium dense (e_0=0.65)	Loose Sand (e_0=0.75)
1	3.7	4	4.3
2	3.5	3.9	4
5	3.4	3.7	3.9
26	3	3.4	3.57

The constant A can be calculated using Equation [6.8] with the same values of exponent p as shown in Table 6-5 before.

The following Figure shows a comparison between the FEM results and the analytical function for rotation around the top in a range of n between n = 1 and n = 2D.

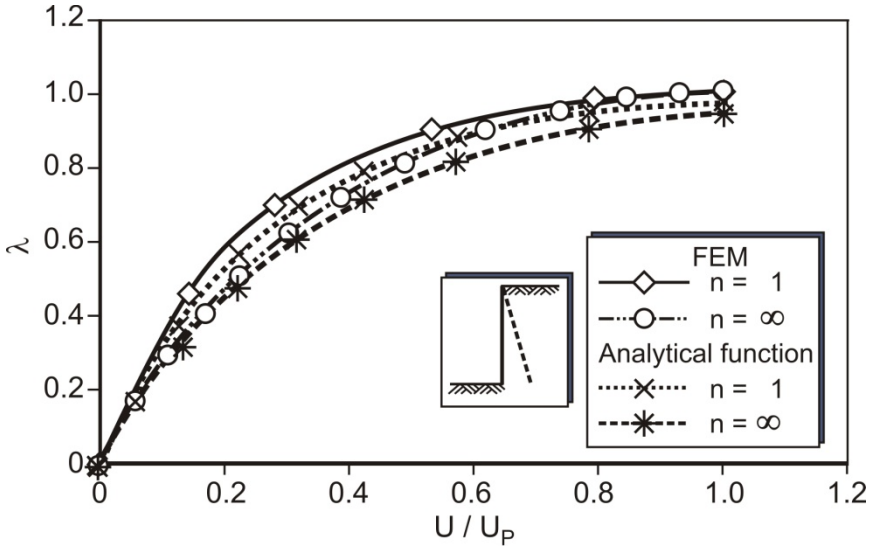

Figure 6-34: Factor λ as a function of U/U_p from FEM results and the analytical function ($e_0 = 0.55$)

The curves show a good agreement up to a value of almost $U/U_p = 0.5$ which is in the serviceability limit state range.

The results of factor λ for rotation around the toe are illustrated in the following Figure 6-35 and in Figure 6-36 below:

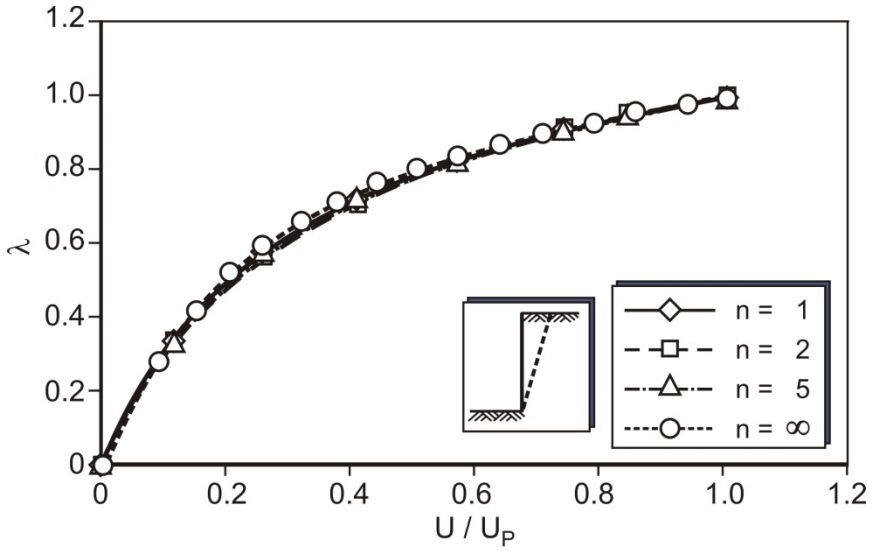

Figure 6-35: Factor λ as a function of U/U_p ($e_0 = 0.55$)

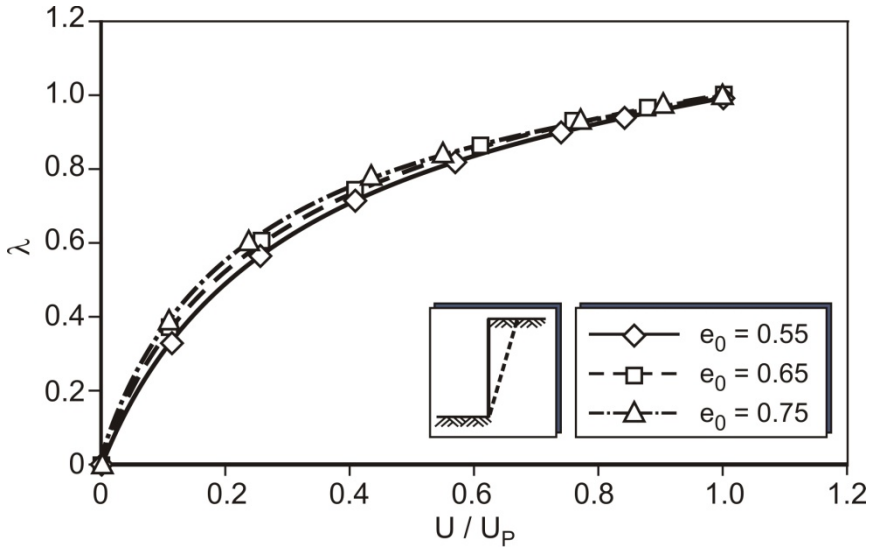

Figure 6-36: Factor λ as a function of U/U_p (H = 10 m, n = 1)

The Figures show new results in which the courses of the functions λ are independent from the spatial ratio or the soil density which is contrary to the results of the parallel movement or rotation around the top. This is due to the mechanism of the movement in which no failure body is formed. The analytical function can also be used for toe rotation mode with a constant value of A=3. The results of FEM toe rotation and the analytical function are illustrated in Figure 6-37.

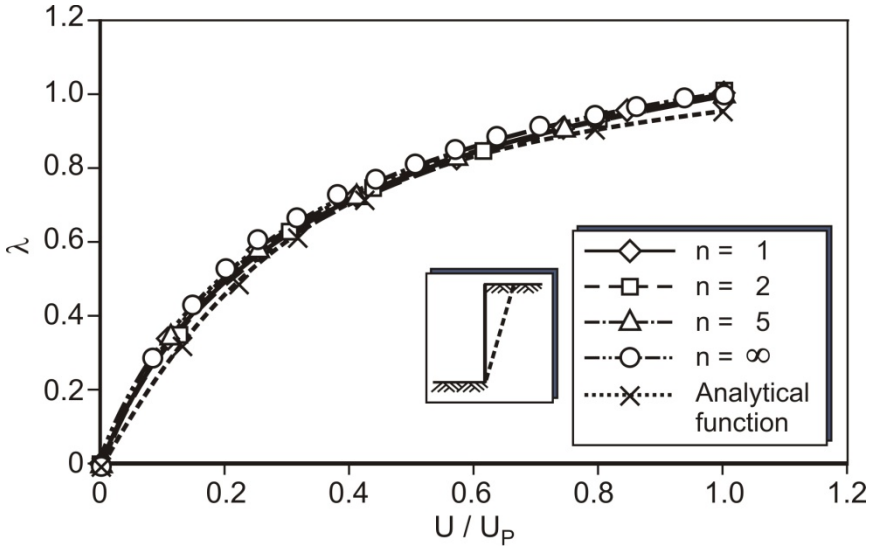

Figure 6-37: Factor λ as a function of U/Up for FEM results and analytical function (Factor A = 3, e_0 = 0.55)

The curves show a good agreement between the FEM results and the analytical function for different values of spatial ratio n. It must be always refer by rotation around the toe to that no peak is formed and the value for K_{ph} or μ is taken by U/H = 0.22 which maybe the reason behind the absence (humility) of the spatial ratio effect by this type of movement.

7 Summary and Conclusion

The consideration of passive earth pressure is a basic problem in geotechnical engineering tasks like design of retaining walls, bridge abutments, foundations or anchor walls. Although most practical problems can be treated by assuming plane strain (2D) conditions, the necessity of consideration of spatial passive earth pressure often occurs.

Relatively few research works has been carried out yet to investigate the spatial or 3D case. The focus of the thesis in hand lies on the magnitude of ultimate spatial passive earth pressure and on the load-displacement relationships with respect to the 2D case. The passive earth pressure in sand acting on rigid walls under parallel translational movement, head rotation and toe rotation was determined by means of 3D finite element simulations. The hypoplastic material law, which is known to predict the complex stress-strain relations of soils rather well, was applied. Since this material law accounts for the stress-dependence of the soil's shear strength, also the scale effect, i.e. the dependence of earth pressure coefficients on the absolute dimensions of a wall, could be investigated.

The effect of spatiality was described by a correction factor μ defined as the ratio of the passive earth pressure coefficient for the spatial case and the coefficient for the 2D case:

$$\mu = \frac{K_{ph3D}}{K_{ph2D}}$$

The numerical results showed that the correction factor μ is of course dependent on the spatiality ratio n and also - but to a much lower degree - on the relative density of the sand soil. Instead, it was found that the wall friction angle as well as the absolute wall dimensions does not significantly affect the correction factors.

Neglecting the effect of the relative density or the initial void ratio e_0, respectively, the following equation valid for medium dense sand might be used to obtain an approximate μ-value for non-cohesive soils:

$$\mu = 1 + 0{,}5 \left(\frac{B}{H}\right)^{1{,}3}$$

μ-values for dense sand are slightly greater and μ-values for loose sand are slightly smaller than given above.

Regarding the deformation mode of the rigid wall, the simulation results confirmed that the greatest ultimate earth pressure occurs with parallel translational wall movement and the smallest with toe rotation. In the latter, even no peak state could be reached. Here a deformation limit was used to define the ultimate state; the passive earth pressure coefficient K_{ph} was calculated for a maximum displacement of 20 % of the wall height.

In the relations of the earth pressure coefficients for different movement modes no clear dependency on spatiality ratio and relative density could be identified. For top rotation, the

maximum passive earth pressure amounts between 80 and 92 % of the value for parallel movement. The use of an average correction factor of 0.85 might be suitable for practical cases. For toe rotation, the resultant earth pressure forces were between 64 and 77 % of the values for the parallel movement case. Thus, the use of a correction factor of 0.67 or 0.70 might be suitable.

The displacement U_p at which the maximum (ultimate) passive earth pressure is reached was found to be the greater, the smaller the spatiality ratio n is. For n = 1, peak displacements can be around 50 % larger than for the 2D case. However, for n-values larger than 5, the peak displacement is almost identical with the 2D value.

The dimensionless peak displacement U_p/H is of course strongly dependent on the relative density of the sand, like it is in the 2D case. A functional description of the ratio of the peak displacements in the 3D and the 2D case was derived from the numerical simulation results. The function parameters are dependent on the spatiality ratio n, but also on the absolute magnitude of the wall height (scale effect). It should be noted that the calculated peak displacements were considerably smaller than the peak displacement predicted by an equation given in DIN 4085. Thus, at least for the conditions considered in this study, the DIN approach lies on the safe side.

This conclusion is valid for the values of K_{ph} at peak while it is to be noticed that during the movement the value of K_{ph} as a function of U/H has to be taken into consideration.

To describe the mobilization of earth pressure resistance with increasing relative displacement U/U_p of the wall, functional mobilization approaches of the following form were derived for the three considered wall deformation modes:

$$\lambda = 1 - e^{-A\,(\frac{U}{U_p})}$$

For parallel movement and top rotation, the function parameter A was found to depend on the spatiality ratio n and on the relative density or initial void ratio, respectively. For toe rotation, no significant effect of n and e_0 was found, which means that a constant parameter A = 0.3 might be used in the function given above. The reason for this result might be that for toe rotation in all cases U_p = 0.2 H was used, since no peak state could be reached.

Finally, the effect of the absolute wall dimensions or the scale of the problem, respectively, was investigated by comparing results obtained for wall heights H of 5, 10 and 15 m. With regard to the earth pressure coefficients, it was found that for H=5m the coefficient is in average about 10 % greater than for H = 10 m. On the contrary, for H = 15 m the coefficients are in average around 10 % smaller than for H = 10 m. Similar deviations were reported by Abdel-Rahman (1999) [1] from 2D case simulations. This makes clear that in practice the angle of internal friction should be devised carefully in cases with large wall dimensions, since the scale effect mentioned above is usually not taken into account in practical calculation methods.

As mentioned above, the scale does not affect the correction factor μ. However, it was found that the relative peak displacement U_p/H decreases with increasing wall height. This shows that peak displacements measured in model tests should not be transferred linearly to the in situ scale.

It must be pointed out that an experimental proof of the general validity of the presented results is missing. Such experimental investigations are highly desirable. Moreover, other soil types including cohesive soils should be investigated numerically and experimentally in future.

Other aspects and research in the future are required. Some of these aspects can be:

- The contact pressure between the wall and the soil due to the stiffness of the soil-wall system for example earth pressure by flexible walls adjacent to dense sand.
- Developing of some calculating methods such as P-y method or the modulus of subgrade reaction method to be able to contain the calculation of the earth pressure against rigid walls (or walls with different rigidity).
- Calculating the earth pressure using FEM in different cases such as due to a surcharge load on the ground surface beside the wall, earth pressure by a retaining wall against a sloped ground surface soil and the effect of the ground pore water pressure on the earth pressure calculations.
- The spatial earth pressure coefficient under cycle or dynamic loads which requires experimental and numerical researches including a developing for some appropriate constitutive laws.

8 References

[1] Abdel-Rahman, K (1999): Numerische Untersuchungen von Maßstabseffekten beim Erddruck in Sand. Schriftenreihe des Lehrstuhls Baugrund-Grundbau der Universität Dortmund, Heft 23, Dortmund.

[2] AL-Diban, I. (2000): Das Tragverhalten horizontal belasteter, in nichtbindigem Boden eingespannter starrer Träger, in ebenem und geböschtem Gelände. Heft 7, Institut für Geotechnik, Technische Universität Dresden.

[3] AL-Jamal, A.; Wilson, P. (2010): Large-Scale Passive Earth Pressure Load-Displacement Tests and Numerical Simulation. ASCE Journal of Geotechnical and Geoenvironmental Engineering, Volume 136, Issue12, pp.1634-1643.

[4] Bartl, U. (1997): Zum Stand der Erddruckversuche. Heft 2, In Ohde-Kolloquium. Institute für Geotechnik, TU Dresden, pp. 67-87.

[5] Bartl, U.; Franke, D. (1997): Ergebnisse von Modellversuchen zur Untersuchung der Abhängigkeit des stützenden Erddrucks von Wandbewegungen. Heft 4, In Ohde-Kolloqium. Mitteilungen des Instiute für Geotechnik der TU Dresden, pp. 1-27.

[6] Belabdelouhab, F. (1988): Etude expérimentale de la butée discontinue sur modèle réduit. PhD thesis, Institut National des Sciences Appliquées de Lyon, France.

[7] Benmebarek, N.; Benmebarek, S.; Kastner, R.; Soubra, A. H. (2006): Passive and active earth pressures in the presence of groundwater flow. Géotechnique, The Institution of Civil Engineers, London 56 (3), pp. 149–158.

[8] Besler, D. (1997): Wirklichkeitsnahe Erfassung der Fußauflagerung und des Verformumgsverhaltens von gestützten Baugrubenwänden. Heft 22, Dissertation, Lehrstuhl Baugrund-Grundbau, Universität Dortmund.

[9] Besler, D. (1999): Verschiebungsgrößen bei der Mobilisierung des Erdwiderstandes von Sand. Bautechnik 72 (11), pp. 748-755

[10] Blum. H. (1932): Wirtschaftliche Dalbenformen und deren Berechnung. Bautechnik 10, pp. 50-55.

[11] Briaud, J.-L. (1992): Laboratory tests on sand deposit. The national geotechnical experimentation sites at Texas A&M University: unpublished, Texas A&M University USA

[12] Briaud, J.-L.; Chung, M. (1992): Behavior of a full scale tieback wall in sand. Publication of the Texas A&M University, USA.

[13] Briaud, J.L.; Lim, Y. (1999): Tieback Walls in Sand: Numerical Simulation and Design implications. ASCE Journal of Geotechnical and Geoenvironmental Engineering, Volume 25, Issue 2, pp.101-110

[14] Briaud, J.-L; Kim, N.K. (1994): Beam Column Method for Tieback Walls. Publication of the Texas A&M University USA

[15] Brinch Hansen, J.; (1953): Earth pressure calculation, Danish Technical Press, Copenhagen, Denmark.

[16] Brinch Hansen, J.; (1961): The ultimate resistance of rigid piles against tranvsversal forces. Bulletin No12, Danish Technical Press, Copenhagen, Denmark.

[17] Brinch Hansen, J.; (1966): Resistance of a rectangular anchor slab. Bull. No. 21, Danish Geotechnical Institute, Copenhagen.

[18] Brinch Hansen, J.; et al (1960): Hauptprobleme der Bodenmechanik. Berlin, Göttingen, Heidelberg, Springer- Verlag.

[19] Buchholz, W. (1931): Erdwiderstand auf Ankerplatten. Jahrbuch der Hafenbautechnischen Gesellschaft 1930/1931 , Berlin , Kap. 1.10 Erddruck Abschnitt 1.7.

[20] Caquot, A.; Kerisel, J. (1948): Tables for the calculation of passive pressure, active pressure and bearing capacity of foundations. Gauthier-Villars, Paris.

[21] Chen, W. F. (1975): Limit analysis and soil plasticity, Elsevier, Amsterdam.

[22] Ching, S. C. (1994): Discrete element analysis for active and passive distribution on retaining wall, Computers and Geotechnics, Volume 16, pp. 291-310.

[23] Christian J. T. et al (1977): Incremental plasticity analysis of frictional soils. International Journal for numerical and analytical methods in Geotechnics, volume 1, pp. 343-375.

[24] Clayton, C. R. I.; Milititsky, J.; Woods, R. I. (1986): Earth pressure and earth-retaining structures. Blackie Academic And Professional London, Glasgow, New York, Tokyo, Melbourne, Madras.

[25] Colling. C. (1962): Beitrag zur Berechnung freistehender, im Boden eingespannter Dalben. Heft 12, Die Bautechnik. Berlin, pp. 397-403.

[26] Coulomb, C. A. (1776): Essai sur une application des regles des maximas et minmas a quelques problemes de statique relatifs a l'architecture. Mem. Acad. Roy. Pres. Divers Savanta, Vol. 7, Paris.

[27] Douglas, D. J.; Davis, E. H. (1964): The movements of buried footings due to moment and horizontal load and the movement of anchor plates. Geotechnique, London, 14 (2), pp.115–132.

[28] Duncan, J. M., Mokwa, R. L. (2001): Passive earth pressure: theories and tests. J. Geotech. ASCE *tests*, Geoenviron. Engng 127, No. 3, 248-257. 2

[29] Duncan, J. M.; Chin Y.C. (1970): Nonlinear analysis of stress and strain in soils, Journal of soil mechanics and foundations division. Proceedings of the American Society of Civil Engineers, SM5, pp. 1629-1951.

[30] Fang, Y. S; Chen, J. M.; Chen, C.Y. (1997): Earth pressure with sloping backfill. Geotechnical and einviromental eingineering journal, 123(3), pp. 250-259.

[31] German Standard DIN 4085 (Germany, 1987, 2007, Blatt 1und 2), Calculation of earth-pressure, Normenausschuss Bauweisen, DIN Deutsches Institut für Normung e.V. Beuth Verlag GmbH, Berlin.

[32] Graham. J. (1971): Calculation of passive pressure in sand, Canadian Geotechnical Journal, 8, pp. 566–578.

[33] Griffiths, D. V. (1981): Computation of strain softening behavior. in Desai C. S. and Saxena S. K. (eds), Implementation Engineering, BAND 2, pp. 591-603.

[34] Griffiths, D. V. (2008): Reliability of passive earth preaaure. Georisk, Vol.2, pp. 113-121.

[35] Gussmann, P et al (1990): Beiträge zur Anwendung der KEM : Erddruck, Grundbruch, Standsicherheit von Böschungen. Mitteilung 32, IGS Institut für Geotechnik, Unversität Stuttgart.

[36] Gussmann, P. (1986): Die Methode der kinematischen Elemente. Mitteilung 32, Baugrundinstitut, Unversität Stuttgart.

[37] Herle, I. (1997): Hypoplastizität und Granulometrie von Kornge-rüsten, Heft 142, Instituts für Bodenmechanik und Felsmechanik der Universität Karlsruhe.

[38] Herle, I.; Gudehus, G. (1999): Determination of a hypoplastic constitutive model from properties of grain assemblies. Mechanics of Cohesive-frictional Materials, 4: pp. 461-486.

[39] Horn, A. (1970): Sohlreibung und räumlicher Erdwiderstand bei massiven Gründungen in nichtbindigem Boden. Schriftenreihe Straßenbau und Straßenverkehrstechnik 110, Bonn

[40] James, R. G.; Bransby, P. L. (1970): Experimental and theoretical investigations of a passive earth pressure problem. Géotechniques, 20(1), pp. 17-37.

[41] Johnson, E. G. (1953): The effects of Restraining Boundaries of the passive resistance of sand. Master thesis, Department of civil engineering, Princeton, New Jersey.

[42] Jung , S. (2007): Nichtlinearer horizontaler Bettungsmodulansatz für Trägerbohl-wände in mitteldicht gelagertem Sand. Heft12, Institut für Bodenmechanik und Grundbau, Technischen Universität Kaiserslautern.

[43] Kärcher, K. (1968): Erdwiderstand vor schmalen Druckflächen. Bautechnik 45(1), pp. 31.

[44] Kärcher, K. (1972): Erdwiderstand bei Bohlenwänden in bindigen Böden. Bautechnik 49, pp. 264.

[45] Kérisel, J., Absi, E. (1990): Tables de poussée et de butée des terres. 3rd ed. Presses de l'École Nationale des Ponts et Chaussées, Paris.

[46] Kolymbas, D. (2000): Introduction to hypoplasticity. Advances in Geotechnical Engineering and Tunnelling, Puplished by A.A.Ballkema, Rotterdam.

[47] Laumans, H. (1977): Verhalten einer ebenen im Sand eingespannten Wwand bei nichtlinearen Stoffeigenschaften des Bodens. Heft 7, Dissertation, Baugrundinstitut, Universität Stuttgart.

[48] Mao, P. (1993): Erdwiderstand von Sand in Abhängigkeit von Wandbewegungsart und Sättigungsgrad. Heft 16, Dissertation, Fachgebietes Baugrund–Brandbau, Universität Dortmund.

[49] Martin G. R.; Nad Yan, L. (1995): Modelling passive earth pressure for bridge abutments. presented at ASCE Conference, San Diego, California.

[50] Meksaouine, M. (1993): Etude expérimentale et théorique de la poussée passive sur pieux rigides. PhD thesis, Institut National des Sciences Appliquées de Lyon, France.

[51] Merifield, R. S. (2003): Three-Dimensional Lower Bound Solutions for Stability of Plate Anchors in Clay. Journal of Geotechnical and Geoenvironmental Engineering, Vol. 129, No. 3, pp. 243-253.

[52] Meyerhof, G. G. (1973): Uplift resistance of inclined anchors and piles. Proc., 8th Int. Conf., Soil Mechanics and Foundation Engineering, Moscow, Volume2, pp. 167–172.

[53] Michael, A.; Herle, I.; Günter, H. (2005): Numerical investigation of the spatial passive earth pressure. Institute of Geotechnical Engineering, Technische Universität Dresden.

[54] Nakai, T. (1985): Finite element computations for active and passive earth pressure, problems of retaining wall- soils and foundations, vol. 25, no3, pp. 98-112.

[55] Narain, J; Saran, S.; Nandakumaran, P. (1969): Model study of passive pressure in sand. Journal of the soil mechanics and Foundations. Division, ASCE, 95(sm 4), pp. 969-983.

[56] Neuberg, C. (2002): Ein Verfahren zur Berechnung des räumlichen Erddruckes vor parallel verschobenen Trägern. Heft 11, Institut für Geotechnik, Technische Universität Dresden.

[57] ÖNorm B 4434. (1993) Erd- und Grundbau – Erddruckberechnung, Austrian Standards plus GmbH, Wien.

[58] Ovesen, N. K. (1964): Anchor slabs, calculation methods and model tests. Bull. No. 16, Danish Geotechnical Institute, Copenhagen, pp. 5–39.

[59] Paul, O. (1965): Der räumliche Erdwiderstand vor eingespannten Masten. Institut für Geotechnik TU Dresden.

[60] Potts, D. M.; Burland, J. B. (1983): A numerical investigation of the retaining walls of the Bell Common Tunnel, Supplementary report 783, Crowthorne, Transport and Road Research Laboratory.

[61] Potts, D. M.; Fourie, A. B. (1984): The behaviour of a propped retaining wall: results of a numerical experiment, Geotechnique 34 (3), pp. 383–404.

[62] Potts, D. M.; Fourie, A. B. (1985): The effect of wall stiffness on the behaviour of a propped retaining wall, Geotechnique 35 (3), pp. 347–52.

[63] Potts, D. M.; Fourie, A. B. (1986): A numerical study of the effects of wall deformation on earth pressures, Int. J. Numer. Anal Methods Geomech., 10 (3) pp. 383–405.

[64] Potts, D. M.; Knights, M. C. (1985): Finite element techniques for preliminary assessment of a cut and cover tunnel. Tunnelling ’85, The Institute of Mining and Metallurgy, pp. 83–92.

[65] Bellina, C. (1998): Modellversuche zum räumlichen passiven Erddruck. Diplomarbeit Nr. 213 Institut für Geotechnik, Universität für Bodenkultur, Wien.

[66] Josef, S. (1998): Zentrifugen-Modellversuche zum räumlichen passiven Erddruck. Diplomarbeit Nr. 219 Institut für Geotechnik, Universität für Bodenkultur, Wien.

[67] Rahardjo, H.; Fredlund, D. G. (1984): General limit equilibrium method for lateral earth forces. Can. Geotech. J. 21, No. 1, pp. 166–175.

[68] Rankine, W. J. M. (1857): On the stability of loose earth. Philosophical Transactions of the Royal Society, Volume 147, pp. 9–27.

[69] Rauh, R. (1991): Beitrag zum Tragverhalten horizontal belasteter, im nichtbindigen Boden eingespannter Wandsysteme unter Berücksichtigung einer Böschungsgeometrie. Heft 1, Dissertation, Fachbereich Bautechnik, Bergische Universität GH-Wuppertal.

[70] Rowe, R. K. (1978): Soil structure interaction analysis and its application to the prediction of anchor behavior. PhD thesis, Univ. of Sydney, Sydney, Australia.

[71] Rowe, R. K.; Davis, E. H. (1982): The behavior of anchor plates in clay. Geotechnique, Volume 32, Issue 1, pp. 9–23.

[72] Rowe, R.W. (1951): Cantilever sheet piling in Cohesionless Soil. Engineering, 7. Pp. 316-319.

[73] Rowe, R.W.; Peaker, K. (1965): Passive earth pressure measurement. Geotechnique, Volume 15, Issue 1, 57-78.

[74] Schanz, T. (1998): Zur Modellierung des mechanischen Verhaltens von Reibungsmaterialien. Mitteilung 45, Institut für Geotechnik, Universität Stuttgart.

[75] Schweiger, H. F. (1994): On the use of drucker-prager failure criteria for earth pressure problems, Computers and Geotechnics Volume 16, Issue 3, pp. 223-246.

[76] Shamsabadi, A.; Rollins, K.; Kapuskar, M. (2007): Nonlinear soilabutment-bridge structure interaction for seismic performance-baseddesign. Geotech. Geoenviron. Eng. 133 6, pp. 707–720.

[77] Shiau, J. S., et al (2008): Finite element limit analysis of passive earth resistance in cohesionless soils. Japanes Geotechnical Society volume 48, No.6, pp. 843-850.

[78] Sokolovski, V.V. (1960): Statics of Soil Media, Butterworth, London.

[79] Sokolovski, V.V. (1965): Statics of granular media. Pergamon Press, Oxford.

[80] Soubra, A.-H. & Macuh, B. (2002): Active and passive earthpressure coefficients by a kinematical approach. Proc. Instn Civ. Engrs Geotech. Engng 155, No. 2, 119–131.

[81] Terzaghi, K. (1941): General wedge theory of earth pressure. ASCE Trans., 106, pp. 68–80.

[82] Terzaghi, K. (1943): Theoretical soil mechanics, Wiley, New York.

[83] Terzaghi, K., Peck, R. B.; Mezri, G. (1996): Soil mechanics in engineering practice, 3rd Ed., Wiley, New York.

[84] Terzaghi, K.; Peck, R. B. (1967): Soil mechanics in engineering practice, 2nd Ed., Wiley, New York.

[85] Terzaghi, K.; Peck, R. B.; Mezri, G. (1996): Soil mechanics in engineering practice, 3rd Ed., Wiley, New York.

[86] tom Wörden, F. (2010): Untersuchungen zum räumlichen aktiven Erddruck auf starre vertikale Bauteile im nichtbindigen Boden. Heft 68, Institut für Grundbau, Bodenmechanik und Energiewasserbau Leibniz Unversität Hannover.

[87] Ugai, K. (1991): Lateral Earth Pressure Problems Based On Simple Constitutive Equations for Granular Materials, Computer Methods and Advances in Geomechanics, pp. 527-532.

[88] Vermeer, P.A., Neher, N. (1997): "Bemessung von Baugruben in weichen Böden", Heft 41, Mitteilungen des Instituts für Geotechnik, Universität Stuttgart.

[89] Vicente, M.; Silva, D.; Armando, N; Anteao, A. N.; Nuno, C. G. (2007): Nimerical implementation of the kinematical theorem: Application to the determination of 3D passiv earth pressures of cohesionsless soils. IX Internatinal Conference on Computational Plasticity (COMPLAS IXE) , Department of Civil Engineering, Faculty of Sciences and Technology, Universidad Nova de Lisboa.

[90] Vogt, N. (1984): Erdwiderstandesermittlung bei monotonen und wiederholten Wandbewegungen in Sand. Heft 22, Dissertation Baugrundinstitut, Universität Stuttgart.

[91] Weißenbach, A. (1961): Der Erdwiderstand vor schmalen Druckflächen. Mitt. Franzius Institut TH Hannover No. 19, p. 220.

[92] Weißenbach, A. (1975-1977): "Baugruben", Teil I-III, Berlin-München-Düsseldorf, Ernst & Sohn, Berlin.

[93] Weißenbach, A. (1983): "Beitrag zur Ermittlung des Erdwiderstandes", Bauingenieur 58, pp. 161-173.

[94] Weißenbach, A. (1994): Wirtschaftliche Gestaltung von Trägerbohlwänden als Baugrubenverkleidung im Wohnungsbau und erforderliche Maßnahmen zurVermeidung von Bauschäden durch Trägerbohlwand-Baugruben im Bereichbestehender Bebauung, Abschlussbericht, Bau- und Wohnungsforschung, Bauforschungsberichte, Frauenhofer IRB Verlag, Stuttgart.

[95] Weißenbach, A. (1995): Neue Erkenntnisse über mehrfach verankerte Ortbetonwände. Bautechnik 72 (12), pp. 780-799.

[96] Weißenbach, A. (2003): Empfehlungen des Arbeitskreises Baugruben der DGGT zur Anwendung des Bettungsmodulverfahrens und der Finite-Elemente-Methode. EB 102 (Entwurf), EB 103 (Entwurf), Bautechnik 80 (2), 75-80.

[97] Widulinski, L. (2011): Discrete simulations of shear zone patterning in sand in earth pressure problems of a retaining wall, Elsevier, International Journal of solids and structures 48, pp. 1191-1209.

[98] Wolffersdorf, P. A. (1992): Verformungsprognose für stützkonstruktionen. Institut für Bodenmechanik und Felsmechanik. Unversität Karlsruhe Heft 129, Habilitation.

[99] Wolffersdorf, P. A. (1996): A hypoplastic relation for granular materials with a predefined limit state surface. Mechanics of Cohesive-Frictional Materials, 1 (3), pp. 251-271.

[100] Zhou, J. (2011): Numerical simulation using finite element and earth pressure analysis on Double-row pile retaining structures. Advanced Material Researches Vol. 261-263, pp. 923-927.

[101] Zhu, D.; Lee, C. F. (2001): Active and passive critical slip fields for cohesionless soils and calculation of lateral earth pressures, Géotechnique, 51 (5), pp. 407-423.

[102] Ziegler, M. (1986): Berechnung des verschiebungsabhängigen Erddrucks von Sand Dissertation Institut für Bodenmechanik und Felsmechanik, Universität Karlsruhe Heft 101.

[103] Zweck, H. (1953): Erdwiderstand als räumliches Problem, Die Bautechnik. Berlin: Heft 7, pp. 189-193.

[104] Zweck, H. (1959): Die Berechnung verankerter Spundwände in nichtbindigen Böden nach Rowe, Mitteilungsblatt der Bundesanstalt für Wasserbau, Karlsruhe 1959, No. 13.

Annex: More results for the spatial passive earth pressure

Parallel movement

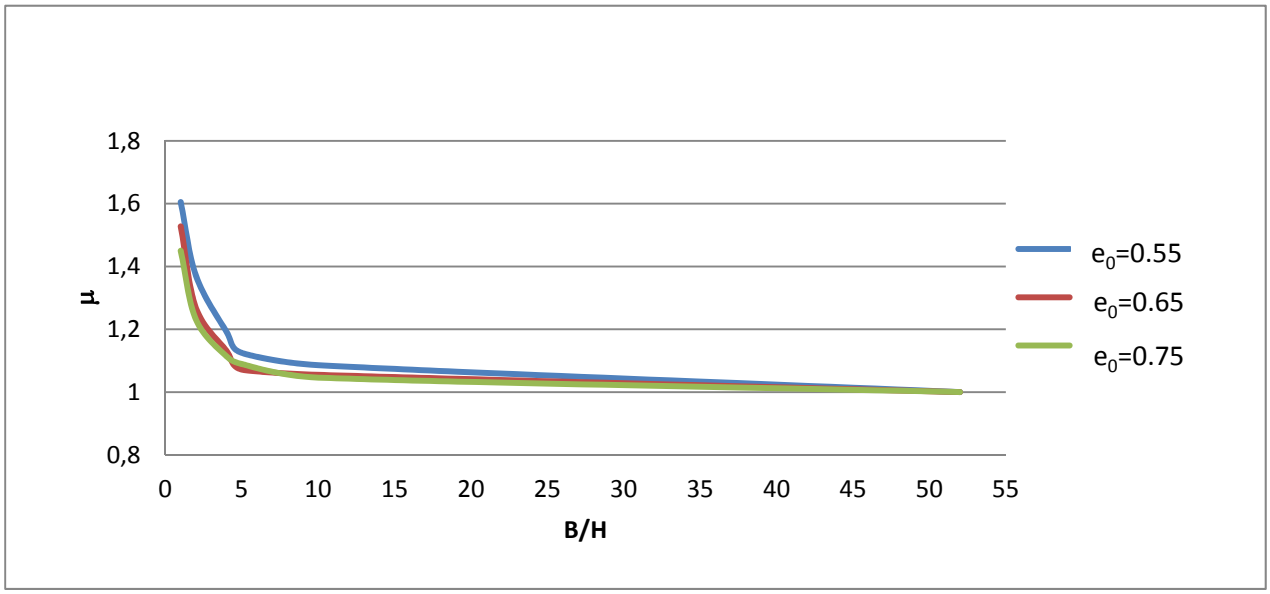

Figure A1: Correction factor μ as function of spatial ratio n (H = 5m)

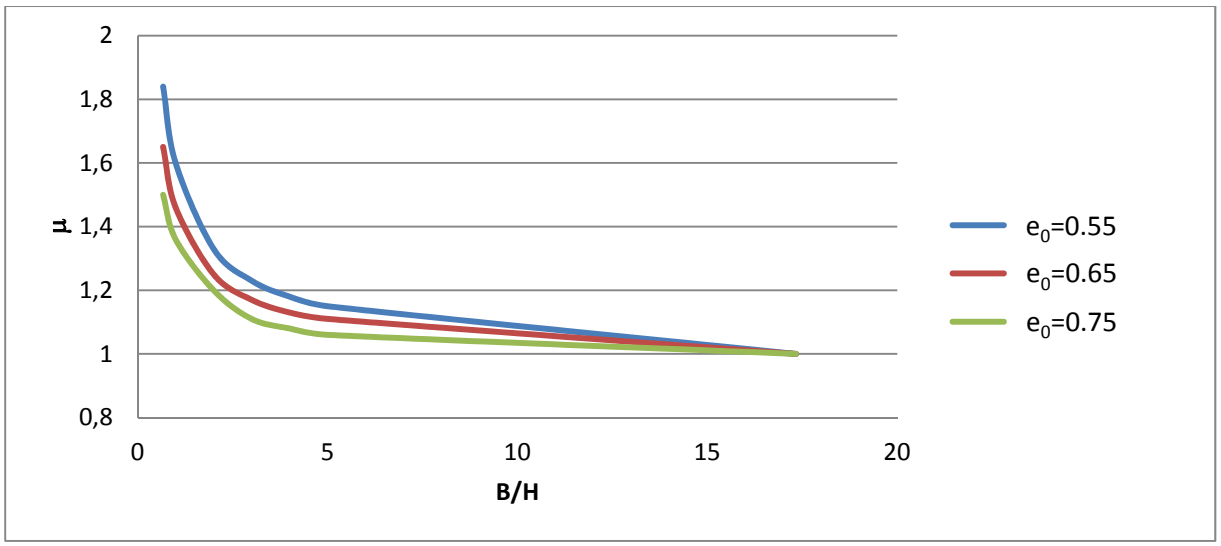

Figure A 2: Correction factor μ as function of spatial ratio n (H = 15m)

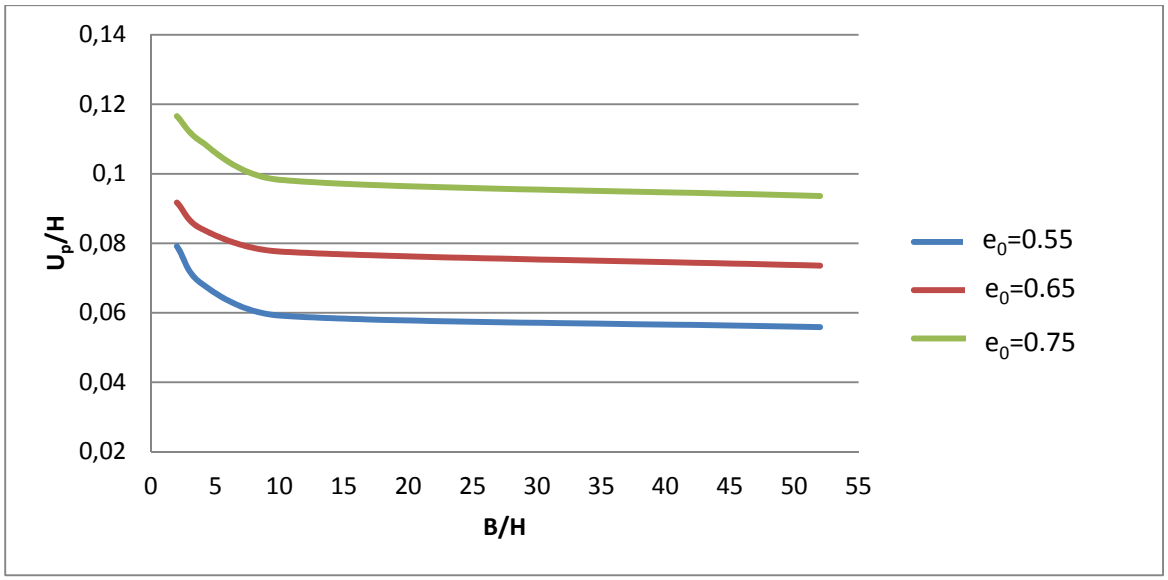

Figure A 3: **Relative displacement of the maximum value at the peak Up/H as a function of the spatial ratio n (H = 5 m)**

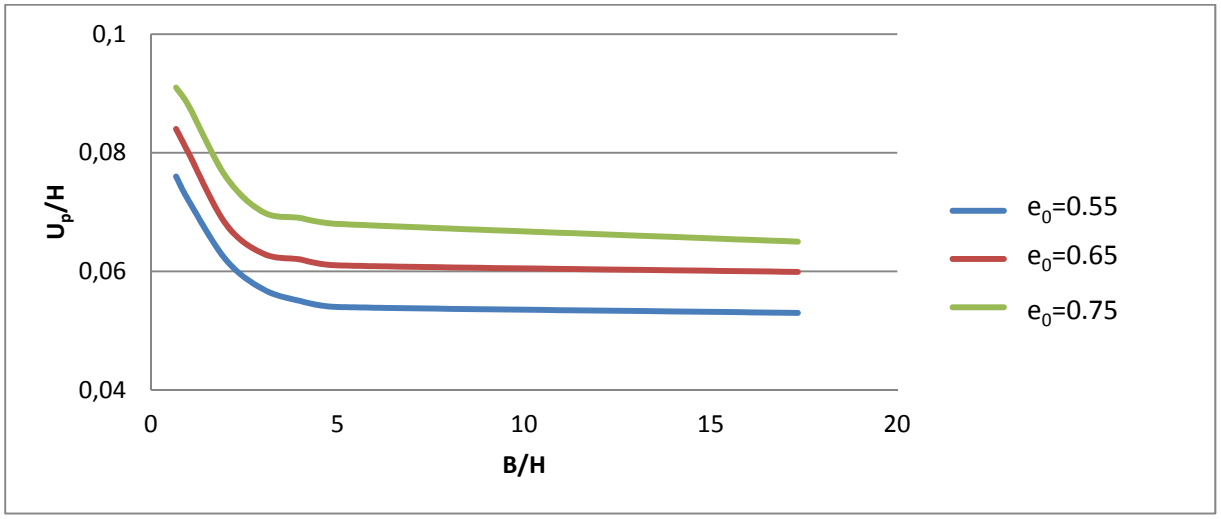

Figure A4: **Relative displacement of the maximum value at the peak U_p/H as a function of the spatial ratio n (H = 15 m)**

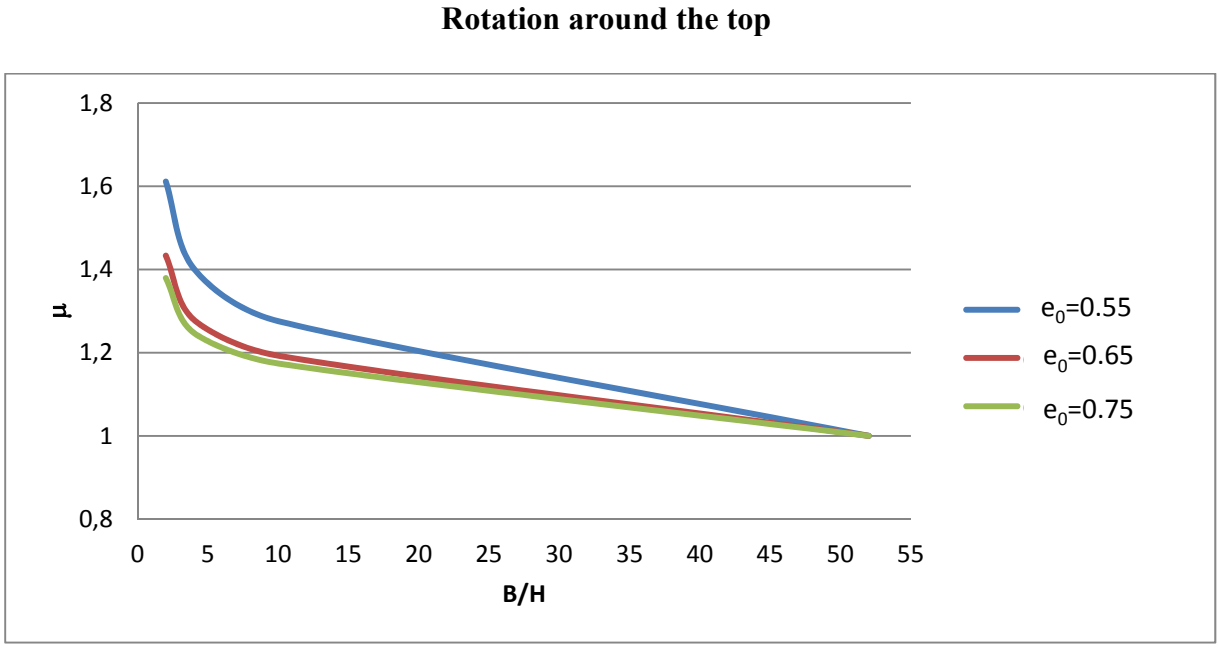

Figure A5: Correction factor μ as function of spatial ratio n (H = 5m)

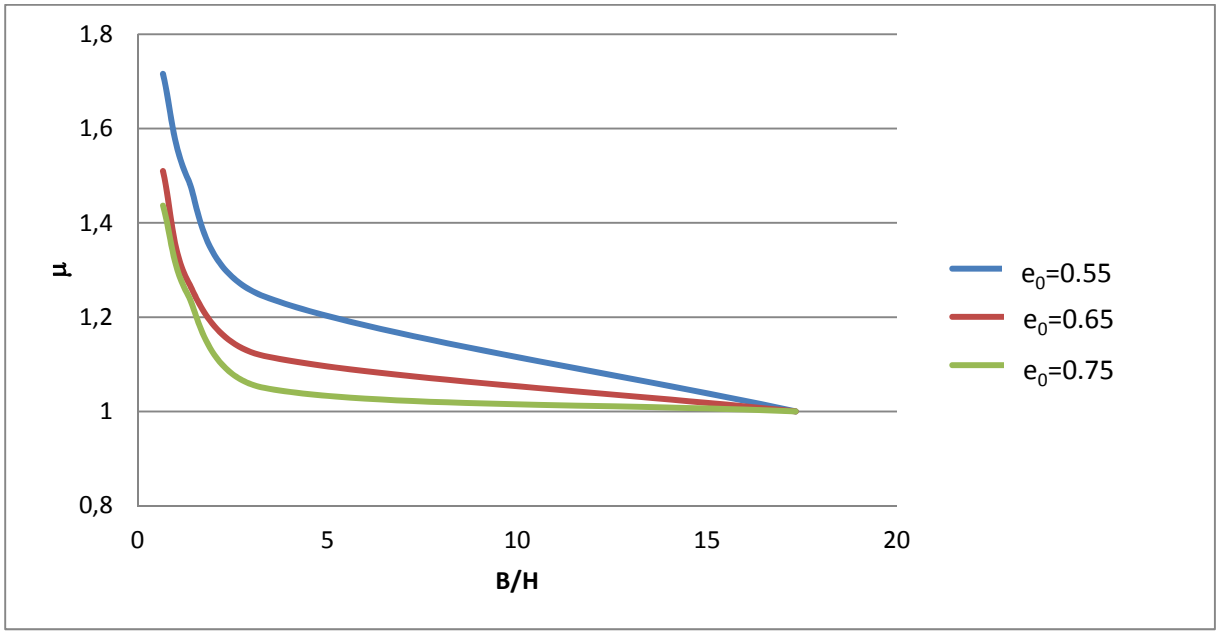

Figure A 6: Correction factor μ as function of spatial ratio n (H = 15m)

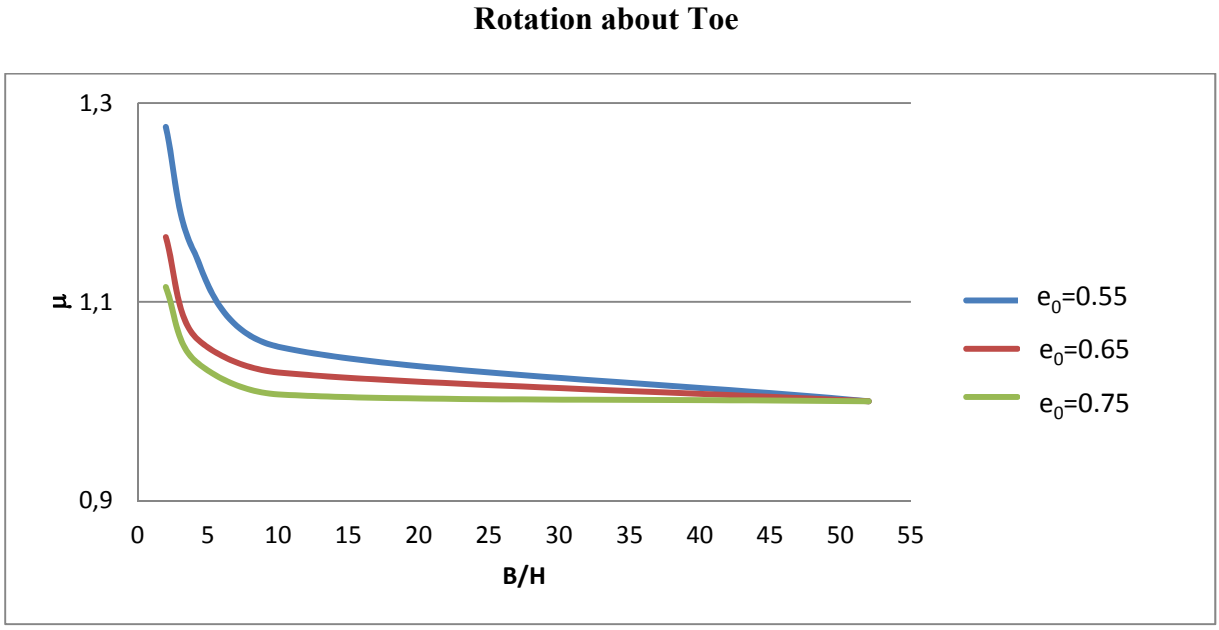

Figure A 7: Correction factor μ as function of spatial ratio n (H = 5m)

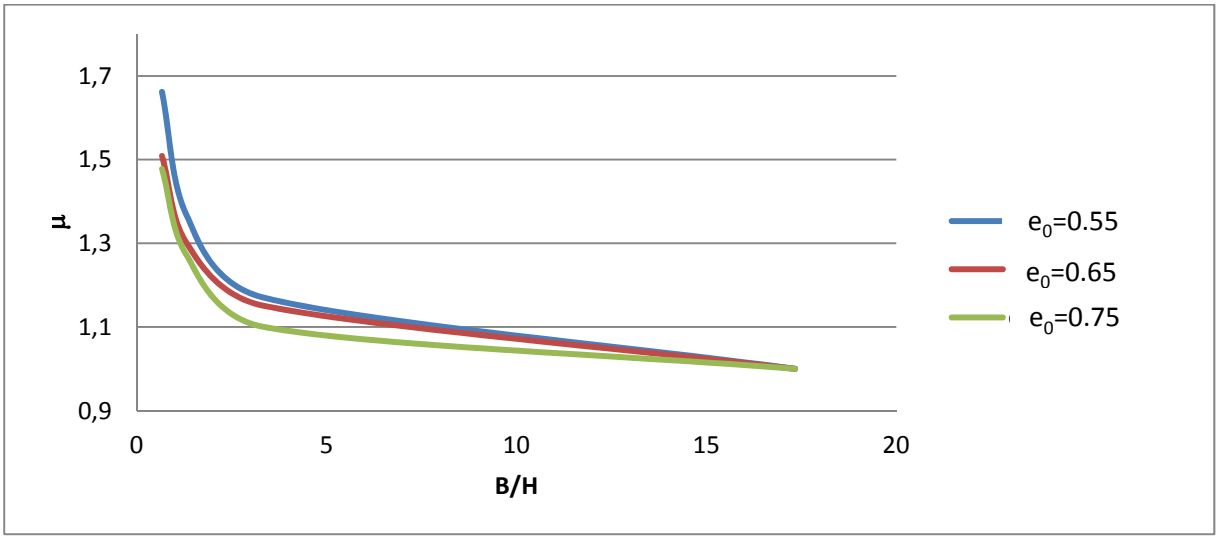

Figure A 8: Correction factor μ as function of spatial ratio n (H = 15m)

Stress distribution

Parallel movement

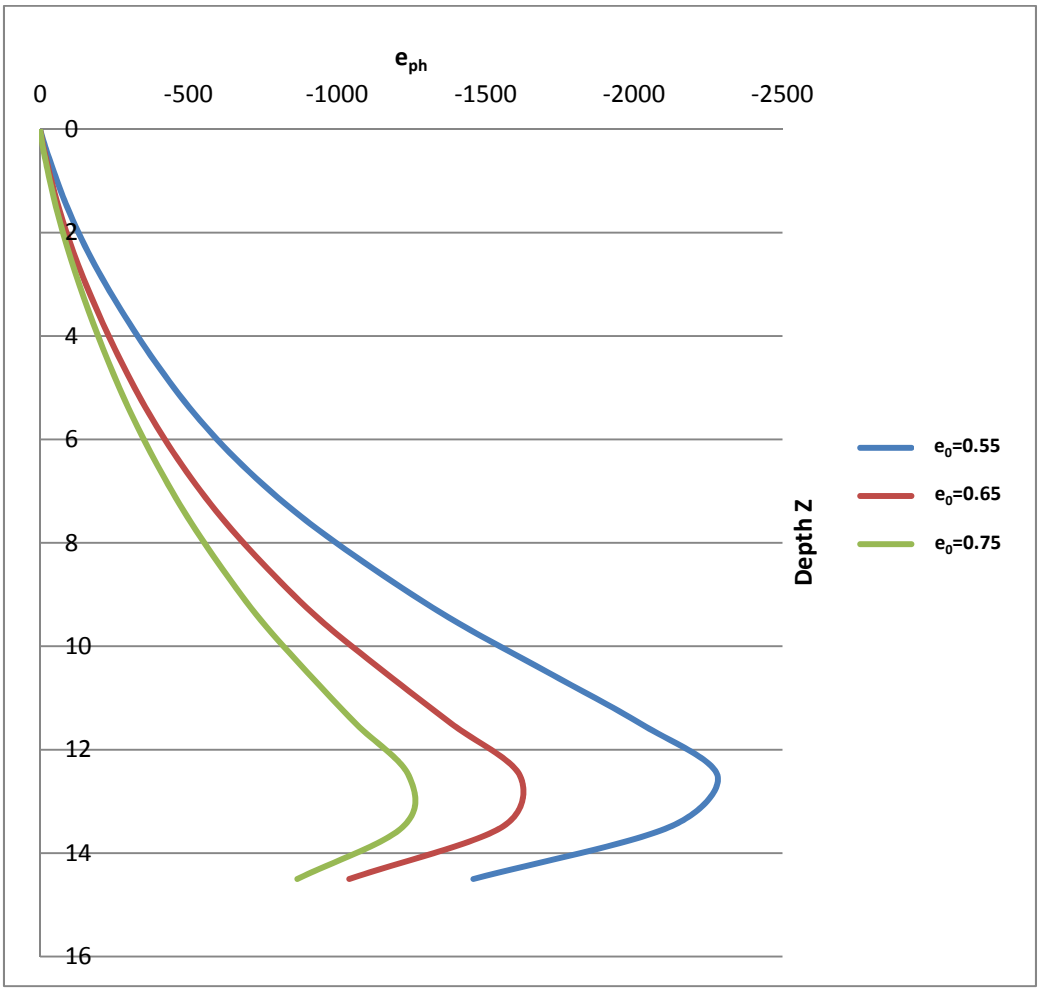

Figure A 9: Horizontal passive stress distributions at peak state in the symmetric plane (x = 0.5 m) for a wall with H = 15 m and B = 10 m (n = 1)

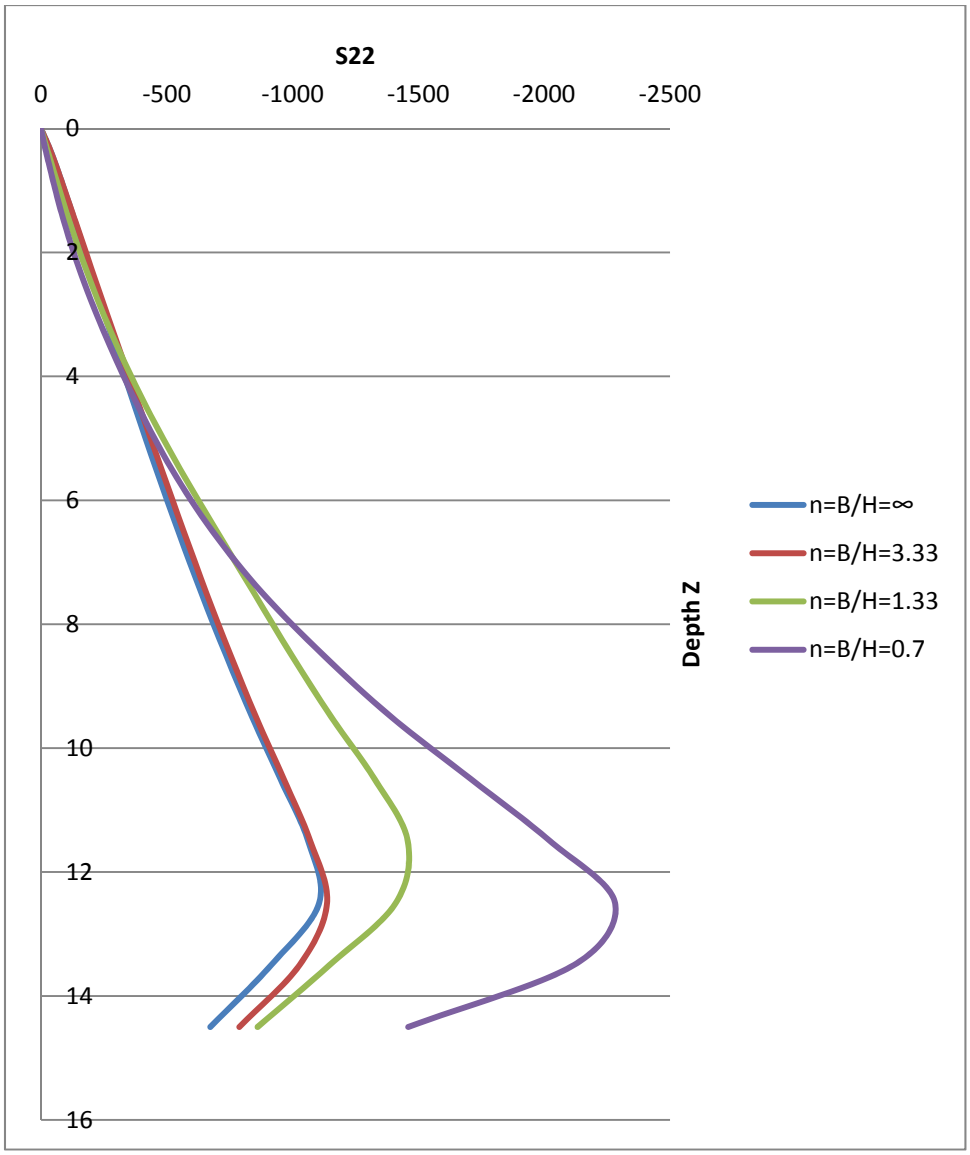

Figure A 10: Stress distributions at peak state in the symmetric plane (x = 0.5 m) for different spatial ratios n (e_0 = 0.55, H = 15 m)

Bisher erschienene Mitteilungshefte des Instituts für Grundbau, Bodenmechanik und Energiewasserbau (IGBE)

Herausgeber: Prof. Dr.-Ing. Dr.-Ing. E.h. Erich Lackner

	Heft 1	Rizkallah, V.	Die erdstatische Bemessung von Wänden und Pfählen in Sandböden (1971)
v)	Heft 2	Lohmann, H.	Ein Beitrag zur Spannungsberechnung in der elastisch-isotropen Halbebene unter tief angreifenden Lasten und Anwendungsmöglichkeiten auf den Baugrund (1971)
v)	Heft 3	Weißenbach, A.	Baugrubensicherung - Berechnung und Konstruktion von Baugrubenumschließungen (1973)
v)	Heft 4	Leonhardt, G.	Die Belastung von starren Rohrleitungen unter Dämmen (1973)
	Heft 5	Rizkallah, V.	Großbohrpfähle - Beitrag zur Abschätzung der lotrechten Tragfähigkeit und der Wirtschaftlichkeit (1973)
	Heft 6	Hahn, F. R.	Ein Beitrag zur Herstellung und Ermittlung der Tragfähigkeit von temporären Erdankern in den Bodenarten der hannoverschen Kreideformation (1974)
	Heft 7	Blümel, W.	Ein Beitrag zum eindimensionalen Konsolidierungsverhalten von Klei im Kompressionsversuch (1974)
	Heft 8	Grade, H.	Ein Beitrag zur Abschätzung der Tragfähigkeit von Verpreßankern in nicht-injizierbaren, nichtbindigen Böden (1974)
	Heft 9	Krämer, U.	Zugwiderstände und Eindringverhalten von Schiffsankern in nichtbindige Böden (1974)
	Heft 10	Krämer, U. Rizkallah, V.	Erfahrungen bei der Ermittlung von Scherparametern im Kastenschergerät (1976)
v)	Heft 11	Richwien, W.	Zum Einfluß der Konsolidierungsdauer auf die wirksame Spannung und die Scherfestigkeit von aufbereitetem Klei (1976)
	Heft 12	Krämer, H.	Abschätzung der Tragfähigkeit von Verpreßankern durch Anwendung der Korrelationstheorie (1977)
	Heft 13	Quast, P.	Ein Beitrag zum Kriechverhalten eines norddeutschen Kleis (1977)
	Heft 14	Paschen, R.	Konsolidierungs- und Scherverhalten von salzhaltigem Klei (1977)
v)	Heft 15	Liedtke, L.	Berechnung der Tragfähigkeit von temporären Erdankern mit der Methode der finiten Elemente (1978)
	Heft 16	Blümel, W.	Ein Verfahren zur Verminderung des Porenwasserdrucks bei Baugruben im Ton durch Entspannungsbohrungen (1979)

Herausgeber: Prof. Dr.-Ing. Dr.-Ing. E.h. Victor Rizkallah

v)	Heft 17	Hellweg, V.	Ein Vorschlag zur Abschätzung des Setzungs- und Sackungsverhaltens nichtbindiger Böden bei Durchnässung (1981)
	Heft 18	Richwien, W.	Das Formänderungs- und Festigkeitsverhalten weicher bindiger Böden (1981)
v)	Heft 19	Maschwitz, G.	Ein Beitrag zur Abschätzung des Tragverhaltens von unbewehrten pfahlartigen Tragelementen (1983)
	Heft 20	Cunze, G.	Ein Beitrag zur Abschätzung des Porenwasserüberdrucks beim Rammen von Verdrängungspfählen in bindige Böden (1985)
	Heft 21	Wehner, T.	Seegangserzeugte Spannungsänderungen im Sandkern eines Seedeichs (1987)

v)	Heft 22	Rizkallah, V. et al.	Festschrift aus Anlaß des 75. Geburtstages von o. Prof. em. Dr.-Ing. Dr.-Ing. E.h. Erich Lackner (1988)
v)	Heft 23	El Sherif, M. M.	Ein Beitrag zur Stabilisierung von bindigen Sedimentböden in Entwicklungsländern (1988)
v)	Heft 24	Buchmann, K.-J.	Zum Tragverhalten ausgesteifter Bohrpfahlwände im Hannoverschen Ton (1988)
	Heft 25	Harder, H.	Numerische Modellierung des "Cone Penetration Tests" in wassergesättigten bindigen Böden (1989)
v)	Heft 26	Rizkallah, V., Hilmer, K.	Bauwerksunterfangung und Baugrundinjektion mit hohen Drücken (Düsenstrahlinjektion) (1989)
v)	Heft 28	Rizkallah, V. et al.	Bauschäden im Spezialtiefbau (Baugruben, Rohrvortriebe, unterirdische Bauanlagen) (1990)
	Heft 29	Rizkallah, V. et al.	Geböschte Baugruben, Baugruben mit Stahlspundwänden (1991)
	Heft 30	Eklu-Natey, D.	Erodierbarkeit zementstabilisierter tropischer Böden im Straßenbau Togos (1992)
	Heft 31	Achmus, M., Rizkallah, V.	Vortrieb von Rechteckprofilen (Belastungen-Bemessung-Anwendung) (1992)
	Heft 32	Jebe, P., Rizkallah, V. et al.	Untersuchung von Hochbauschäden in den neuen Bundesländern Teil 1: Globale Bestandsaufnahme und systematische Erfassung (1993)
	Heft 33	Beilke, O.	Interaktionsverhalten des Bauwerks "Fernwärmeleitung - Bettungsmaterial" (1993)
	Heft 34	Jebe, P., Rizkallah, V. et al.	Untersuchung von Hochbauschäden in den neuen Bundesländern Teil 2: Dokumentation des baulichen Zustands historischer Bauwerke (1993)
v)	Heft 35	Vogel, J.	Untersuchungen bauschadensrelevanter Faktoren beim Vorpressen begehbarer Rohre (1993)
	Heft 36	Vogel, J. et al.	Festschrift aus Anlaß des 60. Geburtstages von Univ.-Prof. Dr.-Ing. V. Rizkallah (1993)
	Heft 38	Vogel, J., Rizkallah, V. et al.	Begehbare und nichtbegehbare Rohrvortriebe Verfahren, Bauschadensfälle und Empfehlungen zur Schadensminimierung (1993)
	Heft 39	Jebe, P., Rizkallah, V.	Beispiele zur Sanierung alter Bausubstanz (1994)
	Heft 41	Achmus, M.	Zur Berechnung der Beanspruchungen und Verschiebungen erdverlegter Fernwärmeleitungen (1995)
	Heft 43	von Bloh, G.	Verfahren zur Ermittlung des Scherverhaltens von Bagger- und Klärschlamm mit der Flügelsonde (1995)
	Heft 44	Clasmeier, H.-D.	Ein Beitrag zur erdstatischen Berechnung von Kreiszellenfangedämmen (1995)
	Heft 45	Hasan, M.	Abschätzung der Eindring- und Reibungswiderstände beim unterirdischen Rohrvortrieb (1996)
	Heft 47	Rizkallah, V. Richwien, A.	Beschleunigte Bestimmung des Wasserdurchlässigkeitsbeiwertes bindiger Böden (1998)
v)	Heft 48	Bruns, T.	Untersuchung des Tragverhaltens von Ortbetonschraubpfählen (1998)
	Heft 49	Döbbelin, J. U. Salveter, G. et al.	Festschrift aus Anlaß des 65. Geburtstages von Univ.-Prof. Dr.-Ing. V. Rizkallah (1998)
	Heft 52	Salveter, G.	Validierung numerischer Verfahren zur Berechnung des Interaktionsverhaltens ”Fernwärmeleitung – Baugrund” (2000)

	Heft 53	Döbbelin, J. U.	Zur geotechnischen Anwendung wissensbasierter Systeme mit Elementen der Fuzzy-Logik (2000)
v)	Heft 54	Baesmann, A. Rizkallah, V.	Berechnung und Bemessung von Pfahl-Plattengründungen (2000)
	Heft 55	Kaiser, J.	Zu Schadensursachen und zur Setzungsproblematik bei herkömmlichen Bauwerksunterfangungen (2000)
	Heft 58	Döbbelin, J.U. Rizkallah, V.	Empfehlungen zur Vermeidung von Planungs- und Ausschreibungsfehlern bei Ingenieurbauwerken (2001)

Herausgeber: Prof. Dr.-Ing. Hanno Müller – Kirchenbauer / Prof. Dr.-Ing. Werner Blümel

Heft 27	Friedrich, W.	Ausbreitung chlorierter Kohlenwasserstoffe bei Einkapselung und Inversionsströmung (1989)
Heft 37	Rogner, J.	Modelle zur Beständigkeitsbewertung von Dichtwandmassen auf der Basis von Lagerungsversuchen (1993)
Heft 40	initiiert von Univ.-Prof.Dr.-Ing. habil. S. Savidis	Festschrift aus Anlaß des 60. Geburtstages von Univ.-Prof. Dr.-Ing. H. Müller – Kirchenbauer
Heft 42	Schlötzer, C.	Filtrationsverhalten von Dichtsuspensionen an flüssigkeitsgestützten Erdwänden (1995)
Heft 46	Brummermann, K.	Schutzschichten für Kunststoffdichtungsbahnen in Deponiebasis-Abdichtungen - Prüfung und Bewertung ihrer Wirksamkeit (1997)
Heft 50	Mbonimpa, M.	Injizierfähigkeit von Feistbindemittelsuspensionen zur Abdichtung von Lockergesteinen (1998)
Heft 51	Düser, O.	Verwertung von aus Bauschutt aufbereitetem Recyclingmaterial in mineralischen Dichtungssystemen (1999)
Heft 56	Stoewahse, C.	Ermittlung des Reibungsverhaltens von Geokunststoffen und Erdstoffen im Rahmenschergerät (2001)
Heft 57	Gawalek, K.	Silikatgele auf Organosilanbasis für Abdichtungsinjektionen im Lockergestein (2001)

Herausgeber: Prof. Dr.-Ing. Martin Achmus / Prof. Dr.-Ing. Werner Blümel

Heft 59	Doll, H.	Dimensionierung von Kunststofflinern – Close-Fit-Verfahren (2001)
Heft 60	Kuk, M.	Untersuchungen zur Beeinflussung der Feistbindemittelausbreitung im Lockergestein durch Filtrationsmechanismen (2004)
Heft 61	Achmus, M. Kaiser, J. tom Wörden, F.	Bauwerkserschütterungen durch Tiefbauarbeiten (2005)
Heft 62	Mansour, B.G.S.	Investigations on Design and Rehabilitation Options for River Barrages with Special Respect to Piping (2005)
Heft 63	Achmus, M.	Bodenmechanik und Grundbau - Grundlagen und Konzepte (2007)
Heft 64	Weidlich, I.	Untersuchung zur Reibung an zyklisch axial verschobenen erdverlegten Rohren (2008)
Heft 65	Kuo, Y.-S.	On the behavior of large-diameter piles under cyclic lateral load (2008)
Heft 66	Maßmann, J.	Modeling of Excavation Induced Coupled Hydraulic-Mechanical Processes in Claystone (2009)

Heft 67	Müller-Kirchenbauer, A.	Funktionsnachweis für geotextile Tondichtungsbahnen in Deponieoberflächenabdichtungen (2009)
Heft 68	tom Wörden, F.	Untersuchungen zum räumlichen aktiven Erddruck auf starre vertikale Bauteile im nichtbindigen Boden (2010)
Heft 69	Quast, A.	Zur Baugrundsteifigkeit bei der gesamtdynamischen Berechnung von Windenergieanlagen (2010)
Heft 70	Bosseler, B.	Prüfung und Bewertung von Produkten und Verfahren zum Bau und zur Instandhaltung unterirdicher Kanälen und Leitungen (2010)

Bisher erschienene Mitteilungshefte des Instituts für Geotechnik (IGtH)

Herausgeber: Prof. Dr.-Ing. Martin Achmus

Heft 71	Peralta, P.	Investigations on the behavior of large diameter piles under long-term lateral cyclic loading in cohesionless soil (2010)
Heft 72	Ahlinhan, M.F.	Untersuchungen zur inneren Erosionsstabilität nichtbindiger Böden (2011)
Heft 73	Linero-Molina, C.	Vulkanische Ascheböden als Straßenbaustoff (2011)
Heft 74	Ghassoun, S.	Numerical Modeling of Spatial Passive Earth Pressure (2012)

v) = vergriffen

Schutzgebühr: € 15,–/Heft